Synthesis of Biogenic Carbon-Based Nanomaterials for Targeted Delivery, Antibacterial-Wound Healing and Sensing

A Dissertation

Submitted in Partial Fulfillment of the

Requirements for the Degree of

Doctor of Philosophy in Chemistry

By

Pallabi Paul

Roll No. 216122026

Department of Chemistry

Indian Institute of Technology Guwahati

Guwahati, Assam-781039

August 2025

Dedicated

to

My family

INDIAN INSTITUTE OF TECHNOLOGY GUWAHATI

Department of Chemistry

Guwahati- 781039

STATEMENT

I do hereby declare that the matter embodied in this thesis entitled **"Synthesis of Biogenic Carbon-Based Nanomaterials for Targeted Delivery, Antibacterial-Wound Healing and Sensing"** is a work of research and investigation carried out by me, under the supervision of Dr. Lal Mohan Kundu, Department of Chemistry, Indian Institute of Technology, Guwahati, Assam, India.

In keeping with the general practice of reporting scientific observations, due acknowledgments have been made wherever the work described is based on other investigators' findings. I further declare that this work has not been submitted anywhere else for any degree, diploma, associateship, membership, etc., of any Institute or University to the best of my knowledge.

August, 2025 Pallabi Paul

IIT Guwahati

INDIAN INSTITUTE OF TECHNOLOGY GUWAHATI

Department of Chemistry

Guwahati- 781039

CERTIFICATE

It is certified that the thesis entitled **"Synthesis of Biogenic Carbon-Based Nanomaterials for Targeted Delivery, Antibacterial-Wound Healing and Sensing"** being submitted to the Indian Institute of Technology Guwahati by Pallabi Paul (Roll. No. 216122026) for the award of the degree of Doctor of Philosophy in Department of Chemistry, is a bonafide record of research work carried out by her. The information and data reported by her are solely the results of her original findings. She has diligently carried out the investigations and followed the guidelines of the laboratory. This work has not been submitted elsewhere for any degree or diploma.

Dr. Lal Mohan Kundu
(Supervisor)
Associate Professor
Department of Chemistry,
IIT Guwahati
Guwahati-781039, Assam,
India.

ACKNOWLEDGMENT

It gives me immense pleasure in thanking all the people who have contributed significantly throughout this incredible journey of my Ph.D. This thesis would not have been possible without their guidance, support, and encouragement, and I am genuinely obliged and grateful for their time and effort.

I want to extend my deepest and heartfelt gratitude towards my thesis supervisor ***Prof. Lal Mohan Kundu,*** for mentoring me throughout this research period and helping me explore and understand the fascinating field of science and technology with innovative ideas. His esteemed guidance, advice, and encouragement at every step have enabled me to propel my research in a fruitful direction. I would also like to thank him for providing a well-equipped laboratory, vast resources, and dedicated work culture that has enabled my working in his laboratory a pleasant experience. Above all these, he has always been an understanding, kind, and caring guardian to me on the campus. Thank you so much, Sir.

I want to express my gratefulness to my doctoral committee members ***Prof. Bhubaneshwar Mandal***, ***Prof. Gopal Das***, and ***Prof. Ajaikumar B. Kunnumakkara,*** for their critical assessments and valuable suggestions that helped me to focus on the lacking portion of my research and polishing my thesis.

I gratefully acknowledge ***Prof. Siddhartha S. Ghosh***, IIT Guwahati, for helping me in conducting the cell studies of my compound in his lab.

During this period, I had a great time with my research group, who have helped me and gave me a pleasant lab environment. I want to give my heartfelt thanks to my fellow lab mates, ***Mr. Gourav Bhattacharjee***, ***Mrs. Himadree Das***, ***Ms. Neeharika Baruah, Mr. Yogesh Kumar Verma, Mr. Avinash Kumar and Ms. Hiyashree Dutta*** for their constant support professionally and emotionally. I would like to thank my senior ***Ms. Himali Horo*** for her unconditional support during my PhD research. My special thanks will be to ***Mr. Hirak Jyoti Roy, Mr. Gourav Bhattacharjee, Ms. Neeharika Baruah and Ms. Sawna Roy*** for their help

in the biological studies of my work. I also owe my deep sense of thanks to all the staff members of the Department of Chemistry, Centre for the Environment, and CIF, IIT Guwahati for their assistance and technical support.

My special thanks will be to ***IIT Guwahati*** for providing me the fellowship and a healthy atmosphere. For all the instrumental facilities required for my research work, I am truly thankful to ***Center for the Environment***, ***Department of Chemistry*** and ***CIF (IIT Guwahati)***.

I cannot find words to express my gratitude towards my friends ***Srijan, Roop, Malay, Palak, Maitrey, Kiran, Priya, Bipasa and Nandini*** or sharing countless cherished moments during my time at IIT Guwahati. From late-night discussions and joyful celebrations to road trips and research talks, your presence filled my days with positivity and strength. Thank you for making this journey so memorable and uplifting.

At the very end, I would like to thank ***Parents (Ratan Kumar Paul and Jharna Paul)***, ***Bhai (Subhajit Paul) and my husband (Dr. Santu Mandal)*** for their endless love, prayer, and encouragement. This thesis would have remained a dream without their support. And above all, I thank Almighty for everything.

Thank you all for sharing my journey.

Pallabi Paul

August, 2025

CONTENT

ABSTRACT

The synopsis report entitled **"Synthesis of Biogenic Carbon-Based Nanomaterials for Targeted Delivery, Antibacterial-Wound Healing and Sensing"** is divided in five chapters that includes introduction, literature review, experimental findings, summary of research work and future prospects.

- **Chapter 1** presents a concise introduction to the biopolymer-based nanomaterials, their impact on designing biomedical system and sensors. This also highlights the rising of carbon dots their design, synthesis and applications.
- **Chapter 2** presents synthesis of kappa-carrageenan and lysine derived carbon dots. Lysine was used to enhance the photoluminescence properties of carbon dots. The carbon dots can selectively detect folic acid in aqueous medium. The sensitivity of the sensor was checked in real samples. Further, the carbon dots were modified with biotin to make cancer cell-specific delivery of model drug 5-Fu. The cytotoxicity and hemocompatibility of biotin modified drug cargo were evaluated and the target-specificity was evaluated through bioimaging.
- **Chapter 3** presents the development of casein and thymine-derived carbon dots. The carbon dots can selectively detect mercury ion and tetracycline derivatives in aqueous media. The sensor exhibited exceptionally low limits of detection for mercury ions, below the tolerable limit prescribed by the U.S. EPA, as well as for tetracyclines Further, the detection method was integrated to portable paper strips for convenient on-site detection. The efficiency of the sensor was evaluated in different aqueous samples and biological fluids, confirming its practical application.
- **Chapter 4** presents the fabrication of kappa-carrageenan and casein-derived carbon dots as a potential precursor for silver nanoparticle synthesis. The method enables stability of silver nanoparticles in aqueous medium. moreover, surface functional groups help to improve

water solubility of nanoparticles. The antibacterial efficacy of carbon dot-capped silver nanoparticles was examined against *E. coli* and *S. aureus* bacteria.

- **Chapter 5** consists formulation of hydrocaffeic acid modified chitosan hydrogel system. Acrylic acid and conjugated chitosan were crosslinked to form the hydrogel in a radical polymerization reaction. The system exhibited antibacterial and antioxidant properties itself. Further, incorporation of carbon dot-capped silver nanoparticles improved the antibacterial and antioxidant properties of the hydrogel. The hydrogel system exhibited good wound healing ability, biocompatibility and hemocompatibility.

LIST OF ABBREVIATIONS

AgNp	Silver nanoparticle
AIE	Aggregation induced emission
Cas	Casein
CDs	Carbon Dots
CG	Chitosan gel
CH	Chitosan
CLSM	Confocal laser scanning microscope
ClTC	Chlortetracycline
CMC	Carboxymethyl cellulose
DCC	*N*,*N*′-Dicyclohexylcarbodiimide
DD %	Percentage degree of deacetylation
DDS	Drug delivery system
DLS	Dynamic Light Scattering
DMEM	Modified eagle medium
DOX	Doxorubicin
DTC	Doxycycline
EC/*E. coli*	Escherichia coli
EDC	1-Ethyl-3-(3-dimethylaminopropyl) carbodiimide
EDX	Energy Dispersive X-Ray Analysis
FA	Folic acid
FBS	Fetal bovine serum
FL	Fluorescein
FESEM	Field Emission Scanning Electron Microscope
FRET	Förster resonance electron transfer

FETEM	Field Emission Transmission Electron Microscope
FT-IR	Fourier Transform Infrared Spectroscopy
5-FU	5-fluorouracil
IC_{50}	Half-maximal inhibitory concentration
IFE	Inner filter effect
KBr	Potassium Bromide
KC	*Kappa*-carrageenan
KPS	Potassium persulfate
LB	Luria Bertani
LOD	Limit of detection
LMWC	Low molecular weight chitosan
LYS	Lysine
MBA	Methylenebisacrylamide
MIC	Minimum inhibitory concentration
MTT	3-(4,5-dimethylthiazol-2-yl)-2,5diphenyl tetrazolium bromide
MW	Molecular weight
NHS	N-Hydroxysuccinimide
NIR	Near-infrared
PDI	Polydispersity index
PEG	Polyethylene glycol
PET	Photoinduced electron transfer
PI	Propidium iodide
PTX	Paclitaxel
SA	*S. aureus*
SF	Silk fibroin

SPR	Surface plasmon resonance
S-V	Stern-Volmer
TC	Tetracycline
USEPA	United States Environmental Protection Agency
WHO	World Health Organization
XRD	X-Ray Diffraction

LIST OF SYMBOLS

a.u.	Arbitrary unit
nm	Nanometer
mm	Millimeter
cm	Centimeter
cm^{-1}	Inverse centimeter
µl	Microliter
ml	Milliliter
L	Liter
mg	Milligram
g	Gram
c	Concentration
nM	Nanomolar
µM	Micromolar
mM	Millimolar
mmol	Millimole
mg/ml	Milligram per milliliter
µg/ml	Microgram per milliliter
w/w	Weight/weight
v/v	Volume/volume
s	Seconds
min	Minutes
h	Hours
°C	Degree Celsius

°C/min	Degree Celsius per minute
A	Absorbance
% T	Transmittance
λ	Wavelength
Da	Dalton
kDa	Kilo Dalton
Rpm	Rotation per minute
cps	Cycles per second
θ	Theta
W	Watt
%	Percent
±	Plus-minus
×	Multiplication
η	Refractive index
E	Integrated fluorescence intensity
Å	Angstrom

LIST OF TABLES

LIST OF FIGURES

Chapter 1. Introduction and Literature Review

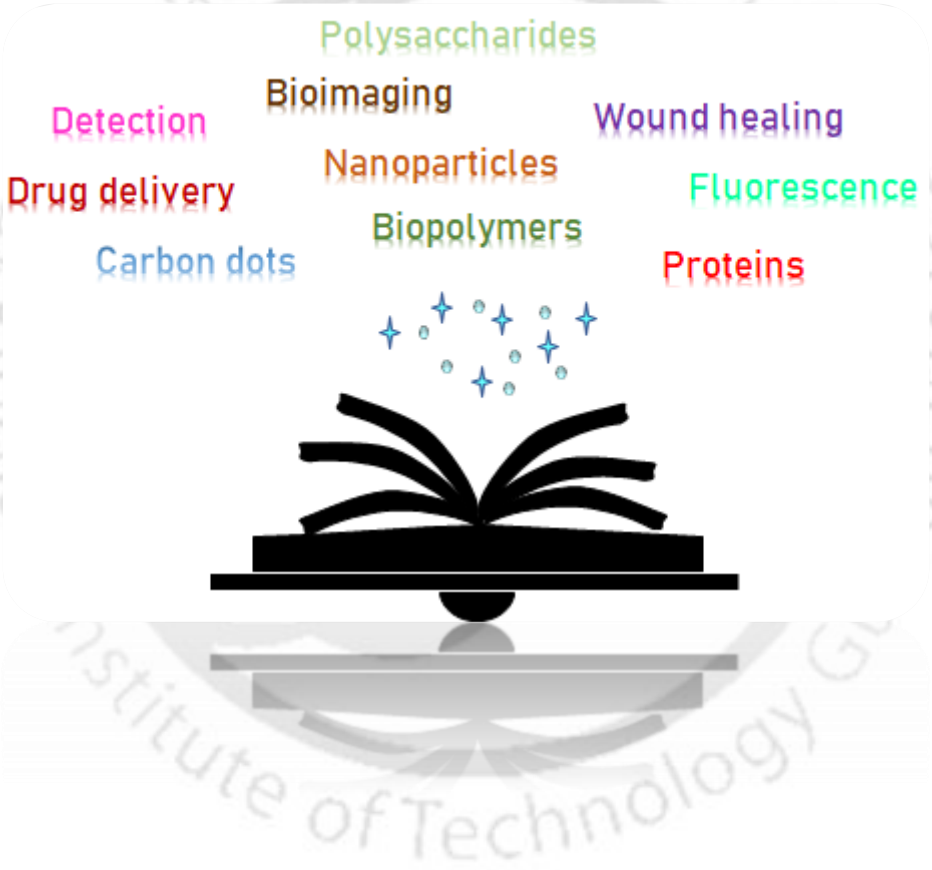

1.1. Introduction

Cancer therapeutics, wound healing, and bioremediation, while often treated as distinct application areas, are connected by their reliance on shared material properties and molecular interactions. In this regard, biopolymer-based materials are employed for their capacity to bind, sequester, transport, or interact selectively with biological or chemical targets. Therefore, we will be discussing these diverse applications together, highlighting how common structural and binding characteristics of biopolymers can be leveraged across medical and environmental systems, providing a coherent framework for understanding their multifunctional potential.

Cancer is one of the lethal diseases caused by the uncontrolled division of abnormal cells. This abnormal growth, often triggered by genetic mutations, can occur in any part of the body and potentially spread to other regions. In response to the significant mortality associated with cancer, researchers have developed several antitumor drugs, including 5-fluorouracil, doxorubicin, paclitaxel, ciprofloxacin, etc. (Figure 1.1). While these drugs exhibit cytotoxic effects against tumor cells, they also damage healthy cells due to their lack of target specificity. Furthermore, their low bioavailability often requires high doses, increasing the risk of severe long-term side effects. To address these limitations, the development of target-specific drug delivery systems is essential. Nanomaterials offer great potential as drug carriers due to their tunable surface properties, ability for chemical modification, small size, and stimuli-responsive behavior. However, concerns regarding their toxicity and biocompatibility remain a major challenge. Therefore, there is an urgent need for the development of safe, efficient, and target-specific nanocarrier systems for improved cancer therapy.

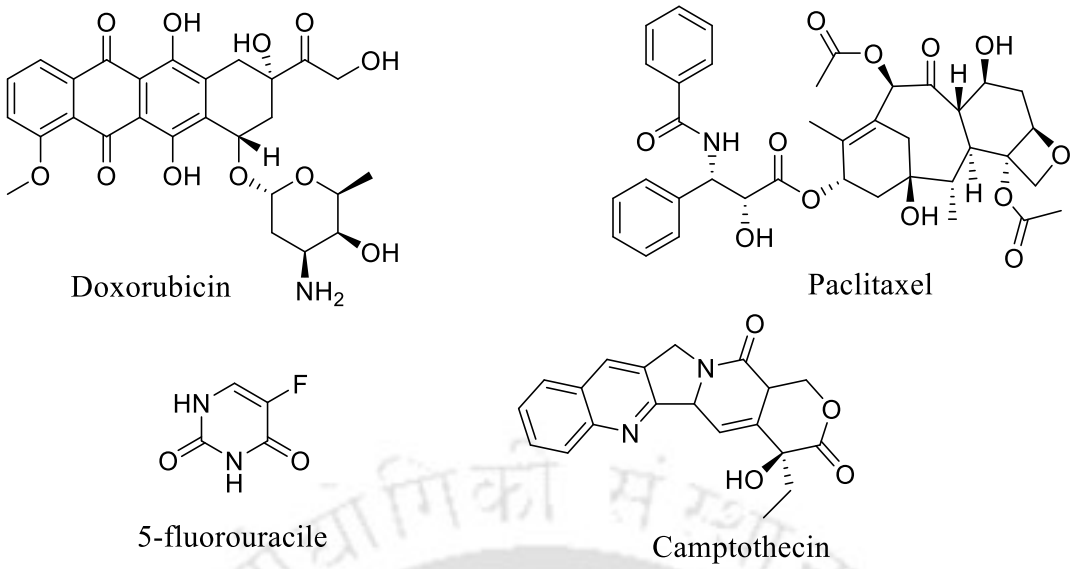

Figure 1.1. Chemical structure of some antitumor drugs.

Abrasions are among the most common types of wounds encountered in daily life. The wound healing process goes through a complex and concerted path (Figure 1.2).[1] However, even simple wounds can develop into chronic wounds if they fail to progress through the normal stages of healing within a predictable time frame, typically persisting for more than 4 to 6 weeks. Chronic wounds possess significant clinical risks, such as infection, inflammation, tissue necrosis, and a substantial economic burden on healthcare systems. Moreover, bacterial infection leads the chronic wound at critical stage. Therefore, effective multifunctional wound care systems are necessary.

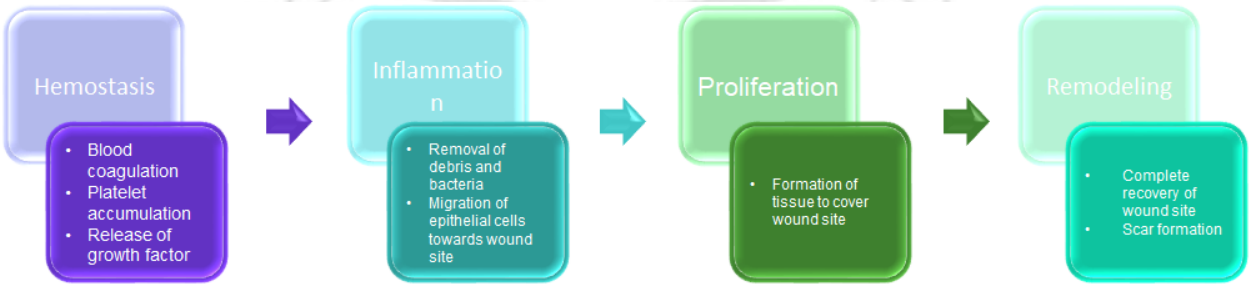

Figure 1.2. The phases of wound healing.

Apart from the biomedical sector, water remediation is critically important, especially in light of the growing global population and the limited availability of clean freshwater. Improper

waste disposal, industrialization, and agricultural runoff are the common causes of groundwater contamination with dyes, pesticides, antibiotics, heavy metals, pathogens, etc. This contamination poses a serious risk to humans and the ecosystem. Therefore, developing cost-effective, efficient materials is necessary to monitor the level of contaminants and their removal from the water body.

The use of biopolymers for the fabrication of nanomaterials significantly impacts the development of such low-cost, sustainable, and biocompatible materials. Here, we will be discussing the benefits of bio-polymer-derived nanomaterials.

Biopolymer-derived Nanomaterials: Impact on Drug Delivery

Biopolymer-derived nanoparticles serve as efficient carriers for therapeutic agents due to their biodegradability, biocompatibility, non-toxicity, and low immunogenicity. Drugs can be incorporated into nanoparticles by surface adsorption after nanoparticle formation or encapsulation during synthesis. Drug loading efficiency critically depends on factors like particle size, hydrophilic nature of the drug, molecular weight, and drug–polymer interactions. However, drug release mechanisms occur through surface desorption, diffusion through the matrix, polymer erosion, or a combination of these. Biopolymer-derived nanoparticles provide adequate advantages as they enhance drug absorption, protect against degradation, extend circulation time, and enable targeted delivery with simple surface modifications. The drug delivery mechanism depends on the epithelial barriers and vascular endothelium (continuous in healthy tissue and fenestrated in pathological conditions). The junction between continuous endothelium is between 2 and 6 nm in healthy tissue. However, the fenestrated endothelium has large openings between the junctions of 100 nm to 2 µm. Due to their small size, nanoparticles can easily cross biological barriers, making them promising carriers for drug or gene delivery. Xie et al. reported the synthesis of folic acid conjugated chitosan nanoparticles with an average particle size of 100-200 nm using electrostatic interaction.[2] The nanoparticles

exhibited enhanced half-life and 5-6 times greater cellular uptake in the rat breast cancer cell line (MADB-106). Jaradat et al. developed alginate nanoparticles via the proton gelation technique for the delivery of 5-Fluorouracil.[3] Zhang et al. reported the synthesis of silk nanoparticles containing dimethylcurcumin (ASC-J9) and copper sulfide (CuS).[4] The composite material exhibited synergetic photothermal ability against breast cancer. The nanocarriers exhibited high cellular uptake and biocompatibility, showing strong selectivity for cancer cells and potent anticancer activity. Additionally, their therapeutic efficacy was further amplified upon exposure to infrared (IR) laser irradiation. Moreover, the composite exhibited controlled tumor growth and good hemocompatibility.

Biopolymer-derived Nanomaterials: Impact on Wound Healing

Biopolymer-based materials offer significant advantages in tissue engineering and wound healing due to their reported biodegradability, biocompatibility, low toxicity, and generally favorable immunogenic profiles.[5,6] Moreover, hydrophilic functional groups enable cell adhesion and proliferation, making them ideal materials for tissue regeneration. Biopolymers such as collagen, chitosan, and alginate can degrade into non-toxic byproducts, with degradation rates that can be tuned to match the healing process. Biopolymers help to maintain a moist environment, promote fluid exchange, and, in some cases, provide antimicrobial activity. The mechanical properties of the biopolymers can be tuned according to tissue types. These features collectively make biopolymers highly valuable for advanced wound dressing applications. Lu et al. reported the synthesis of silver nanoparticle/chitosan composite dressing.[7] The outer layer of the dressing was modified with stearic acid to maintain hydrophobicity, which could exhibit self-cleaning properties by minimizing water and contaminant adhesion. Khan et al. reported silicon dioxide nanoparticles (n-SiO_2) and hydroxyapatite nanoparticles containing xyloglucan-methacrylic acid-based nanocomposite.[8] The porosity of the material can be regulated by n-SiO_2 composition. Moreover, the

nanocomposite exhibited antibacterial activity against gram-positive and gram-negative bacteria along with tissue engineering properties. Additionally, biopolymer-derived nanofibers through electrospinning have gathered wide attention in tissue engineering.[9]

Biopolymer-derived Nanomaterials: Impact on Pollutant Detection

Over the past decades, nanomaterials have been extensively used as a potential replacement for traditional water treatment methods at reduced cost and sustainably. Due to their small size and large surface area, nanomaterials provide dense reaction sites. The dispersion of nanoparticles in water faces challenges like mineral sorption, aggregation, microbiological activity, and the formation of corrosion products. Surfactants and biopolymers are useful alternatives to prevent aggregation, improve stability, and incorporate antimicrobial activity. However, surfactants generate toxicity in the water system. Alternatively, biopolymers offer several advantages like biodegradability, non-toxicity, disinfection, antimicrobial activity, etc. Development of biopolymer-based nanomaterials for water remediation serves to monitor the level of pollutants, separation of pollutants from water, degradation, and removal of contaminants. Mohamed et al. reported a molecular imprinted chitosan-titanium oxide nanocomposite (CTNC) for the selective removal of Rose Bengal dye from industrial water.[10] CTNC exhibited high surface area and uniform mesoporous channels that can uptake 79.3 mg/g dye with monolayer adsorption. Saraf et al. reported a starch hydrogel manganese dioxide (MnO_2) nanocomposite and superabsorbent cotton fabric that exhibited photo catalytic activity, antibacterial properties, and biocompatibility.[11] Mohammadi et al. reported nitrogen and fluorinated carbon dots (N, F-CDs) modified sodium alginate hydrogel for the detection of polyfluoroalkyl substances (PFASs).[12] The sensor exhibited a limit of detection as low as 0.001 ppt with high sensitivity.

We have discussed various biopolymer-based nanomaterials, including non-metallic nanoparticles such as biopolymeric nanoparticles (e.g., chitosan nanoparticles, silk

nanoparticles), metallic nanoparticles (e.g., silver, gold, and manganese oxide nanoparticles), nanocomposites, and carbon dots (CDs). Among these, CDs represent a particularly promising class of nanomaterials due to their excellent water dispersibility, intrinsic photoluminescence, low cost, and biocompatibility. Furthermore, surface modification of CDs can significantly enhance their therapeutic efficiency, making them highly versatile for biomedical and other advanced applications. Therefore, we will be discussing the synthesis, functionalization, and broad application potential of CDs in the next section.

1.2. Historical Evaluation of CDs

Carbon-based nanomaterials have gathered great attention in a broad range of applications. CDs are one of the fluorescent carbon-based nanomaterials with a zero-dimensional, quasi-spherical shape and a size of <10 nm. Excellent photoluminescence, high quantum yields, simple preparation, and low toxicity make CDs appealing for a broad range of applications in sensing and detection, catalysis, optoelectronics, biomedicine, drug delivery, bioimaging, *etc*. Sun et al. reported CDs for the first time during the arc discharge method synthesis of single-walled carbon tubes (SWCT).[13] Later, new synthetic techniques such as laser ablation, chemical oxidation, pyrolysis, and template-assisted path were discovered. As synthesis methods evolved, so did doping strategies. Doping significantly expanded the range of CDs' tunable properties and enhanced their optical, electronic, and chemical features.

1.3. Structural Properties of CDs

CDs can be classified into four types based on carbon core structure and surface groups, namely, i) graphene quantum dots (GQDs), ii) carbon quantum dots (CQDs), iii) carbon nanodots (CNDs), and iv) carbonized polymer dots (CPDs).[14–16] GQDs consist of small graphene fragments with a crystalline graphene lattice and chemical groups on the edge or between interlayers. These contribute to unique properties such as the edge effect and the

quantum confinement effect (QCE).[17] GQDs possess a lateral diameter of less than 20 nm, and a few layers of graphene sheets, with a typical height of ≈2.5 nm.[18] CQDs are usually spherical and possess functional groups on the surface. CQDs exhibit intrinsic state luminescence and size QCE, where the QCE of size enables the regulation of the wavelength of photoluminescence.[19,20] CNDs have a carbonized amorphous nature. The photoluminescent property of CNDs originates from the graphitic carbon core and defects.[21] CPDs are synthesized from polymers and retain some structural characteristics of the parent polymers and various surface functional groups.[22] The photoluminescence property of CPDs originates from the combination of molecular state, subdomain state, surface state, and crosslink-enhanced emission effect.[23,24] The structure of CDs often describes a core-shell structure where the core generally consists of sp^2 or sp^3 hybridized carbon atoms and the shell comprises abundant surface functional groups.[25,26] The core structure of CDs depends on several parameters, such as precursors, reaction conditions, degree of polymerization, carbonization, etc. Moreover, the size and core structure are regulated by QCE. The change in electronic energy levels near the Fermi level from continuous to discrete, depending upon particle size, is known as QCE.[27] QCE induces a bandgap in the CDs, leading to enhanced optical and electronic properties. Similar to QCE, various defects, such as line, plane, volume, and plane defects, are observed in CDs.[28] These defects play a crucial role in the photophysical and surface properties of CDs. The number of defects can be tuned by introducing oxygen atom, which results in more conjugated π-domains.[29]

1.4. Optical Features of CDs

The CDs exhibit strong absorption in the UV region and a shoulder peak from 300 to 400 nm. The UV absorption is attributed to π-π* transition within the aromatic core, while the shoulder peak is ascribed to the n-π* transition from the functional groups with lone pair electrons, respectively.[30,31] In addition to their absorption characteristics, CDs possess intrinsic

fluorescence properties. The fluorescence originates from different mechanisms such as luminescence from the π-domain with QCE, luminescence due to interaction of surface groups and carbon core, specific molecular structure, and CEE effect. Conjugation with complex energy levels and fluorescence centers causes excitation-dependent emission.[32] Diverse photoluminescence states and chemical environments are the reason for solvent-dependent and excitation-dependent emission of CDs. However, fluorescence intensity can be tuned using surface passivation and the CEE effect. Surface passivation by electronegative hetero atoms like nitrogen, sulfur, phosphorus, boron, etc., induces excitations at the defect band gap, enabling the red shift in emission and enhanced photoluminescence.[33] Moreover, the optical property of CDs is highly inclined towards the choice of precursors, doping element, pH of the medium, pressure, reaction time, and temperature. Apart from conventional photoluminescence, CDs can exhibit two or more photon absorption, aggregation-induced emission (AIE), room temperature phosphorescence (RTP), and thermally activated delayed fluorescence [34–37]

1.5. Synthetic Methods

In pursuing high-quality CDs with superior photoluminescence properties and expanded applications, continuous advancements have been made in the synthetic procedure. Generally, two main approaches are followed: top-down and bottom-up (Figure 1.3).

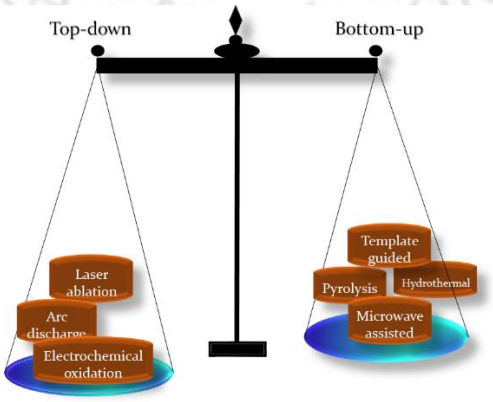

Figure 1.3. Synthetic method of CDs.

1.5.1. Top-down

During the top-down approach, large mass carbon materials are cut down to small carbon nanoparticles such as activated carbon, graphene, graphite, nanodiamonds, etc. Arc discharge, electrochemical synthesis, and laser ablation are the standard applied techniques in the top-down method. In this process, perfect sp^2 domains are generated in the carbon core, but the luminescent property is compromised. In the arc-discharge method, carbon atoms are evaporated by a plasma of helium gas between two carbon electrodes in a controlled environment.[13] This method has several advantages: simple purification, an environmentally friendly technique, and small-sized material generation. However, the process is limited to low yield and difficulty in surface passivation. Caigas and group reported diethylenetriamine-doped WS_2 QDs using the pulsed laser ablation method. In this method, an ethanol mixture of WS_2 with diethylenetriamine was used. The mixture was first vaporized and pulsed with the laser. Later, the vapor was condensed and purified to obtain QDs.[38] The technique has adequate advantages, such as CDs can be produced in a controlled size and with high purity. Despite these benefits, the method presents limitations, including complex steps and harsh conditions to enhance photoluminescence. Wang et al. reported an electrochemical method for the synthesis of CDs from glycine in NaOH solution. In this strongly basic environment, the ammonium group of glycine is deprotonated, generating the anionic form of the molecule. This anionic glycine is more nucleophilic and can undergo electro-polymerization at the electrode surface. Subsequent carbonization and surface passivation steps lead to the formation of CDs with stable photoluminescent properties.[39] Similar to previous top-down methods, this is also affected by a complex surface passivation process, time-consuming synthesis, and high synthetic cost.

1.5.2. Bottom-up

A bottom-up approach is used to overcome the complexity and enhance the photoluminescent property. In this process, CDs are prepared using carbonization and condensation. Pyrolysis, hydrothermal, template-assisted, microwave, and ultrasonic are examples of a bottom-up approach. In pyrolysis, precursor materials are carbonized at high temperatures. Horo et al. reported the synthesis of CDs from chitosan and silk using the pyrolysis method. The reaction yielded uniformly sized CDs with 65% quantum yield.[6] Pyrolysis has several advantages, such as easy doping, low synthetic cost, and a simple pathway. Template-assisted CDs require a silica template to guide the CDs' formation. Using silica nanospheres as a template, Liu and his group reported the synthesis of CDs from phenol/formaldehyde using pyrolysis.[40] The template helps to grow in a specific shape or structure and prevents aggregation. The template can be removed using NaOH or HF solution treatment. Prathap et al. fabricated CDs from *Prosopis juliflora* leaf extract using hydrothermal treatment.[41] In this technique, the precursor material is suspended in water and carbonized at a temperature and pressure. Similarly, microwave or ultrasound-assisted CD synthesis involves simple pyrolysis in the presence of a microwave or ultrasound.[42]

1.6. Factors Affecting Photoluminescence of CDs

Tunable photoluminescence is one of the unique advantages that contribute to the wide range of applications of CDs. Both the core and surface structures are responsible for the photoluminescence behavior of CDs (Figure 1.4). By adjusting reaction conditions, as well as modifying the core and surface states through doping and other chemical treatments, it is possible to tune their emission properties. In this section, we will briefly discuss the key factors that influence the photoluminescence of CDs.

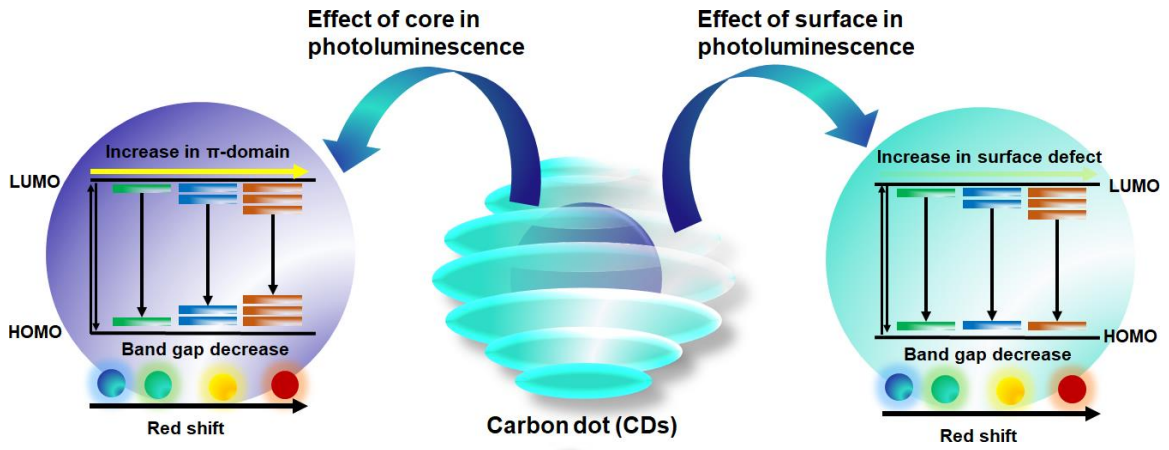

Figure 1.4. Effect of core and surface on fluorescence.

1.6.1. Effect of Doping on Photoluminescent Property

As explained in the previous section, numerous approaches have been developed for the successful synthesis of CDs. However, the as-synthesized CDs often exhibit low emission efficiency, limiting their potential for large-scale applications. To address this challenge, elemental doping has emerged as an effective strategy to enhance their emission intensity. Doping elements are generally classified into metal and non-metal dopants. Non-metal doping is often preferred to minimize the risk of additional toxicity associated with metal dopants. Both single-element and co-doping strategies are employed to improve performance. Among these, nitrogen (N) doping is the most widely used approach to enhance emission. Due to its high electronegativity, nitrogen increases the number of electrons in the CD system, leading to improved electronic transitions, which in turn, enhance the fluorescence properties of CDs, making them particularly suitable for biomedical applications.[43] Compared to N-doped CDs, S-doped CDs are rarely used due to toxic precursors like sulfuric acid, sodium thiosulfate, and waste frying oil.[44] In this regard, Yang et al. designed multicolor emissive CDs from crystal violet and sulfuric acid.[45] However, P-doped CDs are widely used to alter the optical and electronic properties in thin films.[46] In recent years, co-doping of hetero atoms has gathered wide attention. Due to the synergistic effect between the doped heteroatoms, unique electronic

structures are generated. This co-doping has a potential role in broadening the application of CDs in biosensing, photocatalysis, and nanomedicine.

Usually, small molecules are used as doping materials. We have used biomolecules such as amino acids, nucleobases as doping agent owing to their superior biocompatibility, low cost, availability, hydrophilic functional groups, and presence of hetero atoms.

1.6.2. Effect of Reaction Time, Condition, and pH of the Medium in CDs Synthesis

Reaction time, reaction condition, and pH play a vital role in developing CDs' structure, morphology, and size. As the temperature and duration of the reaction increase, the degree of carbonization also increases proportionally. This promotes a higher degree of conjugation within the carbon core, forming larger sub-domains. Consequently, the bandgap becomes narrower, resulting in a red shift in the emission. However, the longer reaction time and temperature endow a highly carbonized core, which can vary the quantum yield of CDs. Liu et al. reported the formation of CDs from citric acid and ethylenediamine. They have varied the reaction time, and the resulting quantum yield exhibited an enhanced quantum yield after 5 hours of treatment.[47] Similarly, Miao and co-workers synthesized multicolor emissive CDs from citric acid and urea under varying reaction temperatures ranging from 140 °C to 200 °C and different ratios of precursors, demonstrating the influence of thermal conditions on the optical properties of the resulting CDs.[48] Therefore, reaction time, precursor composition, and synthesis temperature are key parameters for tuning the optical properties of CDs. Another crucial factor is the pH of the reaction environment, which significantly influences the structural features of the resulting CDs. Adjusting the initial pH can profoundly impact their photoluminescence properties and catalytic performance, making it an essential variable in the design of CDs for specific applications.[49]

1.6.3. Role of Precursors in the Synthesis of CDs

Precursor material plays a fundamental role in synthesizing CDs as it directly influences the size, chemical composition, surface functionality, morphology, and optical properties. CDs can be synthesized from small organic molecules, graphene oxide, metal precursors, plant extract, and biopolymers. Among them, biopolymers possess some unique advantages as they are rich in abundant surface functional groups, non-toxic nature, biodegradability, low cost, renewability, wide availability, and high solubility. Polysaccharides and proteins are two categories of biopolymers that exhibit excellent bioavailability, high photoluminescence, and remarkable chemical and biological features (Figure 1.5). In our work, we have used two polysaccharides (chitosan and kappa-carrageenan) and one protein (casein). Therefore, we will focus on these polymers' role in biosensing, drug delivery, antibacterial, and wound healing.

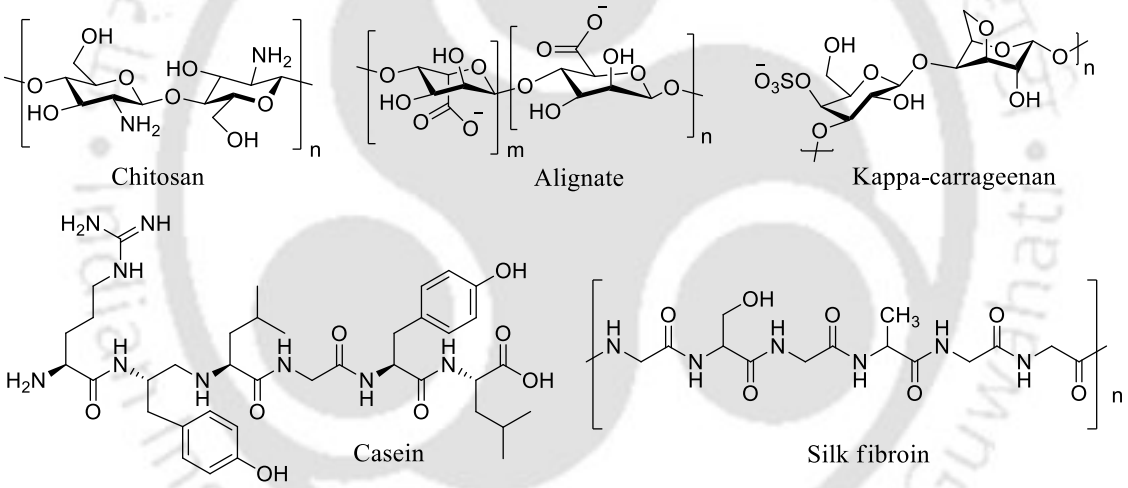

Figure 1.5. Examples of biopolymers as CDs precursors.

Chitosan

Chitosan is a class of naturally occurring linear homopolysaccharides, obtained from the deacetylation of chitin. The chemical structure of chitosan consists of *β*-(1→4)-linked D-glucosamine (deacetylated unit) and *N*-acetyl-D-glucosamine (acetylated unit). Chitin is the second most abundant polymer, found in the cell wall of fungi, the internal shell of cephalopods, and the exoskeleton of insects, etc. Chitosan possesses free amine and hydroxyl

groups in the polymeric backbone, which endow a wide range of modification and derivatization. Due to the enormous scope of modification, chitosan has a wide range of applications in the biomedical sector. Far group reported the synthesis of glycerol-grafted chitosan for the sustainable release of vincristine.[50] Ghosh and group reported the synthesis of chitosan nanoparticles via ionic gelation for oral delivery of rifampicin.[51] Horo and group designed the synthesis of chitosan-capped gold nanoparticles and further formulated microparticles using high tripolyphosphate as an ionic crosslinker.[52] The material exhibited effective delivery of doxorubicin for tumor therapy. Cui et al. reported electrospun chitosan nanofibers.[53] Crosslinked nanofibers resulted in better wet stability, enhanced mechanical strength, and good biocompatibility for wound healing. Similarly, chitosan has been utilized as a coating material[54] and films[55].

***Kappa*-carrageenan**

Kappa-carrageenan (KC), a seaweed polysaccharide, is procured from Chondrus, Eucheuma, Gigartina, and Hypnea (average molecular weight around 100-1000 kDa), consists of repeating units of (1,3)-d-galactopyranose and (1,4)-3,6-anhydro-α-d-galactopyranose and 25-30% ester sulfate groups. [56] Carrageenan is classified according to the number of sulfate groups on the repeating disaccharide units, *viz*, kappa (*κ*-), iota (*γ*-), and lambda (λ-) carrageenan. KC has one sulfate group per disaccharide unit. For the extraction of KC, seaweeds are subjected to an alkaline extraction process and dried into a powder form. The chemical composition of the material depends on the extraction parameters. Salguerio et al. reported a KC hydrogel loaded with gold nanoparticles.[57] They have analyzed the thermal and mechanical strength of the hydrogel and the release kinetics of methylene blue from the gel network. Souza and group reported antibacterial activity of red alga *Hypnea musciformis*-derived KC against *Staphylococcus aureus* and *Candida albicans.*[58] Additionally, KC has diverse applications in the pharmaceutical industry, serving as an immunomodulatory agent, anticancer component,

anticoagulant, and hydrogel precursor.[59–62] KC is used in the food industry as a thickening agent, a lubricant, and an antioxidant [63]

Casein

Casein is the main protein component in bovine milk, which has a high nutritional value. Casein is classified as α_s-casein, β-casein, and κ-casein. Among them, β-casein has excellent functional properties and digestibility due to numerous hydrophilic and hydrophobic amino acids in the building block. Proline present in the protein chain of casein forms alpha-helix, beta strands, and a disulfide bridge, making casein heat stable. Due to its amphiphilic nature, casein forms a micellar structure, which helps in drug encapsulation and delivery. Daik et al. reported casein-based tablet coating using different plasticizers.[64] The group studied the pH-dependent release profile of the drug and post-heating release kinetics. The study revealed that post-heating treatment induces crosslinking and sustained drug release at pH 6.8. It has other potential applications in food packaging, hydrogel, microparticles, nanocarriers, etc.[65–67]

1.7. Applications of CDs

Figure 1.6. Applications of CDs.

Due to their unique structural and physicochemical properties, CDs have found applications across a wide range of fields. We have categorized these applications into four main areas: (a) bioimaging, (b) catalysis, (c) environmental remediation, and (d) optoelectronic devices (Figure 1.6). In this section, we will provide a brief overview of each of these application domains.

1.7.1. Imaging and Therapeutics

Based on strong photoluminescence properties, excellent chemical stability, and pronounced dispersion, CDs are often chosen for bioimaging and anti-counterfeiting applications. Liu et al. reported the synthesis of N-CQDs from the hydrothermal treatment of citric acid and linear polyethyleneimine, resulting in a 37.4% fluorescence quantum yield.[68] Goh and group developed polyethylene glycol-capped CDs from citric acid for real-time bioimaging and target-specific delivery of hyaluronic acid derivatives.[69] Moreover, room-temperature phosphorescence (RTP) is another unique feature that facilitates anti-counterfeiting data and encryption. Li and group reported a universal approach that activates RTP using CDs and boric acid composite as an anti-counterfeiting agent.[70] Formation of a boron-carbon bond reduces the energy gap between the singlet and triplet state, thereby facilitating intersystem crossing (ISC).

Apart from imaging, due to their biocompatible nature, CDs possess immense applications in drug delivery and photothermal treatment. CDs-based drug delivery system also offers the visualization of drug accumulation via its fluorescence properties. In this regard, Gao et al. reported fluorine-doped FCDs that include nucleus targeting properties and successfully deliver doxorubicin and boron dipyrromethene.[71] The FCDs exhibited spherical shape and an average size of 9.62 ± 1.4 nm. Drug-conjugate FCDs demonstrated sustained release of doxorubicin up to 100 hours and excellent bioimaging properties. Moreover, CDs can act as nanomedicine. Recent synthetic techniques involve the synthesis of CDs from curcumin.[72]

Hydrophobic curcumin suffers from poor solubility. However, Cur-CDs exhibited excellent solubility and insignificant inhibitory activity against EV71 infection in RD cells with remarkable biocompatibility. Additionally, CDs have gained wide attention as potential phototherapeutic agents. In phototherapy, CDs play the role of a catalyst and generate reactive oxygen species (ROS). Zhao et al. reported lysozyme-gating CDs that can generate ROS and produce heat simultaneously.[73] Yellow fluorescent CDs were prepared from 1,3,6-trinitropyrene and NaOH, which exhibited a 5.7% quantum yield and 73.5% thermal conversion efficiency.

1.7.2. Anti-microbial Activity

The antimicrobial mechanisms of CDs primarily include membrane disruption, generation of reactive oxygen species (ROS), photocatalytic effects, induction of oxidative stress, and inhibition of bacterial metabolism. Among these mechanisms, membrane injury is considered primary, as it leads to the leakage of cytoplasmic contents and promotes the bactericidal effect of CDs. Travlou et al. reported sulfur and nitrogen-doped CDs for antibacterial assays against *Escherichia coli* and *Bacillus subtilis*.[74] The positively charged surface N-CDs exhibited electrostatic interaction with the negatively charged bacterial wall and promoted antibacterial activity. However, S-CDs exhibited a lower bactericidal effect than N-CDs due to the absence of a positive surface. For S-CDs, the bactericidal effect was only observed for *Escherichia coli* in a size-dependent manner.

1.7.3. Environmental Remediation

Conjugated π-domain and hetero atom-rich CDs serve as donor or acceptor systems. Therefore, CDS are widely used as sensors to detect biological pH, proteins, enzymes, nucleic acids, vitamins, and pollutants, such as heavy metals, antibiotics, pesticides, etc. Cui et al. reported the synthesis of CDs from citric acid and ethylenediamine by the hydrothermal method and

conjugated with oligodeoxyribonucleotide and graphene oxide (GO) for the detection of Hg^{+2}.[75] Interaction with GO exhibited turn-off fluorescence by fluorescence resonance energy transfer (FRET) mechanism. The fluorescence was recovered in the presence of Hg^{+2}. To determine physiological pH values in living cells, Tian's group reported two-photon fluorescence aminomethylphenylterpyridine (AE-TPY) CDs.[76] This sensor could determine the pH value gradients in a range of 6.0–8.5 with high sensitivity and selectivity in cells and tissues at a depth of 65–185 μm. In addition, this sensitive sensor was also successfully applied in living cells and tumor tissues of mice, which demonstrated that the CDs-based pH sensors could be further used in vitro and in vivo. Various research groups have reported the detection of molecules based on the colorimetric method using CDs. Liu et al. reported red emissive CDs via hydrothermal treatment of 5-diaminobenzene-sulfonic acid and 4-aminophenylboronic acid hydrochloride (BNS-CDs).[77] Those CDs exhibited excellent selectivity towards Fe^{+3} both in the fluorescence and colorimetric methods. The detailed mechanistic investigation demonstrated that the fluorescence quenching occurred due to the selective coordination of Fe^{+3} with the amine groups of the CDs' surface. CDs are not only utilized for the detection of pollutants but also play a significant role in their removal [78]

1.7.4. Catalysis

Despite detection and separation, degradation is another critical concern. Photocatalytic treatment helps completely degrade the pollutants. Due to excellent water solubility, chemical stability, and eco-friendly nature of CDs, they hold great potential in photocatalytic degradation. The photoluminescence property of CDs can be up-converted to tune the band gap, enabling absorption in the visible and near-infrared regions. Hu et al. reported pure CDs as photocatalysts for the degradation of methylene blue dye using reflux of activated carbon powder and bamboo shoot powder with HNO_3.[79] The catalytic efficiency was influenced by the functional groups (C=O, COOH). Apart from pure CDs, CDs-nanocomposites are also used

for catalytic degradation. Ke et al. developed CDs using hydrothermal treatment utilizing L-ascorbic acid as a precursor.[80] The nanocomposite was prepared using TiO_2, which yielded a visible spectrum and effectively degraded methylene blue under visible light irradiation.

1.7.5. Optoelectronic Devices

Easy synthetic protocol, adjustable photoluminescence, non-toxic and low-cost CDs are used in solar cells, light-emitting diodes, supercapacitors, etc. Diao et al. reported GQDs/n-silicon heterojunction solar cells that possess a hole transport layer and an electron blocking layer.[81] The performance of these solar cells exhibited tunable power conversion efficiency (PCE) depending on the size of the GQDs and the thickness of the functional layers. Wei et al. reported that calcinated N, P, and O co-doped CPDs and hydrogel were used for supercapacitor applications that generated electron-rich regions.[82] The CPDs helped to reduce interface resistance of porous carbon materials and enhanced conductive stability of the electrode at high scan rates. Hu and group reported polyethyleneimine-functionalized CPDs (PEI-CPDs)-modified cathode having a small size and excellent dispersity.[83] Large number of amine groups enhanced the performance of the Li–S batteries with high sulfur loadings under high current density situations. The strong chemical bonding enabled Li^+ ion conductivity at the cathode–electrolyte interface.

1.8. Conclusion

In summary, CDs have emerged as a promising class of fluorogenic nanomaterials due to their unique combination of small size, tunable photoluminescence, excellent biocompatibility, and low toxicity. The properties of CDs can be regulated through synthesis parameters such as reaction time, temperature, and pH, allowing for specific applications. Moreover, biopolymer-based CDs exhibit additional superior properties of the precursor material. With growing research interest, CDs are being used as sensors, optical devices, photocatalysis, delivery of

therapeutics, UV protector material, bioimaging, MRI contrast agent, and anti-counterfeiting agent. CDs' eco-friendly synthesis and versatile surface functionality make them key materials in next-generation nanotechnology and biomedical innovations.

Objectives of the Research Work:

Various synthetic modifications and doping for CDs have been reported earlier. Still, the effect of doping of biomolecules or crosslinking of biopolymers has not been explored well. Therefore, the synthesis and application of CDs can be extended in the following direction:

(a) **Chemical modification of biogenic CDs for targeted delivery of therapeutics:** Given their non-toxic nature and surface functionalization potential, CDs are promising candidates for tumor-specific drug delivery. Conjugation with targeting moieties can enable selective delivery to tumor cells, thereby minimizing toxicity to healthy tissues.

(b) **Nucleobase doping for sensing applications:** The effect of nucleobase doping on the optical properties of CDs, particularly their photoluminescence behavior, for potential applications in biomolecular detection was investigated.

(c) **CDs as precursors for silver nanoparticles:** Although silver nanoparticles exhibit excellent antibacterial properties, they often suffer from issues such as precursor toxicity and aggregation. Biogenic CDs can serve as a stabilizing and biocompatible precursor to mitigate these drawbacks.

(d) **Biogenic CDs embedded multifunctional hydrogels:** Incorporating biogenic CDs capped with silver nanoparticles into hydrogels can enhance their multifunctional properties, offering potential applications in antimicrobial wound dressings and tissue engineering.

Chapter 2. Synthesis of Kappa-Carrageenan and Lysine Derived Carbon Dots for Selective Detection of Folic Acid and Biotin Conjugation for Targeted Delivery of 5-Fu

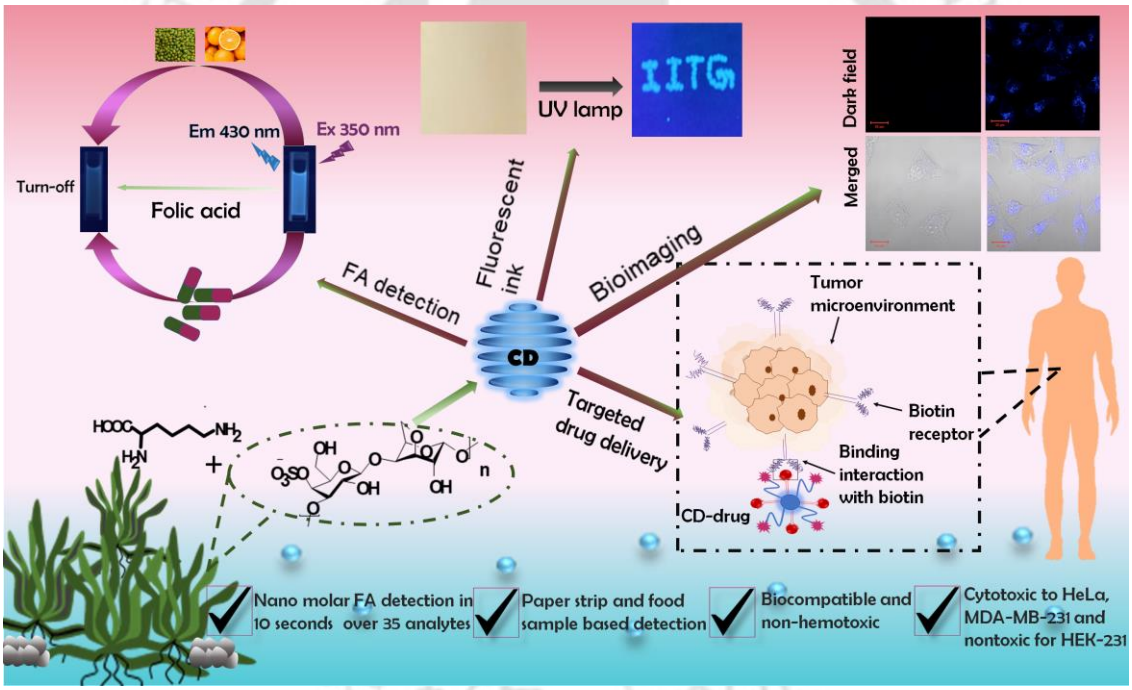

2.1. Overview

Vitamin B9, or folic acid (FA), plays a vital role in our metabolic processes, such as in the biosynthesis of methionine from homocysteine, the production of red blood cells, and in promoting the maturation of young bone marrow cells.[84–86] FA enhances one-carbon metabolism, promoting stability and proper genome function.[87] Common precursors of FA are green vegetables, green gram dal, broccoli, avocado, pig liver, or FA tablet. Inadequate intake of FA causes anemia, neural tube defects during pregnancy, cardiovascular exacerbation, and Alzheimer's disease.[88,89] An overdose causes nausea, zinc deficiency, and masks vitamin B12 deficiency, leading to additional neuropathy in adults.[90] Moreover, the enhanced concentration of FA increases the risk of cancer, such as prostate, breast, cervical, and ovarian.[91,92] The folate receptors are recognized as cancer biomarkers; hence, the vitamin is used for targeted drug delivery of chemotherapeutic drugs. The industrial processing of FA creates a significant amount of pharmaceutical waste. Poor biodegradability of FA and high chemical oxygen demand (COD) reduce drinking water quality, leading to significant environmental problems and increasing potential risks to ecosystems in the long run. This highlights the importance of quantification of FA in different aqueous media to manage the waste in an environment-friendly manner.

An effective approach to addressing cancer involves early diagnosis and high-throughput drug targeting. Nanomaterials, particularly CDs, hold significant promise in cancer diagnosis and tumor treatment due to their diverse biomodification capabilities, enhanced cellular penetration, and favorable biodistribution. Additionally, the surface of nanomaterials, rich in readily tunable functional groups, facilitates the conjugation of cancer cell-targeting molecules. In this context, several targeting moieties, such as peptides, aptamers, and small molecules, have been employed. Small molecules like biotin and folic acid are especially useful, because their complementary receptors are often overexpressed on tumor cells.

Previous reports on FA detection highlight that the probes are typically functionalized with amine (NH_2) groups, which play a key role in the detection mechanism.[93,94] For example, the probable interaction may occur due to ground-state complex formation by a reaction between the amine group of fluorophores and the carboxyl group of FA, electrostatic interaction, and charge transfer. Moreover, the N-doped CDs can be synthetically tuned for substantial spectral overlap with target FA. Herein, we have synthesized blue fluorescent CDs with remarkable optical properties, good quantum yield, excellent stability in saline water, a wide pH range, and long-term preservation (Scheme 1). Interestingly, the bare CDs exhibited the predicted turn-off fluorescence quenching in the presence of FA within just 10 seconds of interaction. We also evaluated the efficiency of these fluorescent CDs for FA detection in wastewater, food samples, and commercially available FA tablets. Additionally, we conducted on-site detection of FA using CD-coated paper strips and selectivity over 35 plausible co-existing analytes. CDs containing hydrophilic functional groups exhibited excellent biocompatibility. Considering the turn-off fluorescence of CDs in the presence of FA and a greater quantity of biotin receptor on tumor surface[95], we have covalently conjugated biotin (BT) with the CDs to produce a tumor-specific drug carrier. The synthesized CDBT exhibited notable cell death in triple-negative breast cancer cell lines MDA-MB-231 and HeLa cells in a dose-dependent manner. Confocal imaging studies revealed impressive uptake of CDBT in tumor cells. The chemotherapeutic drug 5-fluorouracil (5-Fu) was encapsulated in CDBT with high loading efficiency, and cellular studies were performed. To prove that CDs can be used in blood streams, a hemolysis assay was performed that showed the CDs to be nontoxic to blood cells up to 400 µg/ml.

2.2. Experimental section

2.2.1. Materials

Kappa-carrageenan (KC), 5-Fluorouracil (>99%), N-Hydroxysuccinimide (NHS) (97%), N, N′-Dicyclohexylcarbodiimide (DCC) (99%), L-lysine hydrochloride (LYS) (>98%), folic acid

(FA) (98%) and 3-(4,5-dimethylthiazol-2-yl)-2,5-diphenyltetrazolium bromide dye (MTT) were procured from Sigma Aldrich (St. Louis, MO, United States). Biotin (>98%) and Dulbecco's modified Eagle's medium (DMEM) were purchased from Tokyo Chemical Industry (Tokyo, Japan) and Himedia, respectively. All reagents were used without further purification.

2.2.2. Characterizations

UV–Vis absorbance spectra were recorded using Agilent Cary 100 UV–Vis spectrophotometer. The Attenuated Total Reflectance Infrared (ATR-IR) spectra were recorded using PerkinElmer UATR Two at ambient condition in the region 400-4000 cm^{-1}. The size of the CDs was analyzed by Jeol 2100F Field Emission Transmission Electron Microscope (FETEM). For the analysis, a dilute CDs droplet was cast on a copper grid and dried overnight in a desiccator. The fluorescence intensities were analyzed using 1 mg/ml concentration by Horiba Scientific Fluoromax-4 Spectrofluorometer. The crystalline/amorphous property of the materials was determined by powder X-ray diffraction (XRD) using Rigaku SmartLab 9 kW X-ray diffractometer fitted with CuKα radiation of λ = 1.54 Å in a 2θ range of 5–60◦. The surface morphology and roughness of the material were analyzed by Bruker, Innova series atomic force microscopy (AFM) using TESPA-V2, Bruker antimony doped silicon tips. The elemental analysis was determined by Leica DM 2500 M Optical microscope and Zeiss Sigma Field Emission Scanning Electron Microscope (FESEM). Interaction between CDs and FA was analyzed by iTC 200 Micro-calorimeter, GE Health Care. Fluorescence lifetimes were measured using Picosecond Time-resolved and Steady State Luminescence Spectrometer on an Edinburg Instruments Lifespec II & FSP 920 instrument. Pawley refinement was carried out using Materials Studio software.

2.2.3. Synthesis of CDs from KC and LYS

Amine-functionalized CDs were prepared through a single-step pyrolysis method.[96] The precursors, KC and LYS were mixed in various weight ratios (1:0, 1:3, 1:6, 1:9) and ground thoroughly. The blended mixture was then transferred into a reaction vessel under constant nitrogen purge at 200 ºC. After four hours, the black solid was produced which was then crushed and dispersed in 15 mL of double-distilled water. Subsequently, the sample was sonicated and filtered to obtain the desired CDs with homogeneous particle size and stored at 4 ºC for further use. The QY of CDs was calculated using the relative method.

$$QY_S = QY_{Ref} \times {}^{A_{Ref}}/_{A_S} \times {}^{E_S}/_{E_R} \times ({}^{\eta_S}/_{\eta_{Ref}})^2$$

Where A is absorbance at excitation wavelength, E is the integrated fluorescence intensity, and η is the refractive index of the solvent. Sample and reference dye have been denoted as S and Ref. Quinine sulphate has been used as reference dye (54% QY in .1 M H_2SO_4).

2.2.4. Fluorometric Detection of Folic Acid (FA) by CDs in PBS Buffer

First, 20 µL of CD stock solution (3.2 mg/mL) was diluted to 1 mL in phosphate buffer saline (PBS) of pH 7.4. Then, 5 mM stock solutions of various analytes were also prepared in PBS. Each analyte solution was then added (10-100 µL) to the carbon dot solution to measure fluorescence intensity. The quenching efficiency (QE) was calculated using the standard formula [QE % = $(1-F/F_0) \times 100$], where F_0 is the initial fluorescence intensity, and F is the fluorescence intensity after the addition of the analyte.

2.2.5. Fluorescence Detection of FA in Food Supplements and FA Tablets

Orange and green gram dal were used for FA detection procured from local market in Guwahati, India. Green gram dal was rinsed properly and dried in oven at 60 ºC. The sample was grinded properly to obtain powder. Powdered sample of 3g was dissolved in 15 mL PBS 7.4 buffer solution and vortexed for 15 minutes. The solid particles were removed by centrifugation at 10000 rpm for 10 minutes at 5 ºC. The supernatant was used for folic acid

detection.

Two FOLVITE® (Pfizer Ltd.) tablets were grinded to powder and added to 4 mL PBS buffer. Further the solution was vortexed and centrifuged at prescribed condition to obtain homogeneous supernatant.

For the detection of folic acid in orange, primarily the sample was squeezed and 1 mL orange juice was collected and poured onto a falcon tube containing 9 mL PBS buffer. The pulp and other particles were removed by centrifugation at 10000 rpm for 10 minutes at 5 ºC.

2.2.6. Fluorescence Detection of FA in Different Aqueous Media

20 µL of CDs solution from stock solution was obtained and mixed with 980 µL of PBS. Fluorescence titrations were performed in a quartz fluorescence cuvette. In all titrations, excitation wavelength was 350 nm. 5 mM FA solution in different water samples (PBS, milliQ water, lake water, river water, and tap water) were prepared by proper dilution. 100 µL of FA added to check QE.

2.2.7. Fluorescence Detection of FA in Different pH

For fluorescence titration, PBS buffer solutions ranging from pH 2 to 11 were prepared. 20 µL of CDs aliquot was mixed with 980 µL of PBS buffer. Fluorescence titrations were performed in a quartz fluorescence cuvette. In all titrations, excitation wavelength was 350 nm. 5 mM FA solution was prepared in PBS buffer. 100 µL of FA was added to check QE.

2.2.7. Synthesis of Biotin-conjugated CDs for Targeted Delivery of 5-Fu (CDBTFu)

The conjugation of biotin with CDs was prepared using a two-step synthesis process. In the first step, biotin-NHS ester (BT-NHS) was prepared and conjugated to CDs using a reported protocol.[6] For the synthesis of CDBT, 40 mg of CDs in sodium bicarbonate buffer (pH 9) were added dropwise to 80 mg BT-NHS in DMSO (1.5 mL) and stirred for 16 hours. Then, the

mixture was dialyzed against distilled water to remove unreacted biotin. FT-IR analysis confirmed the formation of CDBT.

For CDBTFu preparation, 5-Fu was introduced to 20 mL of CDBT solution under stirring for 24 hours at room temperature. The solution was centrifuged to a pellet using ultracentrifugation at 24000 rpm for 1 hour. The concentration of the unloaded drug was calculated by UV analysis (265 nm) of supernatant. Drug encapsulation efficiency (DEE) and drug loading efficiency (DLE) were calculated using the following formulae:

$$\text{DEE (\%)} = \frac{\text{Total amount of drug} - \text{Free drug}}{\text{Total amount of drug}} * 100$$

$$\text{DLE (\%)} = \frac{\text{Total amount of drug} - \text{Free drug}}{\text{Amount of carbon dot}} * 100$$

2.2.8. *In-vitro* release of 5-Fu from CDBTFu

The synthesized CDBTFu was dispersed in freshly prepared PBS, poured into a dialysis tube of 1000 Da, and dipped in a buffer solution with pH 4.5, 6, and 7.4, respectively. The release of 5-Fu from the carbon dots was measured at around 37 ºC, maintaining physiological conditions. A 1 mL aliquot was taken from the buffer solution while replacing the same amount with fresh buffer after a specific time interval. The absorbance values were measured by UV-vis spectroscopy at 266 nm. The experiment was triplicated, and the standard deviation was calculated. Finally, the released concentrations were measured by a calibration plot of 5-Fu in PBS media.

2.2.9. Cell Viability Assay

The cell viability assay of CDBTFu was conducted on MDA-MB-231, HeLa, and HEK-293 cells using MTT assay. For each cell line, 5×10^3 cells per well were seeded into a 96-well plate in DMEM media and incubated under 5% CO_2 humidified condition at 37 °C for 24 hours.

Later, the cells were treated with samples (CDs, 5-Fu, CDFu, and CDBTFu) of varying concentrations (100, 150, 200, 250, and 300 µM) and kept for incubation for 48 hours. After treatment, the culture media was discarded. 0.5 mg/mL MTT solution was added to the well plate and incubated for 2 hours, followed by the addition of DMSO. Subsequently, the absorbance of the violet formazan product was determined at 570 nm using a multi-plate reader. The obtained absorbance value is directly proportional to the viable cells present. All the studies were triplicated.

2.2.10. Bioimaging

The cellular uptake of CDs and CDBT on HeLa, MDA-MB-231 cells was analyzed through confocal imaging. The cells were grown in a 6-well plate containing a coverslip at the bottom. Each well was filled with 1.5×10^5 cells and allowed to incubate for 24 hours. 200 µg/ml sample were dispersed in media and incubated for another 24h at 37°C. Following incubation, cells were washed twice using PBS and treated with 4% formaldehyde solution for 10 min. After that, the cells were washed thrice with PBS to remove unbounded particles and visualized using confocal laser scanning microscopy (ZEISS LSM-880).

2.2.11. Hemolysis assay

Maintaining proper safety protocol, we examined the hemocompatibility of CDs using human blood. Fresh whole blood (approximately 2 mL) was initially centrifuged at 1500 rpm for 5 minutes at 4 °C to separate the serum. The pellet containing red blood cells was washed several times and dispersed in PBS to prepare 5% solution. In a sterile tube, 50 mL of blood sample and 50 mL of CDs of different concentrations (100 µg/mL, 200 µg/mL, and 400 µg/mL) were mixed and kept in an incubator at 37 °C for 2 hours. 50 mL PBS and 50 mL 0.5% Triton X-100 were taken as positive and negative control, respectively. The absorbance of the supernatant was measured using a plate reader at 540 nm. The experiment was performed with

the permission of the Institute Ethical Committee (IHEC/LMK/12/2023). The rate of hemolysis was calculated using the following standard equation:

$$\text{Rate of hemolysis} = \frac{A_{Sample} - A_{Negative}}{A_{Positive} - A_{Negative}} * 100$$

A_{Sample} is the absorbance of different concentrations of CDs, $A_{Negative}$ is the absorbance in the presence of PBS, and $A_{Positive}$ is the absorbance in the presence of Triton X-100.

2.3. Results and Discussions

2.3.1. Optical Properties of Amine-functionalized CDs

The optical properties of the blue fluorescent CDs were explored using UV-Vis and fluorescent spectroscopy. CDs obtained from pure KC, prepared as control, exhibited a colorless solution in visible light with a maximum absorbance at 280 nm. In contrast, the desired CDs synthesized from KC and LYS resulted in a yellow solution under visible light with an absorption peak at 293 nm and shoulder from 324 to 390 nm (Figure 2.1a). The peak at 280 nm and 293 nm can be ascribed to the π-π^* transition due to the presence of the C=C bond, and the broad shoulder peak can be attributed to the n- π^* transition.[97]. The colorless nature of pure KC-derived CDs could be due to the presence of hydroxyl and sulfonic groups, which often act as non-radiative components. CDs (1:9 of KC: LYS) exhibited the most intense fluorescence maxima at 430 nm when excited at 350 nm (Figure 2.1b and Figure 2.2a) with an excitation-dependent shift in fluorescence maxima (Figure 2.1C).[98] This optical behavior can be described by the distribution of the size of carbon dots, distribution of different emissive trap sites, or formation of aromatic fluorophores, free zig-zag site, hetero atom doping, and edge defects.[99,100]

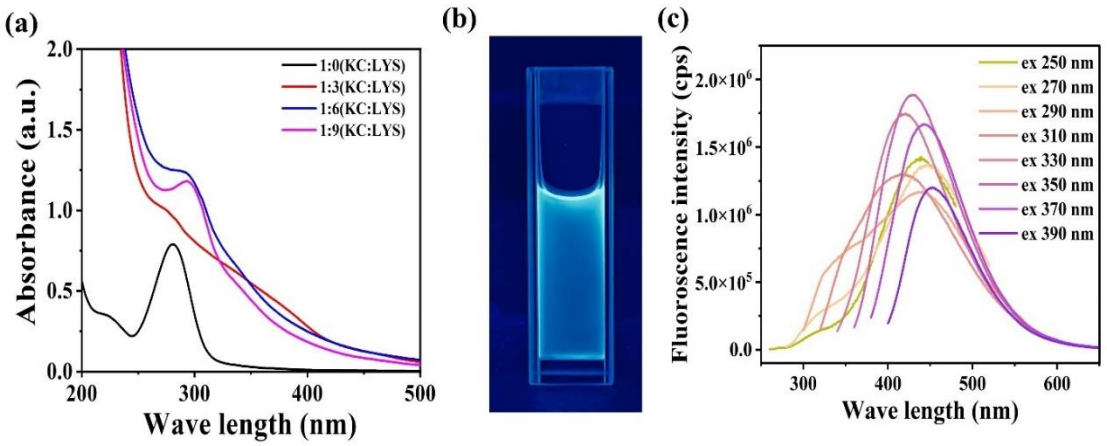

Figure 2.1. (a) UV–Vis absorption spectra of CDs prepared from different ratios of KC and LYS, (b) digital image of CDs (1:9) under UV lamp, and (c) excitation-dependent fluorescence emission spectra of the CDs (1:9).

2.3.2. Quantum Yield (QY) Calculation

The quantum yield of pristine KC CD (1:0 of KC: LYS) was about 15%, and pure LYS-derived CD (0:1 of KC: LYS) was 32 %. The high yield of CDs without surface passivation is presumably due to the sulfonic acid group in KC [101] and the amine group of LYS. Quantum yield of CDs synthesized from KC and LYS with 1:3 and 1:6 ratios yielded 35 % and 40 %, respectively. CDs 1:9 of KC: LYS resulted in the highest quantum yield of 49 %, much higher than pristine KC and LYS, making it a worthy biomaterial for bioimaging. Henceforth, all the experiments were performed using this desired CD (1:9 of KC: LYS). Notably, the QY and fluorescence intensity were enhanced with increasing LYS concentration, possibly due to the stabilization of energy traps after surface passivation (Figure 2.2b).

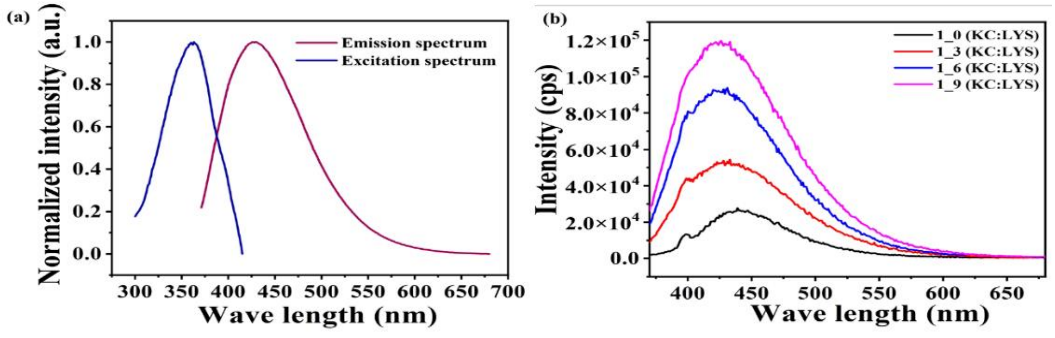

Figure 2.2. (a) Excitation and emission spectrum of CDs, (b)Fluorescence emission spectrum of different ratios (KC: LYS) carbon dots.

2.3.3. Stability of CDs (1:9 of KC: LYS) in Different pH, NaCl Solutions, and Storage time

The stability of CDs was analyzed in different pH mediums ranging from 2-11 and different NaCl concentrations. Initially, pH solutions were prepared using the PBS buffer. The fluorescent intensity of CDs remained stable across the pH range (Figure 2.3a). However, the highest emission intensity was found at pH 7.4, which is also the physiological pH. The influence of electrolytes on CDs was analyzed in different salt concentrations. The result was significant, demonstrating the stability of the NaCl solution up to 1 M (Figure 2.3b). Furthermore, the material has shown constant intensity over three months of storage (Figure 2.3c). The observations suggest the excellent storage stability of synthesized CD (1:9 of KC: LYS).

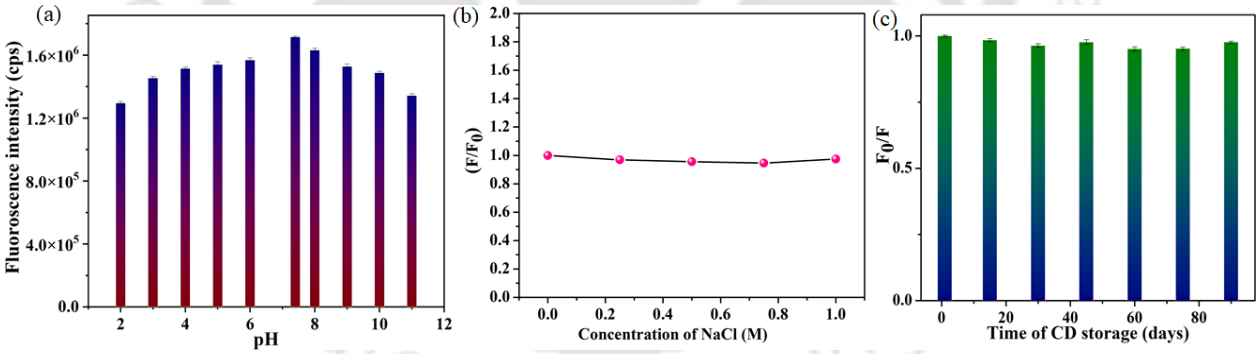

Figure 2.3. Stability of CDs in presence of (a) different pH ranges (2-11), (b) saline water, and (c) storage time.

2.3.4. Characterization of CDs (1:9 of KC: LYS)

Initially, we performed FETEM analysis to confirm the homogeneous formation of CDs with an average size of 3 ± 1.5 nm (Figure 2.4a-b). In addition, high-resolution TEM (HRTEM) data showed a lattice spacing of 0.25 nm between the planes from the Inverse Fast Fourier Transition

(IFFT) graph (Figure 2.4c). Selected area electron diffraction pattern (SAED) resulted in the formation of amorphous CDs (Figure 2.4d). The synthesized amorphous CD clearly deviates from the XRD pattern of the precursors LYS or KC (Figure 2.5a-b). The height profile data obtained from AFM also supports FETEM data, which shows that the size of particles is around 2-4 nm (Figure 2.4e-f).

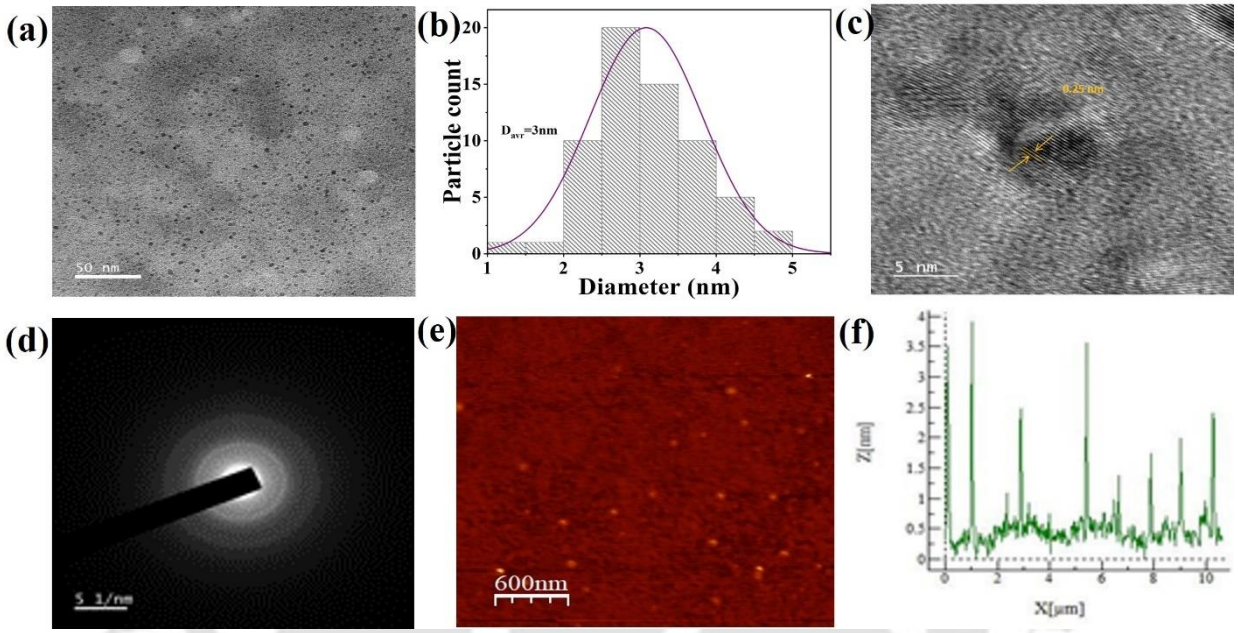

Figure 2.4. (a) FETEM image of CDs in 50 nm scale bar, (b) size distribution curve of CDs obtained from FETEM, (c) HRTEM of CDs (5 nm scale bar), (d) SAED pattern of CDs, (e) AFM image of CDs in 600 nm scale bar, and (f) AFM height profile of CDs.

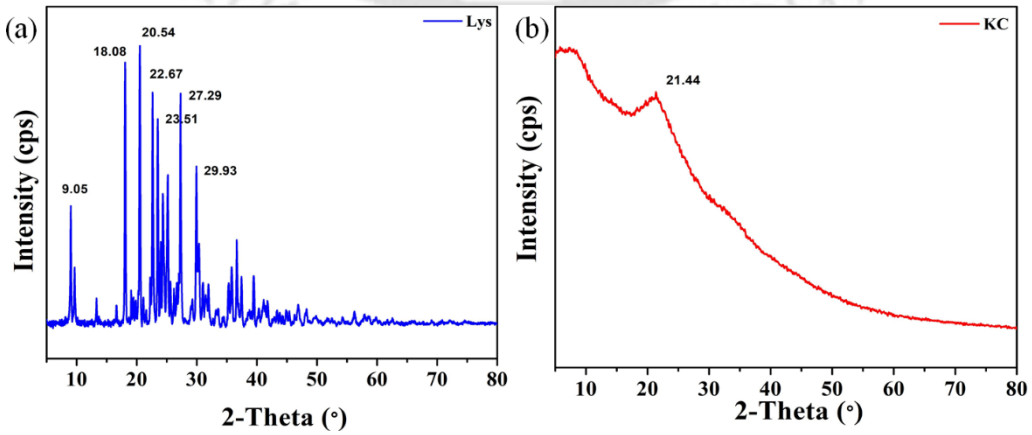

Figure 2.5. Powder XRD pattern of (a) LYS and (b) KC.

In addition, X-ray photoelectron spectroscopy (XPS) was conducted to characterize the surface functional groups such as -SO_3H, -NH_2, -Cl, -OH. The binding energies for CDs were observed at 284.3 eV for C_{1s}, 531.3 eV for O_{1s}, 400.3 eV for N_{1s}, 197.3 eV for $Cl_{2p,}$ and 168.7 eV for S_{2p} (Figure 2.6a). The sulfonic acid group of KC was evident from the deconvoluted sulfur graph.[102] Formation of the C-Cl bond was confirmed from high-resolution data of Cl_{2p} at 200.1 eV (Figure 2.6f).[103]

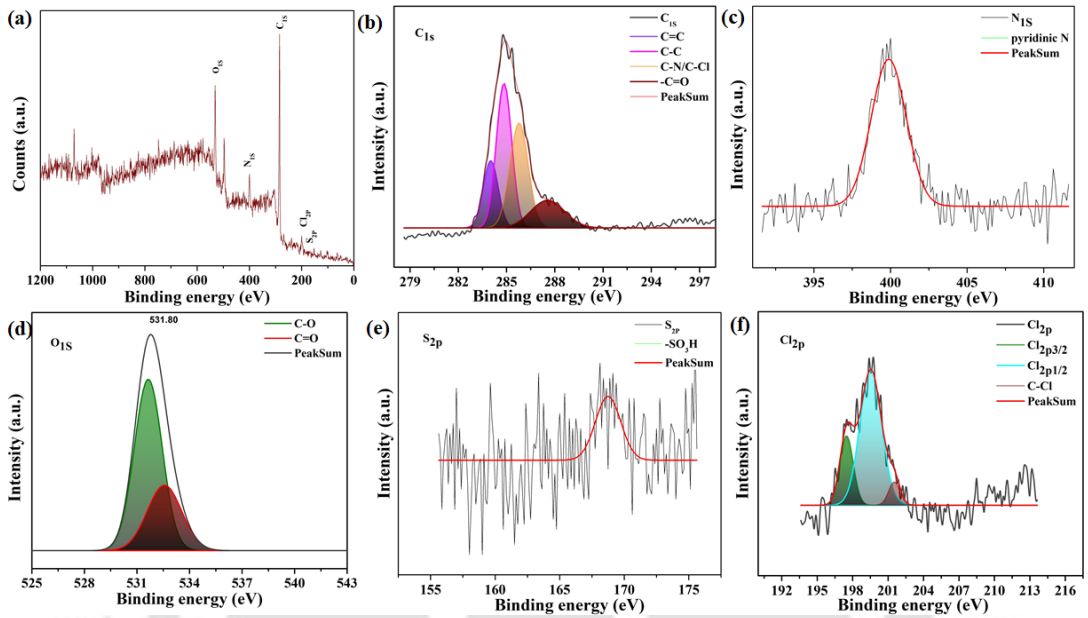

Figure 2.6. (a) XPS pattern of CDs. Deconvoluted high-resolution spectrum of (b) C_{1s}, (c) N_{1S}, (d) O_{1s}, (e) $S_{2p,}$ and (f) Cl_{2p}.

2.3.5. Sensing of FA by CDs in PBS buffer

The fluorescence intensity of CDs attained the highest value at pH 7.4 when excited at λ_{max} 350 nm. Hence, further sensing was explored at the same pH in PBS. About 98% fluorescence quenching of CDs was observed after FA titration (Figure 2.7a). The fluorescence emission at 430 nm diminished within 10 seconds after adding 100 µL of 5 mM FA stock solution (455 µM) (Figure 2.7b).

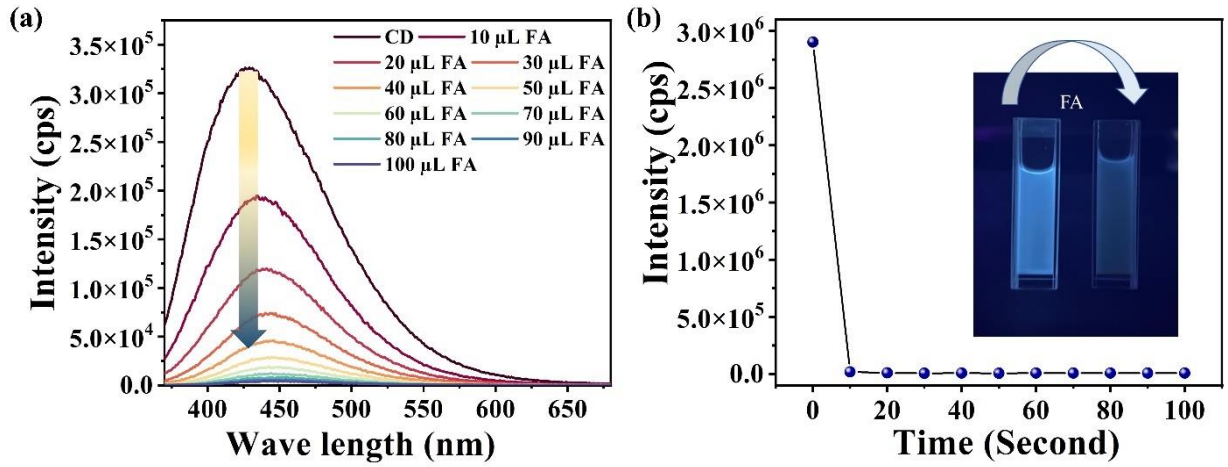

Figure 2.7. (a) Turn off fluorescence of CDs with sequential addition (0−100 µL) of 5 mM FA in PBS buffer, (b) Time-resolved luminescence study of CDs with the addition of 5 mM 100 µL FA. (Inset: image of blue CDs before and after addition of FA under UV lamp).

To understand the selectivity of CDs for FA, a fluorometric test was conducted in the presence of relevant co-analytes. This comprehensive evaluation included a range of amino acids, various biomolecules, vitamins, carboxylic acid-containing compounds, and metal ions to assess the sensor's specificity and reliability. Approximately 1-15 % quenching was determined for other analytes, negligible compared to folic acid, which showed about 98 % quenching (Figure 2.9a-c). Moreover, the quenching percentage did not change significantly for other analytes even after adding high analyte concentration. However, a systematic fluorescence quenching was observed for our CDs with a gradual increase in FA concentration (Figure 2.8). To prove the selectivity of our CD towards FA, we have studied fluorometric assay in the presence of the other co-analytes. Similar fluorescence quenching was evident after adding FA in the mixture containing other co-analytes, demonstrating selective detection of FA (Figure 2.10).

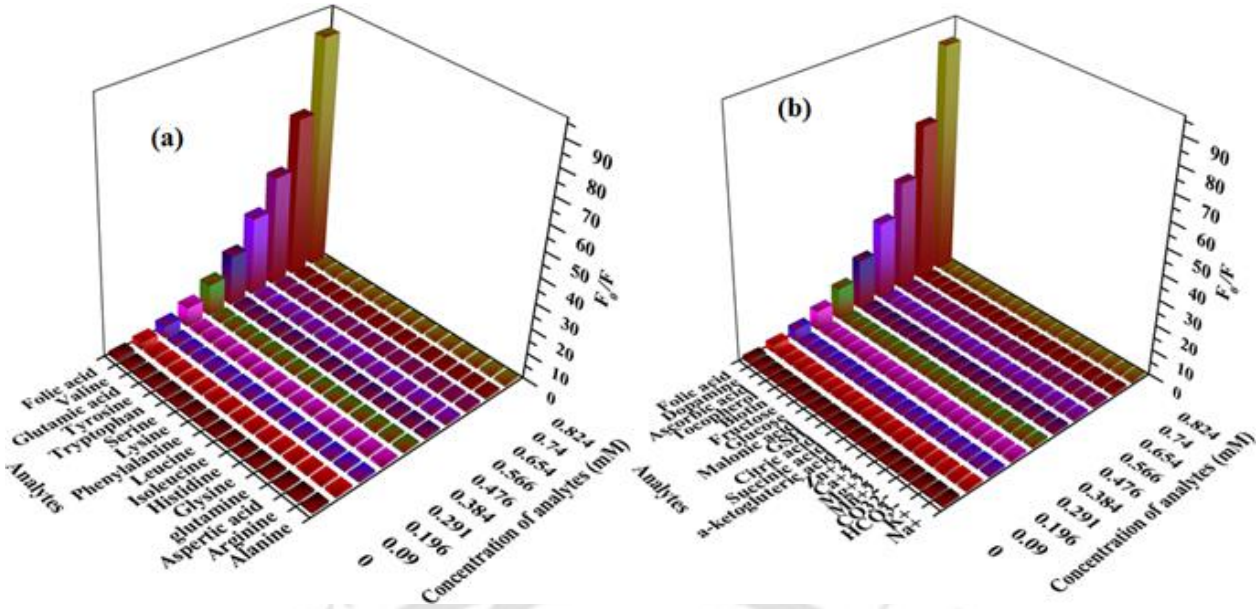

Figure 2.8. Stern-Volmer plot for decreasing intensity of CDs with increasing concentration of different analytes (5 mM) in PBS media. (a) for amino acids. (b) for other vitamins, metal ions, carboxylic acids and biomolecules.

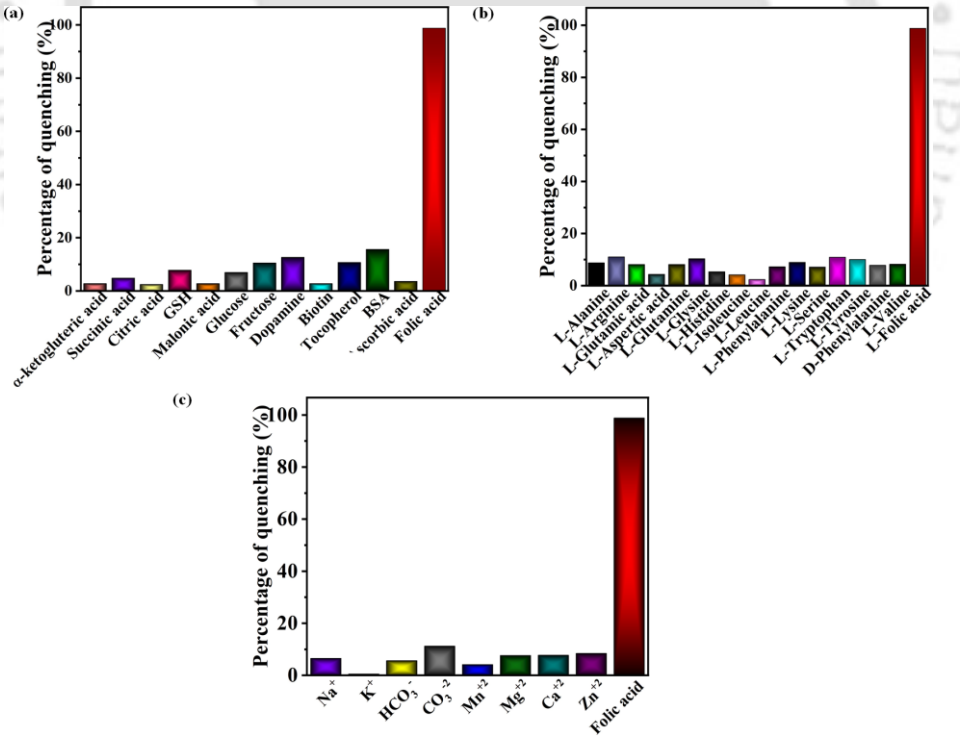

Figure 2.9. Selective sensing of folic acid by CDs: (a) quenching efficiency of CDs in the presence of dicarboxylic acids and biomolecules, (b) in the presence of amino acids, and (c) in the presence of ions. The concentration of all analytes was 455 µM.

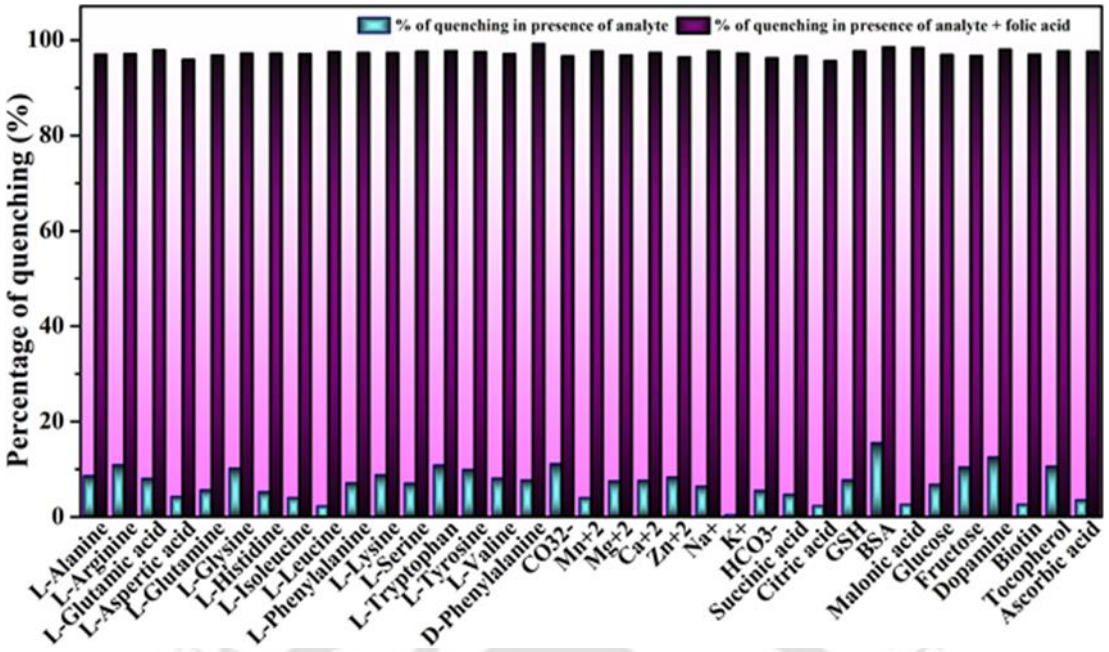

Figure 2.10. Quenching percentage of CDs in presence of amino acids, biomolecules (glucose, fructose, dopamine, GSH, BSA), carboxylic acid containing molecules (citric acid, α-ketoglutaric acid, succinic acid, malonic acid), vitamins (ascorbic acid, biotin, tocopherol), and metal ions and after addition of FA.

2.3.6. Determination of Quenching Constant and LOD Value

The quenching constant (K_{SV}, M^{-1}) was evaluated using the Stern–Volmer (S–V) equation, $F_0/F=1+ K_{SV}[Q]$. Here, F_0 and F are the initial and final fluorescence intensity of CDs, K_{SV} is the Stern–Volmer quenching constant, and Q is the concentration of the analytes (M). Stern–Volmer plot exhibited a non-linear quenching at a higher concentration of FA and a linear nature at a lower concentration (Figure 2.11a-b). From the Stern–Volmer plot, the value of K_{SV} was quite high (1.01×10^6 M^{-1}), indicating favorable interaction between CDs and FA. LOD value was 40 nM (LOD= 3σ/N, σ is the standard deviation of the blank sample, N is the slope obtained from the curve) (Table 2.1, Figure 2.12) with a linear range of 24 nM-10 µM. The LOD value is comparable we the recent reports (Table 2.2).

Table 2.1. Statistical details of different analytical parameters for the detection of FA by CDs.

Concentration range (nM)	*Slopes*	*Intercepts*	*Correlation coefficient (R^2)*	*(Standard deviation from residuals) $S_{y/x}$*	*LOD (nM)*	*Regression equation*
0-227	194.592	312245	0.98732	2637.2	40.6575	-194.592X + 312245
	196.621	310454.2	0.98793	2685.6	40.9763	-196.621X + 310454
	196.895	315563.3	0.97908	2685.6	40.9192	-196.895X + 315563
Average	196.036	312754.2	0.984777	2669.467	40.8517	-196.036X + 312754
SD	1.259925	2592.342	0.004943	27.94375	0.169999	-(196.036 ± 1.25992)X + (312754.2 ± 2592.342

Table 2.2. Comparison table of different sensors for FA detection.

Sl. No.	*Material*	*Analytical Method*	*Sample*	*Response Time*	*LOD*	*Linear Range*	*Ref*
1	HCA-CD	Fluorometric	Urine	5 minutes	0.49 μM	4.0-100 μM	[104]
2	Paper@CD	Fluorometric	Urine, orange	12 minu	0.28	1.0-300 μM	[105]

			juice	tes	µ M		
3	AA-CD	Fluorometric	Oatmeal, milk, juice, tablet	1 minu tes	40 n M	1.0-100 µM	[106]
4	N, S, I-CD s	Fluorometric	----	5 minu tes	84 n M	0.1-175 µM	[94]
5	Eu-MOF	Fluorometric	Tablet	90 seco nd	0.3 µ M	1.26-12.5 mM	[107]
6	β-CD-CuNCs	Fluorometric	Blood serum	----	0.4 7 µ M	4.95-47.6 µM	[108]
7	MB/ERG O/GCE	Electrochemic ally	Tablet	----	0.5 µ M	4.0-167 µM	[109]
8	**CDs**	Fluorometric	Green gram dal, orange juice, tablet	10 seco nd	40 nm	24 nM-10 µM	**This wor k**

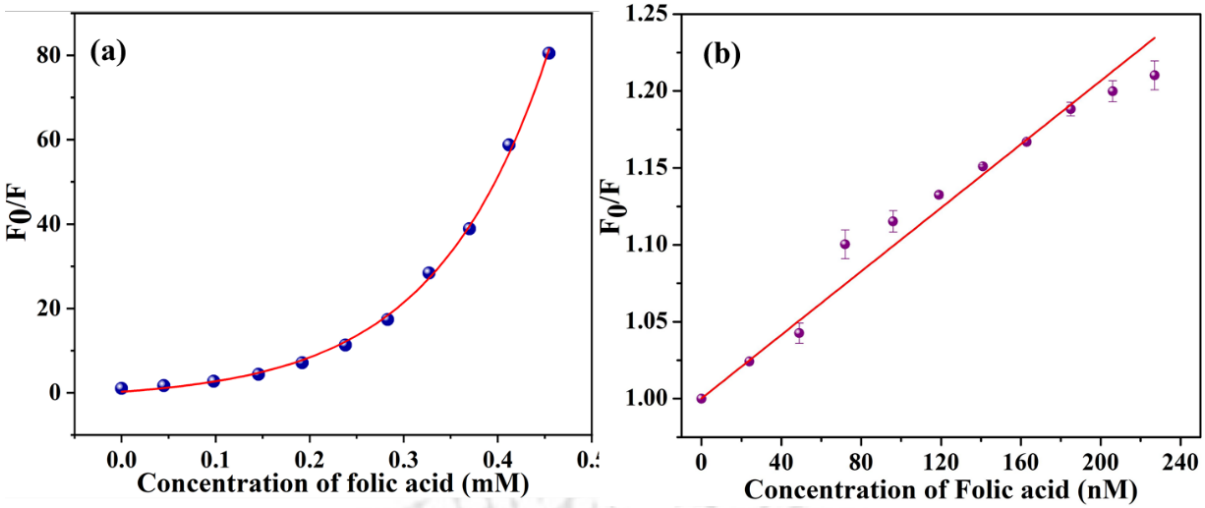

Figure 2.11. Stern-Volmer plot for fluorescence quenching of CDs against FA concentration in PBS medium: (a) millimolar, (b) nanomolar.

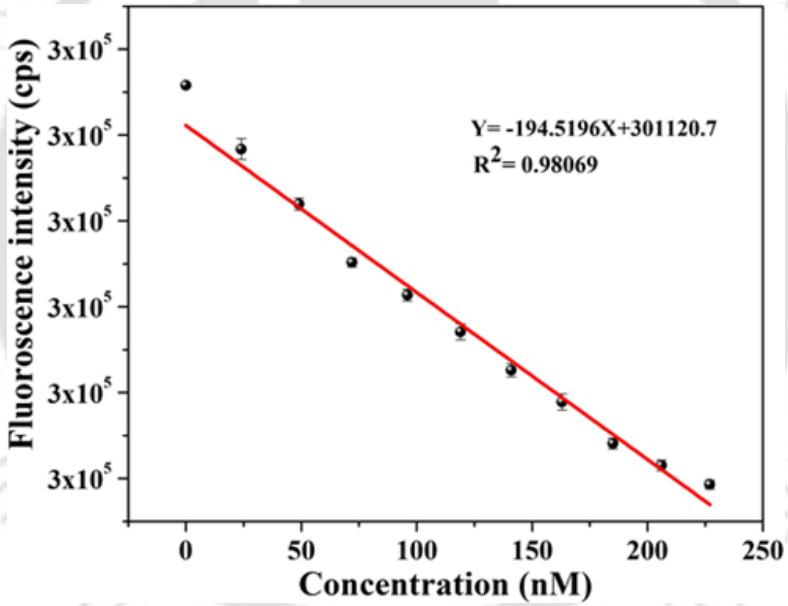

Figure 2.12. Change in fluorescence intensity of CDs against FA concentration in PBS medium.

Considering different pH values of body fluids, it is necessary to understand FA detection over pH ranges. CDs solution was prepared in a wide pH range (2–11), and 100 µL of 5 mM FA was added to each solution. The quenching of emission intensity was calculated before and after adding FA at λ_{max} 430 nm. The result exhibited impressive (approximately 97%)

quenching efficiency for a wide range of pH 4 to 11 (Figure 2.13). A slight reduction in quenching under acidic pH may be due to poor solubility of FA and protonation of functional groups in an acidic medium.

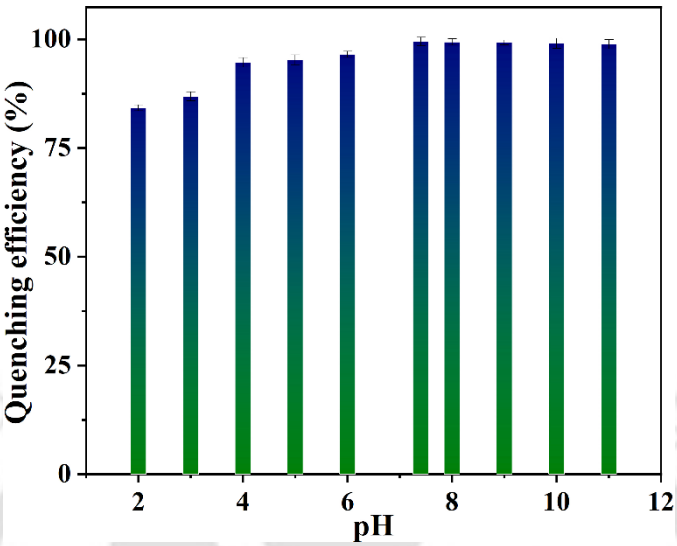

Figure 2.13. Change in quenching percentage of CDs in PBS medium at different pH ranging from 2-11.

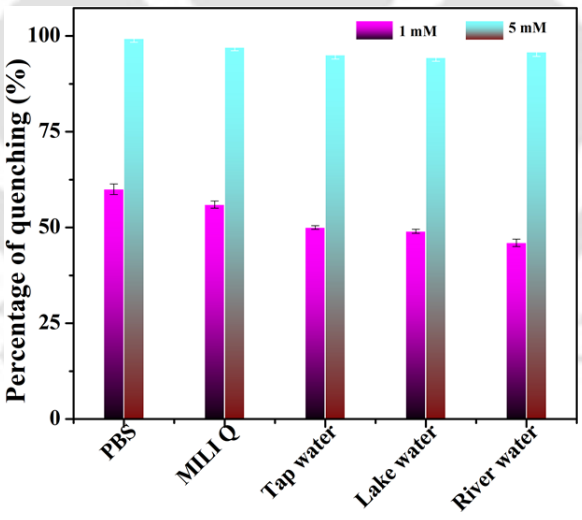

Figure 2.14. Change in quenching percentage of CDs in different aqueous systems.

2.3.7. Detection of FA in Various Aqueous Mediums, Actual Food Samples, and CD-Coated Paper Strips

We have studied the detection of FA in different aqueous mediums: milli-Q water, tap water, lake water, and river water. FA concentration was spiked in each aqueous medium, and fluorescence titrations were performed. Figure 2.14, demonstrates that the synthesized CDs could effectively detect FA under various mediums. We have extended our fluorometric titration of CDs in FA-rich food samples (orange and green gram dal) and FA tablets. The selectivity of the sensor was confirmed even in food supplements and tablets by quenching the fluorescence intensity of CDs with incremental addition of respective extracts (Figure 2.15a-c).

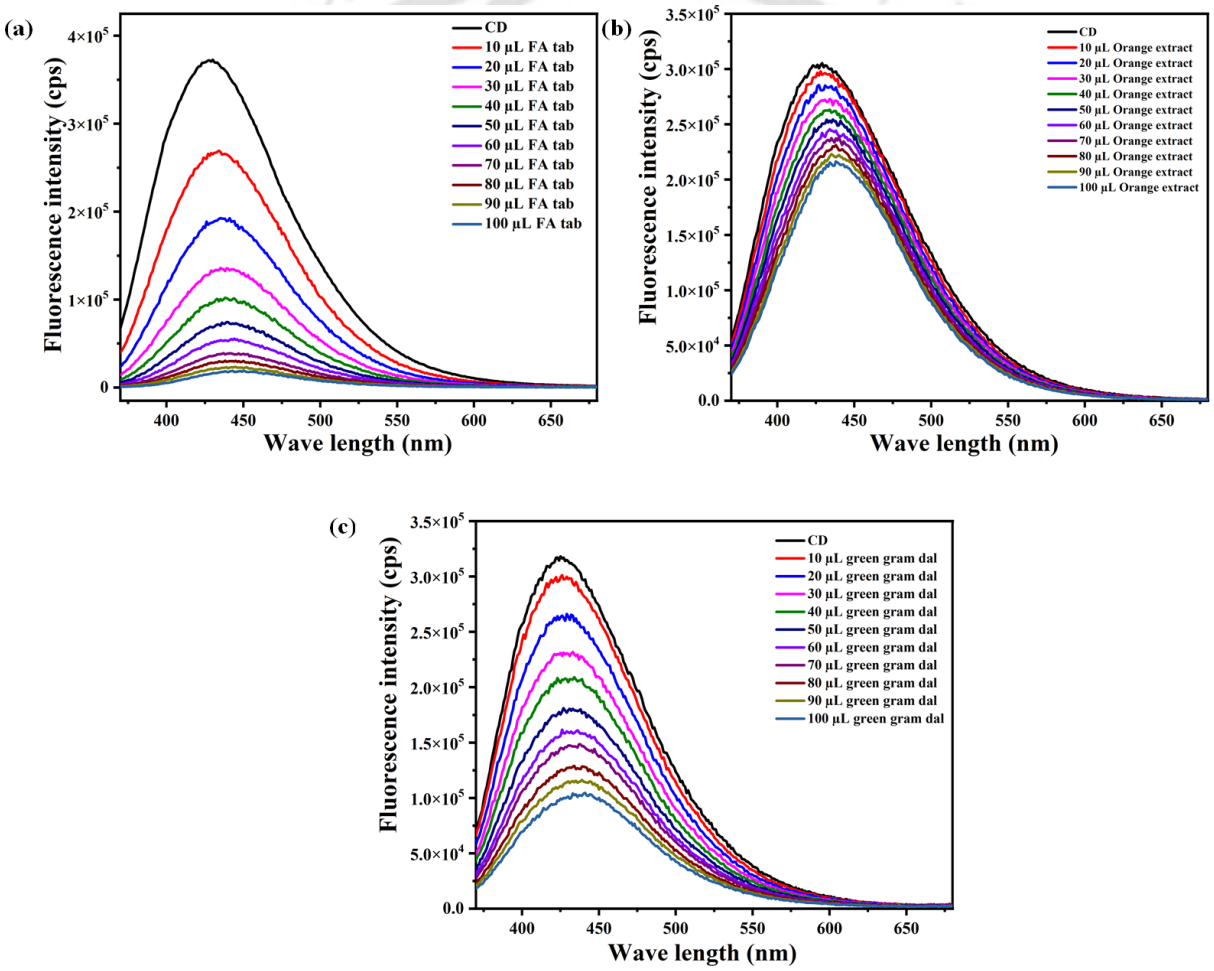

Figure 2.15. Change in fluorescence emission intensity of CDs (in PBS medium) upon sequential addition of (a) 100 µL of FA tablet extract, (b) orange extract and (c) green gram dal extract.

CD-coated paper strips could further demonstrate rapid and selective detection for on-site, portable, and naked-eye detection of FA without any special equipment. Firstly, paper strips were prepared through dip-coating of filter paper in CD solution, and then 20 µL of FA ranging from 10^{-3}-10^{-9} M was drop-casted on the same paper. Black spots were found on bright fluorescent CD-coated paper strips under UV exposure, suggesting a potential application of the CDs as portable paper strips for on-site detection of FA (Figure 2.16c-d). As can be seen in Figure 5(a-b), the inscription with CD solution can be clearly visualized under UV light, which lasts for months.

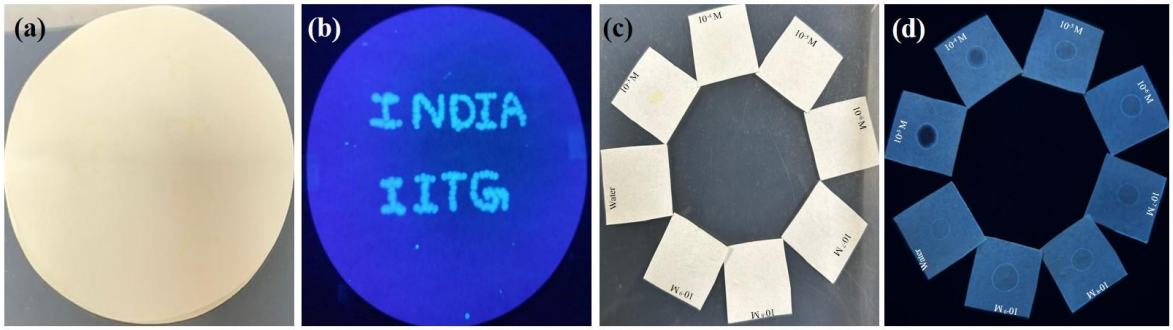

Figure 2.16. Inscription on filter paper with CDs: (a) in daylight, (b) under UV lamp; CD coated paper strips drop cast with FA: (c) in daylight, (d) under UV lamp.

2.3.8. Probable Mechanism of FA Detection

We have performed several investigations to determine the correct mechanism of FA detection. In general, the turn-off fluorescence phenomenon is explained by non-illuminating, ground state complex formation,[110] fluorescence resonance energy transfer (FRET),[111] photo-induced electron transfer (PET),[112] or an inner filter effect (IFE)[113]. We have observed a significant overlap between the absorbance spectrum of FA and the excitation spectrum of CDs. In contrast, the other analytes did not exhibit any spectral overlap (Figure 2.17).

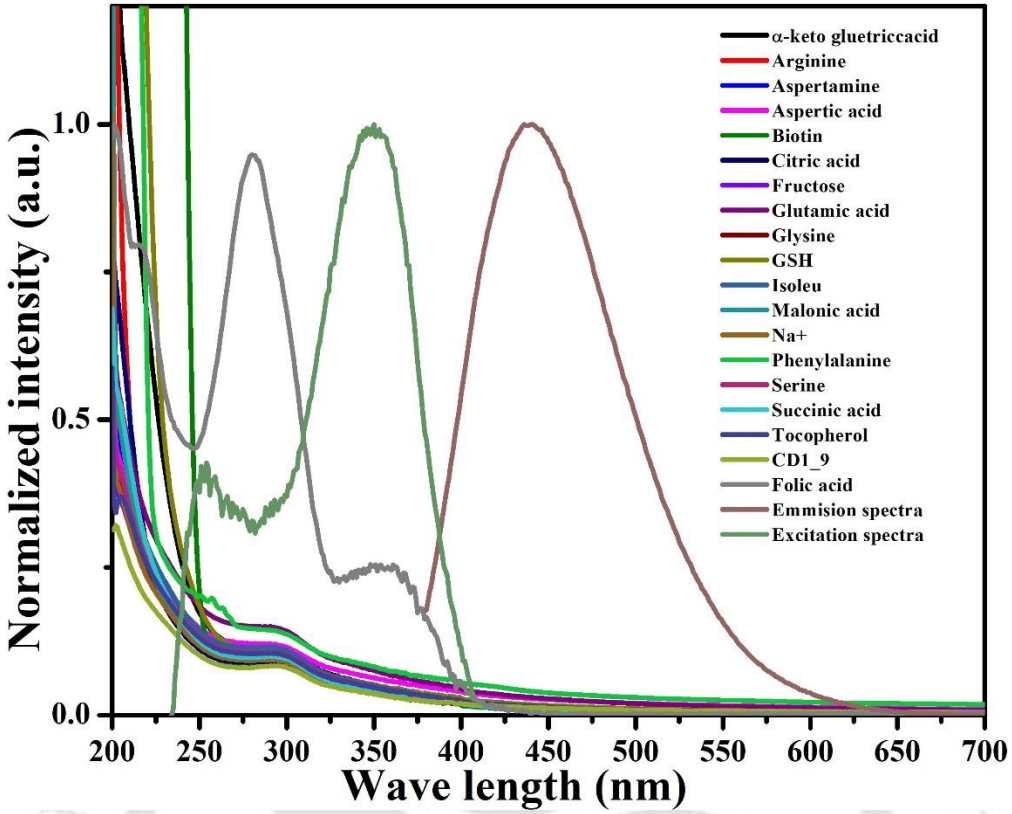

Figure 2.17. Normalized UV-absorption spectra of analytes, excitation and emission spectra of CDs.

TRPL assessment of the fresh and analyte-treated probe CDs showed fluorescence lifetime to be 4.34 ns and 4.25 ns, respectively (Figure 2.18 and Table 2.3). With τ_0/τ nearly equal to one, it indicates static quenching or IFE and eliminates the possibility of FRET and PET.[114]

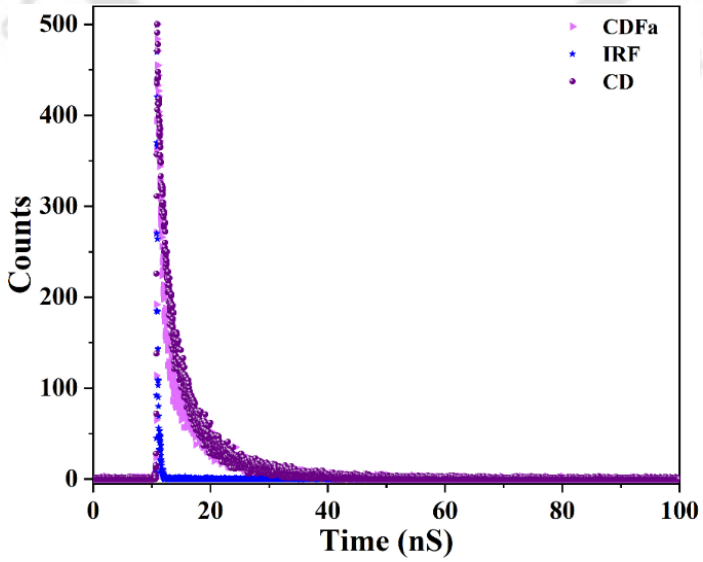

Figure 2.18. Time-resolved photoluminescence (TRPL) decay profile of CDs in presence and absence of FA.

Table 2.3. Fluorescence lifetime of CDs before and after addition of FA.

Volume of FA (µL)	a_1	a_2	τ_1 (ns)	τ_2 (ns)	$<\tau>^*$ (ns)	χ 2
0	0.355	0.644	0.716	6.348	4.342	1.001
100	0.369	0.63	1.489	5.878	4.252	1.010

Moreover, the fluorescence titration of CDs with FA at excitation wavelengths λ_{max} 350 nm and λ_{max} 400 nm showed a decrement in quenching efficiency from 98% to 36%, suggesting an excitation-dependent process (Figure 2.19). Clearly, the diminished spectral overlap between CD and FA at 400 nm compared to 350 nm reduces the quenching efficiency.

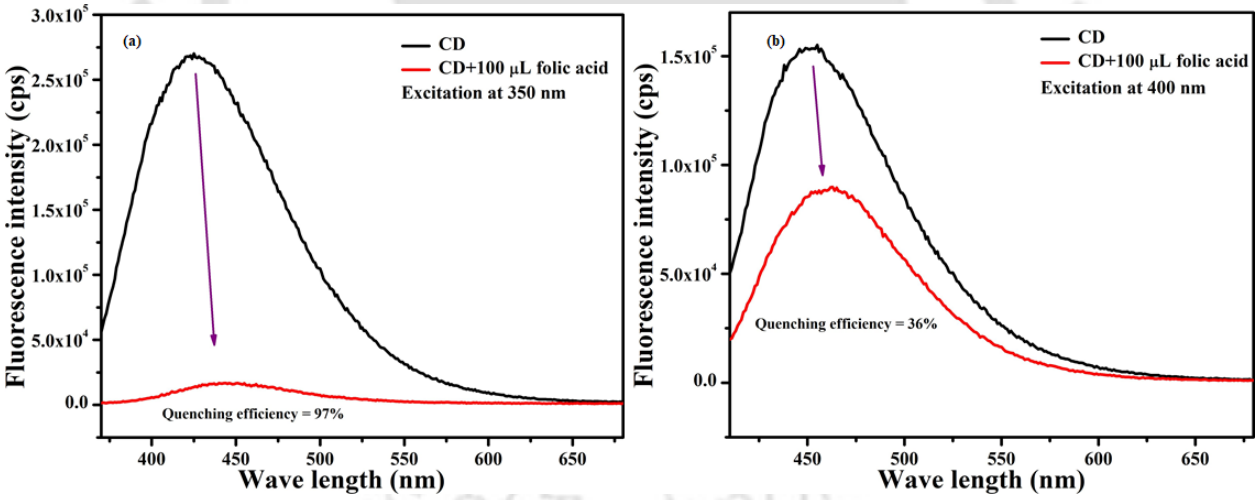

Figure 2.19. (a) Change in fluorescence intensity upon addition of 100 µL FA (λ_{ex} = 350 nm), (b) change in fluorescence intensity upon addition of 100 µL FA (λ_{ex} = 400 nm).

The involvement of IFE was also determined by estimating the corrected fluorescence of CDs upon titration with FA with the following formulae.[115]

$$\frac{F_{corrected}}{F_{observed}} = \frac{2.3dA_{ex}}{1-10^{-dA_{ex}}} * 10^{gA_{em}} * \frac{2.3sA_{em}}{1-10^{-sA_{em}}}$$

Where, $F_{observed}$ is the actual FL intensity; $F_{corrected}$ is the corrected fluorescence intensity after removing the IFE from the actual fluorescence intensity; A_{ex} and A_{em} are the absorbance of CDs at 350nm and 430 nm, respectively; s is the width of the excitation beam (0.10 cm); g is the distance between the edges of the cuvette and the excitation beam (0.40 cm in this case); d is the thickness of the cuvette (1.00 cm).

Approximately 40% decrease in quenching from the corrected fluorescence intensity further supported the involvement IFE (Table 2.4 and Figure 2.20). However, to understand rest of the quenching, FT-IR analysis was performed for CDFA. The spectrum indicates generation of a broad peak around NH_2/OH region, presumably due to H-bonding between the probe CDs and the analyte, as earlier report.[116] FETEM analysis of CDFA showed particle size more than 15 nm which is larger as compared to the pristine CDs. Confirming a strong interaction between CDs and FA (Figure 2.21). Therefore, the overall fluorescence-quenching of CDs upon titration with FA can be attributed to a combination of IFE and ground state static quenching.

Table 2.4. IFE correction table of CDs upon FA addition.

Folic acid (μM)	A_{ex}	A_{em}	***Correction factor (CF)***	F_{obs}	F_{corr}	$F_{corr}(0)/F_{corr}$
0	0.06	0.00	1.03	309442.6	319827.5	1
9.9	0.10	0.01	1.13	277315	314286.7	1.01
19	0.17	0.01	1.23	249540.3	308651.5	1.03
29	0.25	0.02	1.44	210647.5	303894.8	1.05
38	0.32	0.02	1.45	205054.3	298038.2	1.07
47	0.39	0.02	1.55	188892	294601.7	1.08

56	0.46	0.03	1.67	172410.7	289496.5	1.10
65	0.54	0.03	1.82	156083.5	284323.2	1.12
74	0.60	0.03	1.91	139471.5	267523.1	1.19
82	0.66	0.04	2.03	117155.6	258792.2	1.23
90	0.73	0.04	2.14	107853.6	252809	1.26

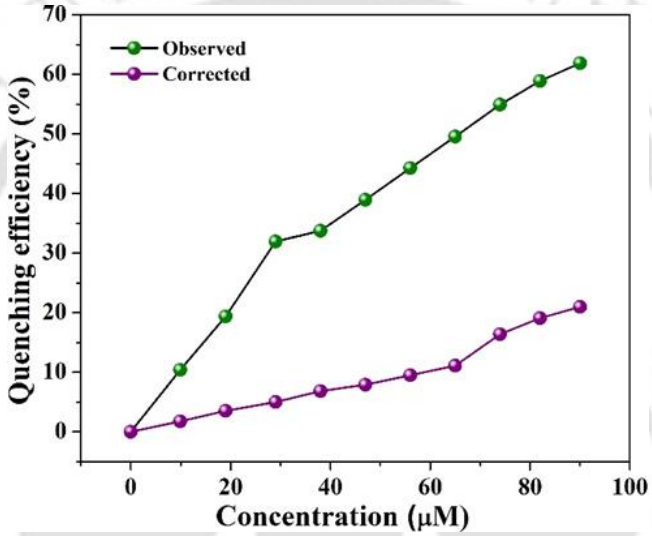

Figure 2.20. Quenching efficiency of CDs observed (green line) and corrected (purple line) measurements after sequential addition of FA. Corrected quenching efficiency refers to the quenching efficiency when IFE contribution is not considered.

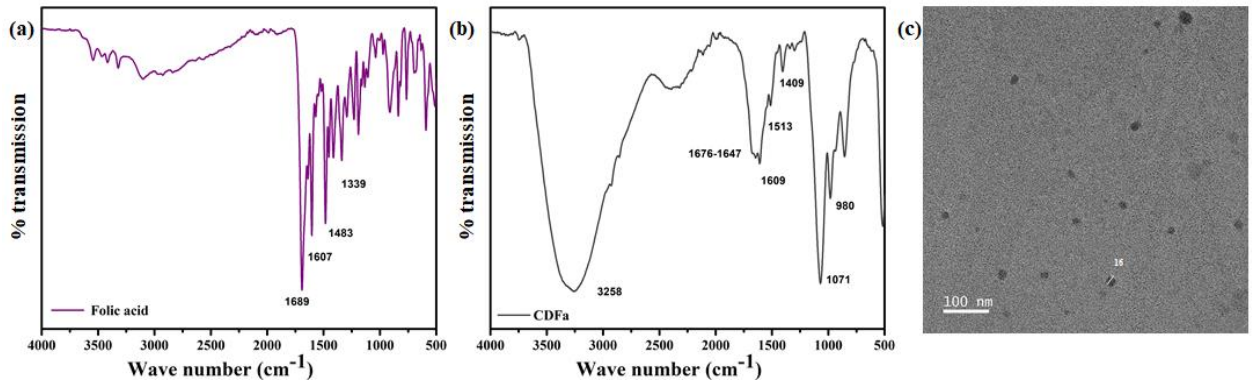

Figure 2.21. FT-IR spectrum of (a) FA, (b) CDFA, and (c) FETEM of CDFA.

2.3.9. Synthesis and Characterization of Drug-loaded, Biotin-conjugated CD (CDBTFu)

FT-IR characteristic peaks of Lys displayed a broad spectrum at 2882 cm^{-1} for C-H stretching, 1626 cm^{-1} for carbonyl stretching due to the -COOH group, and 1499 cm^{-1} for NH_3^+. For KC, characteristic peaks originated at 3392 cm^{-1}, 2966 cm^{-1}, 1223 cm^{-1}, 1035 cm^{-1}, 924 cm^{-1}, and 840 cm^{-1}, interpreting the presence of hydrogen-bonded OH group, C-H asymmetric stretching vibration, sulfate esters, C-O-C stretching, 3,6-anhydro-galactose residue, bending from pyranose residue (Figure 2.22a-b).[117,118]

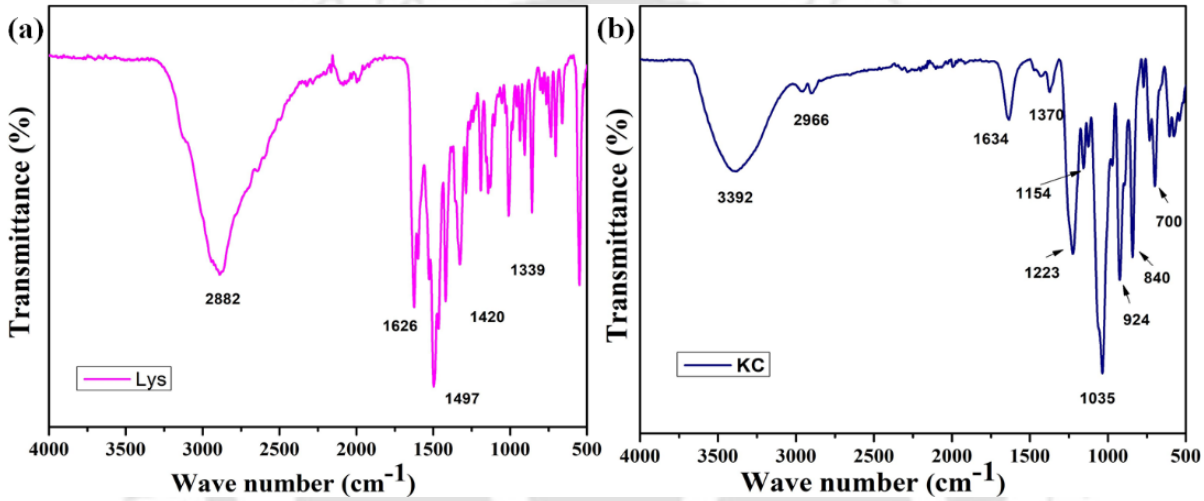

Figure 2.22. FT-IR spectrum of (a) KC and (b) LYS.

FT-IR spectrum of biotin, (N-hydroxy succinimide) NHS, BT-NHS. Biotin has characteristic peak for N-H and O-H around 3300 cm^{-1}, C-H stretching at 2927 cm^{-1} and C=O at 1690 cm^{-1}. NHS has sharp peak for N-O bond at 1781 cm^{-1} and C=O at 1683 cm^{-1}. Two prominent peaks at 1818 cm^{-1} and 1788 cm^{-1} were perceived from NHS ester and NHS C=O stretching vibration, and the broad peak around 1696 cm^{-1} corresponded to C-O stretching vibration for CDBT (Figure 2.23).

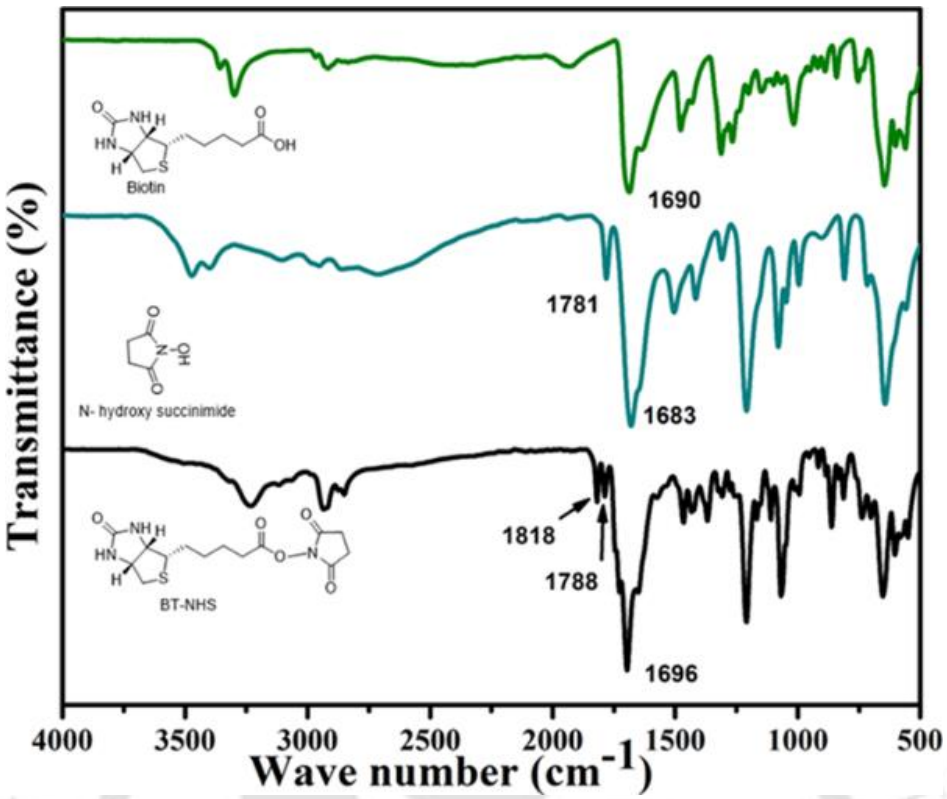

Figure 2.23. FT-IR spectrum of biotin, NHS and BT-NHS.

FT-IR analysis of CDs (1:9) exhibited characteristics peaks at 3387 cm^{-1}, 3125 cm^{-1}, 2934 cm^{-1}, 1657 cm^{1}, 1531 cm^{-1}, 1020 cm^{-1} and 954 cm^{-1} corresponding to -OH, -NH_2, C-H stretching vibration, C=O stretching, N-H bending, C-O-C and 3,6-anhydro-galactose residue, respectively (Figure 2.24a).[119] Presence of these functional groups makes the surface of the CDs hydrophilic for better water solubility. Therefore, it can also be a promising carrier in drug delivery and sensing biomolecules in aqueous media. Further, the formation of CDBT and CDBTFu were confirmed by FT-IR analysis where the spectrum of CDBT displayed peaks at 3233 cm^{-1} for N–H stretching, 2929 cm^{-1} for C-H stretching, and 1470 cm^{-1},1307 cm^{-1} for amide II, amide III respectively and a sharp peak at 1654 cm^{-1} for C=O stretching (amide I), confirming the formation of amide bond between CDs and biotin (Figure 2.24b). The spectrum of CDBTFu revealed the characteristic peaks of 5-Fu with a slight shift at 1509 cm^{-1}, 1246 cm^{-1}, and 748 cm^{-1} for C-N stretching, C-F stretching, and C-H stretching, respectively (Figure 2.24c-d).[120,121]

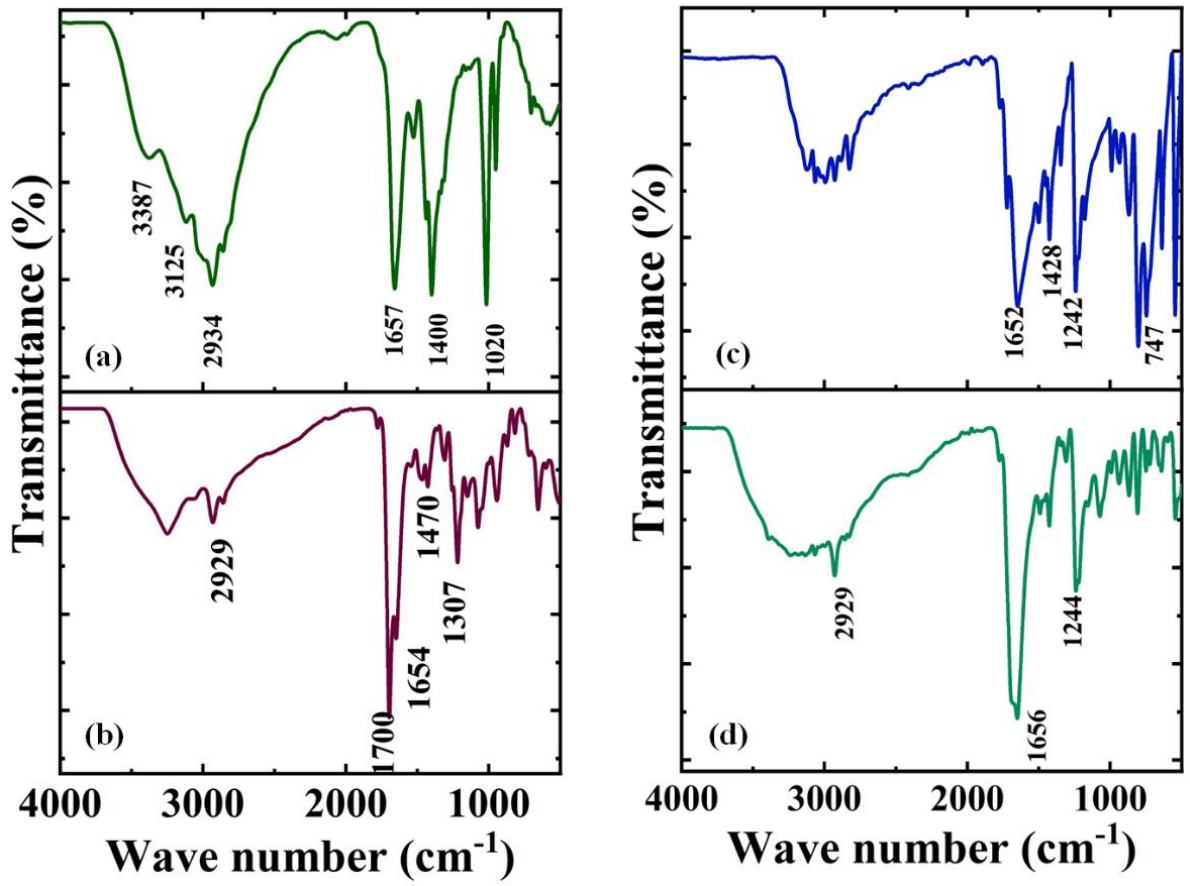

Figure 2.24. FT-IR spectrum of (a) CDs, (b) CDBT (c) 5-Fu, and (d) CDBTFu.

Energy Dispersive X-ray Spectroscopy (EDS) and XRD analysis were performed to understand the elemental composition of the material and its crystallinity. CDs yielded the following composition: 60.13 % C, 19.29 % O, 9.56 % N, 0.52 % S, and 10.5 % Cl, whereas the EDX data of CDBTFu revealed a hike in the percentage of specific atoms like F (3.97%), S (3.24%) and N (17.08%) which eventually confirmed the adduct formation (Figure 2.25).

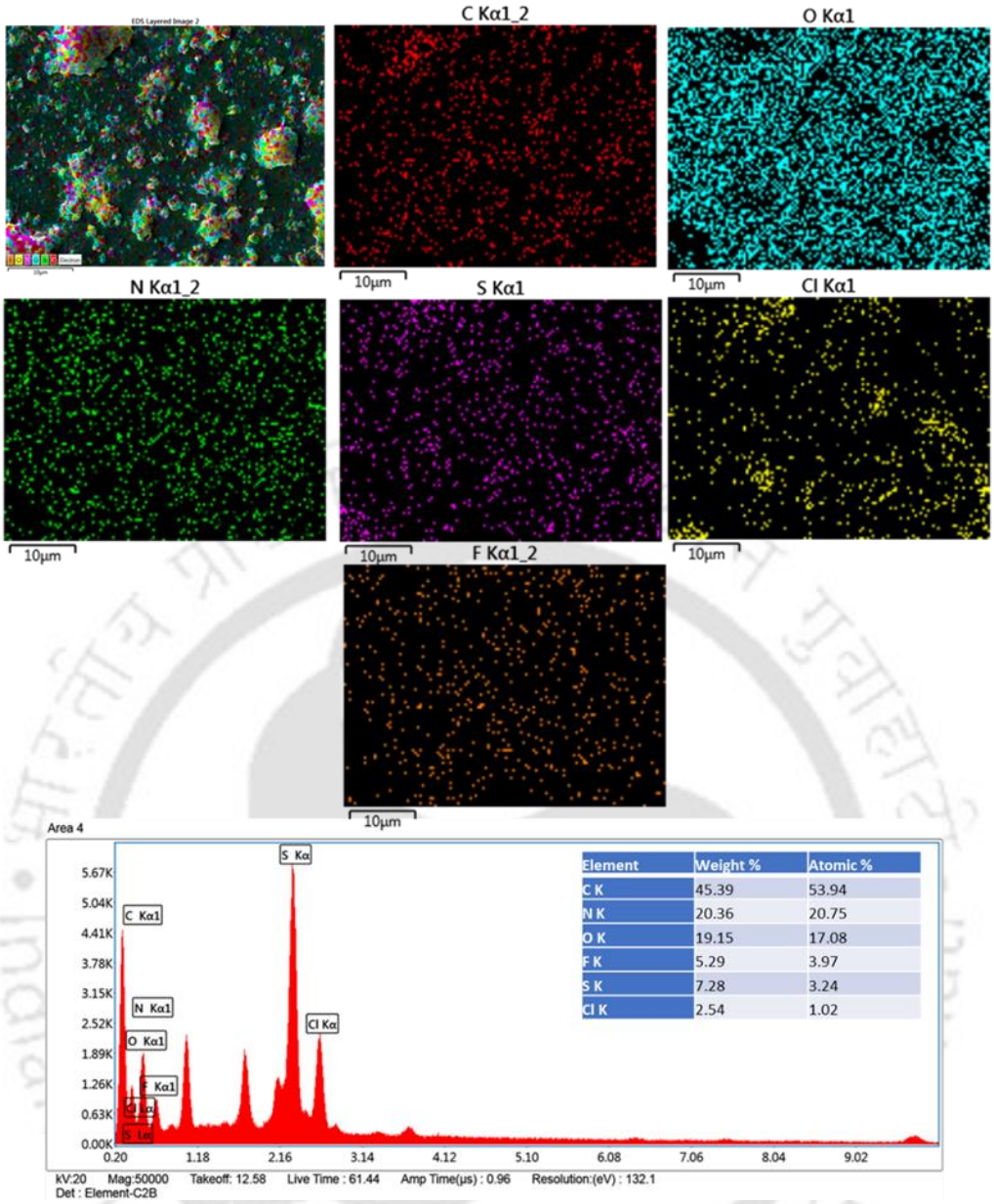

Figure 2.25. EDX elemental mapping of CDBTFu and their weight percentage.

Further, XRD analysis of CD exhibited a broad peak at 2θ = 23.5º, indicating the amorphous nature of CD (Figure 2.26a). However, CDBTFu shows a peak at 28.5º, which overlaps with 5-Fu, indicating successful loading of the drug on the surface of CDs (Figure 2.26b-c). From the XPS spectra of CDBTFu, characteristic peaks were distinguished at 284.5 eV, 531.5 eV, 400.4 eV, 201.5 eV, 162.9 eV for C_{1s}, O_{1s}, N_{1s}, Cl_{2p}, and S_{2p}, respectively (Figure 2.26e). The band for S_{2p} was found to be shifted, and the deconvoluted spectrum indicated the presence of

the C-S-C bond of biotin (Figure 2.27d). A new peak was observed at 688.1 eV, which verified the existence of F_{1s} and confirmed the conjugation with biotin and 5-Fu loading.[122]

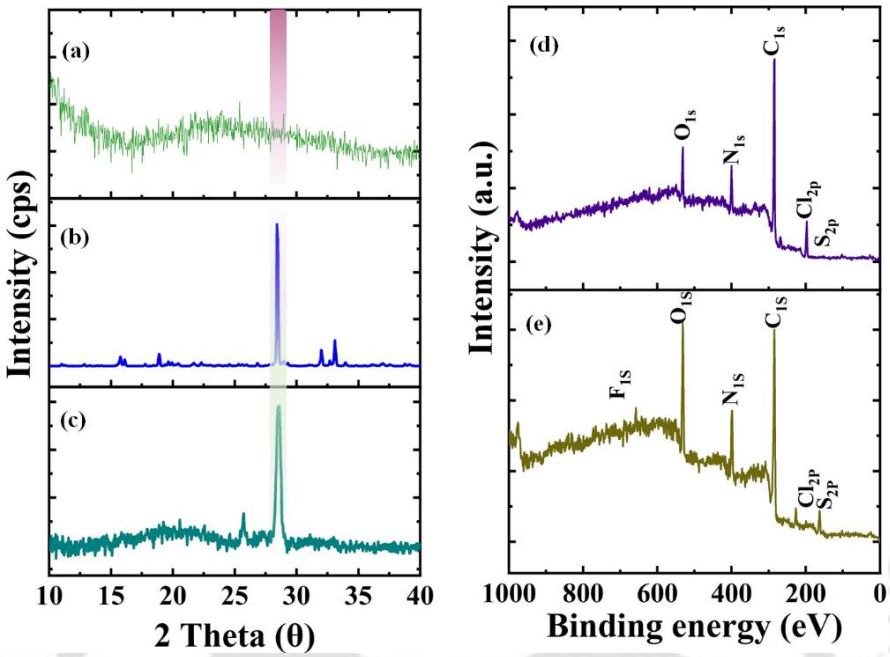

Figure 2.26. Powder XRD analysis of (a) CDs, (b) 5-Fu, and (c) CDBTFu. Figure (d) and (e) represent the XPS spectra of CDs and CDBTFu, respectively.

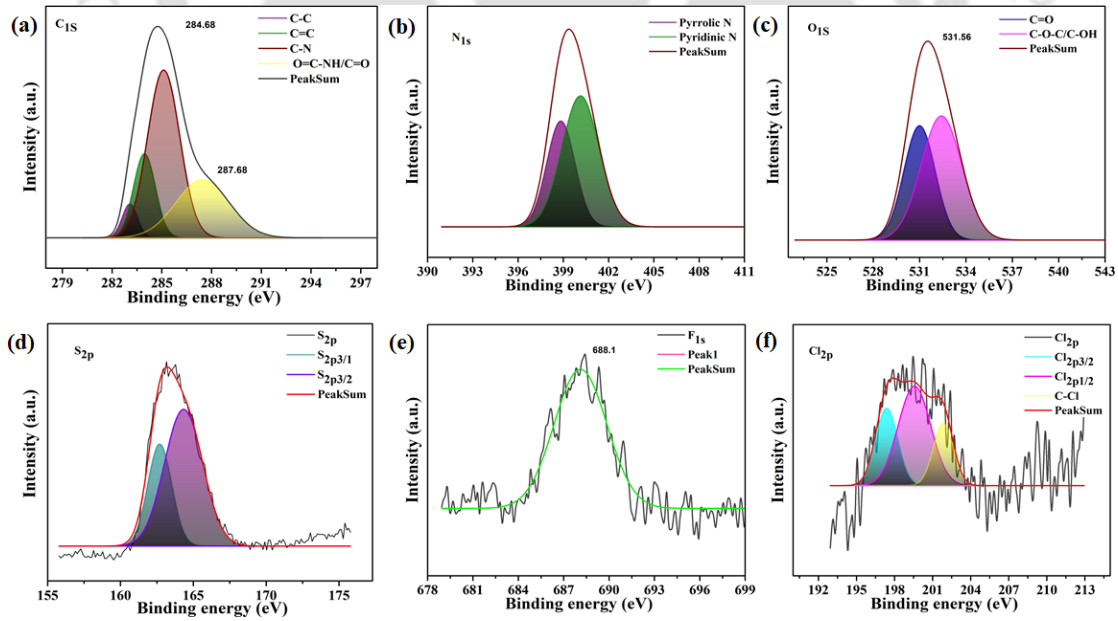

Figure 2.27. Deconvoluted high-resolution XPS spectrum (a) C_{1s}, (b) N_{1S}, (c) O_{1s}, (d) $S_{2p,}$ and (e) Cl_{2p} of CDBTFu.

2.3.10. Drug Loading and Drug Release Study

The model drug 5-Fu was loaded to explore CDBT for cancer theragnostic study. The hydrophilic CDs resulted in remarkable drug encapsulation efficiency (DEE) and drug loading efficiency (DLE) of about 96 % and 75 %, respectively. Using KC and LYS in a ratio of 1:9 resulted in excellent hydrophilicity with enhanced drug loading efficiency compared to previous studies (Table 2.5).[123]

Table 2.5. Comparison table of 5-Fu loading and application.

Material	***5-Fu loading %***	***Stimulus***	***Cell lines***	***Reference***
Bi-QCS-AuNPs@collagen	DEE = 87.46 ± 0.21%	pH	HeLa, human fibroblast cell line, A549	[124]
SiNP	DEE = 75%	pH	MCF7, A549, MC3T3	[125]
5Fu-N@PEGCDs	DEE= 52.3%	pH	A375, HEK	[126]
5-FU@M0F-801	DEE = 88.6%, DLE = 70%	pH	HEK, SW480	[127]
5-FU-CS-CQD-Apt	DEE = 84.7 ± 5.5% DLE = 37.2 ± 3.8%	pH	MCF-7	[128]
CDBTFu	DEE = 96±0.55 % DLE = 75±0.3%	pH	MDA-MB-231, HeLa, HEK	**This work**

Physiological pH was utilized as a stimulus for on-site drug delivery as the pH value reportedly varies in tissues and tumor cells. For example, the extracellular tumor environment possesses an acidic pH (6.1-6.5) than physiological pH (7.4) due to the production of lactic acid, whereas endosomes and lysosomes have even lower pH (5.0-5.4).[129,130] Therefore, we have performed the release study in three different pH solutions (4.5, 6, and 7.4) at 37 ℃ to understand the *in-vitro* release study of 5-Fu (Figure 2.28). In pH 7.4, about 18 % of the drug was released in the first 9 hours, and then sustained release was observed up to 45 % after 50 hours. The initial burst release at pH 7.4 may be due to the release of loosely bound 5-Fu from the carrier surface. However, only 30 % release was found at pH 6.0 in the first 9 hours, and sustained release up to 60 % was calculated after 40 hours, which supports sensitivity towards endosomal or lysosomal pH. Lowering the pH value to 4.5 significantly enhances the burst release and showed a maximum release of up to 80% in 48 hours.

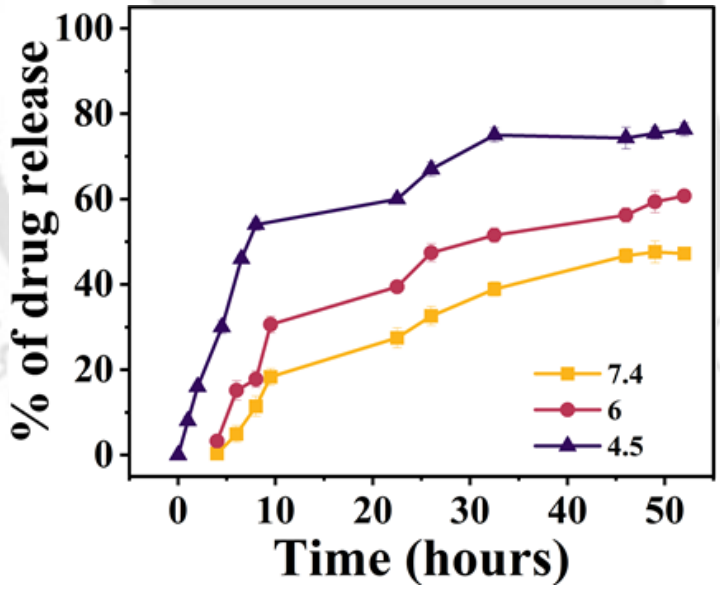

Figure 2.28. Drug release study from CDBTFu at pH 4.5 (blue), pH 6 (pink), and pH 7.4 (yellow).

2.3.11. Cytotoxicity assay

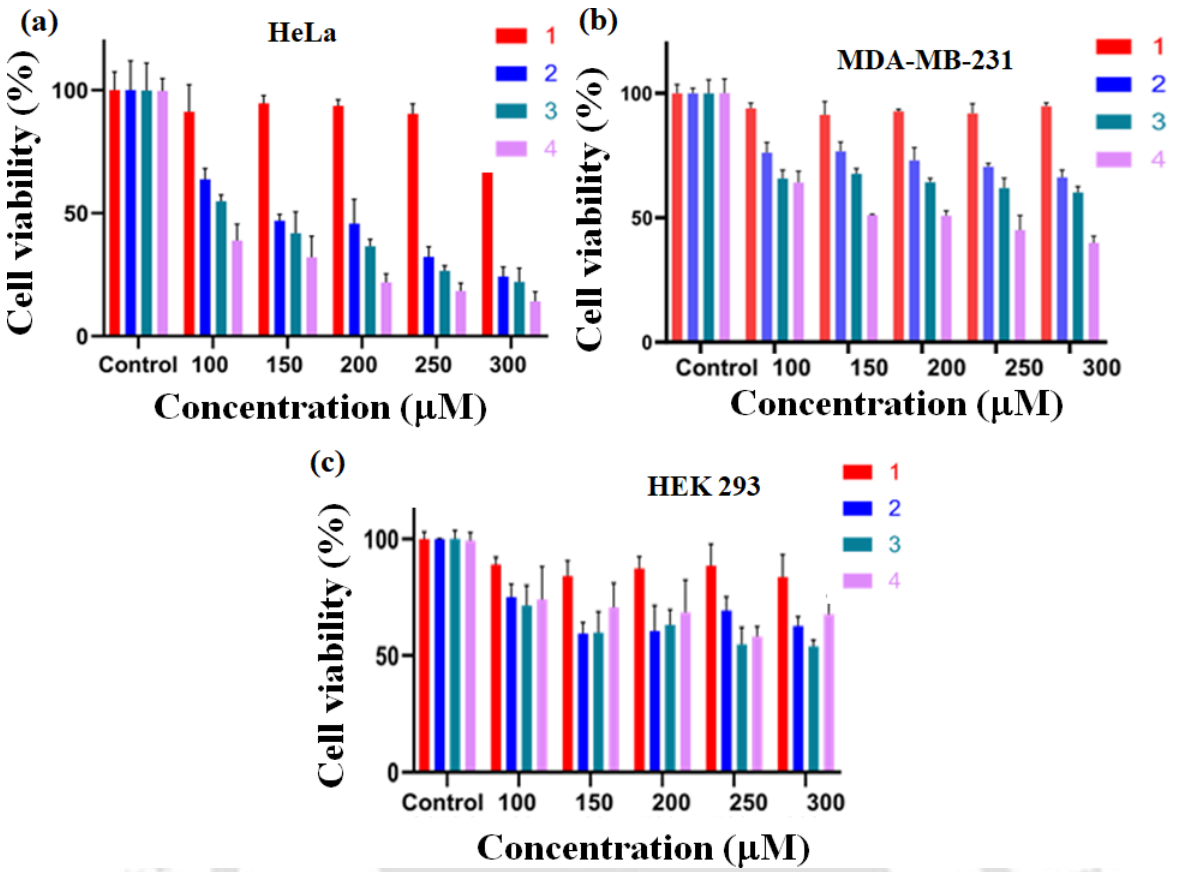

Figure 2.29. MTT assay for cell viability in: (a) HeLa, (b) MDA-MB-231, and (c) HEK-293 cell lines. Cells were treated with (1) CDs, (2) 5-Fu, (3) CDFu, and (4) CDBTFu.

The effectiveness of a drug delivery system can be enhanced by minimizing the side effects. To ensure the application of our designed drug cargo, a cell viability assay was performed with four sets of samples (CDs, 5-Fu, CDFu, and CDBTFu) over three types of cell lines, including two cancer cell lines and one healthy cell line (Figure 2.29a-c). Pristine CDs have exhibited an excellent nontoxic nature in all three cell lines, inferring a safe drug carrier. The IC_{50} value of 5-Fu in the triple-negative breast cancer cell line (MDA-MB-231) was 247 µM, and for CDBTFu, was185 µM. This could be due to the tumor-targeting biotin conjugated to the CDs, which showed the improved drug uptake. Similarly, the IC_{50} value of CDBTFu (81 µM) was significantly improved in HeLa cell line compared to pure 5-Fu (175 µM). The cytotoxic effects of CDBTFu on HeLa and MDA-MB-231 have depicted excellent dose-dependent behavior. To prove the cell-targeting effect of biotin, the cytotoxicity of CDBTFu was studied in healthy

cells. An MTT assay was performed in the human embryonic kidney (HEK-293) cell line. The observed IC_{50} value for CDBTFu was about 300 µM, far more significant than in other cell lines, confirming less toxicity towards healthy cells. The low internalization of CDBTFu is presumably due to the lower expression of biotin receptors in healthy cells.

2.3.12. Cellular Uptake of CDBT Conjugate

A cellular uptake study was performed using confocal laser scanning microscopy (CLSM). The enhanced fluorescence intensity of CDBT-treated cells confirmed the internalization of the synthesized CDBT. HeLa and MDA-MB-231 cell lines are known to have overexpressed biotin receptors. The cell lines were treated with CDs and CDBT for 24 hours. The fluorescence images depicted the enhanced intensity inside cells, signifying the upregulated internalization of CDs in the case of CDBT-treated cell lines (Figure 2.30 and Figure 2.31). Therefore, the improved cellular uptake of biotin-conjugated drug vehicle confirms the target-specific nature towards cancer cells with higher expression of biotin receptors.

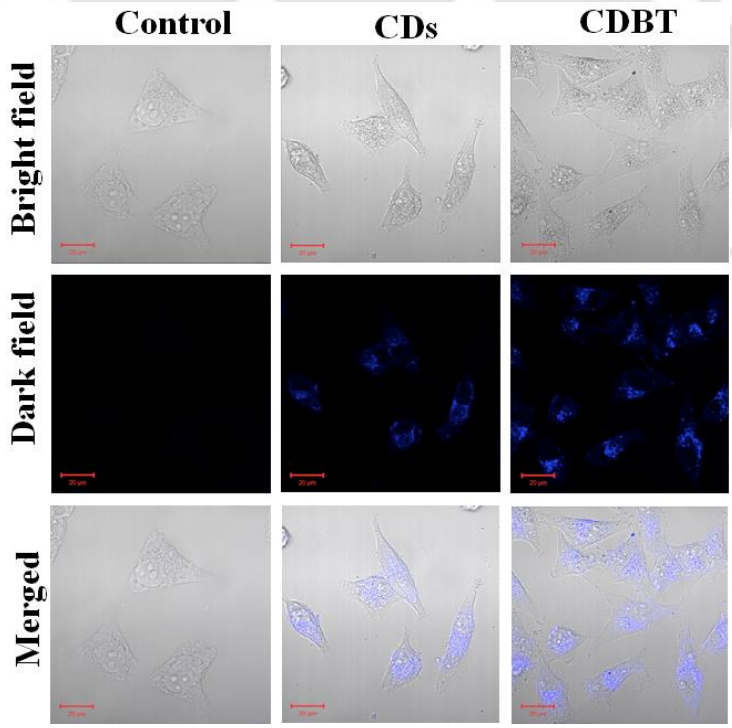

Figure 2.30. CLSM image of HeLa cells treated with CDs and CDBT, respectively (scale bar is 20 µm). The fluorescent images were observed at λ_{ex} 350 nm and λ_{em} 430 nm.

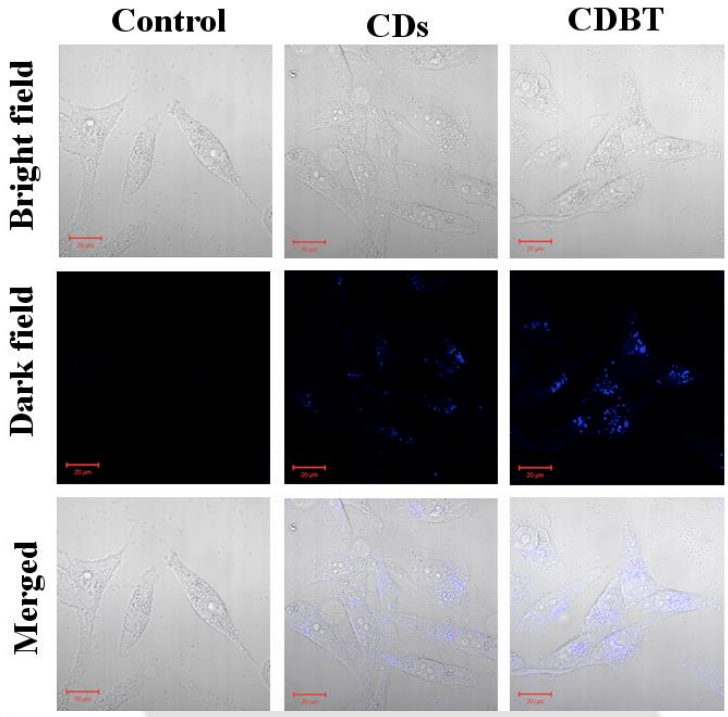

Figure 2.31. CLSM image of MDA-MB-231 cells treated with CDs and CDBT, respectively (scale bar is 20 µm). The fluorescent images were observed at λ_{ex} 350 nm and λ_{em} 430 nm.

2.3.13. Hemotoxicity of CDs

The impact of CDs on blood compatibility was evaluated through a hemolysis assay of human blood samples. The clear supernatant after PBS treatment exhibited no heme release and red supernatant after Triton X-100 treatment suggested complete heme release. Different concentrations of CDs 100 µg/mL, 200 µg/mL, and 400 µg/mL exhibited 0.67%, 1.06%, and 1.7% RBC lysis, respectively (Figure 2.32). The heme release data supports the non-hemotoxic nature of CDs up to 400 µg/mL.[131]

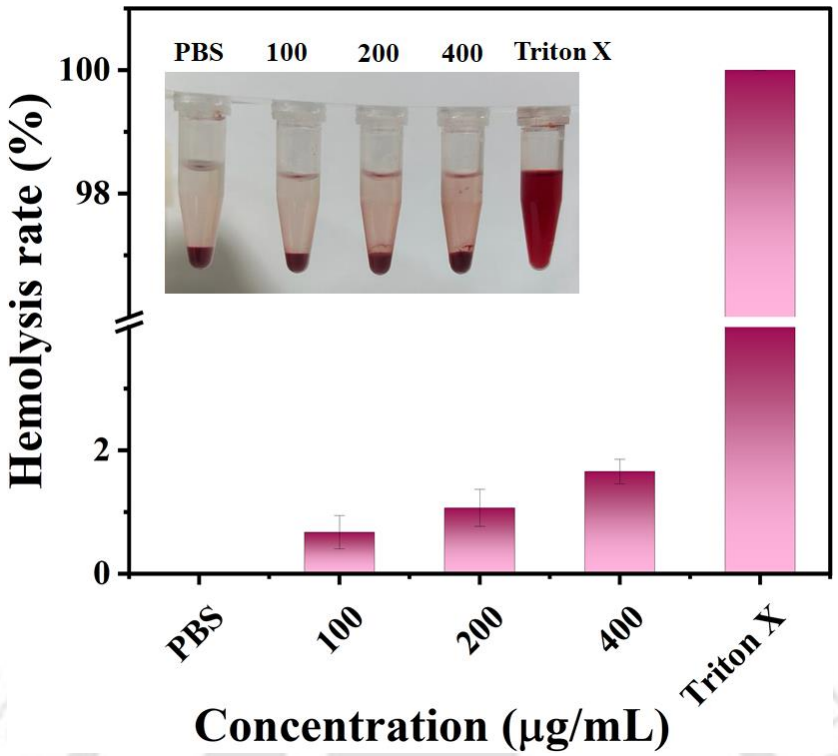

Figure 2.32. Study of hemolysis with increasing concentration of CDs with negative (PBS) and positive (Triton X-100) control. (Inset: the digital images of heme-release after treatment with CDs).

2.4. Conclusion

Hetero atom-doped blue-fluorescent carbon dots were synthesized in a single step from sea weed-based polymer KC and amino acid LYS for high-throughput detection of folic acid. The CDs have exhibited excellent stability over a wide pH range, high saline concentration, and long storage time. It has excellent selectivity towards FA among 35 other co-existing analytes within only 10 seconds. Moreover, the CDs can efficiently detect FA in actual samples such as orange extract, green gram dal, and FA tablets. A detailed study unveiled the mechanism of quenching as a combination of IFE and static quenching. For practical application, paper strip-based detection was successfully done. The material can act as a superior platform to invisible ink. In addition, biotin-conjugated drug cargo has displayed high drug encapsulation and pH-stimulated release of chemotherapeutic drug 5-Fu. In-vitro cytotoxicity data from MDA-MB-

231 and HeLa cells showed low IC_{50} values of 185 µM and 81 µM, respectively. In contrast, healthy cells HEK-293 showed an IC_{50} value greater than 300 µM. The low IC_{50} values for cancer cells can be explained by the high cellular uptake of CDBT, confirmed by CLSM imaging. Our synthesized CDs showed high effectiveness for FA detection at the nano-molar level and cancer-targeting drug delivery tool.

Chapter 3. Synthesis of Casein and Thymine Derived Carbon Dots for the Detection of Hg^{+2} and Tetracycline in Aqueous Media

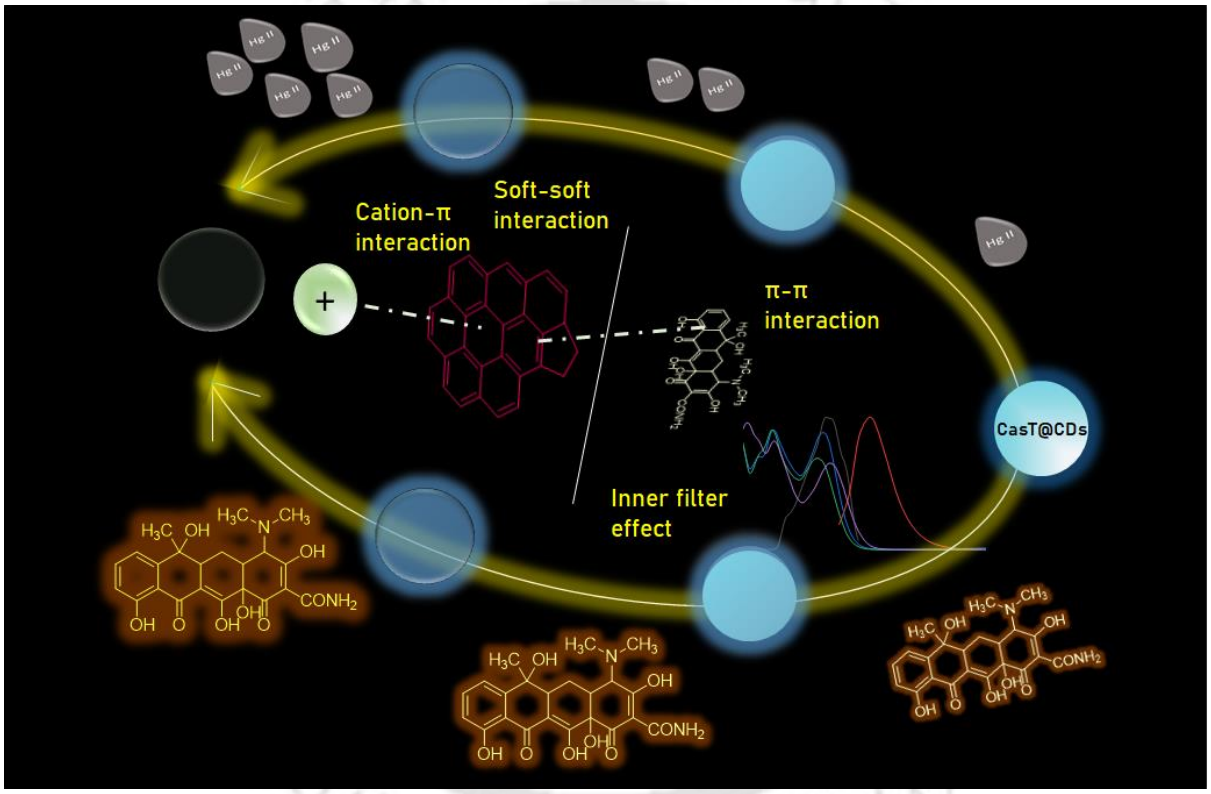

3.1. Overview

Water remediation has become a serious concern with the growth of civilization. This remediation includes (i) detection of contaminants and (ii) their successful removal. Among the contaminants, antibiotics and heavy metals have been found to be two major contaminants in today's scenario.[132–134] Tetracyclines and its derivatives are widespread and commonly used antibiotics for pneumonia, respiratory tract infections, and pelvic inflammatory diseases.[135–137] Therefore, the detection of the class of tetracyclines is necessary. Similarly, heavy metal contamination is caused by natural and anthropic sources like cement manufacturing, mining, combustion of fossil fuels, battery processing, and volcanic and oceanic emissions. Among them, mercury (Hg) has a massive toxic and long-lasting impact on the ecosystem. mercury is one of the heavy metals which generates multiple life threatening diseases like Minamata, cancer, cardiovascular diseases, neurological disorders etc.[138,139] Organic mercury causes potential damage to health compared to elemental mercury, for example, bacteria and yeast convert inorganic Hg^{+2} into organic methyl mercury (MeHg) in the gastrointestinal tract, which can even cross the blood-brain barriers.[140] Therefore, the selective detection of these pollutants in aqueous medium is necessary to address their detrimental effects on water quality and the ecosystem. Additionally, an overdose of antibiotics exhibits detrimental effects on health. Hence, there is a pressing need to develop sensors capable of accurately detecting therapeutic levels in biological fluids such as serum and urine.

Over the past few years, the luminescence technique has gathered ubiquitous attention for various detection applications owing to its simple functioning and selective detection, with facile and rapid visualization of analytes. The growth of nanotechnology has led to several novel fluorescent materials, such as quantum dots,[141,142] nanoparticles,[143,144] metal-organic framework (MOF),[145,146] and nanometal clusters[147,148] as efficient probes. CDs are one the those

unique fluorogenic material that can effectively detect analytes without causing adverse effect towards environment. Therefore, we have selected casein (Cas) and thymine (T) as precursor.

Herein, we have strategically designed nitrogen-doped carbon dots from casein milk protein and nucleobase thymine (CasT@CDs) using the pyrolysis method. In the present work, we have targeted two major contaminants, Mercury (Hg^{+2}) and TC, for their detection in aqueous medium. Hg^{+2} is a well-known soft cation and TC possesses four conjugated fused rings, which may have feasible interaction with sp^2-hybridized carbon dots. The nanodot exhibited extraordinary stability in various conditions, such as temperature, salt solution, UV radiation and long storage time. The precursor material contains amino acid residues, generating an excellent quantum yield of CasT@CDs 36%. It is noteworthy that the fluorescence quenching was observed for Hg^{+2} and tetracyclines (TC, ClTC, DTC) in CasT@CDs with an ultra-small response time of less than 10 seconds. Moreover, these polymeric nanodots have demonstrated shallow limits of detection (LOD) for Hg^{+2} (5.35 nM, which is lower than the USPEA guidelines) and tetracyclines (10.4 nM, 11.3 nM, and 11.7 nM for TC, DTC, and ClTC, respectively). The synthesized CasT@CDs can detect TC in biofluids such as milk, urine, and serum samples and Hg^{+2} in various aqueous media (tap water, lake water, and river water) and cigarette samples, showcasing our synthesized CDs' real-life applicability. Additionally, we have prepared CasT@CDs coated paper strips for the rapid and handy detection of analytes that have exhibited nanomolar detection of Hg^{+2} and TC in water.

3.2. Experimental Section

3.2.1. Materials

Casein sodium was procured from the Tokyo Chemical Industry (Tokyo, Japan). Tetracycline hydrochloride (TC), 7-hlorotetracycline hydrochloride (ClTC), doxycycline hydrochloride (DTC), ampicillin sodium salt (AMP), gentamycin Sulfate, kanamycin sulfate, ibuprofen,

naproxen, and vancomycin hydrochloride were obtained from Sigma Aldrich (St. Louis, MO, United States). Metal salts were procured from Alfa Aesar (Heysham, England) and Tokyo Chemical Industry (Tokyo, Japan). All the analytes were used without further purification.

3.2.2. Synthesis of CasT@CDs from Milk Protein

Nitrogen-rich CasT@CDs were prepared using the pyrolysis method. 200 mg of Cas: T (1.66:1) was transferred into a reaction vessel under constant nitrogen purge at three different temperatures (170 ℃, 200 ℃, and 240 ℃) for 2 hours. After the reaction, the brown-colored mixture was obtained and ground thoroughly. Then, the solid product was dispersed in double-deionized water and filtered to remove large particles. The yellow-colored supernatant was stored at 4 ℃. The formation of CasT@CDs was confirmed using spectroscopic analysis (such as UV-vis and fluorescence spectroscopy), and the size, composition, and morphology were analyzed using FETEM, XPS, XRD, and FT-IR.

3.2.3. Fluorometric Detection of TC in Milk, Urine, and Serum

A milk sample was procured from the local market, and 0.1 M HCl was added to precipitate the protein. The clear supernatant was obtained after centrifugation at 9000 rpm for 15 minutes. Later, the supernatant was diluted (1:10) in DI water and titrated against CasT@CDs to check the interference. The supernatant was then spiked with a known concentration of TC, and fluorescence was analyzed. Urine sample (10 mL) was collected from a healthy volunteer. The sample was digested with 500 µL of HNO_3 to eliminate the dispersed living organisms. After centrifugation at 8000 rpm for 10 minutes, a clear supernatant was procured for the experiments.[112] The supernatant was diluted (1:20) with water, and interferences were checked. To check the recovery percentage, TC of different concentrations was spiked. The selectivity of CasT@CDs towards TC in serum samples was also studied. Initially, 5 mL of blood sample was collected from a healthy volunteer. The whole blood sample was centrifuged at 5000 rpm

for 20 minutes at 4 ℃ to obtain the plasma. Later, the solution was diluted (1:20) in water and spiked with a pre-determined concentration of TC. For each case, a blank test was performed with the extract only and was considered as background.

3.2.4. Fluorometric Detection of Hg^{+2} in Different Aqueous Media and Cigarette Samples

2 mg CasT@CDs was dispersed in 2 mL of water to obtain a stable suspension. 20 µL of an aliquot was mixed with 980 µL of deionized water, and the presence of Hg^{+2} or TC was tested. After examination of background interference, 20 µL of CasT@CDs was added to 980 µL of various aqueous media, and a known concentration of Hg^{+2} was added. Stock solutions of Hg^{+2} were made in river, lake, and tap water, respectively.

The sample preparation was made from an earlier reported protocol.[149] Briefly, cigarette sample was procured from the local market. After removing the outside membrane, the solid mixture was dried in the oven for 24 hours. The sample was ground using a mortar pestle and added portion-wise to piranha solution (3:1 H_2SO_4 and H_2O_2). The clear supernatant was diluted (1:50) using distilled water, and the pH was adjusted to 8. The solution was titrated against CasT@CDs, and known Hg^{+2} was spiked.

3.3. Results and Discussions

3.3.1. Physiochemical Properties of CasT@CDs

The preparation of CasT@CDs involves a simple pyrolysis process. After preliminary checking for the formation of CDs under a UV lamp (inset image Figure 1a), the photophysical properties of CasT@CDs, dispersed in deionized water, were investigated using UV-visible and fluorescence spectroscopy. CasT@CDs exhibited one prominent hump at 265 nm and a shoulder peak at 335 nm (Figure 3.1a). The peaks can be attributed to the π-π^* transition of C=C groups from the aromatic ring of amino acid present in the protein chain and n-π^* originated from C-O/C-N.[6] The fluorescence scanning from 250 to 400 nm excitation of CDs,

exhibited the two highest emission intensity while excitation at 330 nm and 370 nm. However, excitation spectrum of 370 nm resulted highest intensity at 445 nm with an excitation-dependent 100 nm red shift (Figure 3.1b). Therefore, for further studies we have used λ_{max} at 370 nm. The origin of fluorescence emission for CDs can be attributed to surface-state molecular fluorescence and the quantum confinement effect.[150,151] Herein, the precursor material is enriched with hetero atoms such as nitrogen, oxygen which introduces another HOMO state, leading to the possibility of more electronic transitions.[152] Moreover, the red shift in the photoluminescent spectrum for the CDs is due to different degrees of surface oxidation that occurred during changes in reaction parameters.

The quantum yield (QY) of CasT@CDs was calculated using the relative method with a reference dye quinine sulfate using the following formula:

$$QY_{Sample} = QY_{Reference} \times \frac{A_{Reference} E_{Sample}}{A_{Sample} E_{Reference}} \times \left(\frac{\eta_{Sample}}{\eta_{Reference}}\right)^2$$

Where A is the absorbance at the excitation wavelength, E is integrated fluorescence intensity, and η is the refractive index of the solvent. The QY was found to be 36% from 2 hours of carbonization, which was further used for the rest of the experiments. Hence, we proceed with the rest of the work with the CasT@CDs obtained after 2 hours of carbonization at 200 ℃.

3.3.2. Characterizations of CasT@CDs

The FETEM of CasT@CDs showed that the prepared carbon dots were well dispersed. The average particle size was 4.2 nm (from the histogram plot, Figure 3.1c-d). The HRTEM image exhibited a highly amorphous nature of CasT@CDs (Figure 3.1f).[153] Figure 1g showed a traditional PXRD with a broad hump around 2θ = 22.5º, which simultaneously supports the highly amorphous nature of CDs, similar to previous reports and complemented the SAED pattern (Figure 3.1e).[154] The highly disordered amorphous nature originated from hetero atom-

rich surface groups. Four major peaks were found in the FT-IR spectrum of CDs at around 3224cm^{-1}, 2961 cm^{-1}, 1668 cm^{-1}, and 1453 cm^{-1} that can be attributed to OH/NH_2, C-H stretching, carbonyl stretching, and C-N stretching (Figure 3.1h).[155,156] XPS was performed to understand the chemical structure of the blue CDs. This analysis provided detailed information on the elemental composition and the chemical states of the elements present in the CDs, offering insights into their surface chemistry and functional groups. The XPS pattern of CasT@CDs displayed three sharp peaks for C1s, N1s, and O1s at 285.9 eV, 398.9 eV, and 531.6 eV, respectively (Figure 3.1i).[157,158] EDS elemental composition supported the presence of C, O and N as, 41%, 36% and 22%, respectively (Figure 3.2).

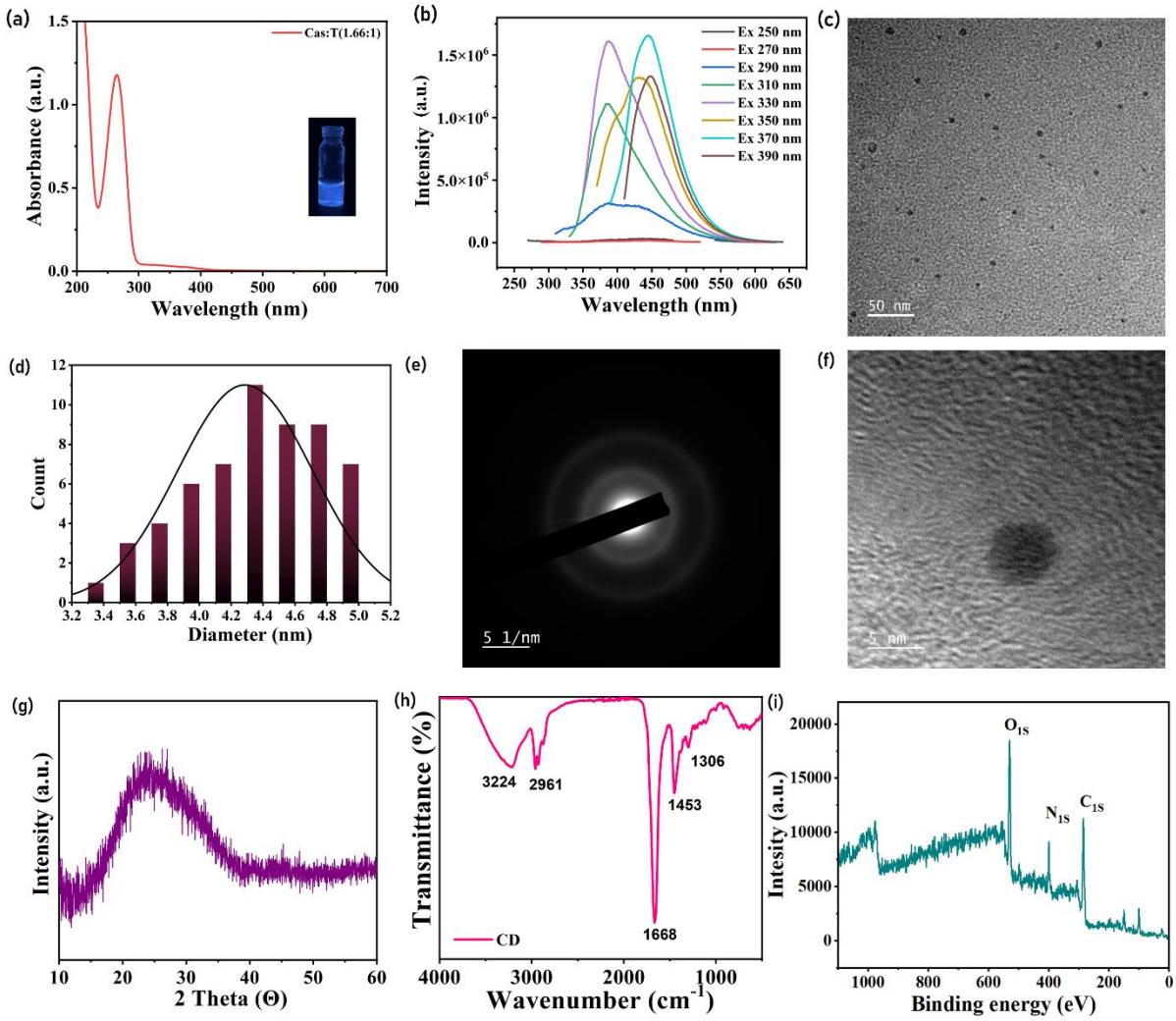

Figure 3.1. (a) UV absorption spectrum of CasT@CDs synthesized at 200 ℃ for 2 hours. (the Inset image is for the CasT@CDs under UV lamp). (b) The fluorescence emission spectrum of CDs synthesized at 200 ℃ for using various excitation wavelengths. (c) FETEM image of CasT@CDs in 50 nm scale bar and (d) is the particle size distribution plot. (e) SAED pattern of CasT@CDs (f) is the HRTEM image of CasT@CDs exhibiting no crystalline planes. (g) XRD pattern. (h) the FT-IR spectrum, and (i) the XPS pattern of CasT@CDs.

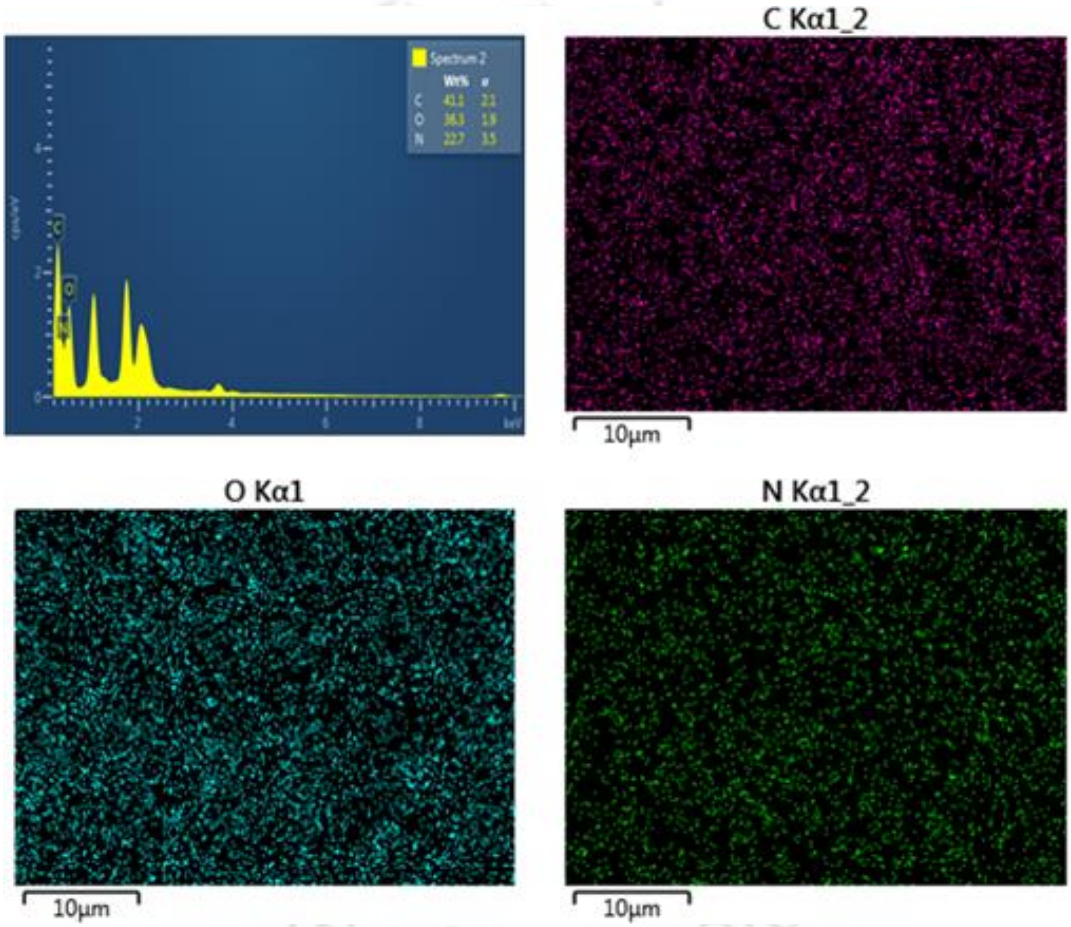

Figure 3.2. EDX elemental composition and mapping of CasT@CDs.

To assess the potential use of CasT@CDs as a sensor, the stability of the probe was investigated under various experimental conditions. The probe has exhibited excellent stability across multiple pH solutions of phosphate buffer saline (PBS) and NaCl solutions (Figure 3.3a-b), inferring potential use in broad experimental conditions. The fluorescence intensity was recorded in UV exposure at an interval of 30 minutes. The emission intensity maxima

decreased only 15% upon 4.5 hours of UV radiation (Figure 3.3c). The effect of temperature on fluorescence intensity was also studied which yielded <20 % loss of intensity at 85 ℃ (Figure 3.3d). Moreover, it exhibits almost the same fluorescent intensity even up to three months of storage (Figure 3.3e). Such excellent stability indicating CasT@CDs can be utilized as potential nanosensor.

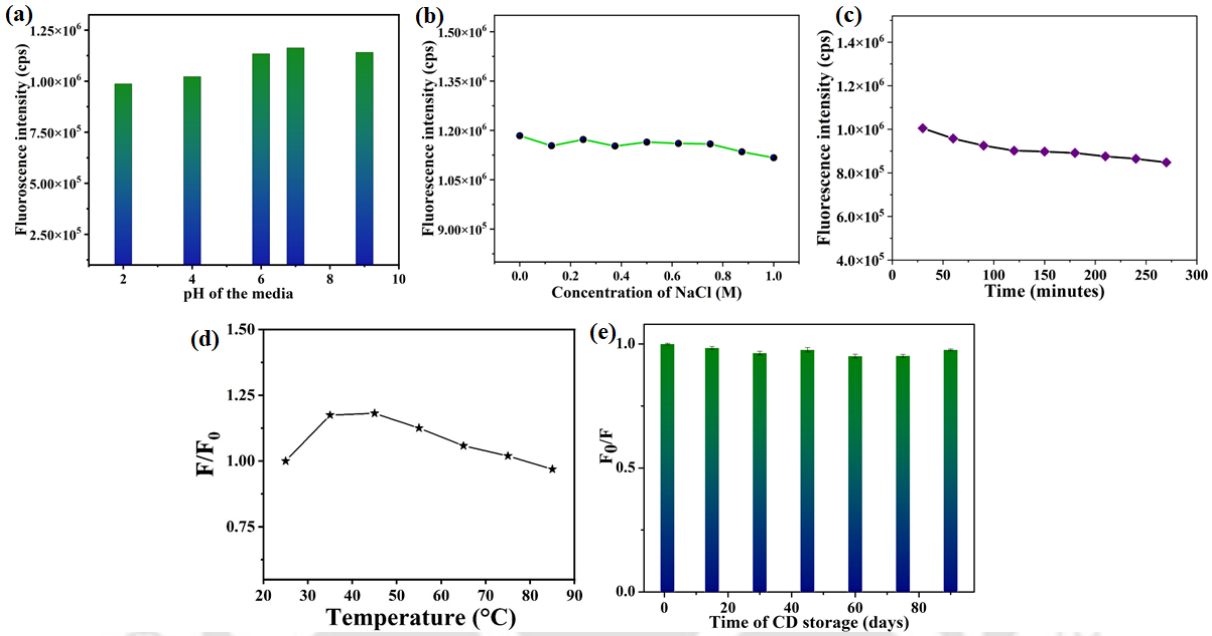

Figure 3.3. Stability of CasT@CDs (a) depending on pH ranges from 2-11, (b) depending on NaCl concentration, (c) depending on UV radiation, (d) depending upon temperature, and (e) storage time.

3.3.4. Detection of TC using CasT@CDs

Considering the threats caused by leftover antibiotic residue in fish, soil, water, and milk we have used our CasT@CDs as a nanosensor for the detection of TCs. Fluorescence titration of CasT@CDs against 100 µL 5 mM TC resulted in an instant turn-off fluorescence in less than 10 seconds in the aqueous medium (Figure 3.4a-b). To confirm the precise affinity of CasT@CDs towards TC antibiotics, fluorescence emission was recorded in the presence of some common analytes (amino acids, vitamins, dopamine, fructose, and glucose) and series of

antibiotics (ampicillin, gentamycin, ciprofloxacin, ibuprofen, vancomycin, kanamycin, naproxen, and streptomycin, and tetracycline) to monitor the change in photoluminescence properties of CasT@CDs. The result exhibited diminished fluorescence intensity of the nanosensor with a gradual increase in TC concentration (Figure 3.5) and excellent selectivity towards TC even in the presence of other analytes (Figure 3.4e-f). The result further made us curious about the effect of other TC derivatives. Hence, we performed the fluorescence titration of CasT@CDs against another two derivatives of TC, i.e., ClTC and DTC, with the aforementioned experimental condition. Interestingly, the experiment exhibited a similar turn-off phenomenon of fluorescent nanosensors (Figure 3.4c-d). TC antibiotics contain a linear fused tetracyclic nucleus with various functional groups, which may be the reason for interaction with the nanoprobe leading to turn-off fluorescence.

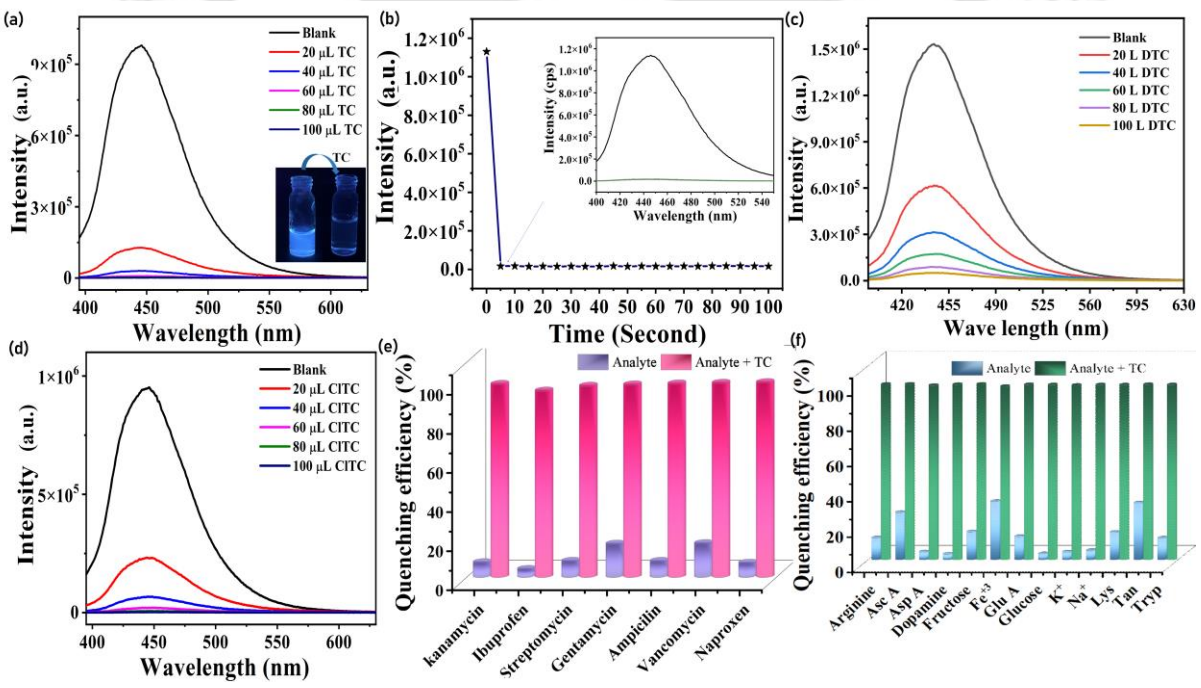

Figure 3.4. Fluorescence response at 445 nm of CasT@CDs in the presence of (a) TC, (c) DTC, and (d) ClTC. (b) time-dependent response of CasT@CDs to estimate the saturation time of quenching after adding 5 mM 100 µL TC (inset image is the fluorescence spectrum of the time-dependent experiment), and (c) digital image of CasT@CDs under a UV lamp (365 nm)

before and after addition of TC. Fluorescence quenching efficiency of CasT@CDs in the presence of (e) antibiotics. (f) Change in fluorescence response in presence and absence of TC with other analytes (arginine, ascorbic acid, aspartic acid, dopamine, fructose, Fe^{+3}, glutamic acid, glucose, K^+, Na^+, lysine, tannic acid and tryptophan).

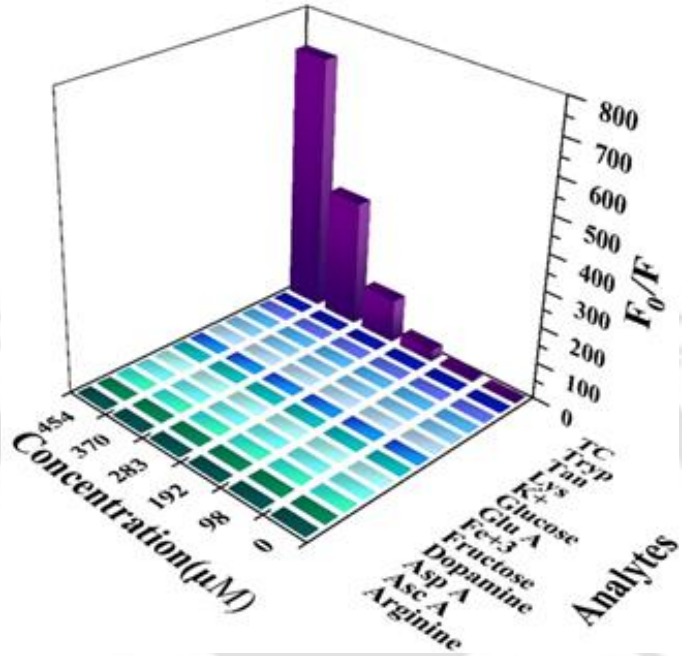

Figure 3.5. Stern-Volmer plot for analytes against CasT@CDs titration upon incremental addition of 100 μL of 5 mM analytes (λex = 370 nm).

Stern−Volmer (SV) equation ($I_0/I = 1 + K_q[Q]$) was employed to better understand the fluorescence quenching of CasT@CDs depending on the TC concentration. Here, I_0 and I are denoted as the fluorescence intensity of our probe dispersed in water before and after the addition of TCs, respectively, and Kq is the quenching constant. The value for SV constant $K_{SV} = \tau_0 * K_q$, where τ_0 is the fluorescence lifetime of CasT@CDs. SV plot was found to be linear in a low concentration range of TCs where the values of K_{SV} were obtained as 1×10^5, 8.09×10^4 and 8.7×10^4 and the LOD (= 3σ/N, σ is the standard deviation of the blank sample, N is the slope obtained from the curve) values were 10.4 nM, 11.3 nM, and 11.7 nM for TC, DTC, and ClTC respectively (Figure 3.6-3.8, and Table 3.2). The calculation for σ has been demonstrated

in Table 3.1. CasT@CDs possesses exceptional selectivity rapid response to a broad range of antibiotics and low limit of detection, making it unique among other nanosensors (Table 3.3).

Table 3.1. Calculation of slandered deviation from blank fluorescence reading of CasT@CDs.

Fluorescence intensity (F)	**Average (F')**	**F – F'**	**$(F - F')^2$**	**$\sum(F - F')^2$**	**$\sum(F - F')^2/N$**	**$\sqrt{(\sum(F - F')^2/N)}$**
1.85E+06	1.83E+06	1.80E+04	3.24E+08	9.37E+08	7.81E+07	8.84E+03
1.83E+06	1.83E+06	4.66E+03	2.17E+07			
1.83E+06	1.83E+06	2.33E+03	5.44E+06			
1.84E+06	1.83E+06	9.91E+03	9.83E+07			
1.84E+06	1.82E+06	1.80E+04	3.24E+08			
1.83E+06	1.82E+06	4.84E+03	2.34E+07			
1.83E+06	1.82E+06	4.39E+03	1.93E+07			
1.83E+06	1.82E+06	1.07E+04	1.14E+08			
1.81E+06	1.82E+06	-1.67E+03	2.80E+06			
1.81E+06	1.82E+06	-2.20E+03	4.84E+06			

1.82E+06	1.82E+06	0.00E+00	0.00E+00
1.85E+06	1.83E+06	1.80E+04	3.24E+08

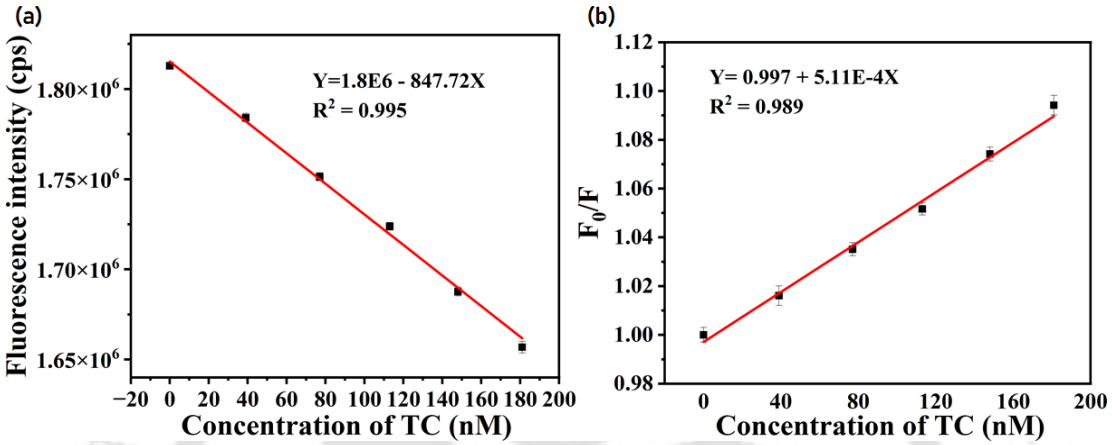

Figure 3.6. (a) Change in fluorescence emission intensity of CasT@CDs (in water) upon addition of TC and (b) Stern-Volmer plot.

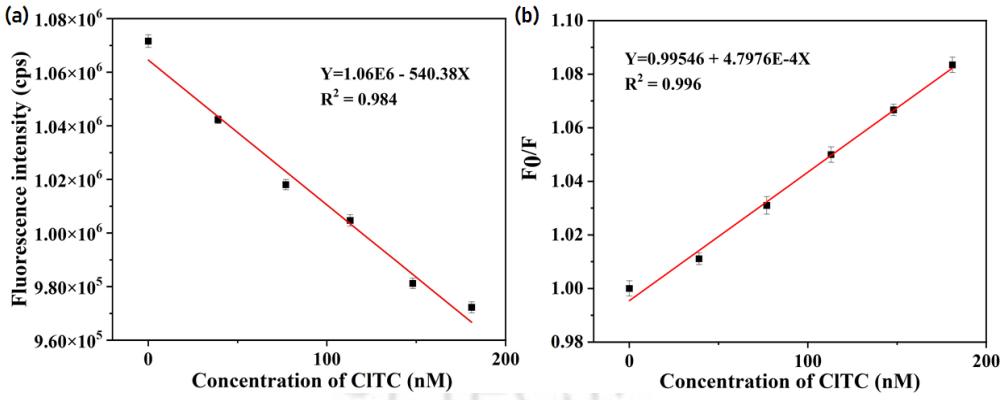

Figure 3.7. (a) Change in fluorescence emission intensity of CasT@CDs (in water) upon addition of ClTC and (b) Stern-Volmer plot.

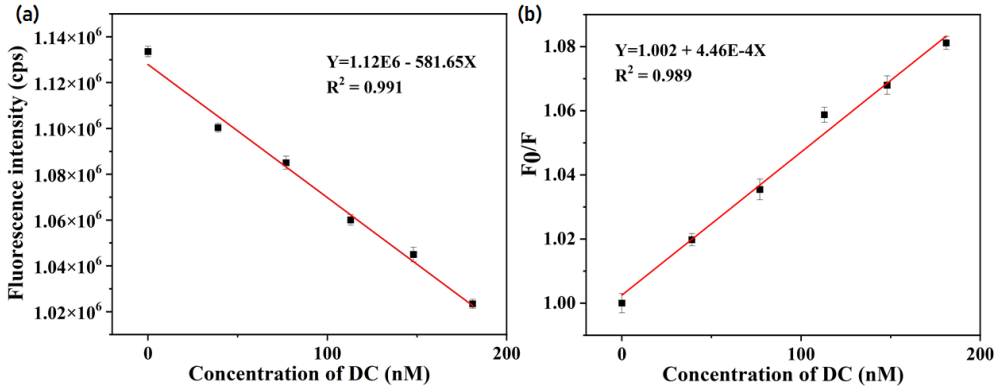

Figure 3.8. (a) Change in fluorescence emission intensity of CasT@CDs (in water) upon addition of DC and (b) Stern-Volmer plot.

Table 3.2. LOD of TC, ClTC and DTC.

Analyte	*Concentration range (nM)*	*Slope*	*Intercept*	*Correlation coefficient (R^2)*	*LOD (nM)*	*Regression equation*
TC	39 – 182	847	1.81E6	0.998	10.4	1.81E6 - 847X
DC	39 – 182	781	1.12E6	0.995	11.3	1.12E6 - 781X
ClTC	39 – 182	736	1.06E6	0.991	11.7	1.06E6 - 736X

Table 3.3. Summarized table for CDs used in TC detection and their selectivity.

Material	*Antibiotics*	*Sample*	*Response Time*	*LOD*	*Ref*
Atta-CDs-Eu Atta-CDs	TC	Lake water, Tap water, milk, honey	5 min	8.7 nM	[141]

N-CDs form cellulose diacetate and ammonium hydroxide	TC	--	--	0.06 µM	[159]
Blue CDs from tobacco	TC OTC CTC	Paper strips	10 min 10 min 60 min	5.18 nM 6.06 nM 14 nM	[160]
Citric acid and glutathione derived CDs	TC	Milk, paper strips	--	5.2×10^{-7} mol/L	[116]
CD–Eu^{3+}	TC, OTC	Smartphone	1 min	11 nM	[161]
B-CDs from green jujube and ethylenediamine	TC	Lake water	--	0.061 µM	[162]
PS-CDs from papaya seeds and ethylenediamine	TC	Milk, orange juice, tap water, and honey	--	120 nM	[163]
CasT@CDs	TC ClTC DTC	Milk, urine, serum	<10 sec	10.4 nM 11.7 nM 11.3 nM	**This work**

3.3.5. Mechanism for TC Detection

The fluorescence turn-off phenomenon can occur through distinct sensing mechanisms such as photo-induced electron transfer (PET), FRET, IFE, and reaction-based sensing.[116,164] A reaction-based mechanism involves the formation of a ground-state complex or some interaction between the probe and sensing molecule. Charge transfer mechanisms such as the IFE process occur due to spectral overlap between the excitation spectrum of fluorophore and absorbance spectrum of acceptor without changing fluorescence lifetime, i.e., static quenching. However, FRET involves spectral overlap between the emission spectrum of the acceptor and absorbance spectrum of the donor, a 1-10 nm distance between receptor and probe, while electron transfer occurs in the PET process. The FRET and PET processes exhibit a considerable change in fluorescence over time, indicating dynamic quenching.

In order to investigate the fluorescence quenching mechanism of CasT@CDs in the presence of TCs, a TRPL study was performed initially. For the experiment, 100 µL TC solution was added to 1 mL nanosensor dispersion mixture and fluorescence lifetime measurement was carried out in the presence and absence of TC. The pristine CasT@CDs exhibited lifetime decay as 5.8 ns, and the presence of TC in the same mixture resulted in a value of 5.6 ns (Figure 3.9 and Table 3.4). The negligible change in the assay ruled out the possibility of dynamic turn-off mechanisms, i.e., FRET or PET.[114] The absorbance spectrum of CasT@CDs, TC and mixture of CasT@CDs after addition of TC resulted a merged spectrum (Figure 3.10). The finding could not clear the mechanism of quenching. Therefore, a temperature-dependent fluorescence assay was performed in the presence of different concentrations of TC with varying temperatures (25 ℃, 35 ℃, 45 ℃, and 55 ℃). The K_{SV} value obtained from I_0/I vs. concentration resulted in a lower value with an increased temperature, indicating the static quenching (Figure 3.11).[165]

Table 3.4. Fluorescence lifetime of CasT@CDs before and after addition of TC and Hg^{+2} (λex = 370 nm).

Sample	*Analyte volume (μL)*	τ_1 *(ns)*	τ_2 *(ns)*	f_1	f_2	$<\tau>^*$ *(ns)*	χ *2*
CasT@CDs	0	1.628	6.427	12.679	87.321	5.818	1.049
CasT@CDs+TC	100	1.517	6.218	13.021	86.979	5.605	1.034
CasT@CDs+Hg^{+2}	100	0.63	6.023	9.523	90.477	5.509	1.021

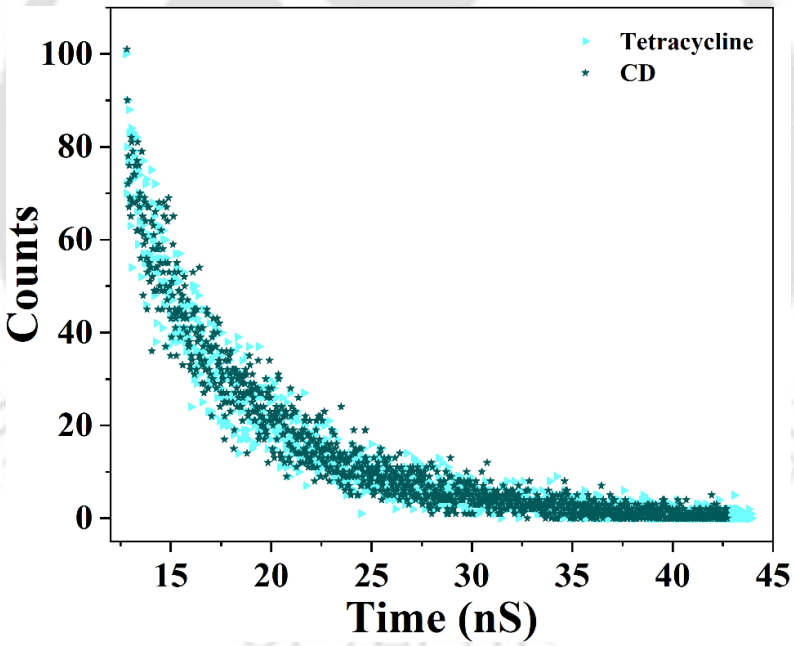

Figure 3.9. Time resolve photoluminescence decay of CasT@CDs before and addition of 100 μL 5 mM TC.

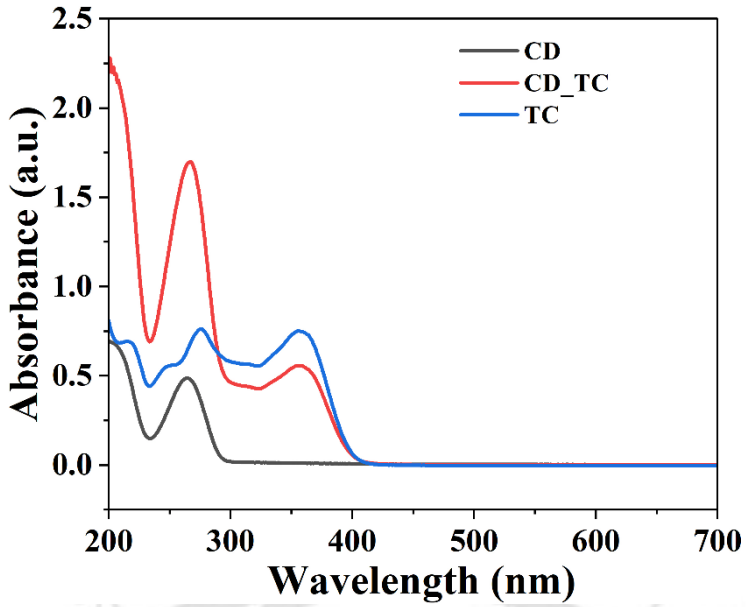

Figure 3.10. Absorbance spectrum of CasT@CDs and after addition of TC.

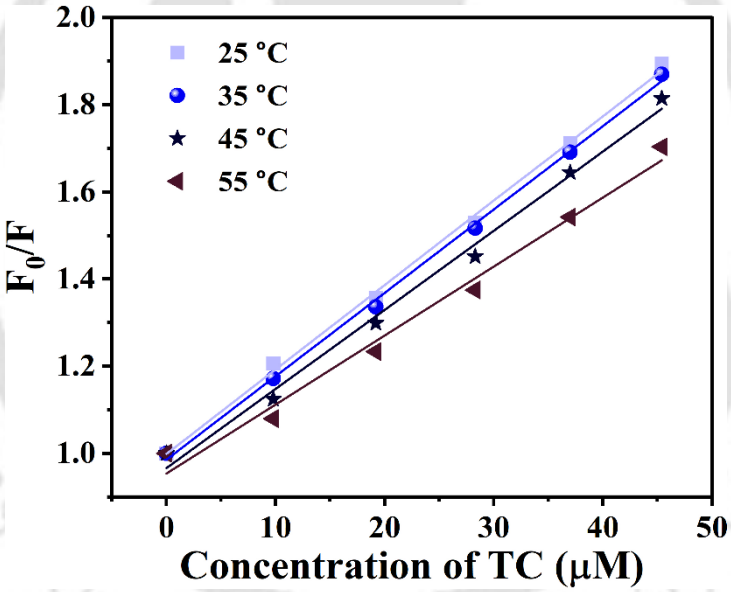

Figure 3.11. Fluorescence titration between CasT@CDs and TC at different temperature.

A pH-dependent fluorometric titration was performed between CasT@CDs and TC in order to understand the involvement of electrostatic interaction. The analysis displayed a regular enhancement in quenching efficiency (QE) (94.7% - 99.7%) with increasing pH from 2 to 9 (Figure 3.12a). The small but progressive loss in fluorescence intensity towards basic media demonstrates the electrostatic interaction between the nanosensor and TC. To summarize, we

performed one fluorometric titration in the presence of different NaCl concentrations from 0 to 1 M (Figure 3.12b). A control experiment was also performed with CasT@CDs in salt solution up to 1 M to check the effect of salt on the fluorescence intensity. The control experiment clearly defined no prominent effect (Figure 3.3b). However, the strong electrolyte hampered the quenching efficiency, which gradually decreased up to 30% with increasing NaCl concentration, indicating a possible electrostatic interaction between CasT@CDs and TC, which is possibly due to the specific π-π interaction of the carbon core and four fused aromatic rings. The result demonstrates the reason behind insignificant quenching caused by other antibiotics because those does not have fused conjugated rings. Interestingly, the high salt concentration could not effect a huge change in the turn-off event. Hence, the sensing mechanism is not only due to electrostatic interaction.

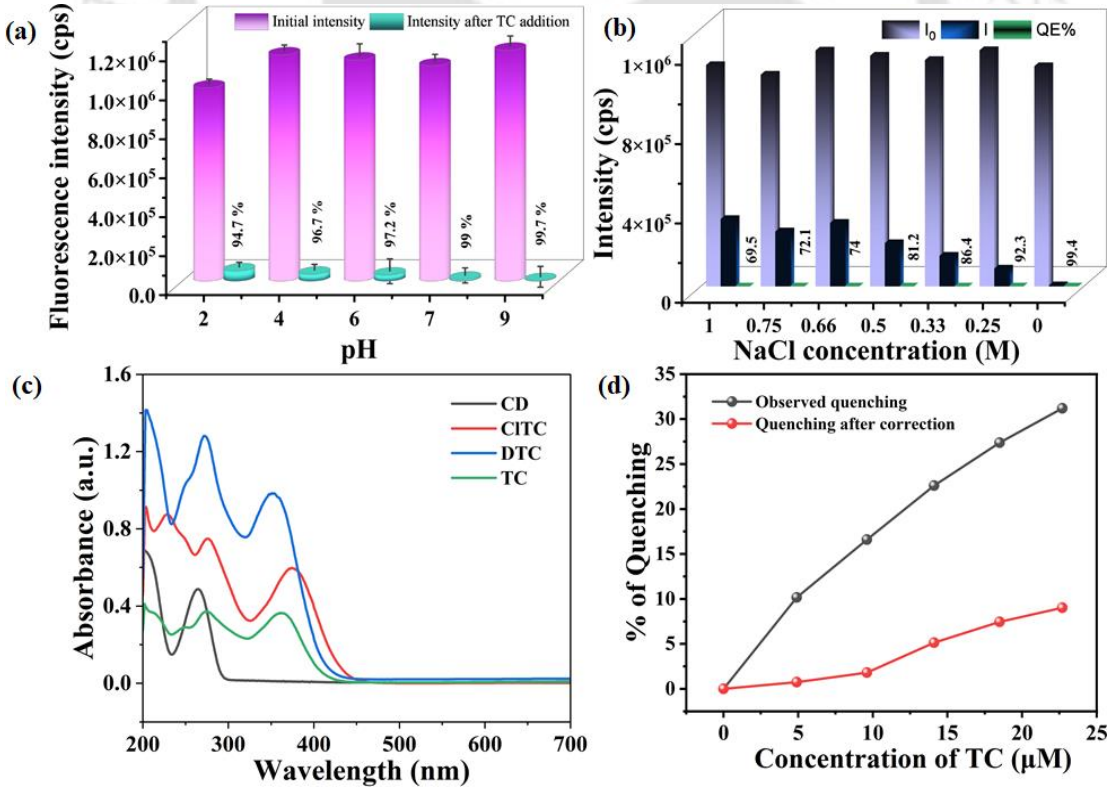

Figure 3.12. (a) pH-dependent titration between CasT@CDs and TC. (b) Effect of NaCl concentration on fluorescence quenching efficiency of CasT@CDs in the presence of TC. (c) UV-vis spectrum of TC, DTC, ClTC, and CD. (d) Observed (black curve) and corrected (red

curve) quenching efficiency of CasT@CDs after adding TC with different concentrations. Corrected quenching efficiency refers to the quenching efficiency when the IFE contribution is not considered.

To investigate further, we checked the possibility of IFE. TC antibiotics possess a broad absorption spectrum that exhibits spectral overlap with the excitation spectrum of CasT@CDs (Figure 3.12c). Therefore, correction factors were calculated to obtain actual quenching efficiency (Table 3.5), and the QE for the observed and corrected fluorescence intensities was plotted against the different concentrations of TC (Figure 12d). The resulting graph exhibited 22% fluorescence quenching due to IFE correction, indicating the partial presence of IFE. Hence, the fluorescence quenching of CasT@CDs in the presence of TC is the combination of electrostatic interaction and IFE.

Table 3.5. IFE correction table for TC.

TC (μM)	A_{ex}	A_{em}	***Correction factor (CF)***	F_{obs}	F_{corr}	$F_{corr}(0)/F_{corr}$
0	.14	.063	1.24	1095070	1357887	1
4.9	.23	.064	1.37	983703.7	1347674	1.007578
9.6	0.30	0.064	1.46	913254.8	1333352	1.018401
14.1	0.36	0.062	1.52	847500.5	1288201	1.054096
18.5	0.41	0.062	1.58	795341.7	1256640	1.08057
22.7	0.49	0.064	1.64	753388.1	1235556	1.099008

3.3.6. Hg^{+2} Detection by CasT@CDs

The use of mercury during industrial processing creates numerous lethal health hazards and severe environmental pollution. To monitor the level of mercury in water, we prepared a 2 mM

aqueous solution of Hg^{+2} ions and titrated it with CD solution. The fluorescence response was recorded and QE was found to be 82% [QE = $(1-F/F_0) \times 100$] (Figure 3.13a and 3.13c). A time-dependent study was executed from 0 to 105 seconds that exhibited the saturation of fluorescence intensity in less than a second, suggesting the rapid detection capability of CasT@CDs and the real-life application of the probe (Figure 3.13b). The very low LOD value of 5.35 nM was calculated for Hg^{+2} (Figure 3.14-3.15). The LOD is lower than the permissible range and the rapid response time making our sensor as an ideal probe for monitoring Hg^{+2} in environment (Table 3.6).

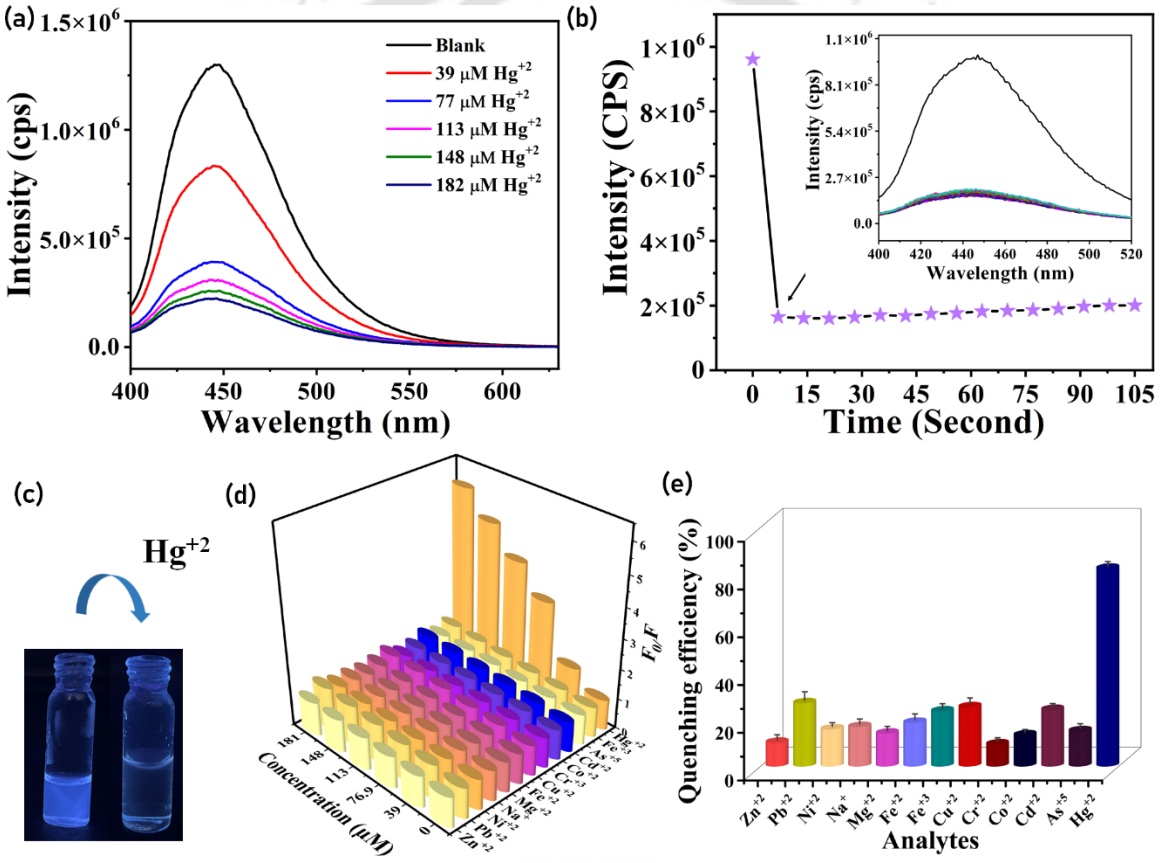

Figure 3.13. Fluorescence response at 445 nm of CasT@CDs in the presence of (a) Hg^{+2}. (b) The time-dependent response of CasT@CDs to estimate the saturation time of quenching after the addition of 100 µL Hg^{+2} (2 mM) (inset image is the fluorescence spectrum of the time-dependent experiment). (c) The digital image of CasT@CDs under the UV lamp (365 nm) before and after the addition of Hg^{+2}. (d) Stern-Volmer plot of turn-off quenching in the

emission intensity of CasT@CDs after gradual addition of analytes, and (e) the plot of quenching efficiency of CasT@CDs in the presence of cations and Hg^{+2} in the same mixture.

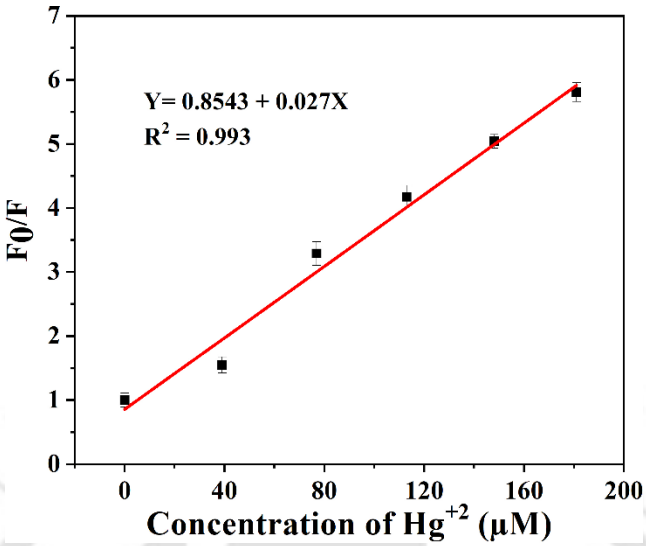

Figure 3.14. Stern-Volmer plot for fluorescence quenching of CasT@CDs in water against increasing different concentrations of Hg^{+2} ion in micromolar concentration (λex = 370 nm).

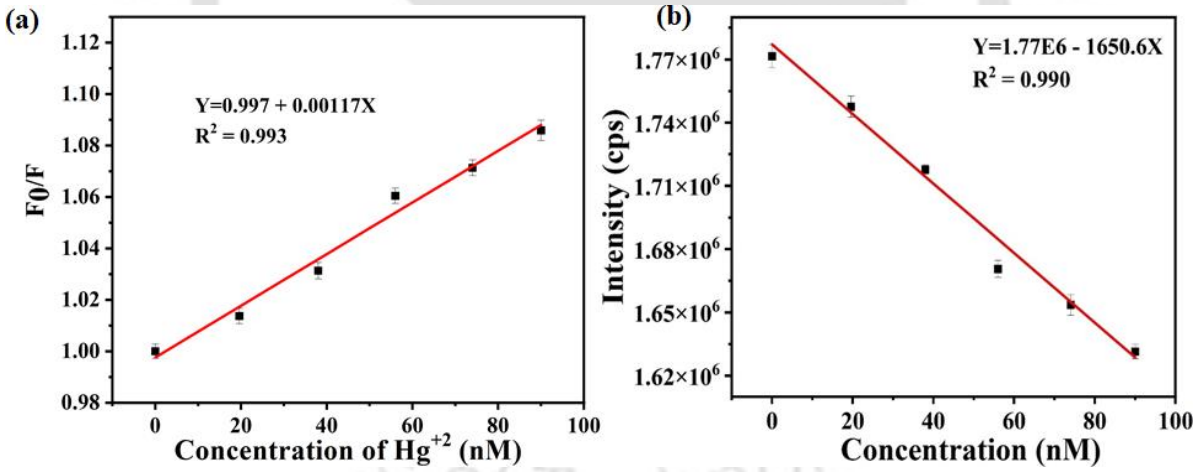

Figure 3.15. (a) Stern-Volmer plot for fluorescence quenching of CasT@CDs in water against increasing different concentrations of Hg^{+2} ion in nanomolar concentration (λex = 370 nm). (b) Change in fluorescence emission intensity of CDs in water upon sequential addition of Hg^{+2} in nano molar concentration (λex = 370 nm).

Table 3.6. Summarized table for probes used in Hg^{+2} detection and their selectivity.

Material	*Analytical Method*	*Sample*	*Response Time*	*LOD (ng/mL)*	*Ref*
M-CDs	Fluorescence	Groundwater, river water, Waste water, Tap water	1 minute	5.6 µg/L	[142]
NH2-Cd-BDC	Fluorescence	---	---	0.58 µM	[166]
CD	Fluorescence	Lake, sea, river water	---	2.47 nM	[167]
CuNCs	Fluorescence	Water	8 min	18 µg/L	[168]
NAC-QDs	Fluorescence	Spring, wastewater, groundwater	5 min	0.75 µg/L	[169]
UiO-66-NH2@Au	Colorimetric and ratiometric fluorescent	River, Tap water	30 min	9 nM	[170]
Citric acid (CA) and melamine (ME) CDs	Fluorescence	Breast milk	--	0.44 µM	[171]
Citric acid and m-phenylenediamine CDs	Fluorescence	Paper strip test	--	61 nM	[172]

Nitrogen-doped, PEGylated carbon dots (C-dots)	Fluorescence	---	---	18 pM	[173]
N-CDs from L-Arginine	Fluorescence	Cabbage, apple	5 min	0.188 µM	[174]
Hf-UiO-66-NHCSNHCH$_3$	Fluorescence	water	0.16 min	4 nM	[175]
CasT@CDs	Fluorescence	Lake water, tap water, river water	<10 sec	4.3 nM	**This work**

The affinity of CasT@CDs towards other heavy metal ions was studied through similar experiments. 2 mM of competitive analytes were prepared, and 100 µL of analyte solution was titrated with CasT@CDs to determine the QE. The result demonstrated that only Hg^{+2} ions exhibit more than 80% quenching, and the fluorescence intensity decreased gradually with increasing concentration. In contrast, other analytes do not participate in quenching even at elevated concentrations (Figure 3.13d). The effect of coexisting analytes was verified by treating the CDs suspension in the presence of a competitive analyte, followed by the addition of Hg^{+2}. Figure 13e displays that the affinity towards Hg^{+2} remains undisturbed even in the presence of analytes. None of the competitive analytes interfered in the interaction between CasT@CDs and Hg^{+2} ions. The effect of counter anions on CasT@CDs was also studied, and the results showed a negligible response (Figure 3.16). To verify the salt effect on the selectivity of CasT@CDs, fluorometric titrations were performed with three different salts of Hg^{+2} ($HgCl_2$, $Hg(OAc)_2$, and $Hg(NO_3)_2$). However, the QE was analogous for the three salts (Figure 3.17).

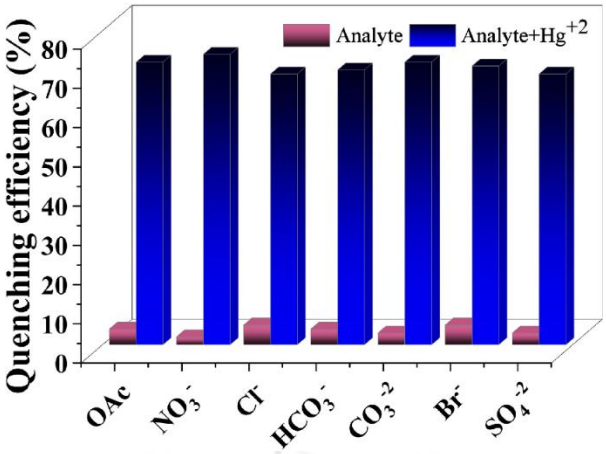

Figure 3.16. The plot of quenching efficiency of CasT@CDs in the presence of counter anion and Hg^{+2} in the same mixture.

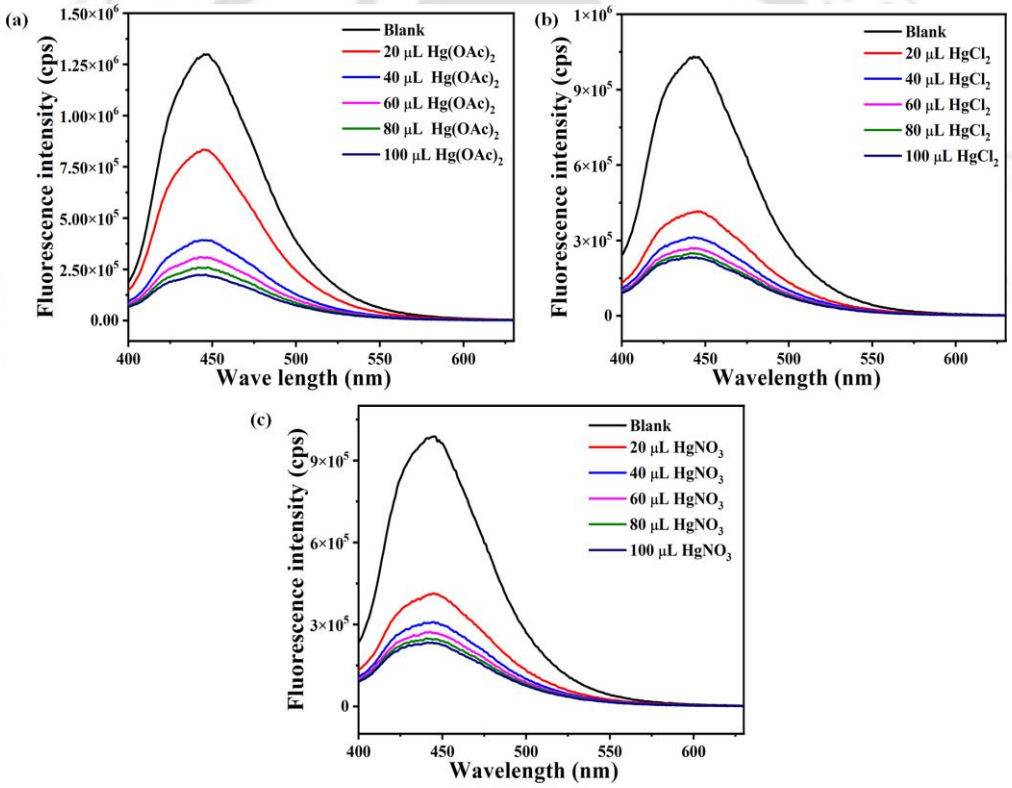

Figure 3.17. Fluorescence titration between 1mg/mL CasT@CDs and three different salts of 100 µL of 2 mM Hg^{+2} solution (a) $Hg(OAc)_2$, (b) $HgCl_2$, and (c) $HgNO_3$.

3.3.7. Mechanism for Hg^{+2} Detection

Fluorescence turn-off phenomenon of CasT@CDs in the presence of Hg^{+2} was studied through systematic experimental investigations. Lifetime decay was analyzed, where CasT@CDs

exhibited a lifetime value of 5.5 ns. The lifetime change is negligible compared to bare CasT@CDs (5.8 ns) (Figure 3.18 and Table 3.4). Temperature-dependent fluorescence titration was performed with our chemosensor and Hg^{+2}, exhibiting a noticeable gradual decay in the K_{SV} value with increasing temperature (Figure 3.19). The abovementioned data further complemented the static quenching mechanism.[176] Hg^{+2} is a soft cation that can interact with soft elements such as N and S. Subsequently, Hg^{+2} demonstrates a strong cation-π interaction with conjugated systems. Synthesized CasT@CDs possess numerous nitrogen atoms in the carbon dot backbone and surface area with sp^2 carbon core. Therefore, an XPS analysis was performed to check the interaction, which exhibited only C, N, and O presence in the bare CDs. In contrast, a sharp peak of Hg^{+2} was found along with C, N, and O in the mercury-treated CDs (Figure 3.20a-b). The high-resolution elements data exhibited a shift in C1s and N1s but no change for O1s. A significant change in the C=C bond demonstrates the cationic-π interaction (Figure 3.21a-b). Moreover, the integrated area for pyrrolic nitrogen has decreased, and pyridinic nitrogen has increased, supporting the interaction between nitrogen and Hg^{+2} because the presence of pyrrolic N-H induces strong cation-π interactions (Figure 3.22c-d).[177,178] However, the peak area of O has neither been shifted nor diminished (Figure 3.21e-f). pH-dependent fluorescence study has a promising role in understanding the existence of electrostatic interaction between the analyte and sensor.

Therefore, a pH-based fluorescence experiment was performed that exhibited minimal quenching from 2 to 7, but a dramatic change in quenching efficiency at pH 9 was observed (Figure 3.22a-c). An additional pH-dependent zeta potential measurement of CasT@CDs was performed to examine the change of surface charge. The surface charge of carbon dots was found to be more negative in an alkaline medium (Figure 3.23). Carboxyl and hydroxyl groups may be the reason for the negative surface charge of CasT@CDs. The data clearly described the electrostatic interaction between positively charged Hg^{+2} ions and negatively charged

CasT@CDs. Thus, from XPS and pH-dependent analysis, it can be inferred that the quenching process presumably occurs due to a combination of electrostatic interaction, to be more precise, cation-π interaction between the sp^2 carbon of CasT@CDs and soft-soft interaction between N and Hg^{+2}.

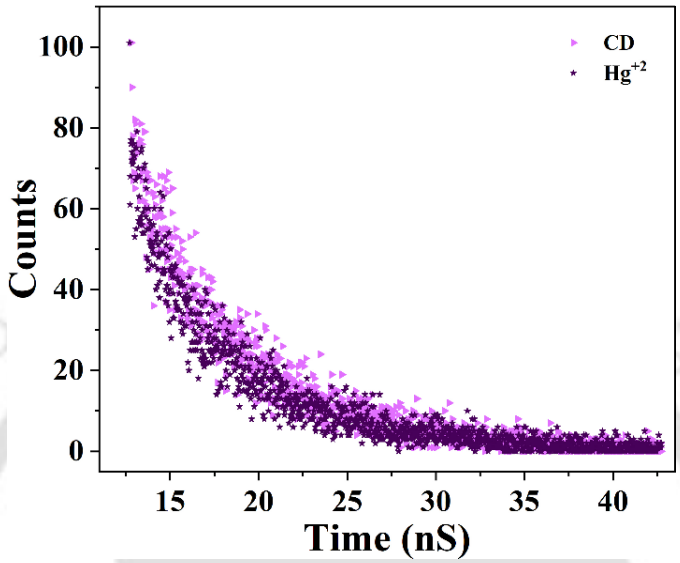

Figure 3.18. Time-resolved photoluminescence decay of CasT@CDs before and after the addition of 100 µL 2 mM Hg^{+2}.

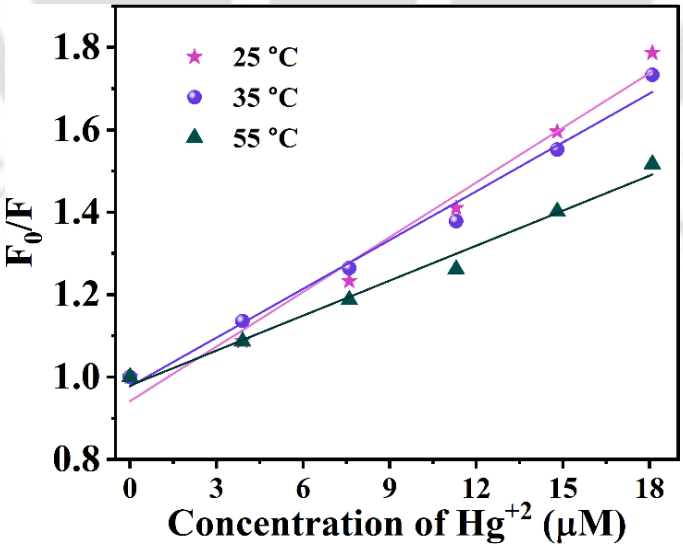

Figure 3.19. Temperature-dependent fluorescence response of CasT@CDs dispersed in water after addition of concentrations of Hg^{+2} solution.

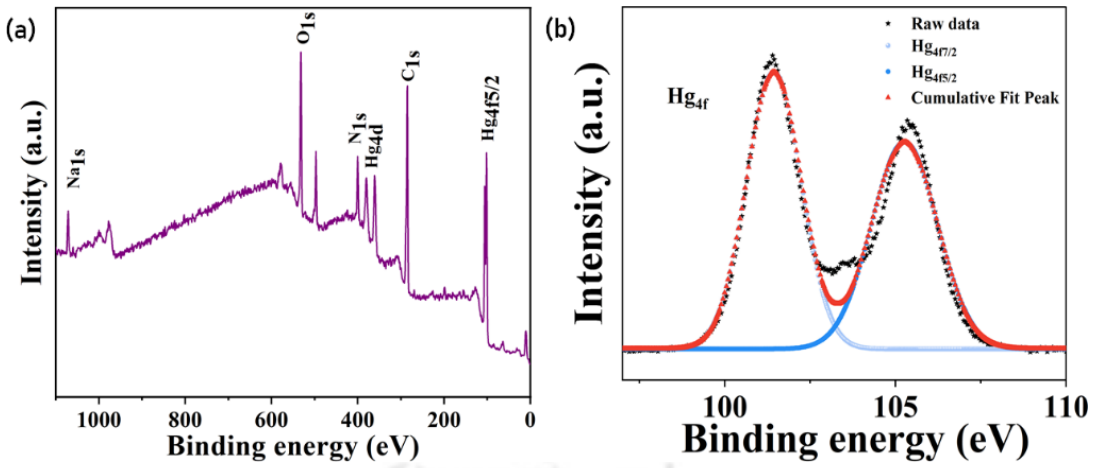

Figure 3.20. (a) XPS spectrum of CasT@CDs + Hg^{+2}. (b) XPS deconvoluted spectrum of Hg_{4f} from CasT@CDs after treatment with Hg^{+2}.

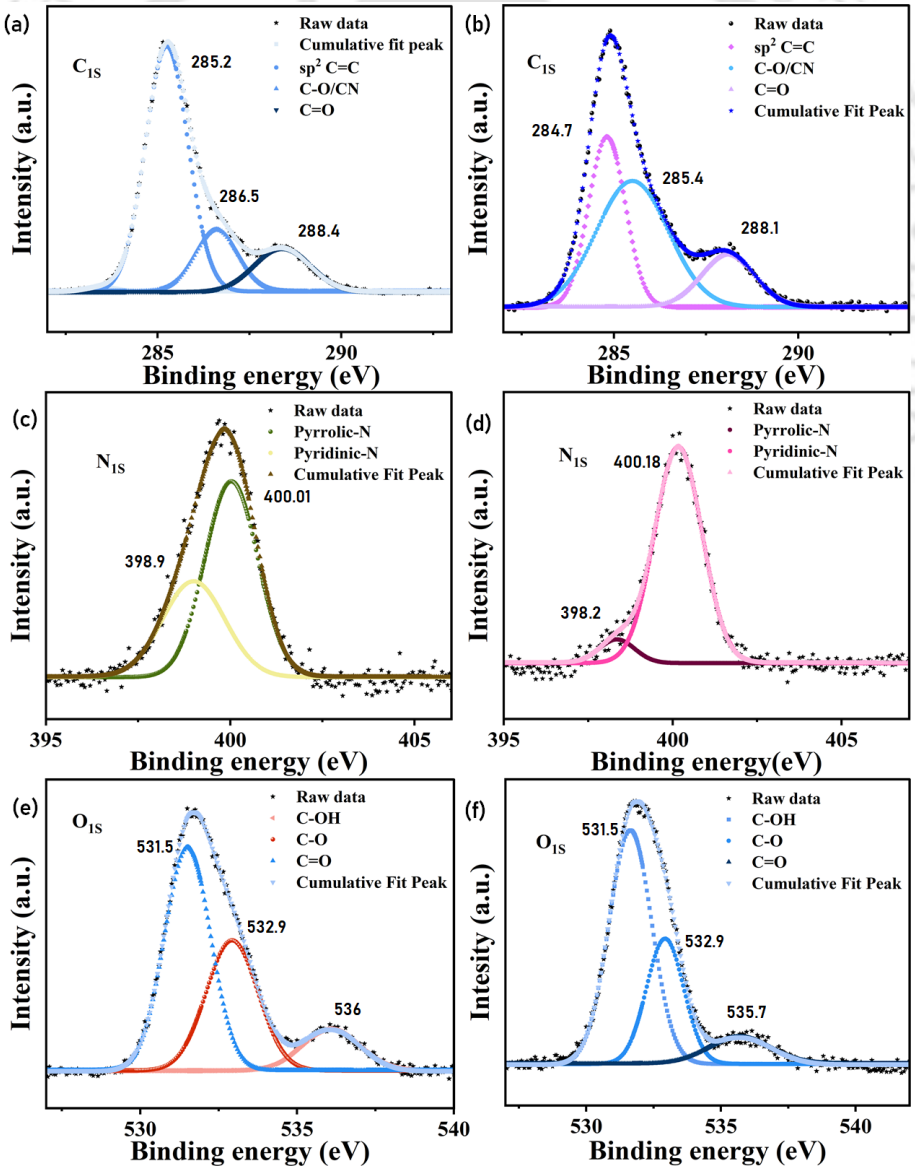

Figure 3.21. XPS deconvoluted spectrum of (a-b) C1s, (c-d) N1s, and (e-f) O1s of CasT@CDs and Hg^{+2}-treated CasT@CDs exhibiting interaction between fluorophore and analyte.

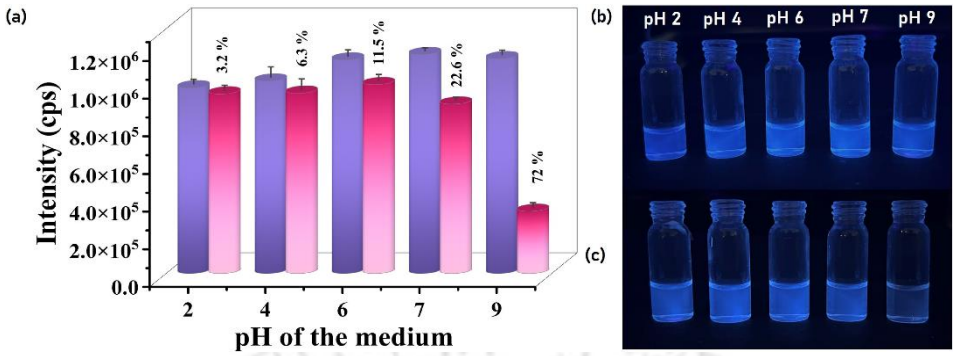

Figure 3.22. (a) Fluorescence emission of CasT@CDs at 445 nm in the presence of Hg^{+2} in several pH media exhibiting a distinct change in quenching efficiency. (b) The digital image of the same experiment under a UV lamp.

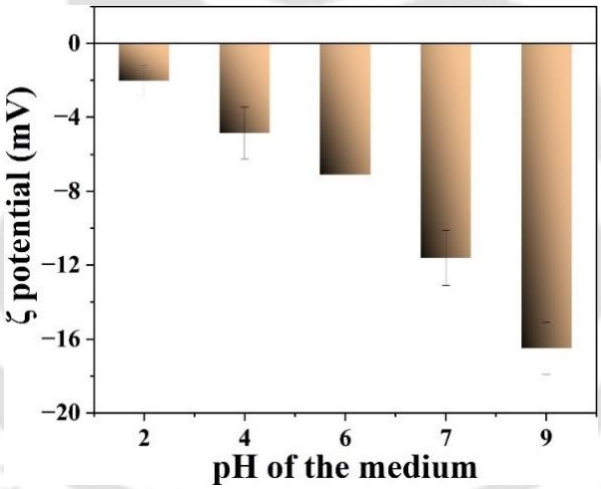

Figure 3.23. Zeta potential of CasT@CDs dispersed in PBS buffer solution of different pH.

3.3.8. Detection of TC and Hg^{+2} in Real Samples (Milk, Urine, Human Blood Serum, Lake Water, River Water, and Tap Water)

The successful fulfilment of the designed fluorescent CasT@CDs lies in their ability to perform selective, facile, and rapid detection of analytes in real-world samples. This demonstrates the practical applicability of the nanosensor, ensuring that it can effectively monitor contaminants such as heavy metals and antibiotics in complex environments like water, serum, and food

products. Therefore, the emission intensity of CasT@CDs was evaluated in real samples. A series of fluorescence studies was performed in different media with spiked concentrations of TC and Hg^{+2}. CasT@CDs were suspended in the aforementioned media. For TC, milk, urine, and blood serum were used as dispersion media. After adding the spiked TC solution, the emission intensity was assessed in a spectrofluorometer. The intensity gradually decreased with increasing TC concentration. The recovery percentage was obtained at around 99-100% (Table 3.7).

Table 3.7. Detection of TC in milk, urine, and serum.

Sample name	*TC spiked (µM)*	*TC found in fluorescence (µM)*	*RSD (n=3) (Relative standard deviation)*	*Recovery (%)*
Milk	9.8	9.7	0.5	99.4
	19.2	19.3	1.8	100.5
	28.3	27.9	2.5	98.5
Serum	9.8	9.9	1.2	101.0
	19.2	19.3	0.9	100.5
	28.3	28.4	3.1	100.3
Urine	9.8	9.8	0.8	100.2
	19.2	19.3	2.1	100.5
	28.3	28.1	2.7	99.2

The verification of CasT@CDs for selective detection of Hg^{+2} in different aqueous media, such as lake water, river water, tap water, and cigarette samples, was done using similar fluorometric studies. Initially, the presence of mercury ions was checked in the medium through fluorescence titration between CasT@CDs and the aqueous media. The data displayed no trace of Hg^{+2} ions in the medium. To ensure the ability of CasT@CDs quantitatively, the known concentration of Hg^{+2} ion was spiked and checked using fluorescence, which exhibited around 99% recovery of the sample from the medium (Table 3.8). The cigarette sample contains mercury;[149] therefore, samples were prepared, and a fluorescence assay was performed, which exhibited prominent fluorescence quenching (Figure 3.24). The assay proves the selectivity towards Hg^{+2} in real samples.

Table 3.8. Detection of Hg^{+2} in river water, tap water, and lake water.

Source	*Hg^{+2} spiked (nM)*	*Hg^{+2} found (nM)*	*RSD (n=3) (Relative standard deviation)*	*Recovery (%)*
River water	29	28.5	0.8	98.0
	57	58.0	1.2	101.0
	85	87.0	1.9	102.0
Tap water	29	30.0	1.6	103.0
	57	58.0	1.8	101.0
	85	86.0	0.9	101.0
Lake water	29	30.0	0.9	103.0
	57	56.9	1.4	99.8
	85	84.9	2.1	99.8

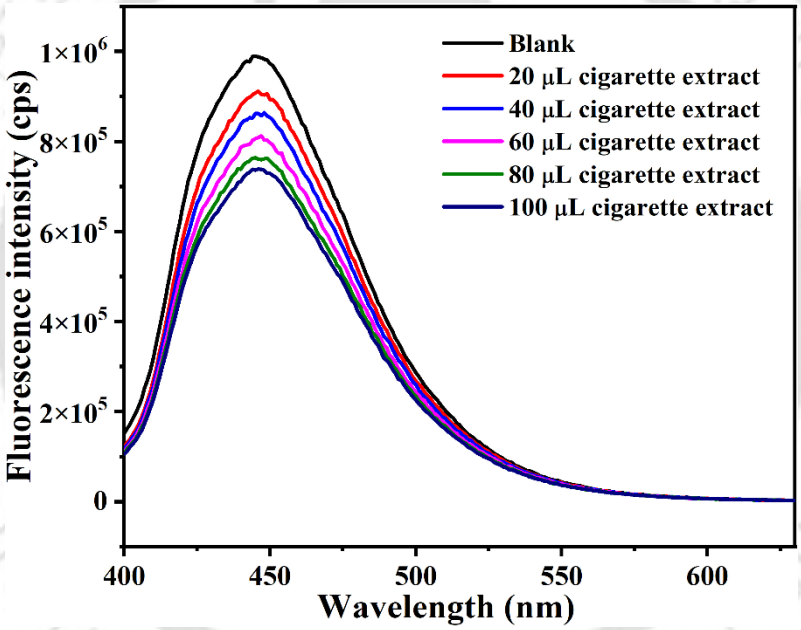

Figure 3.24. Change in fluorescence emission intensity of CasT@CDs in water upon sequentially adding cigarette extract (λex = 370 nm).

3.3.9. CasT@CDs Coated Paper Strips for Portable and Rapid Detection of TC and Hg^{+2}

Paper strips offer unique advantages for fluorometric detection, such as portability, affordability, and user-friendliness, making them highly suitable for point-of-care diagnostics and on-site analyses. Moreover, visual detection can be achieved without a complex instrumental setup.[179,180] Therefore, we prepared portable paper strips for detection. Initially,

CasT@CDs-coated paper strips were prepared using a dip coating method. The filter papers were dipped in the CD solution and dispersed in water. Then, the paper strips were dried in the oven, and the same process was repeated to get a homogeneous coating of CasT@CDs. TC and Hg^{+2} were added to the paper strips, and after drying, the change was observed under a UV lamp (365 nm). The experiment suggested nanomolar detection of Hg^{+2} and TC (Figure 3.25a-b).

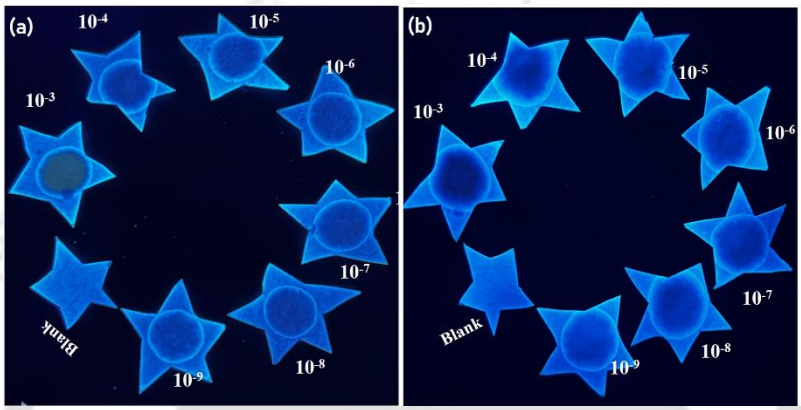

Figure 3.25. Real-life application of CasT@CDs using CDs coated paper strips for the detection of (a) TC and (b) Hg^{+2} from water.

3.4. Conclusion

This article summarizes the green synthesis of fluorescent carbon dots from milk protein casein and thymine using the one-step pyrolysis method to detect the tetracycline antibiotics and toxic Hg^{+2} ions in aqueous medium. The synthesis yielded an average size of 4.2 nm blue fluorescent carbon dots. A systematic investigation of the stability of carbon dots (in NaCl solution, different pH, storage time) has exhibited excellent results. Several characterization studies, such as FETEM, XPS, XRD, EDS, and FT-IR, were employed to understand the shape, morphology, and structural composition of the prepared CDs. The CasT@CDs possess a unique affinity towards tetracycline (TC, ClTC, and DTC) and Hg^{+2} in the presence of numerous co-existing analytes. A comprehensive study of the mechanism confirmed that the ultra-fast (less than 10 s) turn-off quenching phenomenon in antibiotic exposure was due to

static quenching and partial IFE. However, for Hg^{+2}, static was solely responsible. The affinity of CasT@CDs towards analytes has been proved in different aqueous media, food samples, and biofluids. Moreover, prepared CasT@CDs coated paper strips exhibited nanomolar and rapid on-site detection of TC and Hg^{+2}. The practical applicability of the sensor was demonstrated through real sample analysis, including the detection of mercury ions in lake water, river water, and tap water, and tetracycline in serum, urine, and milk samples. Moreover, considering the low LOD of TC and TC derivatives, our sensor can be applied in monitoring the TC level in different aqueous media. These results highlight its potential role in promoting environmental and public health safety. This innovative approach provides a promising solution for the early detection of hazardous pollutants, contributing to the preservation of both public health and ecological balance.

Chapter 4. Formulation of Biogenic Carbon Dot-Capped Silver Nanoparticles for Potential Antibacterial Activity

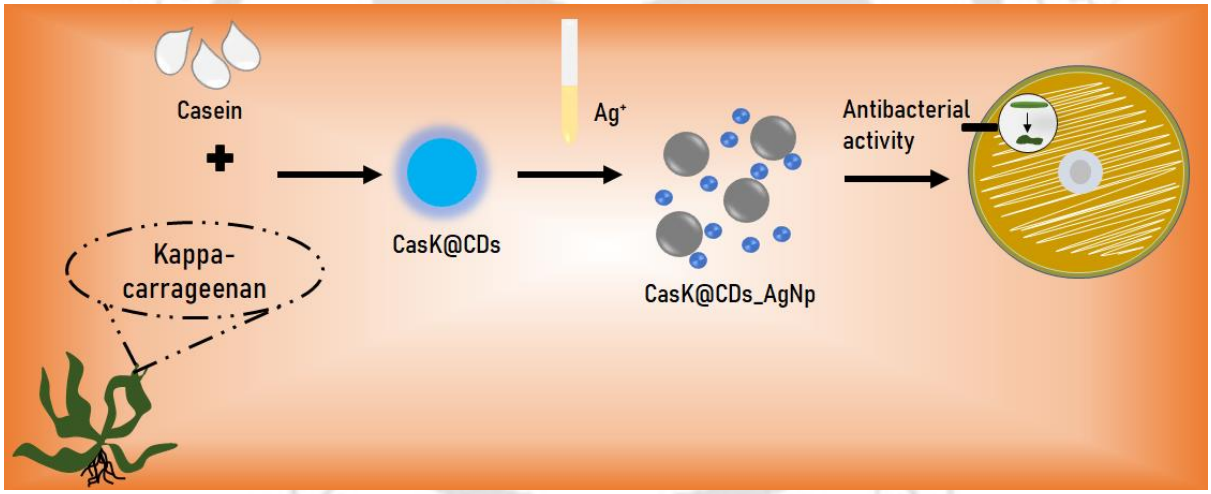

4.1. Overview

The growth in the discovery of antibiotics emerged rapidly after the discovery of penicillin in 1928. Numerous antimicrobial agents were isolated from natural sources and synthesized chemically, significantly reducing the morbidity and mortality associated with bacterial infections. Indiscriminate antibiotic use has resulted in the development of antimicrobial agents that contributed to the rapid emergence and spread of antibiotic-resistant bacterial strains. Consequently, bacterial infections remain a significant global health threat. To address this challenge, the development of novel antimicrobial strategies is of critical importance. In this context, engineered nanoparticles (Nps) have emerged as promising candidates for combating bacterial infections, particularly those caused by multidrug-resistant (MDR) pathogens.

Due to the broad-spectrum antimicrobial activity and strong efficacy against a wide range of bacteria, viruses, and fungi, silver nanoparticles (AgNps) have garnered widespread attention compared to other metal nanoparticles. The antimicrobial properties of AgNps depend on several physicochemical characteristics, such as particle size, shape, stability, and surface chemistry, which play critical roles in determining their antibacterial performance.[181–184] Silver selectively interacts with phosphorus and sulfur-containing biomolecules, major components of cell membranes, DNA bases, and proteins. Initially, AgNps interact with the cell membrane, causing membrane rupture and morphological changes that ultimately lead to cell death.

Despite their numerous advantages, AgNps can exhibit toxicity in healthy cells. The choice of precursor material plays a crucial role in minimizing this toxicity. Currently, biogenic precursors are of great interest to researchers. In this context, plant extracts and plant-based products are widely used. However, preparing plant-based extracts often involves additional complex steps. Alternatively, plant-derived materials such as polysaccharides and proteins are promising due to their easy availability, biodegradability, and cost-effectiveness. Therefore, in this study, we have selected a seaweed-derived polysaccharide, kappa-carrageenan (KC), and

a milk protein, casein (Cas), to derive carbon dots (CasK@CDs) for the synthesis of AgNps. Carbon dots offer several advantages, including enhanced solubility, improved stability, and reduced toxicity of AgNps.

Herein, we have designed KC and Cas-derived carbon dot-capped silver nanoparticles (CasK@CDs_AgNp). CasK@CDs were prepared via one-step pyrolysis, and AgNps were prepared using microwave synthesis. The system is expected to exhibit toxicity against bacteria.

4.2. Experimental Section

4.2.1. Materials

Kappa-carrageenan (KC) and silver nitrate ($AgNO_3$) were purchased from Sigma-Aldrich (St. Louis, MO, United States). Tryptone, sodium chloride (NaCl), and yeast extract were purchased from Himedia. Casein protein (Cas) was procured from Tokyo Chemical Industry (Tokyo, Japan).

4.2.2. Bacterial Culture

The bacteria were cultured in Luria-Bertani (LB) broth. LB broth was prepared by dissolving 1% tryptone, 0.5% NaCl, and 0.5% yeast extract in sterilized water. 100 µL of bacterial suspension was added to 3 mL of sterilized LB tube and cultured overnight at 180 rpm. The turbidity in the culture solution confirmed the bacterial growth. Bacterial suspension was then serially diluted and spread on an agar plate. The plates were incubated at 37 °C for 16 hours, and bacterial colonies were counted. To get a colony-forming unit (cfu) of $10^{6,}$ the number of colonies should be between 300 and 30.

4.2.3. Synthesis of CasK@CDs and CasK@CDs_AgNp

CasK@CDs were prepared by the pyrolysis method. Casein and KC were mixed in three different ratios (1.66:1, 1:1, 1:1.6) and poured into a round-bottom flask with N_2 purge. The

container was kept in a sand bath, and the reaction continued for 2 hours at 200 ℃. The black product was ground using a mortar and pestle and dispersed in double-deionized water. The yellow filtrate was collected and stored for the rest of the experiments. CasK@CDs derived silver nanoparticles were synthesized using a 10 mM $AgNO_3$ stock solution. $AgNO_3$ and CasK@CDs (1.6:1) were mixed in different ratios (300 µM:1 mg/mL, 150 µM:1 mg/mL, 300 µM: 500 µg/mL, and 150 µM: 500 µg/mL) and named as CasK@CDs_AgNPs1, CasK@CDs_AgNPs2, CasK@CDs_AgNPs3, and CasK@CDs_AgNPs4, respectively. The mixture was placed in a microwave reactor at 130 ℃ and 120 watts for 30 minutes. After cooling, a brown solution was observed, indicating the formation of silver nanoparticles.

4.2.4. Agar Well Diffusion Assay

Initially, the antibacterial properties of CasK@CDs_AgNPs (1, 2, 3, and 4) were analyzed keeping CasK@CDs as a control. 50 µL of bacterial suspension of Escherichia coli (E. coli (EC), Gram-negative) and Staphylococcus aureus (S. aureus (SA), Gram-positive) were evenly spread on a LB agar plate. Uniform holes were created in the agar plate. 50 µL of CasK@CDs_AgNPs were poured in the wells and incubated in static conditions at 37 ℃ for 16-20 hours.

4.2.5. Minimum Inhibitory Concentration (MIC) Determination

For the colony-forming unit (CFU) calculation, a stock sample of bacterial suspension was inoculated and diluted serially in Luria-Bertani (LB) media at a 1:10 ratio. 100 µL of the suspension from the tubes was inoculated and spread on an agar plate and incubated at 37 ℃ for 16-20 hours in static conditions. The plate resulting in bacterial colonies between 300 and 30 was considered as 10^6 CFU/mL.

EC and SA were added to 96 96-well plates for a final CFU of 10^6/mL. 100 µL of CasK@CDs_AgNPs were added to the well at variable concentrations (0, 1, 2, 4, 6, 8, 16, and

32 µg/mL) and incubated. The final volume of the well was maintained at 200 µL, and for the blank well, 200 µL of media was added. The MIC of the nanoparticles against EC and SA was determined to be the lowest concentration of CasK@CDs_AgNPs, which prevents the appearance of turbidity and indicates no bacterial growth in the suspension.

Antibiofilm activity of CasK@CDs_AgNP1 against S. aureus and E. coli was examined using FESEM analysis. The bacterial suspension was cultured for 24 hours in LB under static conditions on a cover slip (37 °C). 32 µg/mL of CasK@CDs_AgNp1 was added to the bacterial suspension and further incubated for 24 hours. Samples were fixed using 2.5% glutaraldehyde and washed with ethanol three times. The cover slip was coated with gold before analysis.

4.2.6. Propidium Iodide Labeling

Freshly cultured E. coli and S. aureus of 10^6 CFU/mL were incubated with 8 µg/mL and 16 µg/mL of CasK@CDs_AgNp1 for 2 hours. After incubation, the samples were centrifuged at 5000 rpm for 10 minutes, and the supernatant was removed. Then the bacteria were dispersed in PBS and incubated with a 1:1 acridine orange and propidium iodide mixture for 30 minutes in the dark and centrifuged. The pallet was dispersed in PBS, and microscopic images were captured using a confocal laser scanning microscope (ZEISS LSM-880).

4.3. Results and Discussions

4.3.1. Synthesis and Characterization of CasK@CDs

Initially, the optical properties of biopolymer-derived carbon dots were examined. The carbon dots were synthesized in three different polymer ratios. The UV-visible spectra of CasK@CDs (1:1 and 1:1.6 ratios) exhibited two typical peaks below 300 nm and 350-400 nm, indicating π-π* and n-π* transitions, respectively (Figure 4.1a). CasK@CDs (1.6:1 w/w) exhibited three distinct peaks at 268 nm, 316 nm, and 386 nm, which absorb in the UVC, UVB, and UVA regions (Figure 4.1a inset diagram).[185] Typical π-π* transition occurs due to the electron

transfer in the conjugated core of carbon dots, and n-π* transitions occur due to the transition of non-bonding electrons in hetero atoms to the anti-bonding orbitals. CasK@CDs 1.6:1 has higher nitrogen content, enabling prominent absorption in the UVC, UVB, and UVA regions and highest fluorescence emission. Therefore, all further experiments were conducted using this optimized CasK@CDs 1.6:1. The fluorescence spectrum of CasK@CDs exhibited excitation-dependent emission with red shift and λ_{max}= 330 nm (Figure 4.1b). The stability of carbon dots was evaluated across a range of pH. Under basic conditions, an enhancement in fluorescence intensity was observed at higher pH (Figure 4.1c). However, the UV absorbance spectra exhibited a loss in the absorbance area at 268 nm and 316 nm in basic medium (Figure 4.1d). Such a phenomenon may be attributed to the pH-induced conformation change of the core and surface functional groups of carbon dots. Specifically, the observed changes could result from the quenching effect of H^+ ions in acidic conditions, electrostatic repulsion between negative charges in the structure under basic conditions, and increased conjugation due to delocalization of lone pair electrons of functional groups.[186–189] The fluorescence and absorption spectrum of CasK@CDs remains stable in the pH range of 3.5-8.5, which is essential for biomedical usage of CDs. Synthesized CasK@CDs exhibited good particle distribution with an average particle diameter of 2.8 nm and lattice spacing of 0.24 nm (Figure 4.1e). FTIR spectrum of CasK@CDs revealed presence of O-H (3411 cm^{-1}), N-H (3227 cm^{-1}), C-H (2962 cm^{-1}), C=O (1652 cm^{-1}), bending of N-H/asymmetric COO^- stretching (1451 cm^{-1}), C-N (1299 cm^{-1}), C-O-C (1116 cm^{-1}) groups (Figure 4.1f).[154,190]

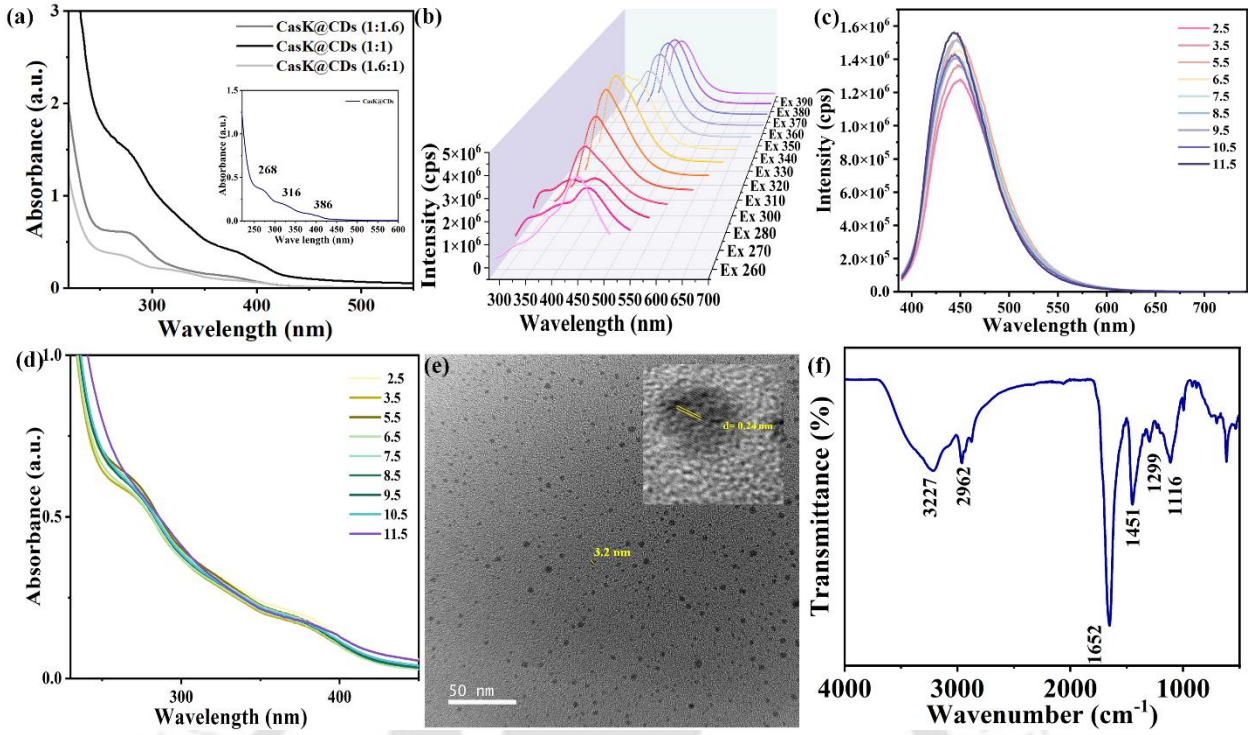

Figure 4.1. Characterization of CasK@CDs. (a) Absorbance spectrum of CasK@CDs (1.6:1) (inset spectrum is for CasK@CDs synthesized in different ratios). (b) Excitation-dependent fluorescence spectrum of CasK@CDs (1.6:1). (c) Change in fluorescence spectrum of CasK@CDs at different buffer media. (d) Change in absorbance spectrum of CasK@CDs at different buffer media. (e) FETEM image of CasK@CDs (1.6:1) (inset HRTEM image). (f) FT-IR spectrum of CasK@CDs.

4.3.2. Synthesis and Characterization of CasK@CDs_AgNp

Despite many novel green routes for synthesizing silver nanoparticles, the present method has a prominent feature due to using carbon dots as reducing and stabilizing agents, which enhance stability, surface functionalization, and biocompatibility. Initially, the UV-visible study confirmed the formation of silver nanoparticles, which exhibited a broad surface plasmon peak at around 440 nm (Figure 4.2a-d).

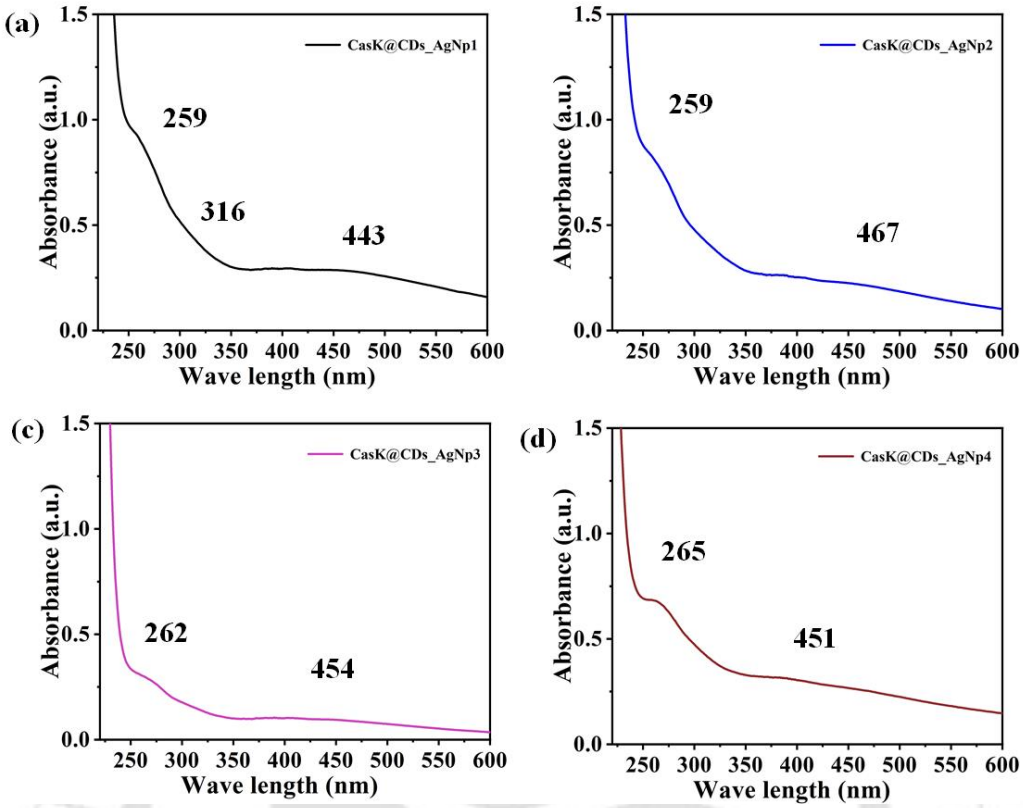

Figure 4.2. (a-d) UV-visible spectra of CasK@CDs_AgNp.

Further, FETEM analysis demonstrated the spherical shape of silver nanoparticles with good dispersion. The lowest particle size ($d_{avarage}$ = 8 nm) was obtained when the concentration of carbon dots was highest among experimental ratios, i.e., CasK@CDs_AgNp1 (Figure 4.3a). The other three sets exhibited average particle sizes of 10-15 nm (Figure 4.3b-d). Selected Area Electron Diffraction (SAED) analysis confirmed the polycrystalline nature of the synthesized nanoparticles, as evidenced by multiple concentric diffraction rings. The high-resolution TEM (HRTEM) image revealed the D-spacing of lattice fringes of 2.3 Å, indicating the 111 plane (Figure 4.4).

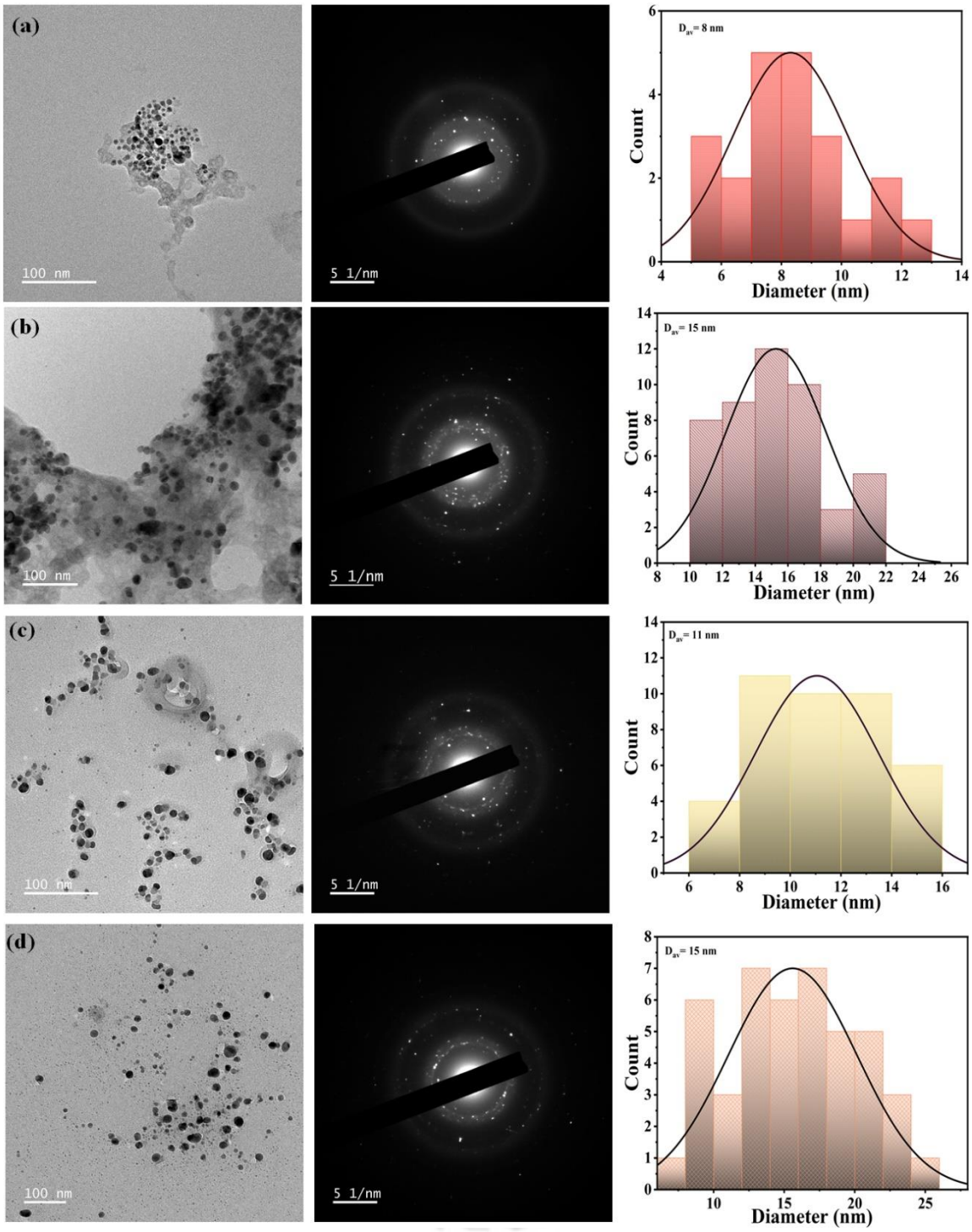

Figure 4.3. (a-d) FETEM image (inset size distribution plot) and SAED pattern of CasK@CDs_AgNp1, CasK@CDs_AgNp2, CasK@CDs_AgNp3, and CasK@CDs_AgNp4, respectively.

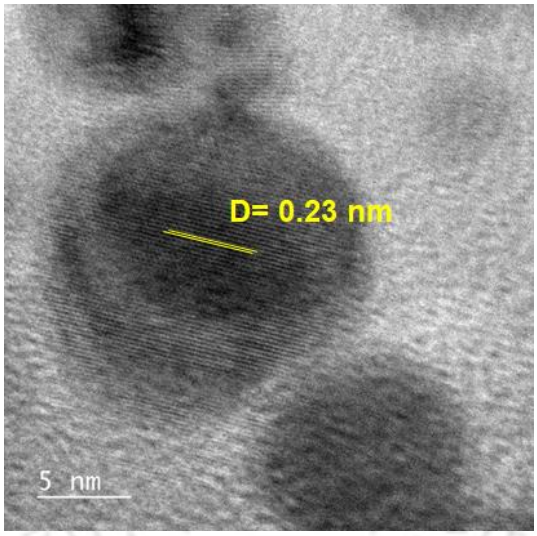

Figure 4.4. HRTEM image of CasK@CDs_AgNp1.

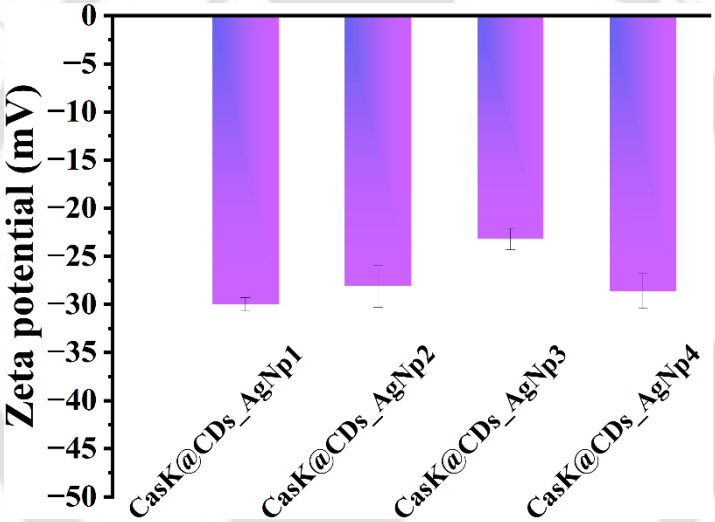

Figure 4.5. Zeta potential of CasK@CDs, CasK@CDs_AgNp1, CasK@CDs_AgNp2, CasK@CDs_AgNp3 and CasK@CDs_AgNp4.

The zeta potential analysis proved a surface charge around -28 mV, leading to a stable colloidal dispersion (Figure 4.5).[191] CasK@CDs possess functional groups such as -OH, -NH_2, and -COOH. Herein, the amine group reduces Ag^+ to Ag^0, while -COOH groups subsequently stabilize the nanoparticles by binding to their surface, thereby preventing aggregation.[192,193] Moreover, abundant -OH groups on the surface of the CDs significantly improve the solubility of the nanoparticles in aqueous medium, enhancing their biomedical applications.

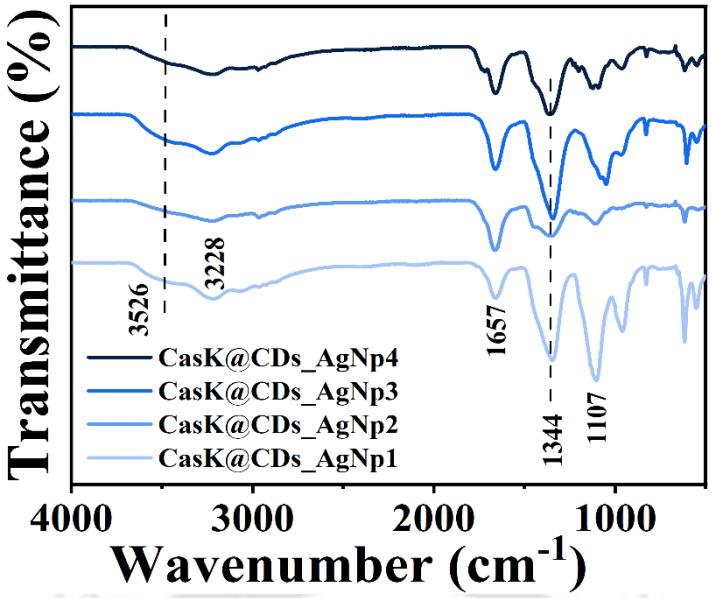

Figure 4.6. FT-IR spectrum of CasK@CDs_AgNp.

FTIR analysis of CasK@CDs_AgNp exhibited a similar pattern for all four sets of synthesized nanoparticles. The pattern exhibited a similar spectrum to bare CasK@CDs with little shift in peak positions (Figure 4.6). The blue shift in O-H stretch at 3411 cm^{-1} to 3526 cm^{-1} indicates disruption in hydrogen bonding due to the formation of silver nanoparticles. Additionally, a shift and overall reduction in intensity of C=O transmission at 1657 cm^{-1} indicates a possible coordination between C=O and the Ag^0 surface. Furthermore, the peak at 1451 cm^{-1} in CasK@CDs underwent a significant blue shift to 1344 cm^{-1}, which may be attributed to changes in the N–H vibrational environment, due to interaction with Ag^0 or altered hydrogen bonding.

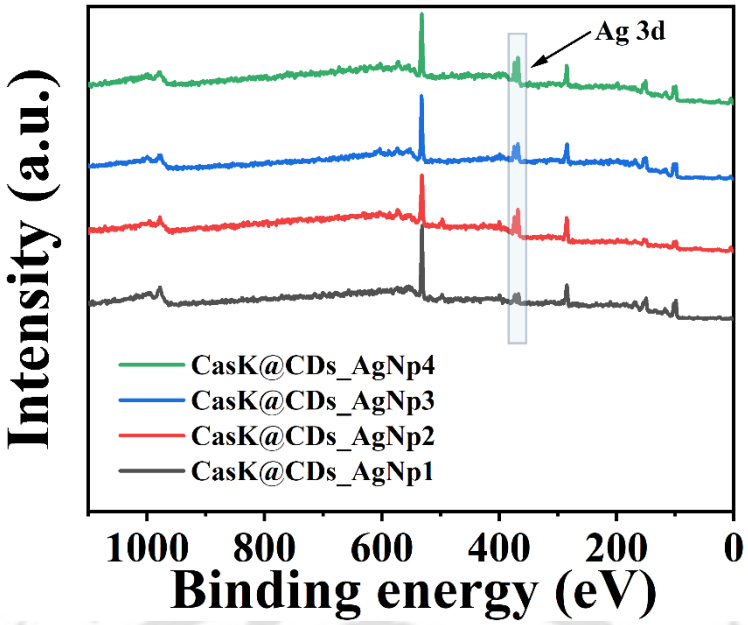

Figure 4.7. XPS pattern of CasK@CDs_AgNp1, CasK@CDs_AgNp2, CasK@CDs_AgNp 3, and CasK@CDs_AgNp4.

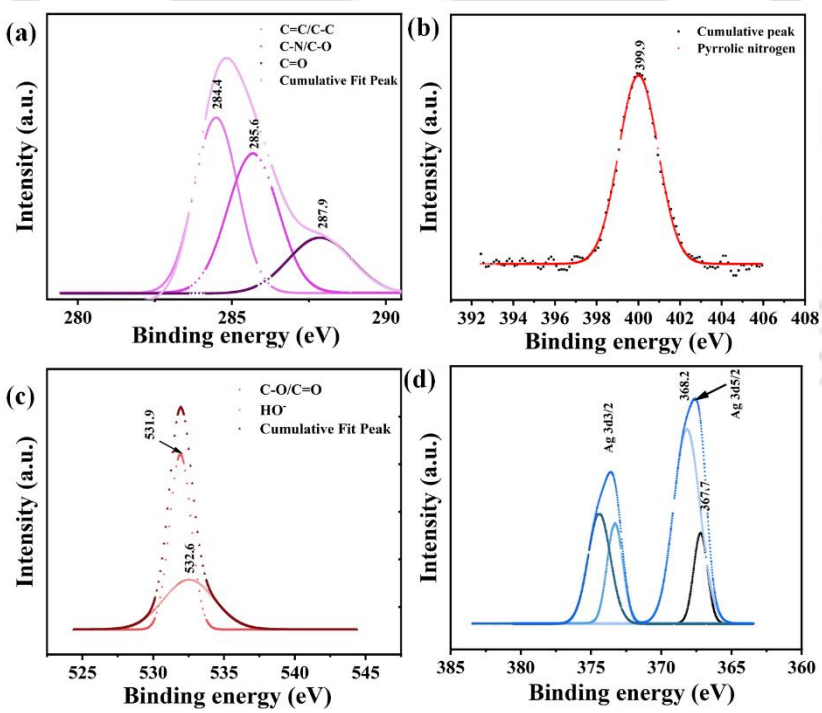

Figure 4.8. Deconvoluted XPS high resolution spectrum of (a) C_{1s}, (b) N_{1s}, (c) O_{1s}, and (d) Ag_{3d}.

We extended our compositional analysis by using XPS to evaluate the oxidation states of silver (Figure 4.7). Four sets of CasK@CDs_AgNp exhibited peaks for Ag $3d_{5/2}$ and Ag $3d_{3/2}$. For a better understanding, the high-resolution spectrum was analyzed. The fitted curve exhibited the simultaneous existence of two oxidation states of silver, at binding energy values (BE) 368.2 eV (Ag^0) and 367.7 eV (Ag^+).[194] Abundance of Ag^0 in the Ag $3d_{5/2,}$ indicating the main contribution to the peak and confirming the synthesis of silver nanoparticles (Figure 8d). The high-resolution fitted spectrum of C_{1s} exhibited three types of bonding, i.e., C=C/C-C, C-N/C-O, and C=O at 284.4, 285.6, and 287.9, respectively (Figure 4.8a). For $N_{1s,}$ only the pyrrolic peak was observed at 399.6 eV (Figure 4.8b).[195] O1s exhibited two binding energies at 531.9 eV (C=O/C-O) and 532.6 eV (OH^-) (Figure 4.8c).[196]

4.3.3. Antibacterial Activity of CasK@CDs_AgNp and CG_CasK@CDs_AgNp Hydrogel

Initially, an agar well diffusion test was performed to check the antibacterial activity of carbon dot-capped silver nanoparticles. CasK@CDs was used as a blank control for the experiment. As shown in Figure 4.9a and 4.9b, the zone of inhibition was significant in the case of four sets of nanoparticles, and the size of the zone depends on the yield of silver nanoparticles formed.

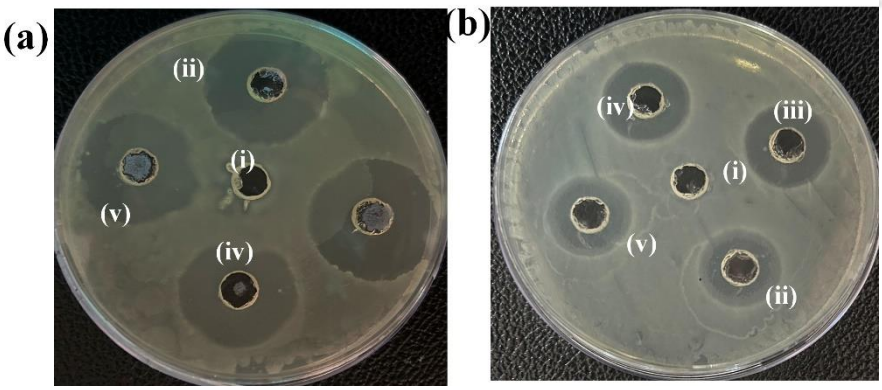

Figure 4.9. Bactericidal activity of (i) CasK@CDs_AgNp1, (ii) CasK@CDs_AgNp2, and (iii) CasK@CDs_AgNp3 against (a) *E. coli,* and (b) *S. aureus*.

Here, the zone of inhibition for of CasK@CDs_AgNp1 and CasK@CDs_AgNp3 exhibited similar values. MIC values for each composition were evaluated with a set of different concentrations of nanoparticles. MIC value is the minimum material concentration required to inhibit bacterial growth after 16 to 24 hours of incubation. The lower MIC value indicates the higher efficiency of the sample. Among the four sets of nanoparticles, CasK@CDs_AgNp1 exhibited the lowest MIC against *E. coli* and *S. aureus*. The bacterial turbidity inside the well vanished from 8 µg/mL and 16 µg/mL for *E. coli* and *S. aureus*, respectively. Following the same trend of silver nanoparticle concentration, the lower MIC value order was found (CasK@CDs_AgNp1< CasK@CDs_AgNp3< CasK@CDs_AgNp2< CasK@CDs_AgNp4). The reason behind the bacterial death was found from the FESEM analysis of nanoparticle-treated bacteria. The image demonstrated that the bacterial morphology has been changed after treatment, and the cell wall has also been ruptured (Figure 4.10).

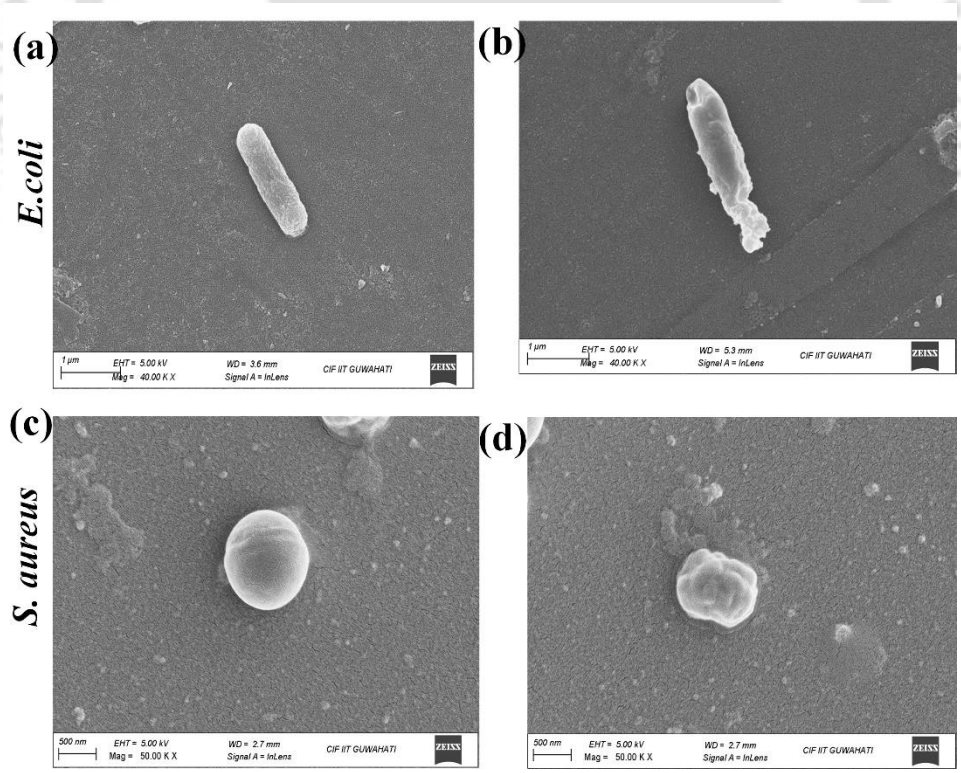

Figure 4.10. (a-b) FESEM image of *E. coli* before and after treatment of CasK@CDs_AgNp1. (c-d) FESEM image of *S. aureus* before and after treatment of CasK@CDs_AgNp1.

Additionally, the effect of CasK@CDs_AgNp1 on bacterial biofilm was investigated using FESEM analysis. The FESEM image of CasK@CDs_AgNp treated bacterial biofilm demonstrated that the deformed bacterial morphology is due to the treatment of CasK@CDs_AgNp (Figure 4.11).

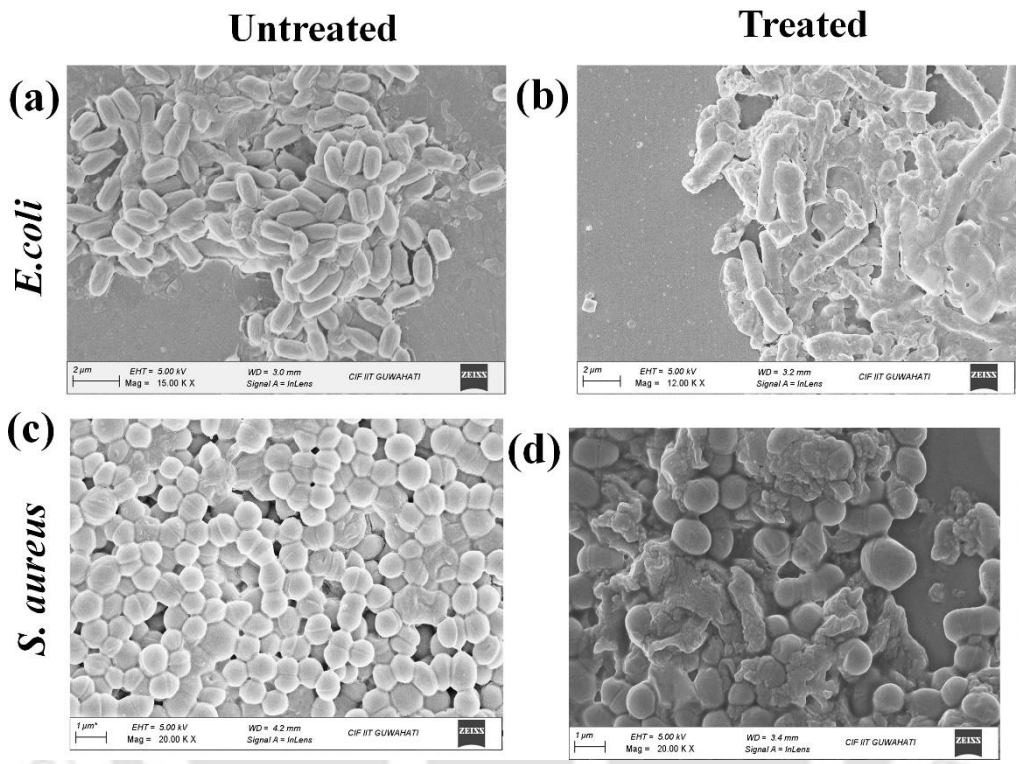

Figure 4.11. FESEM image of *E. coli* after treatment of CG_CasK@CDs_AgNp3 hydrogel. (l) FESEM image of *S. aureus* after treatment of CG_CasK@CDs_AgNp3 hydrogel.

A live-dead assay of bacteria was performed to understand the mechanism behind bacterial death. An enhanced amount of PI on treated bacterial cell wall confirms the membrane disruption, which supports previous outcomes (Figure 4.12a-b). AgNp binds with the bacterial cell wall, leading to better cell permeability and generating ROS in cell which damage protein, DNA, lipids inside cell and increases oxidative stress, further leading to cell death.[197]

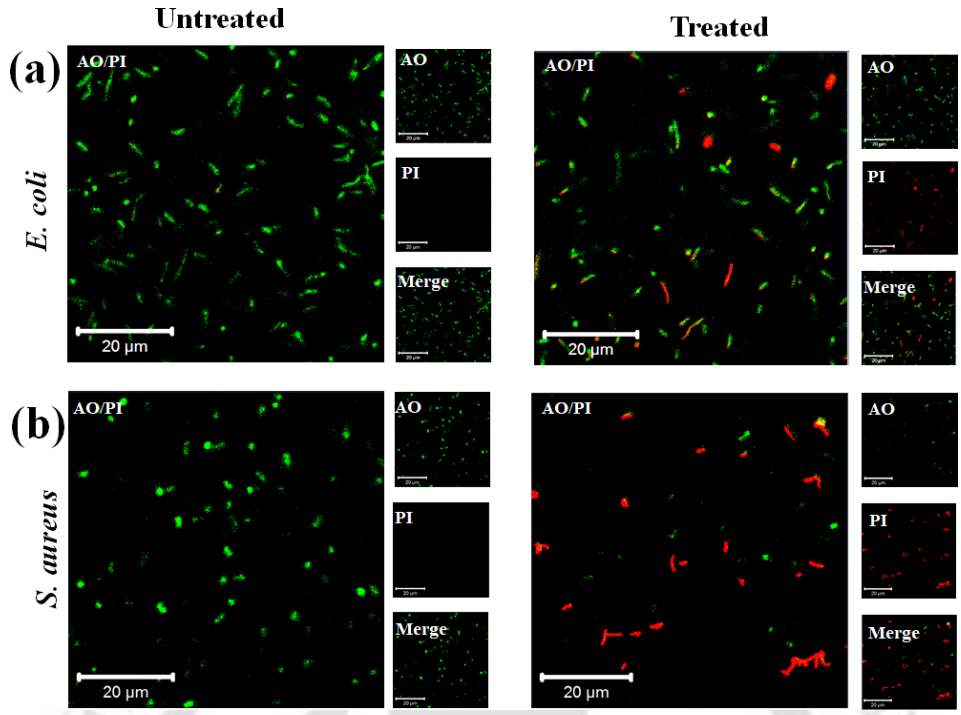

Figure 4.12. Propidium iodide leveling assay of (a) *E. coli* and (b) *S. aureus*.

4.4. Conclusion

In summary, we have developed KC and Cas-derived carbon dots. The CasK@CDs exhibited blue fluorescence under a 365 nm UV lamp. The FETEM analysis confirmed that the average particle size of the CDs is 2.8 nm. The CasK@CDs exhibited overall good stability under different pH solutions. Moreover, CasK@CDs-capped silver nanoparticles exhibited excellent aqueous stability. The nanoparticles possess a high negative surface charge. CasK@CDs_AgNp exhibited MIC values of 8 µg/mL and 16 µg/mL against E. coli and S. aureus bacteria. PI leveling assay and FESEM analysis confirmed that the bacterial death was induced due to the morphological changes of bacteria.

Chapter 5. Synthesis of Carbon Dot-Derived Silver Nanoparticles Embedded Multifunctional Chitosan Hydrogel for Antibacterial, Hemostatic and Wound Healing

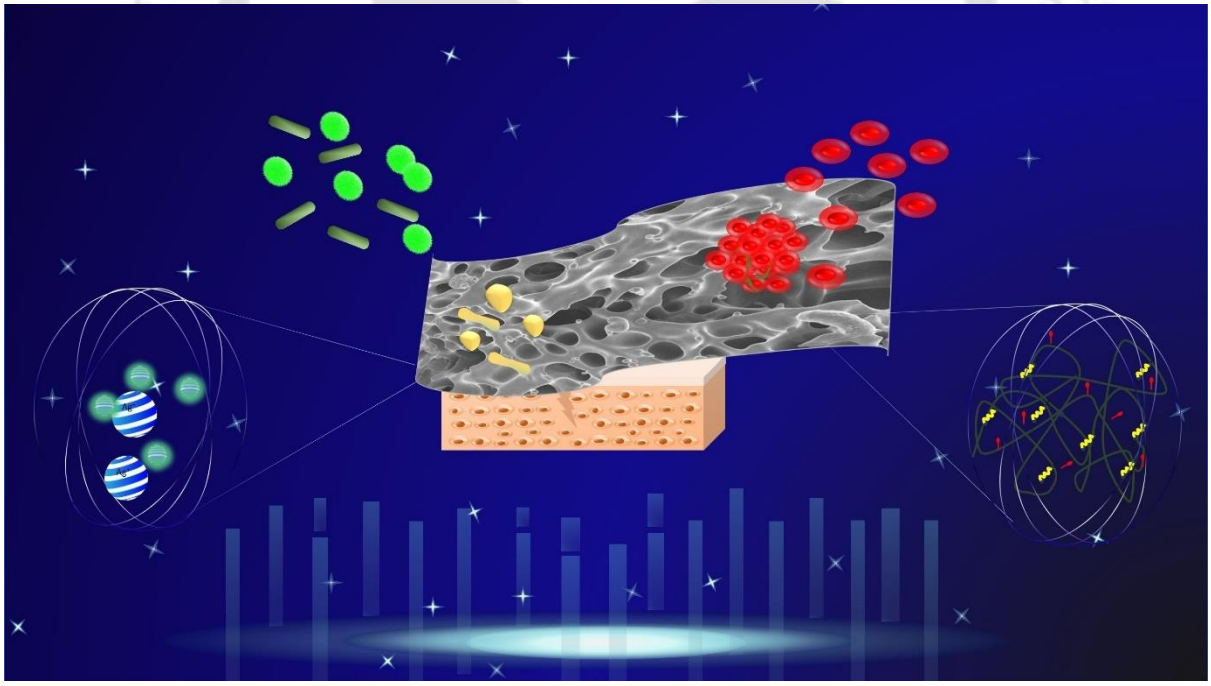

5.1. Overview

The abrasions caused by falling and surgical incisions represent the most common wound types in everyday life, highlighting the need for effective treatment and healing strategies. The healing treatment at special areas such as joints, muscle folds, axillae, and popliteal fossae is more challenging than wounds at flat areas due to poor adhesion, proper wound coverage, and fixation of dressing material. Notably, physiological imbalance and chronic wounds are the non-healing types, which often require critical care and contribute to substantial healthcare costs from $28.1 billion to $ 96.8 billion, including infection management.[198] For clinical purposes, initially, wounds are sterilized by iodine or 70% ethanol solution with a cotton gauze on the wound site. Cotton gauze exhibits several limitations, including insufficient protection against bacterial infections, poor hemostatic properties, adhesiveness, and lack of stretchability. Nonetheless, the use of adhesive tapes to secure the cotton gauze leads to skin irritation. Moreover, the bacterial infections from cotton gauze not only hamper wound healing but also may lead to a chronic wound.[199–202] Thus, designing a stretchable, adhesive, antibacterial, hemostatic, and biocompatible dressing holds great clinical significance.

Developing superior biopolymer-derived materials has brought promising applications in tissue engineering, 3D bioprinting, and wound healing.[203] They also exhibit promising coagulation properties and have high swelling abilities.[204] A large number of biomaterials are used as wound dressing materials, from traditional gauze, adhesive bandage,[205] to modern transparent films,[206,207] hydrocolloids,[208] hydrogels[209,210] and electrospinning fibers[211,212]. Among these, hydrogels were found to be more effective for dressing and wound healing due to high water retention, stretchability, adhesive nature and similarity to extracellular matrix. Biopolymer-based synthetic hydrogels have also been employed as very effective biomimetics for the self-regeneration of tissues.[213,214] The moist hydrogel environment brings better healing efficiency.[215] Additionally, cell fluids and oxygen can easily pass through the hydrogel

network, endowing a compatible wound healing environment. Double network (DN) hydrogels are a class of hydrogels that consists of two interwoven cross-linked networks, which may form by covalent-covalent cross-linking (covalent DN hydrogel), covalent-non-covalent cross-linking (hybrid DN hydrogel), or two non-covalent cross-linking (physical DN hydrogel).[216] The DN hydrogel holds significant impact as it offers good biocompatibility, enhances cell interactions, and improves mechanical strength. Moreover, bioactive agents such as anti-microbial and anti-inflammatory agents, platelet-rich plasma, and fibrin can be incorporated into the hydrogel matrix for sustained release.

Herein, we have designed a new class of stretchable, adhesive, antibacterial, hemostatic, and biocompatible DN hydrogel (CG_CasK@CDs_AgNp) by cross-linking of acrylic acid and hydrocaffeic acid (PAC) modified chitosan (CH). The abundance of free hydroxyl and amine groups in CH contributes to improved biocompatibility and enhanced hemostatic performance of the hydrogel.[217,218] Moreover, the modification of CH by PAC introduces catechol groups, which are known to mimic the adhesive proteins found in mussels, thereby imparting strong tissue adhesion capabilities to the hydrogel system.[219,220] Carbon dot-capped silver nanoparticles have been incorporated during the polymerization reaction to induce antibacterial properties in the hydrogel. We have used the Carbon dot-capped silver nanoparticles that we have discussed in chapter 4. This multifunctional hydrogel thus integrates the structural advantages of a double-network system with the bioactivity conferred by functionalized chitosan and AgNps, making it a promising material for advanced wound dressing applications. Our multifunctional CG_CasK@CDs_AgNp hydrogel exhibited very high swelling (up to 6500%), high adhesive property, good stretchability (>100%), self-healing, high antibacterial efficiency, potential hemostasis, and wound healing.

5.2. Experimental Section

5.2.1. Materials

Kappa-carrageenan (KC), *N*-hydroxysuccinimide (NHS) (97%), *N,N'*-dicyclohexylcarbodiimide (DCC) (99%), and MTT (3-(4,5-dimethylthiazol-2-yl)-2,5-diphenyltetrazolium bromide dye) were procured from Sigma-Aldrich (St. Louis, MO, United States). Casein protein, 3,4-dihydroxyhydrocinnamic acid (PAC) and Dulbecco's modified Eagle's medium (DMEM) were purchased from Tokyo Chemical Industry (Tokyo, Japan) and Himedia, respectively. Low molecular weight chitosan (CH) (poly (β-(1,4)-D-glucosamine), 94% deacetylated, *N*, *N'*-Methylenebisacrylamide (MBA), and potassium per sulphate (KPS) were purchased from Sisco Research Laboratories Pvt. Ltd. (SRL). All reagents were used without further purification.

5.2.2. Synthesis of CHPAC

Conjugation of PAC with CH has been done using EDC/NHS coupling, followed by the previously reported protocol with minor modification.[221] Briefly, 100 mg of CH was dissolved in 10 mL of 1% AcOH solution. 0.5 mM EDC and NHS were added and stirred for a few hours after adding 100 mg PAC. The reaction was continued for 24 hours, and unbounded PAC was removed using dialysis against distilled water for 2 days. The final product was freeze-dried and stored at 4 °C for further use.

5.2.3. Synthesis of CG and CG_CasK@CDs_AgNp Hydrogels

Initially, CHPAC was dispersed in deionized water. A set of three different concentrations of CHPAC was used (40 mg/mL, 32 mg/mL, and 24 mg/mL), and prepared hydrogels were named as CG_CasK@CDs_AgNp1, CG_CasK@CDs_AgNp2, and CG_CasK@CDs_AgNp3. 1.25 mL of AA and CasK@CDs_AgNPs1 were added to reach a final volume of 16 mL and stirred while heating to form a homogenous mixture. Final concentration of CasK@CDs_AgNPs1 was 30 µg/mL. 40 mg KPS and 10 mg MBA were added after the temperature rose to 90 °C and N_2 gas was purged. The formed hydrogel was kept undisturbed for another 30 minutes at a

temperature of 80 ℃ to complete the gelation and kept overnight in excess ethanol to remove unreacted chemicals and freeze-dried at 80 ℃ for 24 hours for characterization.

5.2.4. Morphological Characterization

The lyophilized hydrogel samples were sliced and attached to one side of double-sided conductive carbon tape, and the tape was fixed on the sample stage. All the samples were gold-coated under vacuum conditions for 120 seconds. At a 10-kV accelerating voltage, field emission scanning electron microscopy (FE-SEM, Zeiss, Sigma) was applied to examine the apparent morphology of CG_CasK@CDs_AgNp hydrogels. Simultaneously, the instrument's element energy dispersive X-ray spectroscopy (EDS) was utilized to assess the distribution of the sample elements.

5.2.5. Structure Investigation

The chemical compositions of the CHPAC, CasK@CDs, CasK@CDs_AgNPs, and CG_CasK@CDs_AgNp hydrogels were evaluated using attenuated total reflectance-Fourier transform infrared spectroscopy (ATR-FTIR, IRTracer-100, Shimadzu corporation) with the freeze-dried samples. The thermal properties of CHPAC and CG_CasK@CDs_AgNp hydrogels were investigated using thermogravimetric analysis (TGA), STA7200 thermal analysis system, Hitachi High Technologies, Japan, at a heating rate of 10 ℃ from 25 to 700 ℃ under a nitrogen atmosphere. The crystalline property of CHPAC, CasK@CDs, CasK@CDs_AgNPs, and CG_CasK@CDs_AgNp hydrogels was determined by powder X-ray diffraction (XRD) using Rigaku SmartLab 9 kW X-ray diffractometer fitted with CuKα radiation of $\lambda = 1.54$ Å in a 2θ range of 10−70º. The chemical components of CasK@CDs_AgNPs were detected by X- ray photoelectron spectroscopy (XPS, Thermo Kalpha, Thermo Fisher Scientific), which were adjusted using the C 1s (284.80 eV) binding

energy standard. The size of the nanoparticles was determined by Jeol 2100 F Field Emission Transmission Electron Microscope (FETEM).

5.2.6. Swelling behavior of CG_CasK@CDs_AgNp Hydrogels

The swelling capacity of the hydrogels was investigated in three simulated human environments (gastric juice pH = 1.2, small intestinal fluid pH = 6.8, and body fluid pH = 7.4). Freeze-dried hydrogel was dipped in 10 mL of PBS buffer solutions in closed tubes. The tubes were kept at room temperature for 48 hours. At different time intervals, the hydrogels were taken out and weighed after wiping the surplus surface water. The swelling rate of the hydrogels was determined using the following equation:

$$Swelling\ rate\ (\%) = (\frac{w_t}{w_0} - 1) * 100$$

Where, w_t is the weight of the hydrogel at different times and w_0 is the weight of the freeze-dried hydrogel.

5.2.7. Determination of Rheological Properties

The viscoelastic property of CG_CasK@CDs_AgNp hydrogel was evaluated using a Rheometer (Thermoscientific MARD iQ Air). Initially, the hydrogel samples were mounted on the rheometer plate with a diameter of 20 mm and spacing of 1.0 mm at 25 ℃ to identify the linear viscoelastic region. Strain correlation measurements were carried out to determine the linear viscoelastic region of the hydrogels (0.01−100% strain at a fixed frequency of 1.0 rad/s). A frequency sweep test was performed by scanning at a frequency of 0.1−100 Hz with a constant strain of 2%.

5.2.8. Antioxidant Property and Radical Scavenging Assay

Antioxidant properties of hydrogels were analyzed using the DPPH assay. For the DPPH assay, the pregelation hydrogel mixture was collected and diluted. 100 µM DPPH solution was

prepared in ethanol. DPPH solution, sample and water were mixed in a 4:1:3 ratio. The mixture was vortexed and incubated in the dark for 1 hour. The absorbance of supernatant was recorded at 520 nm, and % of radical scavenging was calculated.

$$\% \text{ of scavenging} = \frac{Abs_I - Abs_S}{Abs_I} \times 100$$

Abs_I is the absorbance of DPPH only and Abs_S is the absorbance after addition of the sample.

5.2.9. Agar Well Diffusion Assay

Initially, the antibacterial properties of CG_CasK@CDs_AgNp (1, 2, and 3) were analyzed keeping CG as a control. 50 µL of bacterial suspension of Escherichia coli (*E. coli* (EC), Gram-negative) and Staphylococcus aureus (*S. aureus* (SA), Gram-positive) were evenly spread on a LB agar plate. Uniform holes were created in the agar plate. 20 mg of the hydrogels were washed in PBS overnight and kept under UV radiation for 30 min to remove any kind of bacterial contamination. Three set of hydrogels were added to the well incubated in static conditions at 37 ℃ for 16-20 hours. The activity of blank hydrogels was also investigated.

5.2.10. Bactericidal Activity of CG_CasK@CDs_AgNp Hydrogels

Fresh cultured EC and SA were taken in a test tube (10^6 CFU/mL). 100 mg of CG_CasK@CDs_AgNp1, CG_CasK@CDs_AgNp2 and CG_CasK@CDs_AgNp3 were added to each tube and incubated at 37 ℃. 100 µL of bacterial suspensions were collected at various time intervals and evenly spread on agar plates, followed by 20 hours of incubation. The digital images were captured to understand the effect of the hydrogel.

5.2.11. Cytocompatibility Assay

The cell viability assay of CG_CasK@CDs_AgNp hydrogel was conducted on Human Dermal Fibroblasts cells (HDF) using the MTT assay. A 100 mg hydrogel sample was dispersed in 10 mL of water and kept in an incubator shaker at 37 ℃ for 24 hours. The supernatant was

collected using centrifugation after 30 minutes of sonication. The supernatant was diluted 1:10 and 1:20 in DMEM media for treatment. 1×10^5 cells/well were seeded into a 96-well plate and incubated under 5% CO_2 humidified conditions at 37 °C. After 24 hours of incubation, the cells were treated with diluted hydrogel extract in triplicate for 24 hours. After discarding the culture media, 10 µL of 0.5 mg/mL MTT was added to the 96-well plate and incubated for two hours, followed by the addition of DMSO. The addition of DMSO generated violet formazan product in the wells. The absorbance values were recorded at 570 nm using a multiplate reader with a reference at 600 nm. The obtained absorbance value is directly proportional to the viable cells present. The cell viability was calculated using the following formula:

$$\%\ cell\ viability = \frac{Abs_{S570} - Abs_{S600}}{Abs_{C570} - Abs_{C600}} \times 100$$

Where Abs_S stands for the absorbance of the sample and Abs_C stands for the absorbance of the control.

5.2.12. Cell Migration Assay

HDF cells (6×10^5 cells/plate) were uniformly seeded in 35 mm plates and cultured overnight. An even scratch line was generated using a 10 µL tip in the plate, and the plates underwent two rounds of washing to remove the detached cells and debris. Later, the hydrogel extracts from the various groups were added to the cells for co-culture treatment. Cell migration was continuously observed at the scratched line and recorded using a ZOE microscope for the different treatment groups. Changes in the scratch width were calculated using ImageJ software to evaluate the cell migration rates.

5.2.13. ROS Clearance Assay

The intracellular ROS-scavenging abilities of CG_CasK@CDs_AgNp hydrogels were evaluated using H_2O_2 (300 µM) to induce ROS. 10×10^4 HDF cells were seeded onto 96-well

plates and cultured overnight at 37 °C. Later, one set of cells was treated without H_2O_2 (control), H_2O_2-treated cells were used as positive control, and the other sets were treated with hydrogel extracts (1:10 dilution). After 24 h of the treatment, 10 µM DCHF-DA was added to each well and incubated at 37 °C in the dark for 30 min. After 30 min, using a Glomax plate reader, fluorescence intensity was measured using a 475 nm excitation wavelength and 500-550 nm emission wavelength.

5.2.14. Hemolysis Assay

The hemolysis assay was performed with the institute's ethical clearance. 2 mL of fresh whole blood was collected from a healthy volunteer in an EDTA tube. The blood sample was mixed gently to inhibit coagulation before the experiment. The blood sample was centrifuged at 1500 rpm for 5 min at a fixed temperature (4 ℃). The plasma was replaced with sterile PBS until the supernatant color turned transparent. The final concentration of red blood cells was 5%. PBS was used as a negative control, and Triton X-100 acted as a positive control. 100 µL of sample and 100 µL of diluted RBC were mixed and incubated at 37 ℃, 180 rpm for 2 hours. The absorbance of the supernatant was evaluated after centrifugation. The % of hemolysis was calculated using the following formula:

$$Rate\ of\ hemolysis\ (\%) = \frac{Abs_S - Abs_N}{Abs_P - Abs_N} \times 100$$

Where Abs_S, Abs_N, and Abs_P stand for absorbance of the sample, negative control, and positive control.

5.3. Results and Discussions

5.3.1. Fabrication and Characterization of CG_CasK@CDs_AgNp Hydrogels

Initially, PAC has been grafted on the polymeric chain of chitosan to enhance the tissue adhesiveness of hydrogels. Three types of CG_CasK@CDs_AgNp hydrogels were prepared

using radical polymerization reaction, keeping CasK@CDs_AgNp concentration unchanged and varying the concentration of CHPAC. Blank CG_CasK@CDs hydrogels were also prepared for comparative analysis. During polymerization, acrylic acid was initially polymerized and cross-linked with MBA. CHPAC acted as a mediator and generated physical and chemical entanglement with CasK@CDs_AgNp and acrylic acid, respectively (Figure 5.3a). Each component of the engineered hydrogel demonstrated appealing contributions in the functional properties of the hydrogels: (1) grafting of PAC incorporated adhesive properties, (2) variable concentration of CHPAC in the hydrogel introduces variation in pore size, leading to enhanced wound healing, (3) biopolymer derived carbon dots endows a sustainable path for the generation of stable AgNp and soft hydrogel formulations. Such induced properties are expected to make the hydrogels a potential candidate for bacterial-infected wound healing.

From the NMR analysis of CHPAC, a new proton peak was found in the aromatic region (δ 7-6.5 ppm) as that of PAC, indicating the successful grafting of PAC on the CH chain (Figure 5.1). Powder XRD analysis of CH exhibited two amorphous peaks at 10.2° and 19.9°, respectively. However, PAC exhibited characteristic crystalline peaks at 13.2°, 17.6°, 23.7°, 24.1°, and 25.4°, respectively. As shown in Figure 5.2a, CHPAC displayed the characteristic amorphous peaks at 8.7°, 11.5°, 18.7° and 23.6°, which are slightly shifted from the precursor materials, inferring the successful grafting. FTIR spectrum of CH presented a broad peak around 3348 cm^{-1} for OH/NH_2, 1651 cm^{-1} for C=O stretching of amide I, 1569 cm^{-1} for N-H bending and 1361 cm^{-1} for C-N stretching originated from the N-acetyl group (Figure 5.2b). The characteristic peaks of PAC at 3348 cm^{-1} can be attributed to the stretching vibration of OH, 1673 cm^{-1} corresponds to C=O stretching bond of carboxylic acid, and 1199 cm^{-1} corresponds to the stretching vibration of C-OH. The peak originated at 1524 cm^{-1}, 1442 cm^{-1} can be attributed to the C-C stretching of the aromatic ring.[222] The characteristic peak of CHPAC exhibited a broad NH/OH peak at 3336 cm^{-1} and the N-H/C-N peak has been shifted

from the precursors. A sharp peak has been found at 1546 cm^{-1} that can be attributed to N-H bending and 1638 cm^{-1} for the C=O stretching frequency. These phenomenon demonstrates the successful conjugation.[6] Percentage of conjugation was found to be 13% (using the calibration curve of PAC at 282 nm).

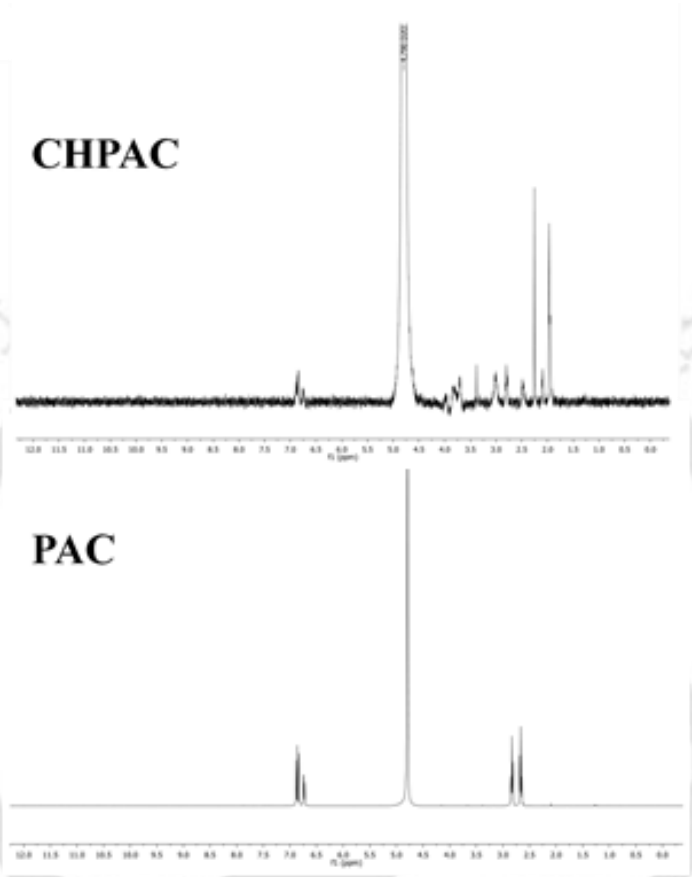

Figure 5.1. NMR spectrums of PAC and CHPAC (in D_2O).

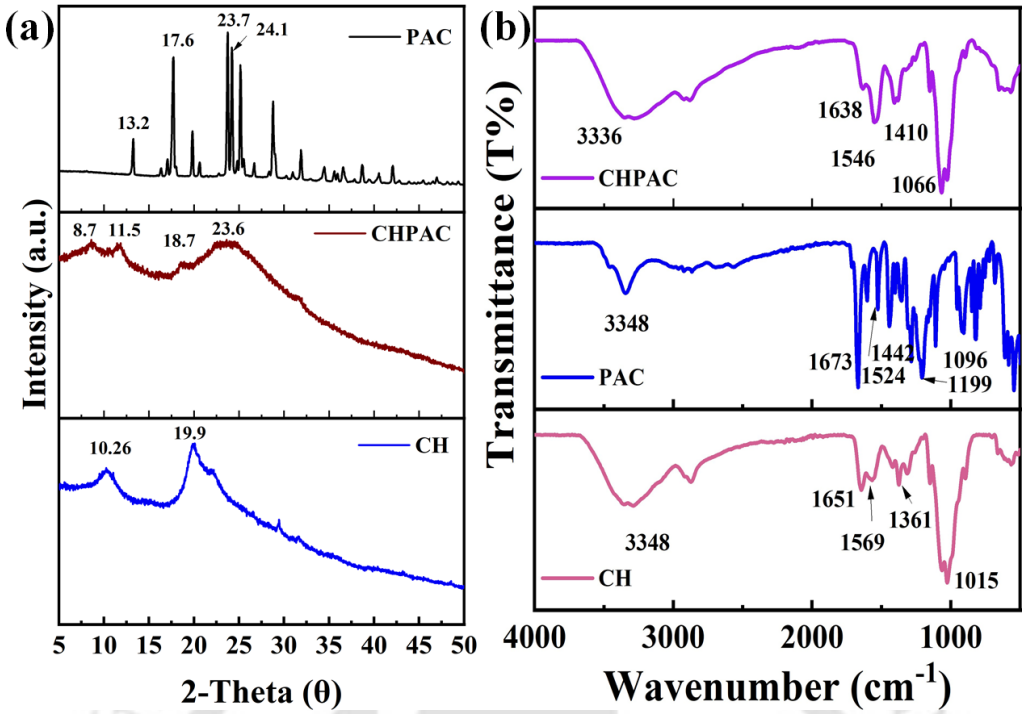

Figure 5.2. (a) Powder-XRD and (b) FT-IR pattern of CH, PAC and CHPAC.

Synthesis of CG_CasK@CDs_AgNp hydrogels was achieved by radical polymerization reaction. At high temperature, $K_2S_2O_8$ dissociates into $SO_4^{\cdot-}$, which initiates the polymerization of acrylic acid. The reaction proceeds through cross-linking of MBA and entanglement with CHPAC (Figure 5.3a). Further, the addition of CasK@CDs_AgNp during the formation of hydrogel generated physical cross-linking in the matrix by H-bonding interaction, π-π interaction with the functional groups of carbon dots, and the π-stacked core, respectively. Moreover, a strong interaction occurs between the hydroxyl group of catechol and silver nanoparticles, which binds the nanoparticles inside the hydrogel network.[223]

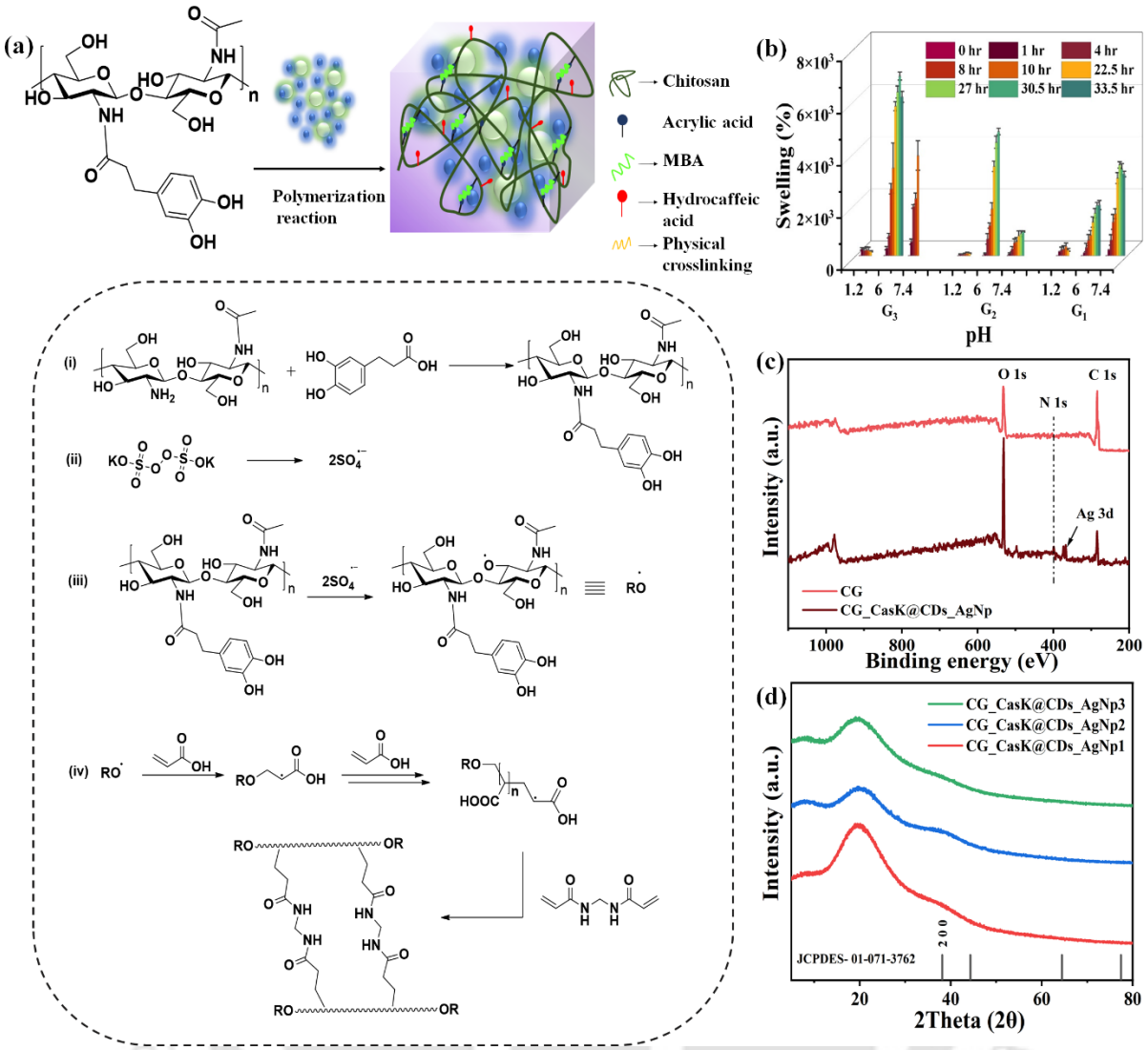

Figure 5.3. (a) Synthesis scheme of CG_CasK@CDs_AgNp hydrogel. (b) Swelling capacity of CG_CasK@CDs_AgNp hydrogel. (c) XPS pattern of CG and CG_CasK@CDs_AgNp hydrogel. (d) XRD pattern of CG_CasK@CDs_AgNp hydrogel.

The structural integrity of hydrogels was characterized by FT-IR, XRD, XPS, FESEM, and TGA. XPS analysis of CG hydrogel confirmed the presence of C 1s (283.9 eV), N 1s (400 eV), and O 1s (531.5 eV) (Figure 5.3c). However, CG_CasK@CDs_AgNp exhibited a new peak that formed at 372 eV, attributed to Ag_{3d}. The high-resolution deconvoluted spectra of Ag_{3d} exhibited a peak at 368.2 eV, similar to CasK@CDs_AgNp.[224] Powder XRD pattern of CG hydrogels exhibited a typical amorphous pattern with a broad hump around 20-22° (Figure

5.4). However, CG_CasK@CDs_AgNp hydrogels exhibited an additional small peak at 38.12° originating from the silver nanoparticles (Figure 5.3d).

In FTIR, the characteristic peaks of CG hydrogel were obtained at 1706 cm^{-1}, 1247 cm^{-1}, and 1165 $cm^{-1,}$ which indicate the presence of C=O stretching, phenolic OH, and C-OH stretching (Figure 5.5a).[225] As shown in Figure 5.5b, the peak at 1247 cm^{-1} was diminished in CG_CasK@CDs_AgNp hydrogels, and the free OH group has been shifted to 3452 cm^{-1}.[226] The abovementioned result supports the interaction of carbon dot-capped silver nanoparticle, which has influenced the hydrogen bonding in the hydrogel network.

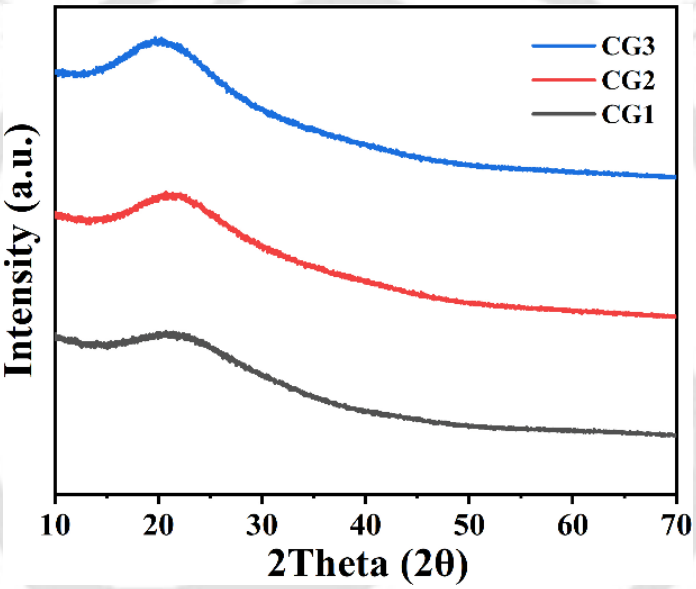

Figure 5.4. XRD pattern of CG hydrogel.

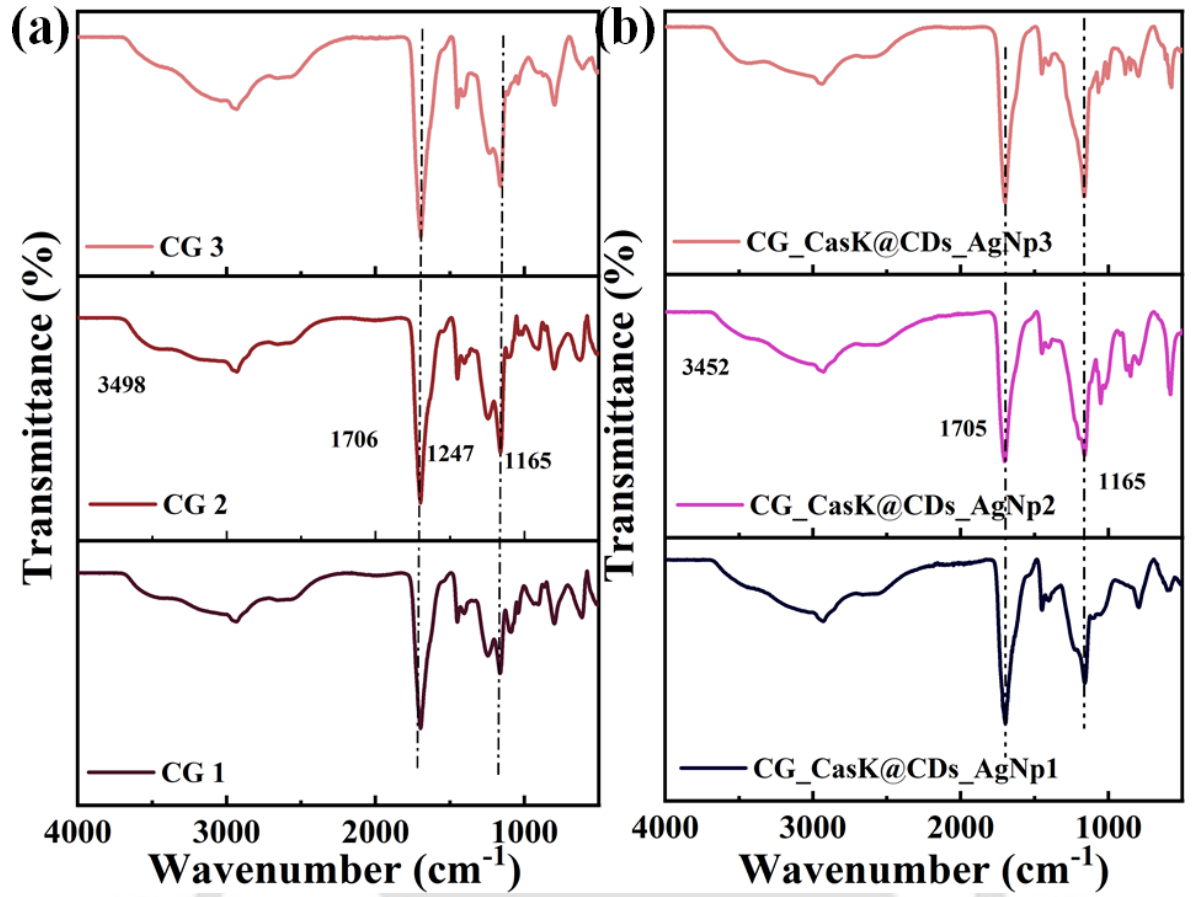

Figure 5.5. FT-IR analysis of (a) CG and (b) CG_CasK@CDs_AgNp hydrogels.

The thermogravimetric profile of CHPAC exhibited two-step degradation with more thermal stability compared to precursor materials (Figure 5.6a-b). Initially, 10% degradation was observed at 101 ℃, which indicates the loss of moisture, and the polymer backbone started to degrade from 206 ℃. 50% degradation was completed at 300 ℃ and further reduction occurred between 300-700 ℃. In contrast, CG hydrogels exhibited a three-step degradation during analysis. The polymeric backbone started to degrade at 130 ℃, followed by degradation of each component. The major degradation occurs between 130-286 ℃ (20%), 300-400 ℃ (30%), and 440-700 ℃ (25%) (Figure 5.7a-b). The primary weight loss up to 286 ℃ is attributed to the degradation of the chitosan chain, followed by the degradation of other components. The trend did not change significantly in the case of CG_CasK@CDs_AgNp hydrogels (Figure

5.7c-d). Only a slight increase in degradation temperature was observed due to the extended cross-linking in the presence of CasK@CDs_AgNp.

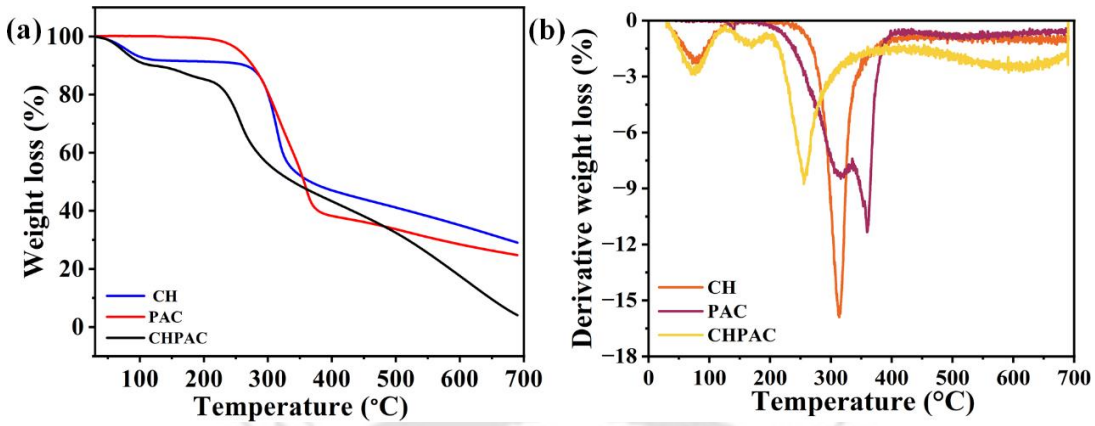

Figure 5.6. (a) TGA analysis of CH, PAC, and CHPAC. (b) Temperature derivative curve of CH, PAC, and CHPAC.

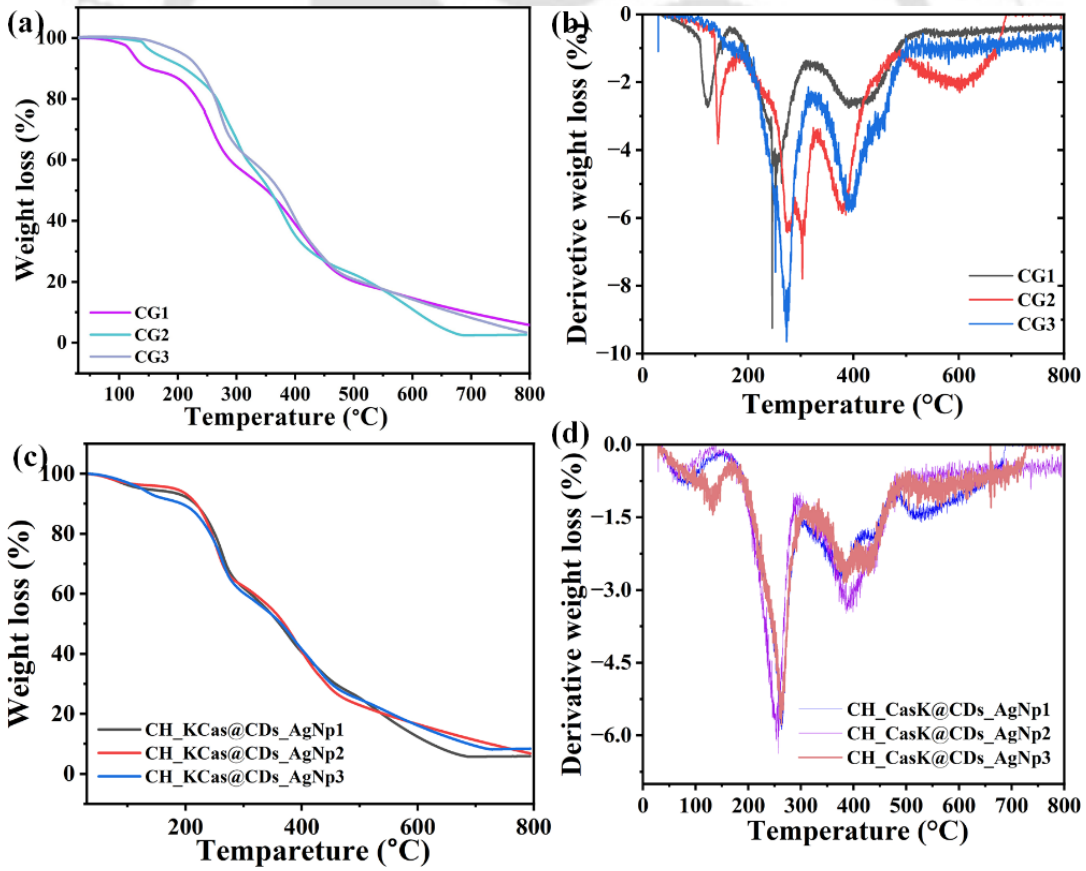

Figure 5.7. TGA analysis of (a) CG and (c) CG_CasK@CDs_AgNp hydrogel. Change in derivative weight loss with temperature of (b) CG and (d) CG_CasK@CDs_AgNp hydrogel.

5.3.2. Swelling Property of the Hydrogel

The swelling property of hydrogel plays a crucial role in the process of wound healing. High water retention capability builds a moist wound environment and good diffusion of nutrients. Therefore, the equilibrium swelling of CG_CasK@CDs_AgNp hydrogel was analyzed at different pH environments. As shown in Figure 5.3b, the highest swelling was achieved at 6.4 pH in the case of hydrogel 3 with 6000% water content. A highly acidic medium did not exhibit good swelling for each hydrogel. However, neutral pH exhibited a higher degree of swelling. The acidic component present in the hydrogel network tends to swell more in neutral to basic conditions due to the repulsion between polymer chains generated from deprotonation.[227] The degree of swelling is highly dependent upon the percentage of CHPAC in the hydrogel. High concentration of CHPAC in the hydrogel generates a higher degree of cross-linking and small pore size, simultaneously leading to lower water retention capacity. The high equilibrium swelling percentage suggests that the hydrogels can maintain a favorable moist environment and promote wound healing.[228]

5.3.3. Morphological Features of CG_CasK@CDs_AgNp Hydrogels

A three-dimensional cross-linked network hydrogel significantly impacts the cell growth, diffusion of nutrients, and body fluids. Moreover, pore size between 50-100 µm plays a vital role in wound closure and therapeutic delivery.[229] From the FESEM analysis of CG hydrogels, nano porous structures were found with a direct proportional amount of CHPAC concentration in the matrix (Figure 5.9a-c). The observation demonstrates the enhanced cross-linking due to CHPAC. Blank hydrogels exhibited a small pore size with comparatively low density of pores compared to AgNps-loaded hydrogels (Figure 5.8a-c). The higher porosity in the presence of hydrophilic carbon dot-derived AgNps was generated due to the physical cross-linking, such as H-bonding interaction, π-π interaction, and electrostatic interactions. The larger pore size (> 60 µm) of CG_CasK@CDs_AgNp hydrogel was observed in the case of

CG_CasK@CDs_AgNp 3. However, the other two sets of hydrogels exhibited a pore size less than 60 µm (Figure 5.8i). Aforementioned observation describes the in-situ presence of CasK@CDs_AgNp during synthesis of CG_CasK@CDs_AgNp hydrogels, which has affected cross-linking and pore size. Water contact angle measurement of CG_CasK@CDs_AgNp hydrogels was found to be less than 90° for each of the hydrogels, indicating the hydrophilic nature of the material (Figure 5.8d-f). Hydrophilic dressing material helps in creating a moist environment, which helps in wound healing. The contact angle exhibited a lower value with increasing amount of CHPAC in the hydrogel system. Hence, our material can help in wound healing.

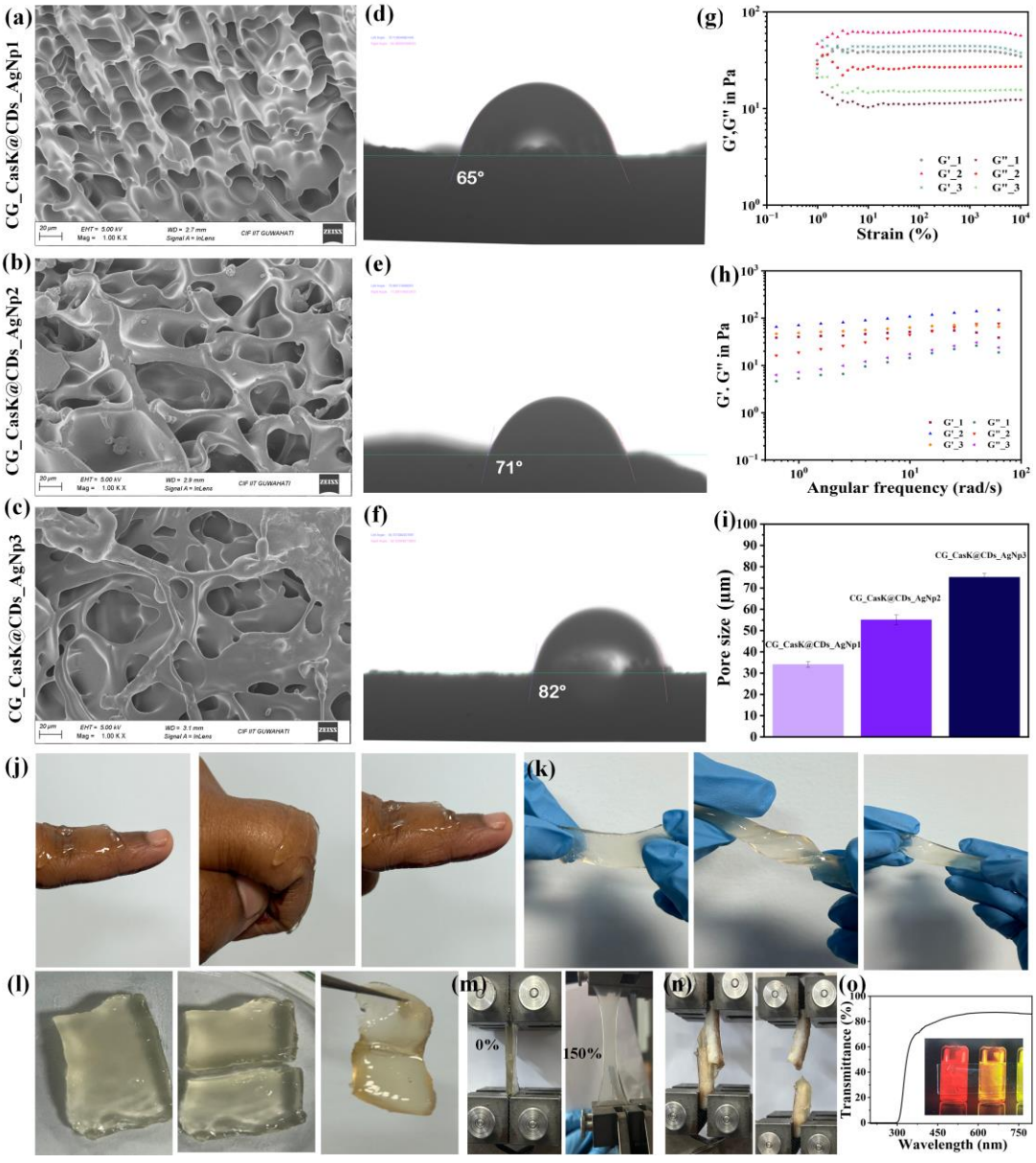

Figure 5.8. Morphological features of CG_CasK@CDs_AgNp hydrogels. (a-c) FESEM images of CG_CasK@CDs_AgNp1, CG_CasK@CDs_AgNp2, and CG_CasK@CDs_AgNp3 hydrogel. (d-f) Image of contact angle of water on CG_CasK@CDs_AgNp hydrogel surface. (g) Rheological assessment of oscillatory strain. (h) Change in G'G" with frequency at a constant strain of 2%. (i) Average pore size of CG_CasK@CDs_AgNp hydrogels from FESEM analysis. (j) Adhesion test of hydrogel with human skin. (k) Flexibility of hydrogel with twisting. (l) Self-healing performance of CG_CasK@CDs_AgNp hydrogel at 37 ℃. (m) Tensile stretching of CG_CasK@CDs_AgNp hydrogel. (n) Adhesion assay of hydrogel with pig skin. (o) Transmittance spectra of CG_CasK@CDs_AgNp hydrogel.

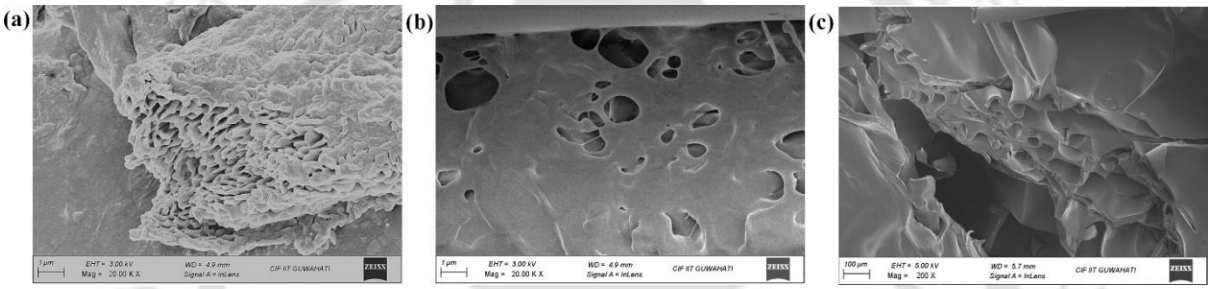

Figure 5.9. FESEM image of CG1, CG2, and CG3.

5.3.4. Rheological Analysis

The viscoelastic properties of CG hydrogels were evaluated by performing rheological analysis through amplitude and frequency sweep tests. In order to determine the deformation behavior or linear viscoelastic range (LVR) and determine the stress, the amplitude sweep test was performed at a constant frequency, and a frequency sweep test was performed in LVR, keeping constant strain. All sets of hydrogels exhibited higher storage modulus (G′) value than loss modulus (G″) at a strain less than 60%, 72% and 51% for CG_CasK@CDs_AgNp1, CG_CasK@CDs_AgNp2, and CG_CasK@CDs_AgNp3, respectively, when a strain sweep test was performed keeping a constant frequency of 1 rad/s (Figure 5.8g). Higher G′ value than G″ with no crossover points up to 100% strain indicated stable structural integrity of the

hydrogels. The frequency sweep test was conducted at a constant strain of 2% within LVR, which further affirmed the stable elastic nature of the hydrogel (Figure 5.8h).[230]

Additionally, the adhesive property of the hydrogel was monitored using CG_CasK@CDs_AgNp3 hydrogel. The sample was cut into a rectangular shape. The hydrogel was applied to the finger joint and bent at different angles, and it subsequently returned to its original position. As depicted in Figure 5.8j, the hydrogels exhibited strong adhesion to bare skin without irritation. The tissue adhesiveness is attributed to the PAC in the chitosan chain, which possesses strong affinity to amine, imidazole, thiols and proteins in tissue. The sticky fibril between pig skin and human skin supports the fact (Figure 5.8n). The CG_CasK@CDs_AgNp hydrogels possess both covalent and non-covalent bonding. Due to the non-covalent bonding, i.e., physical interaction, it exhibited potential self-healing performance. The hydrogel was cut into two pieces, and the cut was healed within 2 hours at 37 °C (Figure 5.8l). Hence, the hydrogel has the potential to balance the requirements of dressing. A hydrogel with optical transparency offers unique advantages such as wound monitoring. CG_CasK@CDs_AgNp hydrogel exhibited greater than 85% transmittance above 500 nm (Figure 5.8o). Hence, the hydrogel can be applied for biomedical applications. The tensile test of hydrogel (CG3, CG_CasK@CDs_AgNp3, and CG_CasK@CDs_AgNp3 attached with pig skin) was performed using a universal testing machine (UTM). The tensile strain for CG3 was 80% and 120% for CG_CasK@CDs_AgNp3. The result clearly indicates the physical cross-linking, inducing high mechanical strength of the hydrogel (Figure 5.10a). When the hydrogel was fixed with pig skin, the strain reached 140% and the strain was 1000 kPa (Figure 5.10b). Moreover, the hydrogel can be twisted or folded without affecting its initial shape (Figure 5.8k). The outcome suggested the hydrogel offers a good mechanical strength with good tissue adhesive property, transparency, and stretching ability.

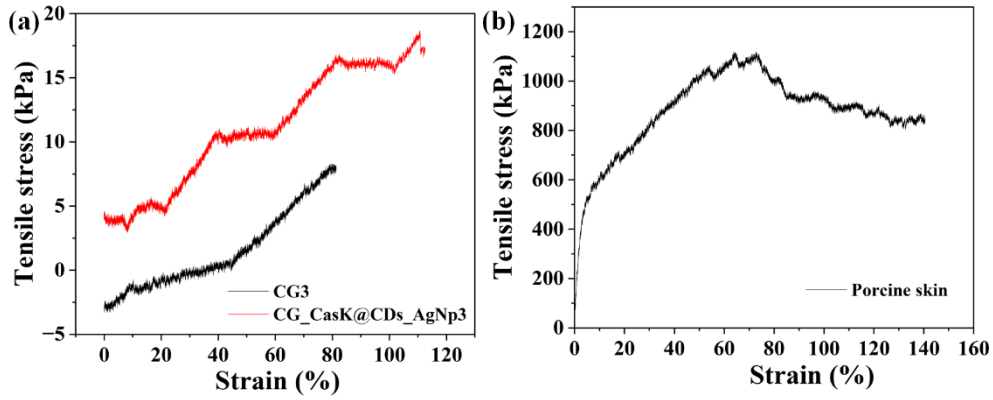

Figure 5.10. (a) Comparison of the adhesive property of hydrogel before and after the addition of CasK@CDs_AgNp. (b) Adhesion strength on pig skin with CG_CasK@CDs_AgNp3.

5.3.5. Antibacterial Activity of CG_CasK@CDs_AgNp Hydrogel

During the analysis of the antibacterial property of hydrogels, 50 mg of the hydrogel sample was placed into the agar well. Despite having the same concentration of CasK@CDs_AgNp in all the hydrogel sets, CG_CasK@CDs_AgNp1 exhibited the largest zone of inhibition for *E. coli* and *S. aureus,* followed by CG_CasK@CDs_AgNp2 and CG_CasK@CDs_AgNp3 (Figure 5.11b and 5.11d). To understand the reason behind such a phenomenon, agar well diffusion assays for CG hydrogel were performed. Interestingly, the assay displayed a small zone of inhibition with increasing concentration of CHPAC (Figure 5.11a and 5.11c). The observation confirmed that the CG hydrogel itself possesses antibacterial effects.

A time-kill assay was performed to understand the time required for the bactericidal action of the nanoparticles loaded hydrogel. The study revealed that hydrogel can kill the bacteria in 9 hours and no revival of bacteria after 24 hours (Figure 5.12-5.13). Further, the interaction between bacteria and hydrogel was analyzed by FESEM. As shown in Figure 5.14a-b, *E. coli* and *S. aureus* exhibited deformed cellular morphology, and few bacteria were attached to the hydrogel surface, which supports the potential anti-biofilm activity of CG_CasK@CDs_AgNp hydrogel.

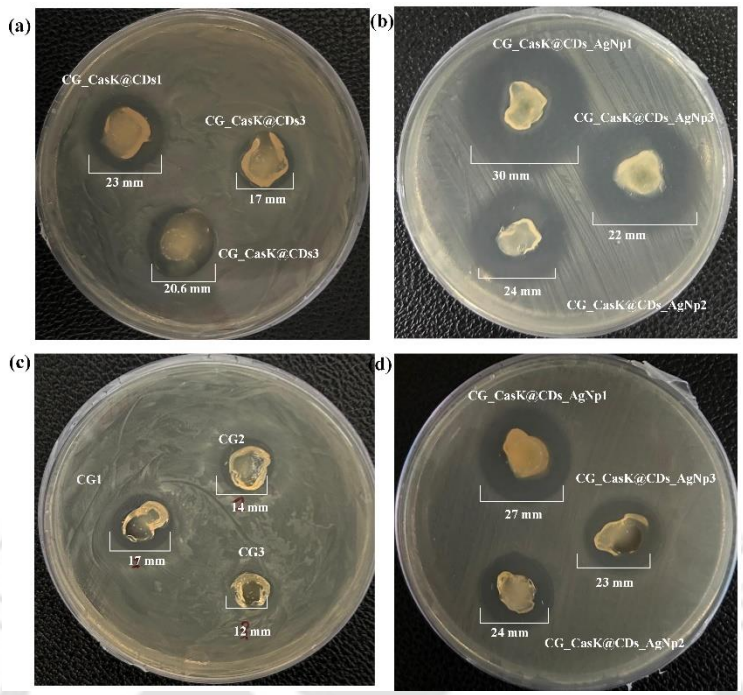

Figure 5.11. Bactericidal activity of CG and CG_CasK@CDs_AgNp hydrogel. (a-b) Agar well test of CasK@CDs_AgNp, CG, and CG_CasK@CDs_AgNp hydrogel against *E. coli*. (c-d). Agar well test of CasK@CDs_AgNp, CG, and CG_CasK@CDs_AgNp hydrogel, respectively, against *S. aureus*.

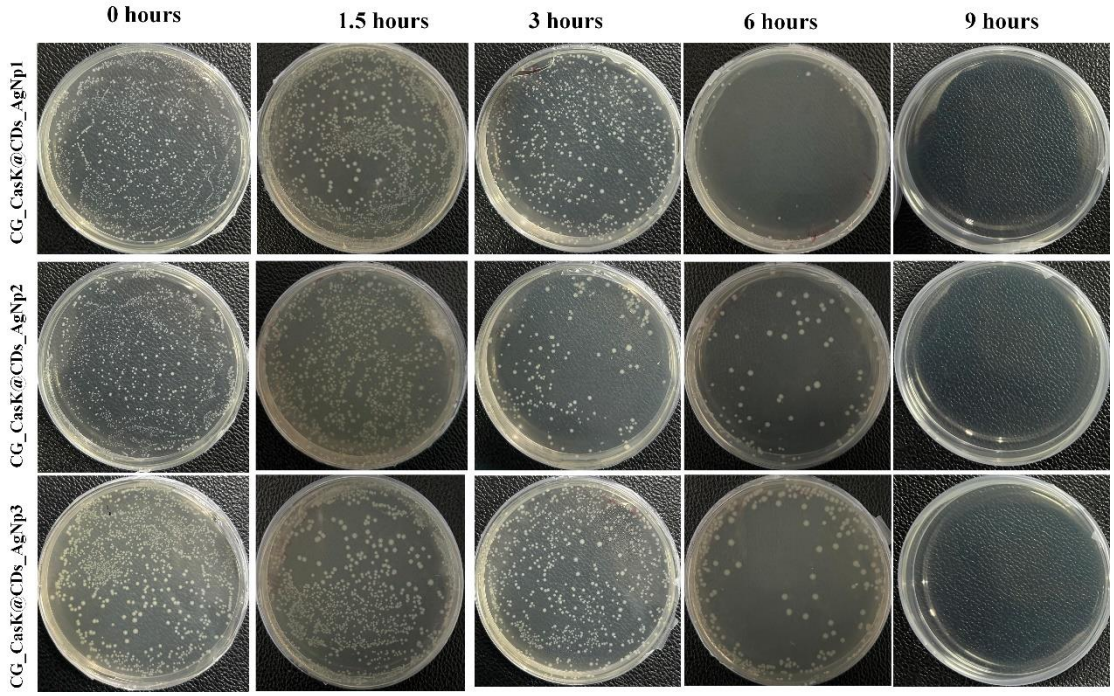

Figure 5.12. Digital image of agar plate experiment of *E. coli* after hydrogel treatment at different time intervals.

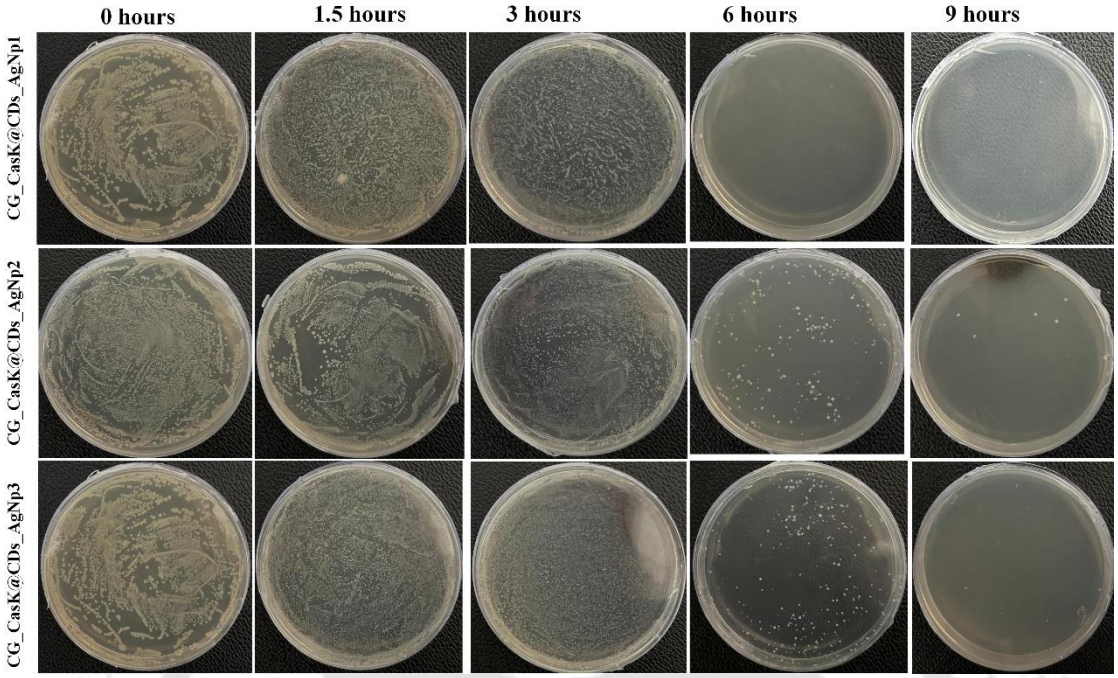

Figure 5.13. Digital image of agar plate experiment of *S. aureus* after hydrogel treatment at different time intervals.

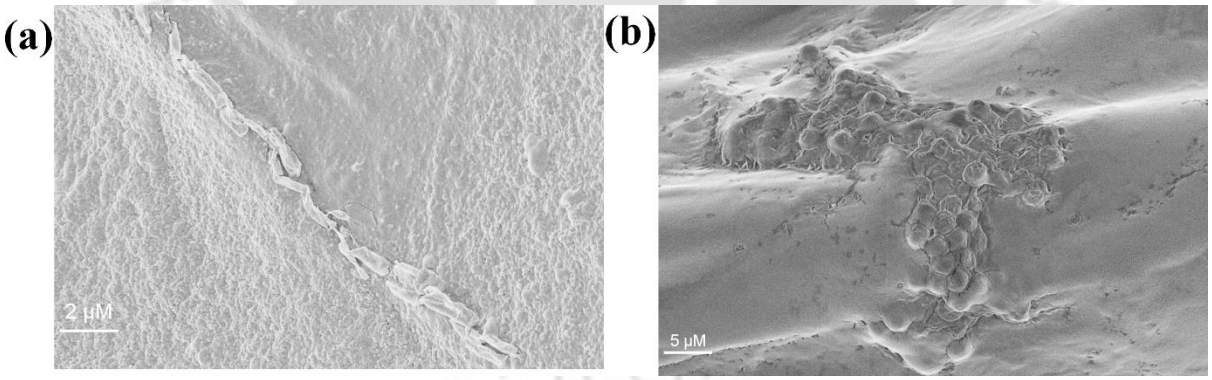

Figure 5.14. FESEM image of (a) *E. coli*, and (d) *S. aureus* after treatment with hydrogel.

5.3.6. Antioxidant Property and Intracellular ROS Generation of Hydrogel

Excessive ROS in the wound site generates oxidative stress, cell necrosis, and other consequences, leading to an inflammatory reaction and wound and scar formation. Therefore, the antioxidant property of CG_CasK@CDs_AgNp hydrogel was evaluated by the change in

the absorbance value of the DPPH solution. Nanoparticle-loaded hydrogel exhibited more free-radical-scavenging activity than CG hydrogels (Figure 5.15a-f). A typical trend in radical scavenging was observed for the hydrogel samples depending upon the concentration of CHPAC, where CG_CasK@CDs_AgNp1, CG_CasK@CDs_AgNp2, and CG_CasK@CDs_AgNp3 exhibited 84±2%, 78±1.5% and 71±3% scavenging, respectively (Figure 5.16). According to Figure 5.16a, the ROS level increased threefold in H_2O_2-treated cells compared to the control. In contrast, hydrogel-treated samples demonstrated insignificant change in ROS levels. On closer examination of the dataset, a slight but statistically insignificant increase in ROS levels was observed in the order: CG_CasK@CDs_AgNp1 < CG_CasK@CDs_AgNp2 < CG_CasK@CDs_AgNp3. This trend may be attributed to the lower concentration of CHPAC in the respective formulations.

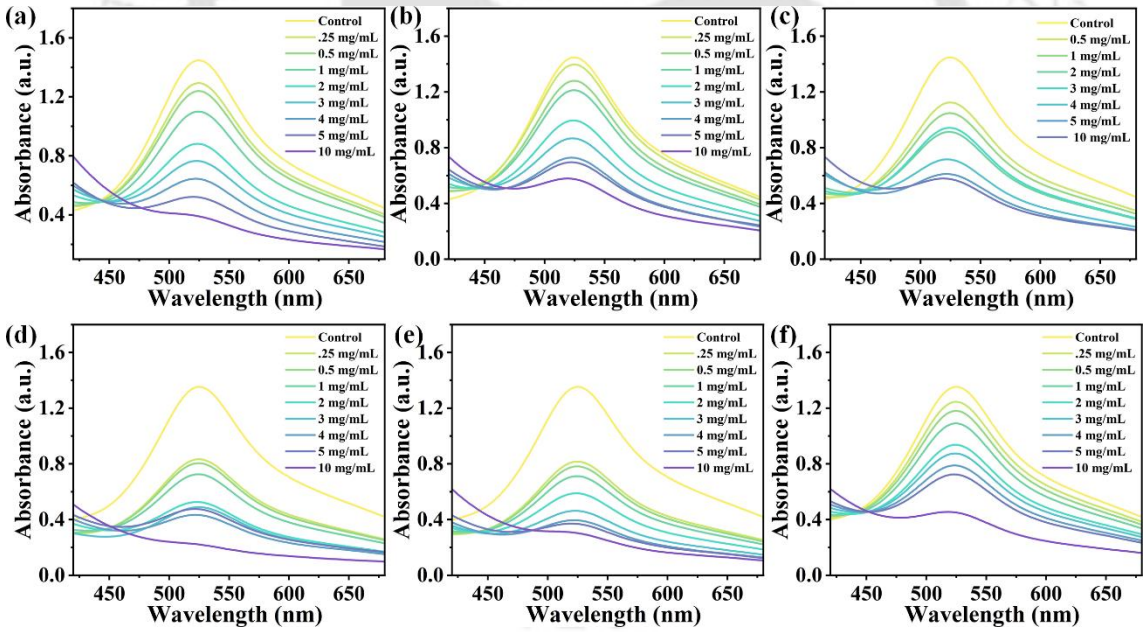

Figure 5.15. Antioxidant property of CG and CG_CasK@CDs_AgNp hydrogels. (a-c) DPPH scavenging response of CG1, CG2, and CG3. (d-f) DPPH scavenging response of CG_CasK@CDs_AgNp1, CG_CasK@CDs_AgNp2, and CG_CasK@CDs_AgNp3 solutions.

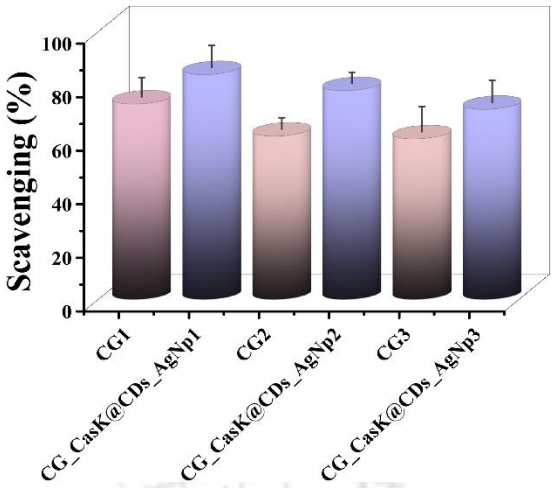

Figure 5.16. Percentage of radical scavenging by CG, and CG_CasK@CDs_AgNp hydrogel.

5.3.7. Biocompatibility and Cell Migration Assay of CG_CasK@CDs_AgNp Hydrogel

Biocompatibility of dressing material is essential for its application in medical settings. Previously, some reports described the toxicity generated by silver nanoparticles. However, in this case, silver nanoparticles have been added during the hydrogel synthesis. Therefore, carbon dot-capped silver nanoparticles can form covalent and non-covalent interactions with the polymeric chains, preventing the release of CasK@CDs_AgNPs in large quantities. Thus, an MTT assay was performed to investigate the effect of silver nanoparticles on HDF cells. The assay resulted in the excellent biocompatible nature of hydrogels. CG_CasK@CDs_AgNp3 hydrogel exhibited maximum cell viability in 1:10 and 1:20 of treatment (Figure 5.16b). Chitosan plays a vital role in wound healing by platelet adhesion and finally promotes the growth of granulation tissue.[231] Thus, the healing ability of the hydrogel was analyzed using a scratch assay at two different time intervals. Figure 5.17 shows that CG_CasK@CDs_AgNp3 exhibited better cell migration among the three sets. From the cell migration rate, it is clear that after 12 hours, the cell migration rate increases drastically (Figure 5.16c). MTT and cell migration data revealed that the hydrogel with a bigger pore size exhibited better cell viability and healing ability, supporting the previous results.

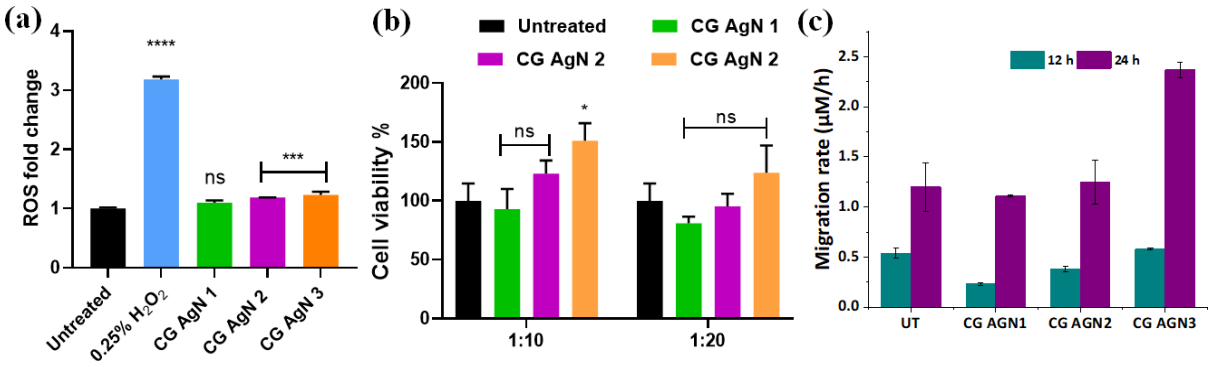

Figure 5.17. (a) Intracellular ROS scavenging ability of hydrogels without H_2O_2 (control group), with 300 µM H_2O_2 (H2O2 group), 300 µM H_2O_2+100 µL CG_CasK@CDs_AgNp1 hydrogel, 300 µM H_2O_2 + CG_CasK@CDs_AgNp2 hydrogel, and 300 µM H_2O_2 + 100 µL CG_CasK@CDs_AgNp3 hydrogel. (b) MTT assay for hydrogel-treated samples at different concentrations of hydrogel extract. (c) Cell migration rate of the HDF cell line after hydrogel treatment.

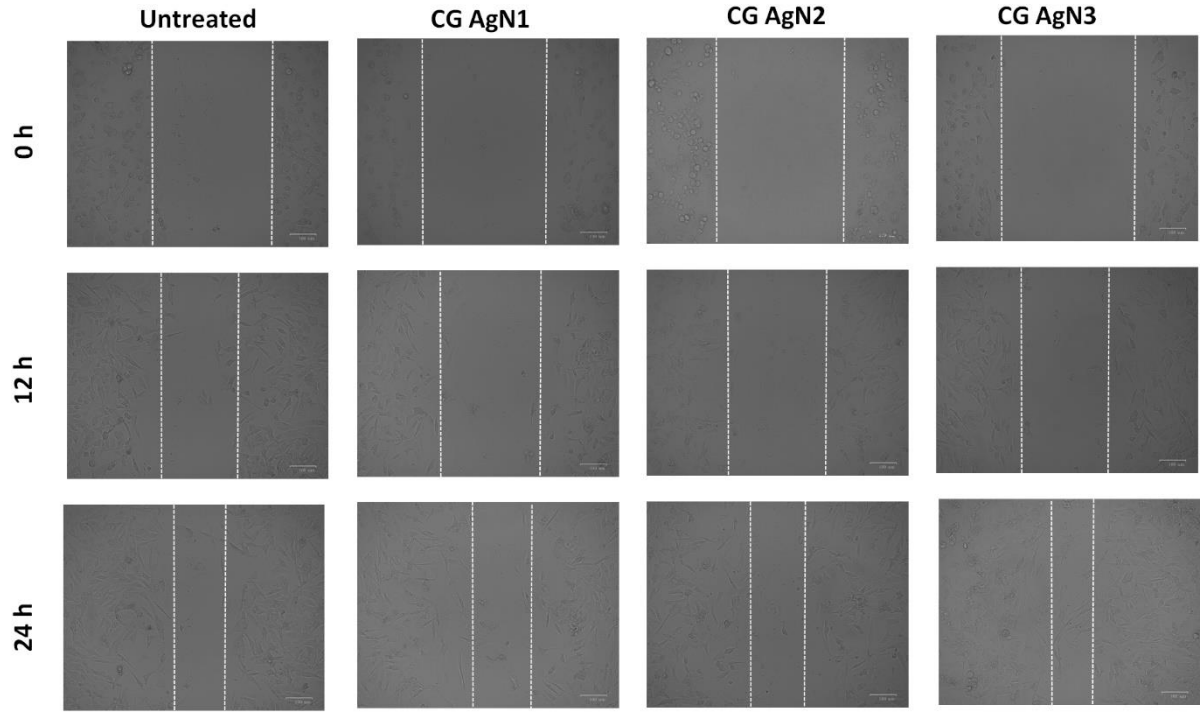

Figure 5.18. Microscopic image of wound scratch test at different time intervals.

5.3.8. Hemocompatibility and Clot Formation by CG_CasK@CDs_AgNp Hydrogel

The initiation of the healing process begins with blood clotting, which eventually transitions to clot dissolution as healing progresses. Blood clotting occurs in a concerted and well-orchestrated manner, starting with vasoconstriction, then platelet plug formation, coagulation cascade activation, clot retraction, and fibrinolysis. Given the critical role of clot formation in wound healing, this process was investigated using a hydrogel surface and cotton as a control. To evaluate clot formation, 100 µL of fresh blood was placed on the surface of the hydrogel and cotton. After 10 minutes, a visible color change from fresh red to dark red was observed on the hydrogel, indicating clot formation (Figure 5.18a-b). In contrast, the blood on the cotton retained its fresh red appearance, suggesting minimal or no clotting activity. FESEM analysis was performed to confirm clot formation further. The study provided detailed morphological evidence of fibrin networks and cellular components, validating the presence of a stable blood clot on the hydrogel surface. As shown in Figure 5.18c, the formation of fibrin and platelets is visible. The result complements the literature that chitosan induces blood clotting. [232] To assess the hemotoxicity of the CG_CasK@CDs_AgNp3 hydrogel, a hemolysis study was conducted. The hydrogel extract was diluted in a 1:10 and 1:20 ratio for the analysis. The result demonstrated non-significant red blood cell lysis (RBC), indicating good blood compatibility (Figure 5.18d).[233] The FESEM analysis of RBCs adhered to the hydrogel surface was analyzed, where no morphological changes were found (Figure 5.18e).

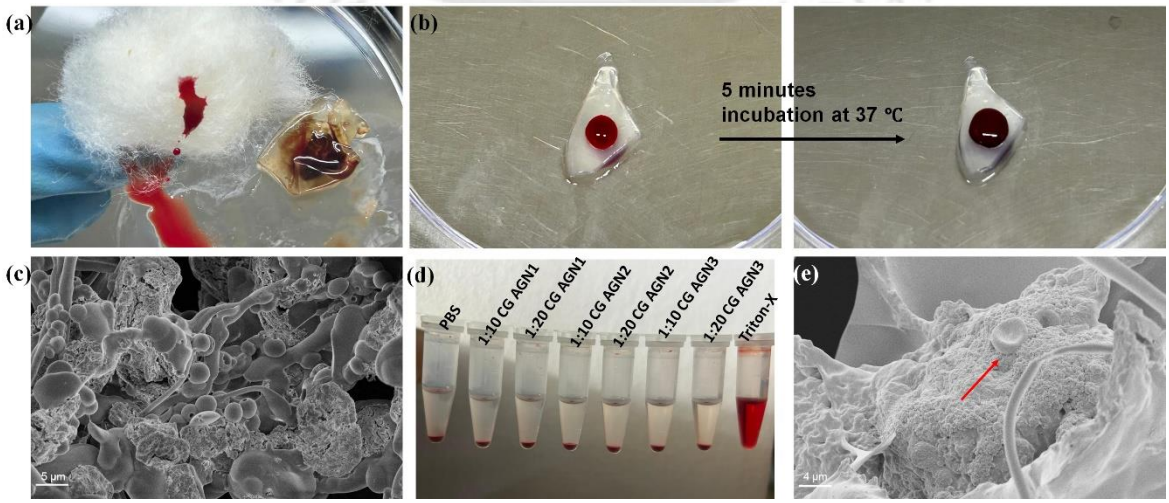

Figure 5.19. Hemocompatibility assay of CG_CasK@CDs_AgNp3 hydrogel. (a) Hemostatic efficiency of hydrogel (cotton has been used as a control). (b) The clot formation on the hydrogel. (c) FESEM image of a blood clot depicting the formation of fibrin. (d) The hemolysis experiment used Triton-X as a positive control and PBS as a negative control. (e) FESEM image of unaffected RBC after hydrogel treatment.

5.4. Conclusion

In summary, biogenic carbon dot-capped silver nanoparticles embedded in chitosan hydrogel have been fabricated and characterized in detail with numerous spectroscopic techniques. The nanoparticles and nanoparticle-embedded hydrogel have exhibited excellent bactericidal activity against *E. coli* and *S. aureus*. The bactericidal efficacy was evaluated by time-killing analysis, PI leveling, and FESEM. The biocompatibility and hemocompatibility of the hydrogel systems were examined through MTT and hemolysis assays. Interestingly, the hydrogel exhibited hemostatic properties. FESEM analysis revealed the formation of a clot and fibrin. The cell scratch assay demonstrates the wound healing ability of the CG_CasK@CDs_AgNp hydrogel, which was further established by the ROS generation assay. We hypothesize that these findings may aid in the development of novel multifunctional wound dressing and wound healing.

SUMMARY AND FUTURE ASPECTS

We have developed different biocompatible systems based on carbon dots, aligning with the current need to understand the sustainable route of developing biopolymer-based materials. These systems offer various desirable properties, including biocompatibility, cell penetrability, functionalization potential, and efficient drug-loading capacity, without compromising cost-effectiveness.

We have synthesized *kappa*-carrageenan and lysine-derived CDs that yielded good photoluminescence. The CDs were designed for the selective detection of folic acid in aqueous medium. Portable paper strips were prepared for the detection of folic acid. Further, biotin was conjugated to CDs for target-specific delivery of the antitumor drug 5-Fu. The delivery system exhibited better cellular uptake in cancer cell lines (HeLa and MDA-MB-231) than the healthy HEK-293 cell line. The hemolysis assay confirmed the hemocompatibility of biotin-conjugated cargo. Similarly, casein and thymine-derived CasT@CDs were prepared to monitor the presence of Hg^{+2} and tetracycline derivatives. The sensor can detect the contaminants in water with a very low LOD value. The effectiveness of the sensor was confirmed in different aqueous systems and biological fluids. Additionally, we have synthesized CDs-capped silver nanoparticles. The CDs were prepared from casein and *kappa*-carrageenan using pyrolysis. CasK@CDs were used as reducing and stabilizing agents for the synthesis of silver nanoparticles. The nanoparticles exhibited excellent antibacterial activity. The bactericidal activity was evaluated using the agar well diffusion method, and a time-killing assay was also performed. Further, we have prepared a chitosan-based hydrogel. Initially, the chitosan chain was modified using hydrocaffeic acid. The hydrogel was prepared with hydrocaffeic acid-modified chitosan and acrylic acid using a polymerization reaction. The hydrogel exhibited antibacterial activity. Previously prepared CasK@CDs-capped silver nanoparticles were incorporated in the hydrogel to enhance the antibacterial property. Additionally, the hydrogel

exhibited hemostatic properties, self-healing ability, biocompatibility, hemocompatibility, and wound healing properties. Overall, synthesized CDs and CDs-derived materials exhibited effective therapeutic efficiency, selective detection, and antibacterial and wound healing efficiency.

Future Prospects

In this thesis work, we have developed biopolymer derived CDs and CDs-derived materials, characterization and applications in different field. However, additional modifications and studied can be done to enhance their effectivity.

1. CDBTFu exhibited excellent selectivity towards cancer cells. Therefore, animal modeling can be done.
2. The chemosensor exhibited high selectivity towards analytes. The real sample analysis also resulted good recovery of sample. The effectivity of the chemo sensors can be studied in waste water, such as industrial effluent, hospital effluent, etc.
3. Stability of CDs-capped silver nanoparticles in saline water and different pH solution can be studied. MTT assay of nanoparticles can be assessed both in healthy and cancer cells.
4. The antibacterial hydrogel exhibited multifunctional properties. the hemostatic behavior pf the hydrogel can be studied in detail. Moreover, animal modeling of hydrogel can be done.

BIBLIOGRAPHY

(1) Velnar, T.; Bailey, T.; Smrkolj, V. The Wound Healing Process: An Overview of the Cellular and Molecular Mechanisms. *J. Int. Med. Res.* **2009**, *37*, 1528–1542.

(2) Xie, M.; Zhao, J.; Feng, X.; Gao, X.; Cheng, W.; Kong, L.; Liang, F. Cell Membrane-Inspired Chitosan Nanoparticles for Prolonged Circulation and Tumor-Targeted Drug Delivery. *Int. J. Biol. Macromol.* **2025**, *304*, 140934.

(3) Jaradat, A.; Alazzo, A.; Bayan, M. F.; Obeidat, W. A Green, Solvent- and Cation-Free Approach for Preparing 5-Fluorouracil-Loaded Alginate Nanoparticles Using Microfluidic Technology. *Pharmaceutics* **2025**, *17*, 1–31.

(4) Zhang, B.; Deng, Y.; Xu, D.; Zhao, X. Dimethylcurcumin and Copper Sulfate-Loaded Silk Nanoparticles for Synergistic Therapy against Breast Cancer. *ACS Biomater. Sci. Eng.* **2025**, *11*, 1539–1548.

(5) Kučuk, N.; Primožič, M.; Knez, Ž.; Leitgeb, M. Sustainable Biodegradable Biopolymer-Based Nanoparticles for Healthcare Applications. *Int. J. Mol. Sci.* **2023**, *24*, 3188. https://doi.org/10.3390/ijms24043188.

(6) Horo, H.; Saha, M.; Das, H.; Mandal, B.; Kundu, L. M. Synthesis of Highly Fluorescent, Amine-Functionalized Carbon Dots from Biotin-Modified Chitosan and Silk-Fibroin Blend for Target-Specific Delivery of Antitumor Agents. *Carbohydr. Polym.* **2022**, *277*, 118862.

(7) Liang, D.; Lu, Z.; Yang, H.; Gao, J.; Chen, R. Novel Asymmetric Wettable AgNPs/Chitosan Wound Dressing: In Vitro and In Vivo Evaluation. *ACS Appl. Mater. Interfaces 2016,* **2016**, *8*, 3958−3968.

(8) Umar, M.; Khan, A.; Mehboob, H.; Izwan, S.; Razak, A.; Anand, T. J. S.; Hassan, R.; Aziz, A.; Amin, R. Development of Polymeric Nanocomposite (Xyloglucan-Co-

Methacrylic Acid/Hydroxyapatite/SiO2) Scaffold for Bone Tissue Engineering Applications—In-Vitro Antibacterial, Cytotoxicity and Cell Culture Evaluation. *Polymers (Basel)*. **2020**, *12*, 1238.

(9) Ramakrishnan, P.; Ramprasath, R.; Mohamed, A. Electrospun Nanofibers of Collagen and Chitosan for Tissue Engineering and Drug Delivery Applications : A Review. *Int. J. Biol. Macromol.* **2025**, *296*, 139663.

(10) Ahmed, M. A.; Abdelbar, N. M.; Mohamed, A. A. Molecular Imprinted Chitosan-TiO2 Nanocomposite for the Selective Removal of Rose Bengal from Wastewater. *Int. J. Biol. Macromol.* **2018**, *107*, 1046–1053.

(11) Saraf, P.; Abdollahi Movaghar, M.; Montazer, M.; Mahmoudi Rad, M. Bio and Photoactive Starch/MnO2 and Starch/MnO2/Cotton Hydrogel Nanocomposite. *Int. J. Biol. Macromol.* **2021**, *193*, 681–692.

(12) Mohammadi, S.; Sandoval-Pauker, C.; Dorado, Z. N.; Senftle, T. P.; Pankow, R.; Sharifan, H. Fluorescent Sodium Alginate Hydrogel-Carbon Dots Sensor for Detecting Perfluorooctanoic Acid in Potable Water. *Anal. Chem.* **2025**, *97*, 10075–10084.

(13) Xu, X.; Ray, R.; Gu, Y.; Ploehn, H. J.; Gearheart, L.; Raker, K.; Scrivens, W. A. Electrophoretic Analysis and Purification of Fluorescent Single-Walled Carbon Nanotube Fragments. *J. Am. Chem. Soc.* **2004**, *126*, 12736–12737.

(14) Gozali Balkanloo, P.; Mohammad Sharifi, K.; Poursattar Marjani, A. Graphene Quantum Dots: Synthesis, Characterization, and Application in Wastewater Treatment: A Review. *Mater. Adv.* **2023**, *4*, 4272–4293.

(15) Hsu, P. C.; Shih, Z. Y.; Lee, C. H.; Chang, H. T. Synthesis and Analytical Applications of Photoluminescent Carbon Nanodots. *Green Chem.* **2012**, *14*, 917–920.

(16) Yu, Y.; Tang, P.; Barnych, B.; Zhao, C.; Sun, G.; Ge, M. Design and Synthesis of Core-

Shell Carbon Polymer Dots with Highly Stable Fluorescence in Polymeric Materials. *ACS Appl. Nano Mater.* **2019**, *2*, 6503–6512.

(17) Sun, H.; Wu, L.; Wei, W.; Qu, X. Recent Advances in Graphene Quantum Dots for Sensing. *Mater. Today* **2013**, *16*, 433–442.

(18) Shen, J.; Zhu, Y.; Yang, X.; Li, C. Graphene Quantum Dots: Emergent Nanolights for Bioimaging, Sensors, Catalysis and Photovoltaic Devices. *Chem. Commun.* **2012**, *48*, 3686–3699.

(19) Yang, Z. C.; Wang, M.; Yong, A. M.; Wong, S. Y.; Zhang, X. H.; Tan, H.; Chang, A. Y.; Li, X.; Wang, J. Intrinsically Fluorescent Carbon Dots with Tunable Emission Derived from Hydrothermal Treatment of Glucose in the Presence of Monopotassium Phosphate. *Chem. Commun.* **2011**, *47*, 11615–11617.

(20) Wang, X.; Cao, L.; Yang, S.; Lu, F.; Meziani, M. J.; Tian, L.; Sun, K. W.; Bloodgood, M. A.; Sun, Y. Bandgap-Like Strong Fluorescence in Functionalized Carbon Nanoparticles. *Angew Chem Int Ed.* **2012**, *49*, 5310–5314.

(21) Shamsipur, M.; Barati, A.; Taherpour, A. A.; Jamshidi, M. Resolving the Multiple Emission Centers in Carbon Dots: From Fluorophore Molecular States to Aromatic Domain States and Carbon-Core States. *J. Phys. Chem. Lett.* **2018**, *9*, 4189–4198.

(22) Ding, H.; Yu, S. B.; Wei, J. S.; Xiong, H. M. Full-Color Light-Emitting Carbon Dots with a Surface-State-Controlled Luminescence Mechanism. *ACS Nano* **2016**, *10* (1), 484–491.

(23) Wang, J. Synthesis of Highly Stable Red-Emissive Carbon Polymer Dots by Modulated Polymerization : From the Mechanism to Application in Intracellular PH Imaging †. *Nanoscale* **2018**, *10*, 22484–22492.

(24) Zhu, S.; Wang, L.; Zhou, N.; Zhao, X.; Song, Y.; Maharjan, S.; Zhang, J.; Lu, L.; Wang,

H.; Yang, B. The Crosslink Enhanced Emission (CEE) in Non-Conjugated Polymer Dots : From the Photoluminescence Mechanism to the Cellular Uptake Mechanism and Internalization †. *Chem. Commun.* **2014**, *1*, 13845–13848.

(25) Zhou, Y.; Sharma, S. K.; Peng, Z.; Leblanc, R. M. Polymers in Carbon Dots : A Review. *Polymers (Basel).* **2017**, *9*, 67.

(26) Mintz, K. J.; Bartoli, M.; Rovere, M.; Zhou, Y.; Hettiarachchi, S. D.; Paudyal, S.; Chen, J.; Domena, J. B.; Liyanage, P. Y.; Sampson, R.; Khadka, D.; Pandey, R. R.; Huang, S.; Chusuei, C. C.; Tagliaferro, A.; Leblanc, R. M. A Deep Investigation into the Structure of Carbon Dots. *Carbon N. Y.* **2021**, *173*, 433–447.

(27) Raty, J.; Galli, G.; Bostedt, C.; Buuren, T. W. Van; Terminello, L. J. Quantum Confinement and Fullerenelike Surface Reconstructions in Nanodiamonds. *PhysRevLett.* **2003**, *90*, 1–4.

(28) Yan, D.; Li, Y.; Huo, J.; Chen, R.; Dai, L.; Wang, S. Defect Chemistry of Nonprecious-Metal Electrocatalysts for Oxygen Reactions. *Adv. Mater.* **2017**, *29*, 1606459.

(29) Yoon, H.; Chang, Y. H.; Song, S. H.; Lee, E.; Jin, S. H.; Park, C.; Lee, J.; Kim, B. H.; Kang, H. J.; Kim, Y. Intrinsic Photoluminescence Emission from Subdomained Graphene Quantum Dots. *Adv. Mater. 2016*, **2016**, *28*, 5255–5261.

(30) Luo, Z.; Lu, Y.; Somers, L. A.; Johnson, A. T. C. High Yield Preparation of Macroscopic Graphene Oxide Membranes. *J. AM. CHEM. SOC. 2009*, **2009**, *131*, 898–899.

(31) Fu, M.; Ehrat, F.; Wang, Y.; Milowska, K. Z.; Reckmeier, C.; Rogach, A. L.; Stolarczyk, J. K.; Urban, A. S.; Feldmann, J. Carbon Dots: A Unique Fluorescent Cocktail of Polycyclic Aromatic Hydrocarbons. *Nano Lett.* **2015**, *15*, 6030−6035.

(32) Yang, B.; Zhu, S.; Song, Y.; Shao, J.; Zhao, X.; Yang, B. Non-Conjugated Polymer Dots with Crosslink- Enhanced Emission in the Absence of Fluorophore Units.

Angew.Chem.Int. Ed. **2015**, *54*, 14626–14637.

(33) Do, S.; Kwon, W.; Kim, Y. H.; Kang, S. R.; Lee, T.; Lee, T. W.; Rhee, S. W. N,S-Induced Electronic States of Carbon Nanodots Toward White Electroluminescence. *Adv. Opt. Mater.* **2016**, *4*, 276–284.

(34) Zhao, Y.; He, B.; Liu, E.; Li, J.; Wang, L.; Chen, S.; Chen, Y.; Tan, Z.; Ng, K. W.; Wang, S.; Tang, Z.; Qu, S. Aluminum-Based Surface Polymerization on Carbon Dots with Aggregation-Enhanced Luminescence. *J. Phys. Chem. Lett.* **2021**, *12*, 4530–4536.

(35) Cao, L.; Wang, X.; Meziani, M. J.; Lu, F.; Wang, H.; Luo, P. G.; Lin, Y.; Harruff, B. A.; Veca, L. M.; Murray, D.; Xie, S. Y.; Sun, Y. P. Carbon Dots for Multiphoton Bioimaging. *J. Am. Chem. Soc.* **2007**, *129*, 11318–11319.

(36) Efremushkin, L.; Bhunia, S. K.; Jelinek, R.; Salomon, A. Carbon Dots-Plasmonics Coupling Enables Energy Transfer and Provides Unique Chemical Signatures. *J. Phys. Chem. Lett.* **2017**, *8*, 6080–6085.

(37) Jiang, K.; Wang, Y.; Cai, C.; Lin, H. Conversion of Carbon Dots from Fluorescence to Ultralong Room-Temperature Phosphorescence by Heating for Security Applications. *Adv. Mater.* **2018**, *30*, 1–8.

(38) Yuan, C.; Yang, C.; Chou, W.; Shen, J. P - Type Doping of WS 2 Quantum Dots via Pulsed Laser Ablation. *ACS Photonics 2018,* **2018**, *5*, 4828−4837.

(39) Wang, C.; Wu, W.; Periasamy, A. P.; Chang, H. Electrochemical Synthesis of Photoluminescent Carbon Nanodots from Glycine for Highly Sensitive Detection of Hemoglobin †. *Green Chem.* **2014**, *16*, 2509–2514.

(40) Liu, R.; Wu, D.; Liu, S.; Koynov, K.; Knoll, W.; Li, Q. An Aqueous Route to Multicolor Photoluminescent Carbon Dots Using Silica Spheres as Carriers **. *Angew. Chem. Int. Ed. 2009,* **2009**, *48*, 4598–4601.

(41) Prathap, N.; Balla, P.; Shivakumar, M. S.; Periyasami, G.; Karuppiah, P.; Ramasamy, K.; Venkatesan, S. Prosopis Juliflora Hydrothermal Synthesis of High Fluorescent Carbon Dots and Its Antibacterial and Bioimaging Applications. *Sci. Rep.* **2023**, *13*, 9676.

(42) Li, H.; He, X.; Liu, Y.; Yu, H.; Kang, Z.; Lee, S. Synthesis of Fluorescent Carbon Nanoparticles Directly from Active Carbon via a One-Step Ultrasonic Treatment. *Mater. Res. Bull.* **2011**, *46*, 147–151.

(43) Naik, V.; Zantye, P.; Gunjal, D.; Gore, A.; Anbhule, P.; Kowshik, M.; Bhosale, S. V; Kolekar, G. Nitrogen-Doped Carbon Dots via Hydrothermal Synthesis : Naked Eye Fluorescent Sensor for Dopamine and Used for Multicolor Cell Imaging. *ACS Appl. Bio Mater. 2019,* **2019**, *2*, 2069−2077.

(44) Xu, Q.; Pu, P.; Zhao, J.; Dong, C.; Gao, C.; Chen, Y. Preparation of Highly Photoluminescent Sulfur- Doped Carbon Dots for Fe (III) Detection †. *J. Mater. Chem. A* **2015**, *3*, 542–546.

(45) Yang, L.; Liu, S.; Quan, T.; Tao, Y.; Tian, M.; Wang, L.; Wang, J.; Wang, D. Sulfuric-Acid-Mediated Synthesis Strategy for Multi-Colour Aggregation- Induced Emission Fluorescent Carbon Dots : Application in Anti- Counterfeiting , Information Encryption , and Rapid Cytoplasmic Imaging. *J. Colloid Interface Sci.* **2022**, *612*, 650–663.

(46) Wang, M.; Li, Y.; Fang, J.; Villa, C. J.; Xu, Y.; Hao, S.; Li, J.; Liu, Y.; Wolverton, C.; Chen, X.; Dravid, V. P.; Lai, Y. Superior Oxygen Reduction Reaction on Phosphorus-Doped Carbon Dot / Graphene Aerogel for All-Solid-State Flexible Al – Air Batteries. *Adv. Energy Mater. 2020,* **2020**, *10*, 1902736.

(47) Zhu, S.; Meng, Q.; Wang, L.; Zhang, J.; Song, Y.; Jin, H.; Zhang, K.; Sun, H.; Wang, H.; Yang, B. Highly Photoluminescent Carbon Dots for Multicolor Patterning, Sensors,

and Bioimaging. *Angew. Chemie - Int. Ed.* **2013**, *52*, 3953–3957.

(48) Miao, X.; Qu, D.; Yang, D.; Nie, B.; Zhao, Y.; Fan, H.; Sun, Z. Synthesis of Carbon Dots with Multiple Color Emission by Controlled Graphitization and Surface Functionalization. *Adv. Mater.* **2018**, *30*, 1704740.

(49) Lu, S.; Cong, R.; Zhu, S.; Zhao, X.; Liu, J.; S.tse, J.; Meng, S.; Yang, B. PH-Dependent Synthesis of Novel Structure-Controllable Polymer-Carbon NanoDots with High Acidophilic Luminescence and Super Carbon Dots Assembly for White Light-Emitting Diodes. *ACS Appl. Mater. Interfaces* **2016**, *8*, 4062–4068.

(50) Farasati Far, B.; Omrani, M.; Naimi Jamal, M. R.; Javanshir, S. Multi-Responsive Chitosan-Based Hydrogels for Controlled Release of Vincristine. *Commun. Chem.* **2023**, *6*, 1–14.

(51) Ghosh, R.; Mondal, S.; Mukherjee, D.; Adhikari, A.; Ahmed, S. A.; Alsantali, R. I.; Khder, A. S.; Altass, H. M.; Moussa, Z.; Das, R.; Bhattacharyya, M.; Pal, S. K. Oral Drug Delivery Using a Polymeric Nanocarrier: Chitosan Nanoparticles in the Delivery of Rifampicin. *Mater. Adv.* **2022**, *3*, 4622–4628.

(52) Horo, H.; Bhattacharyya, S.; Mandal, B.; Kundu, L. M. Synthesis of Functionalized Silk-Coated Chitosan-Gold Nanoparticles and Microparticles for Target-Directed Delivery of Antitumor Agents. *Carbohydr. Polym.* **2021**, *258*, 117659.

(53) Cui, C.; Sun, S.; Wu, S.; Chen, S.; Ma, J.; Zhou, F. Electrospun Chitosan Nanofibers for Wound Healing Application. *Eng. Regen.* **2021**, *2*, 82–90.

(54) Frank, L. A.; Onzi, G. R.; Morawski, A. S.; Pohlmann, A. R.; Guterres, S. S.; Contri, R. V. Chitosan as a Coating Material for Nanoparticles Intended for Biomedical Applications. *React. Funct. Polym.* **2020**, *147*, 104459.

(55) Zhang, C.; Cheng, Y.; Qu, G.; Wu, X.; Ding, Y.; Cheng, Z. Preparation and

Characterization of Galactosylated Chitosan Coated BSA Microspheres Containing 5-Fluorouracil. *Carbohydr. Polym.* **2008**, *72*, 390–397.

(56) Campo, V. L.; Kawano, D. F.; Silva, D. B. da; Carvalho, I. Carrageenans: Biological Properties, Chemical Modifications and Structural Analysis. *Carbohydr. Polym.* **2009**, *77*, 167–180.

(57) Salgueiro, A. M.; Daniel-Da-Silva, A. L.; Fateixa, S.; Trindade, T. κ-Carrageenan Hydrogel Nanocomposites with Release Behavior Mediated by Morphological Distinct Au Nanofillers. *Carbohydr. Polym.* **2013**, *91*, 100–109.

(58) Basto, R.; Fernandes, A.; Silva, J.; Alves, C.; Zo, A.; Pinteus, S.; Ariévilo, J.; Rodrigues, G.; Maria, E.; Cordeiro, S.; Rafael, R.; Almeida, D.; Pedrosa, R.; Maria, N.; Benevides, B. In Vitro Activities of Kappa -Carrageenan Isolated from Red Marine Alga Hypnea Musciformis : Antimicrobial , Anticancer and Neuroprotective Potential. *Int. J. ofBiological Macromol.* **2018**, *112*, 1248–1256.

(59) Frias, A. M.; Carida, M.; Cancedda, R.; Gomes, M. E.; Mano, F.; Reis, R. L. Carrageenan-Based Hydrogels for the Controlled Delivery of PDGF-BB in Bone Tissue Engineering Applications. *Biomacromolecules* **2009**, *10*, 1392–1401.

(60) Bakry, A. M.; Huang, J.; Zhai, Y.; Huang, Q. Myo Fi Brillar Protein with κ - or λ - Carrageenans as Novel Shell Materials for Microencapsulation of Tuna Oil through Complex Coacervation. *Food Hydrocoll.* **2019**, *96*, 43–53.

(61) Wijesekara, I.; Pangestuti, R.; Kim, S. Biological Activities and Potential Health Benefits of Sulfated Polysaccharides Derived from Marine Algae. *Carbohydr. Polym.* **2011**, *84*, 14–21.

(62) Sudharsan, S.; Subhapradha, N.; Seedevi, P. Antioxidant and Anticoagulant Activity of Sulfated Polysaccharide from Gracilaria Debilis (Forsskal). *Int. J. Biol. Macromol.*

2015, *81*, 1031–1038.

(63) Cristiane, M.; Souza, R. De; Marques, C. T.; Maria, C.; Dore, G.; Roberto, F.; Alexandre, H.; Rocha, O.; Leite, E. L. Antioxidant Activities of Sulfated Polysaccharides from Brown and Red Seaweeds. *J Appl Phycol* **2007**, *19*, 153–160.

(64) Diak, O. A.; Amro, B.; Jones, D.; Andrews, G. P. THE MANUFACTURE AND CHARACTERIZATION OF CASEIN FILMS AS NOVEL TABLET COATINGS. *Food Bioprod. Process.* **2000**, *85*, 284–290.

(65) Huang, J.; Wang, L.; Lin, R.; Wang, A. Y.; Yang, L.; Kuang, M.; Qian, W. Casein-Coated Iron Oxide Nanoparticles for High MRI Contrast Enhancement and E Ffi Cient Cell Targeting. *ACS Appl. Mater. Interfaces 2013,* **2013**, *5*, 4632−4639.

(66) Picchio, M. L.; Linck, Y. G.; Monti, G. A.; Gugliotta, L. M.; Minari, R. J.; Alvarez, C. I. Casein Films Crosslinked by Tannic Acid for Food Packaging Applications. *Food Hydrocoll.* **2018**, *84*, 424–434.

(67) Elzoghby, A. O.; El-fotoh, W. S. A.; Elgindy, N. A. Casein-Based Formulations as Promising Controlled Release Drug Delivery Systems. *J. Control. Release* **2011**, *153*, 206–216.

(68) Liu, J.; Liu, X.; Luo, H.; Gao, Y. One-Step Preparation of Nitrogen-Doped and Surface-Passivated Carbon Quantum Dots with High Quantum Yield and Excellent Optical Properties. *RSC Adv.* **2014**, *4*, 7648–7654.

(69) Goh, E. J.; Kim, K. S.; Kim, Y. R.; Jung, H. S.; Beack, S.; Kong, W. H.; Scarcelli, G.; Yun, S. H.; Hahn, S. K. Bioimaging of Hyaluronic Acid Derivatives Using Nanosized Carbon Dots. *Biomacromolecules* **2012**, *13*, 2554–2561.

(70) Li, W.; Zhou, W.; Zhou, Z.; Zhang, H.; Zhang, X.; Zhuang, J.; Liu, Y.; Lei, B.; Hu, C. Phosphorescence A Universal Strategy for Activating the Multicolor Room-

Temperature Afterglow of Carbon Dots in a Boric Acid Matrix Angewandte. *Angew.Chem. Int. Ed.* **2019**, *58*, 7278–7283.

(71) Gao, P.; Liu, S.; Su, Y.; Zheng, M.; Xie, Z. Fluorine-Doped Carbon Dots with Intrinsic Nucleus-Targeting Ability for Drug and Dye Delivery. *Bioconjugate Chem. 2020,* **2020**, *31*, 646−655.

(72) Lin, C.; Chang, L.; Chu, H.; Lin, H.; Chang, P.; Wang, R. Y. L.; Unnikrishnan, B.; Mao, J.; Chen, S. High Amplification of the Antiviral Activity of Curcumin through Transformation into Carbon Quantum Dots. *Small* **2019**, *1902641*, 1–14.

(73) Zhao, S.; Wu, S.; Jia, Q.; Huang, L.; Lan, M.; Wang, P. Lysosome-Targetable Carbon Dots for Highly Efficient Photothermal / Photodynamic Synergistic Cancer Therapy and Photoacoustic / Two-Photon Excited Fluorescence Imaging. *Chem. Eng. J.* **2020**, *388*, 124212.

(74) Travlou, N. A.; Giannakoudakis, D. A.; Algarra, M.; Labella, A. M.; Rodríguez-castell, E. S- and N-Doped Carbon Quantum Dots : Surface Chemistry Dependent Antibacterial Activity. *Carbon N. Y.* **2018**, *135*, 104–111.

(75) Cui, X.; Zhu, L.; Wu, J.; Hou, Y.; Wang, P.; Wang, Z.; Yang, M. Biosensors and Bioelectronics A Fl Uorescent Biosensor Based on Carbon Dots-Labeled Oligodeoxyribonucleotide and Graphene Oxide for Mercury (II) Detection. *Biosens. Bioelectron.* **2015**, *63*, 506–512.

(76) Kong, B.; Zhu, A.; Ding, C.; Zhao, X.; Li, B.; Tian, Y. Carbon Dot-Based Inorganic – Organic Nanosystem for Two-Photon Imaging and Biosensing of PH Variation in Living Cells and Tissues. *Adv. Mater. 2012,* **2012**, *24*, 5844–5848.

(77) Liu, Y.; Duan, W.; Song, W.; Liu, J.; Ren, C.; Wu, J.; Liu, D.; Chen, H. Red Emission B , N , S- Co -Doped Carbon Dots for Colorimetric and Fluorescent Dual Mode

Detection of Fe 3 + Ions in Complex Biological Fluids and Living Cells. *ACS Appl. Mater. Interfaces* **2017**, *9*, 12663−12672.

(78) Liu, F.; Zhang, W.; Chen, W.; Wang, J.; Yang, Q.; Zhu, W.; Wang, J. One-Pot Synthesis of NiFe 2 O 4 Integrated with EDTA-Derived Carbon Dots for Enhanced Removal of Tetracycline. *Chem. Eng. J.* **2017**, *310*, 187–196.

(79) Activity, P.; Hu, S.; Tian, R.; Wu, L.; Zhao, Q.; Yang, J. Chemical Regulation of Carbon Quantum Dots from Synthesis to Photocatalytic Activity. *Chem. Asian J. 2013,* **2013**, *8*, 1035–1041.

(80) Ke, J.; Li, X.; Zhao, Q.; Liu, B.; Liu, S.; Wang, S. Upconversion Carbon Quantum Dots as Visible Light Responsive Component for Efficient Enhancement of Photocatalytic Performance. *J. Colloid Interface Sci.* **2017**, *496*, 425–433.

(81) Diao, S.; Zhang, X.; Shao, Z.; Ding, K.; Jie, J.; Zhang, X. 12.35% Efficient Graphene Quantum Dots/Silicon Heterojunction Solar Cells Using Graphene Transparent Electrode. *Nano Energy* **2017**, *31*, 359–366.

(82) Wei, J.; Ding, C.; Zhang, P.; Ding, H.; Niu, X.; Ma, Y.; Li, C.; Wang, Y.; Xiong, H. Robust Negative Electrode Materials Derived from Carbon Dots and Porous Hydrogels for High-Performance Hybrid Supercapacitors. *Adv. Mater. 2019,* **2019**, *31*, 1806197.

(83) Hu, Y.; Chen, W.; Lei, T.; Zhou, B.; Jiao, Y.; Yan, Y.; Du, X.; Wu, C.; Wang, X.; Wang, Y.; Chen, B.; Xu, J.; Wang, C. Carbon Quantum Dots – Modified Interfacial Interactions and Ion Conductivity for Enhanced High Current Density Performance in Lithium – Sulfur Batteries. *Adv. Energy Mater. 2019,* **2019**, *9*, 1802955.

(84) Green, N. S. Folic Acid Supplementation and Prevention of Birth Defects. *J. Nutr.* **2002**, *132*, 2356S-2360S.

(85) Mahmood, L. The Metabolic Processes of Folic Acid and Vitamin B12 Deficiency. *J.*

Heal. Res. Rev. **2014**, *1* (1), 5.

(86) Jha, R.; Jha, S. Beta Thalassemia. *J. Pathol. Nepal* **2014**, *4*, 663–671.

(87) Stover, P. J. One-Carbon Metabolism-Genome Interactions in Folate-Associated Pathologies. *J. Nutr.* **2009**, *139*, 2402–2405.

(88) Black, R. E.; Allen, L. H.; Bhutta, Z. A.; Caulfield, L. E.; de Onis, M.; Ezzati, M.; Mathers, C.; Rivera, J. Maternal and Child Undernutrition: Global and Regional Exposures and Health Consequences. *Lancet* **2008**, *371*, 243–260.

(89) Bailey, R. L.; West, K. P.; Black, R. E. The Epidemiology of Global Micronutrient Deficiencies. *Ann. Nutr. Metab.* **2015**, *66*, 22–33.

(90) Reynolds, E. H. Benefits and Risks of Folic Acid to the Nervous System. *J. Neurol. Neurosurg. Psychiatry* **2002**, *72*, 567–571.

(91) Duthie, S. J. Folate and Cancer : How DNA Damage , Repair and Methylation Impact on Colon Carcinogenesis. *J Inherit Metab Dis* **2011**, 101–109.

(92) Chen, P.; Li, C.; Li, X.; Li, J.; Chu, R.; Wang, H. Higher Dietary Folate Intake Reduces the Breast Cancer Risk: A Systematic Review and Meta-Analysis. *Br. J. Cancer* **2014**, *110*, 2327–2338.

(93) Wen, Q. L.; Pu, Z. F.; Yang, Y. J.; Wang, J.; Wu, B. C.; Hu, Y. L.; Liu, P.; Ling, J.; Cao, Q. Hyaluronic Acid as a Material for the Synthesis of Fluorescent Carbon Dots and Its Application for Selective Detection of Fe3+ Ion and Folic Acid. *Microchem. J.* **2020**, *159* (May). https://doi.org/10.1016/j.microc.2020.105364.

(94) Mu, Z.; Hua, J.; Yang, Y. N, S, I Co-Doped Carbon Dots for Folic Acid and Temperature Sensing and Applied to Cellular Imaging. *Spectrochim. Acta - Part A Mol. Biomol. Spectrosc.* **2020**, *224*, 117444.

(95) Chen, S.; Zhao, X.; Chen, J.; Chen, J.; Kuznetsova, L.; Wong, S. S.; Ojima, I. Mechanism-Based Tumor-Targeting Drug Delivery System. Validation of Efficient Vitamin Receptor-Mediated Endocytosis and Drug Release. *Bioconjug. Chem.* **2010**, *21*, 979–987.

(96) Rong, M.; Feng, Y.; Wang, Y.; Chen, X. One-Pot Solid Phase Pyrolysis Synthesis of Nitrogen-Doped Carbon Dots for Fe3+ Sensing and Bioimaging. *Sensors Actuators, B Chem.* **2017**, *245*, 868.

(97) Gu, S.; Hsieh, C.; Gandomi, Y. A.; Li, J.; Yue, X. X.; Chang, J. Tailoring Fluorescence Emissions, Quantum Yields, and White Light Emitting from Nitrogen-Doped Graphene and Carbon Nitride Quantum Dots. *Nanoscale* **2019**, *11*, 16553–16561.

(98) Bao, L.; Zhang, Z. L.; Tian, Z. Q.; Zhang, L.; Liu, C.; Lin, Y.; Qi, B.; Pang, D. W. Electrochemical Tuning of Luminescent Carbon Nanodots: From Preparation to Luminescence Mechanism. *Adv. Mater.* **2011**, *23*, 5801–5806. https://doi.org/10.1002/adma.201102866.

(99) Baker, S. N.; Baker, G. A. Luminescent Carbon Nanodots: Emergent Nanolights. *Angew. Chemie - Int. Ed.* **2010**, *49*, 6726–6744. https://doi.org/10.1002/anie.200906623.

(100) Ding, H.; Li, X. H.; Chen, X. B.; Wei, J. S.; Li, X. B.; Xiong, H. M. Surface States of Carbon Dots and Their Influences on Luminescence. *J. Appl. Phys.* **2020**, *127*, 231101.

(101) Wang, Y.; Liu, Y.; Zhao, L.; Sun, L.; Zhao, X.; Xia, Y. κ-Carrageenan-Derived Carbon Dots for Highly Selective and Sensitive Detection of Fe3+ and Oxytetracycline. *J. Mater. Sci.* **2021**, *56*, 1272–1285.

(102) Mu, Z.; Hua, J.; Yang, Y. N, S, I Co-Doped Carbon Dots for Folic Acid and Temperature Sensing and Applied to Cellular Imaging. *Spectrochim. Acta - Part A Mol. Biomol. Spectrosc.* **2020**, *224*.

(103) Wang, W.; Peng, J.; Li, F.; Su, B.; Chen, X.; Chen, X. Phosphorus and Chlorine Co-Doped Carbon Dots with Strong Photoluminescence as a Fluorescent Probe for Ferric Ions. *Microchim. Acta* **2019**, *186*, 32.

(104) Wen, Q. L.; Pu, Z. F.; Yang, Y. J.; Wang, J.; Wu, B. C.; Hu, Y. L.; Liu, P.; Ling, J.; Cao, Q. Hyaluronic Acid as a Material for the Synthesis of Fluorescent Carbon Dots and Its Application for Selective Detection of Fe3+ Ion and Folic Acid. *Microchem. J.* **2020**, *159*, 105364.

(105) Li, W.; Zhang, X.; Miao, C.; Li, R.; Ji, Y. Fluorescent Paper – Based Sensor Based on Carbon Dots for Detection of Folic Acid. *Anal. Bioanal. Chem.* **2020**, *412*, 2805.

(106) Qian, J.; Quan, F.; Zhao, F.; Wu, C.; Wang, Z.; Zhou, L. Chemical Aconitic Acid Derived Carbon Dots : Conjugated Interaction for the Detection of Folic Acid and Fluorescence Targeted Imaging of Folate Receptor Overexpressed Cancer Cells. *Sensors Actuators B* **2018**, *262*, 444.

(107) Kayani, K. F.; Omer, K. M. A Red Luminescent Europium Metal Organic Framework (Eu-MOF) Integrated with a Paper Strip Using Smartphone Visual Detection for Determination of Folic Acid in Pharmaceutical. *New J. Chem.* **2022**, *46*, 8152–8161.

(108) Vegad, Y.; Vardhan, S.; Ghosh, A. K.; Jali, B. R.; Sahoo, S. K. Folic Acid Detection Using β-Cyclodextrin-Functionalized Copper Nanoclusters and Vitamin B 6 Cofactor Pyridoxal. *ACS Appli.Nano Mater.* **2024**, *7*, 4173.

(109) Zhang, D.; Ouyang, X.; Ma, W.; Li, L.; Zhang, Y. Voltammetric Determination of Folic Acid Using Adsorption of Methylene Blue onto Electrodeposited of Reduced Graphene Oxide Film Modified Glassy Carbon Electrode. *Electroanalysis* **2016**, *28*, 312–319.

(110) Li, X.; Chen, L. Fluorescence Probe Based on an Amino-Functionalized Fluorescent Magnetic Nanocomposite for Detection of Folic Acid in Serum. *ACS Appl. Mater.*

Interfaces **2016**, *8*, 31832–31840.

(111) Li, H.; Su, C.; Liu, N.; Lv, T.; Yang, C.; Lu, Q.; Sun, C.; Yan, X. Carbon Dot-Anchored Cobalt Oxyhydroxide Composite-Based Hydrogel Sensor for On-Site Monitoring of Organophosphorus Pesticides. *ACS Appl. Mater. Interfaces* **2022**, *14*, 53340–53347.

(112) Mukherjee, S.; Ghosh, S.; Biswas, S. A MOF Chemosensor for Highly Sensitive and Ultrafast Detection of Folic Acid in Biofriendly Medium, Paper Strips and Real Samples. *Inorg. Chem. Front.* **2022**, *9*, 6288–6298.

(113) Tang, X.; Yu, H.; Bui, B.; Wang, L.; Xing, C.; Wang, S.; Chen, M.; Hu, Z.; Chen, W. Nitrogen-Doped Fluorescence Carbon Dots as Multi-Mechanism Detection for Iodide and Curcumin in Biological and Food Samples. *Bioact. Mater.* **2021**, *6*, 1541–1554.

(114) Panigrahi, S. K.; Mishra, A. K. Inner Filter Effect in Fluorescence Spectroscopy : As a Problem and as a Solution. *"Journal Photochem. Photobiol. C Photochem. Rev.* **2019**, *41*, 100318.

(115) Ghosh, S.; Krishnan, J.; Hossain, S. S.; Dhakshinamoorthy, A.; Biswas, S. MOF-Fabric Composites Based on a Multi-Functional MOF as Luminescent Sensors for a Neurotransmitter and an Anti-Cancer Drug. *ACS Appl. Mater. Interfaces* **2023**, *15*, 26843.

(116) Lin, M.; Zou, H. Y.; Yang, T.; Liu, Z. X.; Liu, H.; Huang, C. Z. An Inner Filter Effect Based Sensor of Tetracycline Hydrochloride as Developed by Loading Photoluminescent Carbon Nanodots in the Electrospun Nanofibers. *Nanoscale* **2016**, *8*, 2999–3007.

(117) Gómez-ordóñez, E.; Rupérez, P. FTIR-ATR Spectroscopy as a Tool for Polysaccharide Identi Fi Cation in Edible Brown and Red Seaweeds. **2011**, *25*, 1514–1520.

(118) Adv, R. S. C. Biodegradable Oligo (Poly-L-Lysine) as a High- Performance Hydration

Inhibitor for Shale. *RSC Adv.* **2015**, *5*, 84947–84958.

(119) Bloch, D. N. .; Sandre, M. .; Zichri, S. B. .; Masato, A. .; Bubacco, L. .; Jelinek, R. Scavenging Neurotoxic Aldehydes Using Lysine Carbon Dots†. *Nanoscale Adv.* **2023**, *5*, 1356–1367.

(120) Menaa, F.; Menaa, B.; Sharts, O. Development of Carbon-Fluorine Spectroscopy for Pharmaceutical and Biomedical Applications. *Faraday Discuss.* **2011**, *149*, 269–278.

(121) Lin, F. H.; Jian, C. H.; Lee, Y. H. A Study of Purified Montmorillonite Intercalated with 5-Fluorouracil as Drug Carrier. *Biomaterials* **2000**, *23*, 70.

(122) Yu, W.; Yu, Z.; Cui, Y.; Bao, Z. Degradation and Speciation of Li Salts during XPS Analysis for Battery Research. *ACS Energy Lett.* **2022**, *7*, 3270–3275.

(123) Stephen, A. Luminescent Chitosan/Carbon Dots as an Effective Nano-Drug Carrier for Neurodegenerative Diseases†. *RSC Adv.* **2020**, *10*, 24386–24396.

(124) Hongsa, N.; Thinbanmai, T.; Luesakul, U.; Sansanaphongpricha, K.; Muangsin, N. A Novel Modified Chitosan/Collagen Coated-Gold Nanoparticles for 5-Fluorouracil Delivery: Synthesis, Characterization, in Vitro Drug Release Studies, Anti-Inflammatory Activity and in Vitro Cytotoxicity Assay. *Carbohydr. Polym.* **2022**, *277*, 118858.

(125) Dhinasekaran, D.; Raj, R.; Rajendran, A. R.; Purushothaman, B.; Subramanian, B.; Prakasarao, A.; Singaravelu, G. Chitosan Mediated 5-Fluorouracil Functionalized Silica Nanoparticle from Rice Husk for Anticancer Activity. *Int. J. Biol. Macromol.* **2020**, *156*, 969–980.

(126) Kaur, N.; Tiwari, P.; Kumar, P.; Biswas, M.; Sonawane, A.; Mobin, S. M. Multifaceted Carbon Dots: Toward PH-Responsive Delivery of 5-Fluorouracil for In Vitro Antiproliferative Activity. *ACS Appl. Bio Mater.* **2023**.

https://doi.org/10.1021/acsabm.3c00228.

(127) Parsaei, M.; Akhbari, K. MOF-801 as a Nanoporous Water-Based Carrier System for in Situ Encapsulation and Sustained Release of 5-FU for Effective Cancer Therapy. *Inorg. Chem.* **2022**, *61*, 5912–5925.

(128) Zavareh, H. S.; Pourmadadi, M.; Moradi, A.; Yazdian, F.; Omidi, M. Chitosan/Carbon Quantum Dot/Aptamer Complex as a Potential Anticancer Drug Delivery System towards the Release of 5-Fluorouracil. *Int. J. Biol. Macromol.* **2020**, *165*, 1422–1430.

(129) Saito, G.; Swanson, J. A.; Lee, K. D. Drug Delivery Strategy Utilizing Conjugation via Reversible Disulfide Linkages: Role and Site of Cellular Reducing Activities. *Adv. Drug Deliv. Rev.* **2003**, *55*, 199–215.

(130) Casey, J. R.; Grinstein, S.; Orlowski, J. Sensors and Regulators of Intracellular PH. *Nat. Rev. Mol. Cell Biol.* **2010**, *11*, 50–61.

(131) Goyal, R.; Jerath, G.; Akhil, R.; Chandrasekharan, A.; Puppala, E. R.; Ponneganti, S.; Sarma, A.; Naidu, V. G. M.; Santhoshkumar, T. R.; Ramakrishnan, V. Geometry Encoded Functional Programming of Tumor Homing Peptides for Targeted Drug Delivery. *J. Control. Release* **2021**, *333*, 16–27.

(132) Rodas-zuluaga, L. I.; Itzel, Y. L.; Sosa-hern, J. E.; Melchor-martínez, E. M.; Aghalari, Z.; Salas, D.; Parra-saldívar, R. Case Studies in Chemical and Environmental Engineering Sources of Antibiotics Pollutants in the Aquatic Environment under SARS-CoV-2 Pandemic Situation. *Case Stud. Chem. Environ. Eng.* **2021**, *4*, 100127.

(133) Hikmat, K.; Aziz, H.; Mustafa, F. S.; Omer, K. M. Heavy Metal Pollution in the Aquatic Environment : E Ffi Cient and Low-Cost Removal Approaches to Eliminate Their Toxicity : A Review. *RSC Adv.* **2023**, *13*, 17595.

(134) Kayani, K. F. Removal of Pharmaceutical Residues from Aquatic Systems Using

Bimetallic Metal – Organic Frameworks (BMOFs): A Critical Review. *RSC Adv.* **2025**, *15*, 20168–20182.

(135) Draveny, M.; Rose, C.; Pinet, A.; Ferrié, L.; Figadère, B.; Brunel, J. M.; Masi, M. Scope and Limitations of Exploiting the Ability of the Chemosensitizer NV716 to Enhance the Activity of Tetracycline Derivatives against Pseudomonas Aeruginosa. *Molecules* **2023**, *28*, 4262. https://doi.org/10.3390/molecules28114262.

(136) Orylska-Ratynska, M.; Placek, W.; Owczarczyk-Saczonek, A. Tetracyclines—An Important Therapeutic Tool for Dermatologists. *Int. J. Environ. Res. Public Health* **2022**, *19*, 7246. https://doi.org/10.3390/ ijerph19127246.

(137) Kayani, K. F. Tetracycline in the Environment : Toxicity , Uses , Occurrence , Detection , and Removal by Covalent Organic Frameworks − Recent Advances and Challenges. *Sep. Purif. Technol.* **2025**, *364*, 132418.

(138) Netto, B. B.; da Silva, E. P.; de Aguiar da Costa, M.; de Rezende, V. L.; Bolan, S. J.; Ceretta, L. B.; Aschner, M.; Dominguini, D.; Gonçalves, C. L. Critical Period of Exposure to Mercury and the Diagnostic of Autism Spectrum Disorder: A Systematic Review. *J. Neurochem.* **2024**, 1–13.

(139) Kayani, K. F.; Mohammed, S. J. Mercury in Aquatic Environments : Toxicity and Advances in Remediation Using Covalent Organic Frameworks. *Mater. Adv.* **2025**, *6*, 3371–3385.

(140) Dufault, R.; Schnoll, R.; Lukiw, W. J.; LeBlanc, B.; Cornett, C.; Patrick, L.; Wallinga, D.; Gilbert, S. G.; Crider, R. Mercury Exposure, Nutritional Deficiencies and Metabolic Disruptions May Affect Learning in Children. *Behav. Brain Funct.* **2009**, *5*, 44. https://doi.org/10.1186/1744-9081-5-44.

(141) Jia, L.; Chen, R.; Xu, J.; Zhang, L.; Chen, X.; Bi, N.; Gou, J.; Zhao, T. A Stick-like

Intelligent Multicolor Nano-Sensor for the Detection of Tetracycline: The Integration of Nano-Clay and Carbon Dots. *J. Hazard. Mater.* **2021**, *413*, 125296. https://doi.org/10.1016/j.jhazmat.2021.125296.

(142) Zhu, P.; Hou, S. L.; Liu, Z.; Zhou, Y.; Alvarez, P. J. J.; Chen, W.; Zhang, T. Multi-Emission Carbon Dots Combining Turn-On Sensing and Fluorescence Quenching Exhibit Ultrahigh Selectivity for Mercury in Real Water Samples. *Environ. Sci. Technol.* **2024**, *58*, 9887–9895. https://doi.org/10.1021/acs.est.4c02355.

(143) Yang, X.; Luo, Y.; Zhu, S.; Feng, Y.; Zhuo, Y.; Dou, Y. Biosensors and Bioelectronics One-Pot Synthesis of High Fl Uorescent Carbon Nanoparticles and Their Applications as Probes for Detection of Tetracyclines. *Biosens. Bioelectron.* **2014**, *56*, 6. https://doi.org/10.1016/j.bios.2013.12.064.

(144) Enhanced, P.; Ye, B.; Yin, B. Highly Sensitive Detection of Mercury (II) Ions by Fluorescence. *Angew. Chem. Int. Ed.* **2008**, *47*, 8386. https://doi.org/10.1002/anie.200803069.

(145) Song, J.; Huang, M.; Lin, X.; Fong, S.; Li, Y.; Jiang, N.; Liu, Y.; Guo, H.; Li, Y. Novel Fe-Based Metal – Organic Framework (MOF) Modified Carbon Nanofiber as a Highly Selective and Sensitive Electrochemical Sensor for Tetracycline Detection. *Chem. Eng. J.* **2022**, *427*, 130913. https://doi.org/10.1016/j.cej.2021.130913.

(146) Samanta, P.; Desai, A. V; Sharma, S.; Chandra, P.; Ghosh, S. K. Selective Recognition of Hg 2+ Ion in Water by a Functionalized Metal − Organic Framework (MOF) Based Chemodosimeter. *Inorg. Chem.* **2018**, *57*, 2360. https://doi.org/10.1021/acs.inorgchem.7b02426.

(147) Wang, Z.; Cheng, C.; Gao, J.; Wang, Q. Copper Clusters-Based Luminescence Assay for Tetracycline and Cellular Imaging Studies. *J. Lumin.* **2017**, *190* (May), 115.

https://doi.org/10.1016/j.jlumin.2017.05.038.

(148) Guo, C.; Irudayaraj, J. Fluorescent Ag Clusters via a Protein-Directed Approach as a Hg(II) Ion Sensor. *Anal. Chem.* **2011**, *83*, 2883–2889. https://doi.org/10.1021/ac1032403.

(149) Gigi, G.; Mohan, A. M. Probe-Impregnated Monolithic Polymer as a Robust Solid-State Colorimetric Chemosensor for Selective Sensing of Hg2+ in Environmental Water and Cigarette Samples. *Environ. Res.* **2023**, *220*, 115210.

(150) Shi, L.; Yang, J. H.; Zeng, H. B.; Chen, Y. M.; Yang, S. C.; Wu, C.; Zeng, H.; Yoshihito, O.; Zhang, Q. Nanoscale Carbon Dots with High Fl Uorescence Quantum Yield : The Fl Uorescence Originates from Organic. *Nanoscale* **2016**, *8*, 14374.

(151) Essner, J. B.; Kist, J. A.; Polo-parada, L.; Baker, G. A. Artifacts and Errors Associated with the Ubiquitous Presence of Fluorescent Impurities in Carbon Nanodots. *Chem. Mater.* **2018**, *30*, 1878.

(152) Zhang, Y.; Yuan, R.; He, M.; Hu, G.; Jiang, J.; Xu, T.; Zhou, L.; Chen, W.; Xiang, W.; Liang, X. Multicolour Nitrogen-Doped Carbon Dots: Tunable Photoluminescence and Sandwich Fluorescent Glass-Based Light-Emitting Diodes†. *Nanoscale* **2017**, *9*, 17849.

(153) Wang, Q.; Zhang, S.; Wang, B.; Yang, X.; Zou, B.; Yang, B.; Lu, S. Pressure-Triggered Aggregation-Induced Emission Enhancement in Red Emissive Amorphous Carbon Dots†. *Nanoscale Horiz* **2019**, *4*, 1227.

(154) Ding, H.; Yu, S.; Wei, J.; Xiong, H. Full-Color Light-Emitting Carbon Dots with a Surface-State-Controlled Luminescence Mechanism. *ACS Nano* **2016**, *10*, 484.

(155) Yang, Z.; Xu, M.; Liu, Y.; He, F.; Gao, F.; Su, Y.; Wei, H.; Zhang, Y. Nitrogen-Doped, Carbon-Rich, Highly Photoluminescent Carbon Dots from Ammonium Citrate. *Nanoscale* **2014**, *6*, 1890–1895.

(156) Yang, Y.; Kong, W.; Li, H.; Liu, J.; Yang, M.; Huang, H.; Liu, Y.; Wang, Z.; Wang, Z.; Sham, T. K.; Zhong, J.; Wang, C.; Liu, Z.; Lee, S. T.; Kang, Z. Fluorescent N-Doped Carbon Dots as in Vitro and in Vivo Nanothermometer. *ACS Appl. Mater. Interfaces* **2015**, *7*, 27324–27330.

(157) Han, Y.; Bian, Y.; Wang, G. A Novel Nitrogen-Doped Carbon Dots as "on-off-on" Fluorescent Sensor for Ultrasensitive and Visual Quantitative Detection of Mercuric (II) and Glutathione. *J. Environ. Chem. Eng.* **2023**, *11*, 110750.

(158) Mohammed, S. J.; Hawaiz, F. E.; Aziz, S. B.; H Al-Jaf, S. Organic Soluble Nitrogen-Doped Carbon Dots (ONCDs) to Reduce the Optical Band Gap of PVC Polymer: Breakthrough in Polymer Composites with Improved Optical Properties. *Opt. Mater. (Amst).* **2024**, *149*, 115014.

(159) Zhao, Z.; Guo, Y.; Zhang, T.; Ma, J.; Li, H.; Zhou, J.; Wang, Z.; Sun, R. Preparation of Carbon Dots from Waste Cellulose Diacetate as a Sensor for Tetracycline Detection and Fluorescence Ink. *Int. J. Biol. Macromol.* **2020**, *164*, 4289–4298.

(160) Miao, H.; Wang, Y.; Yang, X. Carbon Dots Derived from Tobacco for Visually Distinguishing and Detecting Three Kinds of Tetracyclines. *Nanoscale* **2018**, *10*, 8139. https://doi.org/10.1039/c8nr02405g.

(161) Shen, Z.; Zhang, C.; Yu, X.; Li, J.; Wang, Z. Microwave-Assisted Synthesis of Cyclen Functional Carbon Dots to Construct a Ratiometric Fluorescent Probe for Tetracycline Detection †. *J. Mater. Chem. C*, **2018**, *6*, 9636–9641.

(162) Hu, J.; Liao, S.; Bai, Y.; Wu, S. Carbon Dots Derived from Green Jujube as Chemosensor for Tetracycline Detection. *J. Environ. Chem. Eng.* **2024**, *12*, 112595.

(163) Laddha, H.; Yadav, P.; Sharma, M.; Agarwal, M.; Gupta, R. Waste to Value Transformation : Converting Carica Papaya Seeds into Green Fluorescent Carbon Dots

for Simultaneous Selective Detection and Degradation of Tetracycline Hydrochloride in Water. *Environ. Res.* **2023**, *227*, 115820.

(164) Chen, L.; Li, Z.; Dou, Y.; Wang, H.; Chen, C.; Wang, X. Ratiometric Fluoroprobe Based on Eu-MOF@Tb3+ for Detecting Tetracycline Hydrochloride in Freshwater Fish and Its Application in Rapid Visual Detection. *J. Hazard. Mater.* **2024**, *469*, 134045.

(165) Rana, A.; Biswas, S. Electrophilicity Modulated Targeted Luminescence of MOF-Coated Cotton Composite for Dual Analyte Detection in Aqueous Medium. *Inorg. Chem. Front.* **2023**, *10*, 2742–2753.

(166) El Taher, B. J.; Sabouni, R.; Ghommem, M. Luminescent Metal Organic Framework for Selective Detection of Mercury in Aqueous Media: Microwave-Based Synthesis and Evaluation. *Colloids Surfaces A Physicochem. Eng. Asp.* **2020**, *607*, 125477.

(167) Tang, M.; Ren, G.; Zhu, B.; Yu, L.; Liu, X.; Chai, F.; Wu, H.; Wang, C. Facile Synthesis of Orange Emissive Carbon Dots and Their Application for Mercury Ion Detection and Fast Fingerprint Development. *Anal. Methods* **2019**, *11*, 2072.

(168) Phoungsiri, A.; Lerdpiriyaskulkij, N.; Monvisade, P.; Detsri, E.; Mathaweesansurn, A. A Ratiometric Fluorescence Amplification Using Copper Nanoclusters with O-Phenylenediamine Sensor for Determination of Mercury (II) in Natural Water. *Sensors* **2023**, *23*, 5429.

(169) Hu, B.; Hu, L. L.; Chen, M. L.; Wang, J. H. A FRET Ratiometric Fluorescence Sensing System for Mercury Detection and Intracellular Colorimetric Imaging in Live Hela Cells. *Biosens. Bioelectron.* **2013**, *49*, 499–505.

(170) Zhai, Y.; Li, Y.; Huang, X.; Hou, J.; Li, H.; Ai, S. Colorimetric and Ratiometric Fluorescent Dual-Mode Sensitive Detection of Hg2+ Based on UiO-66-NH2@Au Composite. *Spectrochim. Acta - Part A Mol. Biomol. Spectrosc.* **2022**, *275*, 121187.

(171) Pajewska-Szmyt, M.; Buszewski, B.; Gadzała-Kopciuch, R. Carbon Dots as Rapid Assays for Detection of Mercury(II) Ions Based on Turn-off Mode and Breast Milk. *Spectrochim. Acta - Part A Mol. Biomol. Spectrosc.* **2020**, *236*, 118320. https://doi.org/10.1016/j.saa.2020.118320.

(172) Singaravelu, C. M.; Deschanels, X.; Rey, C.; Causse, J. Solid-State Fluorescent Carbon Dots for Fluorimetric Sensing of Hg2+. *ACS Appl. Nano Mater.* **2021**, *4* (6), 6386–6397. https://doi.org/10.1021/acsanm.1c01400.

(173) Gupta, A.; Chaudhary, A.; Mehta, P.; Dwivedi, C.; Khan, S.; Verma, N. C.; Nandi, C. K. Nitrogen-Doped, Thiol-Functionalized Carbon Dots for Ultrasensitive Hg(Ii) Detection. *Chem. Commun.* **2015**, *51*, 10750–10753.

(174) Tan, Q.; Li, X.; Wang, L.; Zhao, J.; Yang, Q.; Sun, P.; Deng, Y.; Shen, G. One-Step Synthesis of Highly Fluorescent Carbon Dots as Fluorescence Sensors for the Parallel Detection of Cadmium and Mercury Ions. *Front. Chem.* **2022**, *10*, 1.

(175) Rana, A.; Biswas, S. Electrophilicity Modulated Targeted Luminescence of MOF-Coated Cotton Composite for Dual Analyte Detection in Aqueous Medium. *Inorg. Chem. Front.* **2023**, 2742–2753.

(176) Rana, A.; Biswas, S. Electrophilicity Modulated Targeted Luminescence of MOF-Coated Cotton Composite for Dual Analyte Detection in Aqueous Medium. *Inorg. Chem. Front.* **2023**, *10*, 2742–2753.

(177) Ma, J. Dougherty, D. The Cation–π Interaction. *Chem. Rev.* **1997**, *97*, 1303.

(178) Wu, S.; Zhou, R.; Chen, H.; Zhang, J.; Wu, P. Highly Efficient Oxygen Photosensitization of Carbon Dots: The Role of Nitrogen Doping. *Nanoscale* **2020**, *12*, 5543. https://doi.org/10.1039/c9nr10986b.

(179) Kayani, K. F.; Abdullah, A. M. Eco-Friendly Fluorescent Detection Method for Cu2+

Ions Combined with Smartphone-Integrated Paper Strip Sensors Based on Highly Fluorescent 2-Aminoterephthalic Acid in Milk Samples. *J. Food Compos. Anal.* **2024**, *135*, 106577.

(180) Kayani, K. F.; Omer, K. M. A Red Luminescent Europium Metal Organic Framework (Eu-MOF) Integrated with a Paper Strip Using Smartphone Visual Detection for Determination of Folic Acid in Pharmaceutical Formulations. *New J. Chem.* **2022**, *46*, 8152–8161.

(181) Panáček, A.; Kvítek, L.; Prucek, R.; Kolář, M.; Večeřová, R.; Pizúrová, N.; Sharma, V. K.; Nevěčná, T.; Zbořil, R. Silver Colloid Nanoparticles: Synthesis, Characterization, and Their Antibacterial Activity. *J. Phys. Chem. B* **2006**, *110*, 16248–16253.

(182) Levard, C.; Reinsch, B. C.; Michel, F. M.; Oumahi, C.; Lowry, G. V.; Brown, G. E. Sulfidation Processes of PVP-Coated Silver Nanoparticles in Aqueous Solution: Impact on Dissolution Rate. *Environ. Sci. Technol.* **2011**, *45*, 5260–5266.

(183) Pal, S.; Tak, Y. K.; Song, J. M. Does the Antibacterial Activity of Silver Nanoparticles Depend on the Shape of the Nanoparticle? A Study of the Gram-Negative Bacterium Escherichia Coli. *Appl. Environ. Microbiol.* **2007**, *73*, 1712–1720.

(184) Kawata, K.; Osawa, M.; Okabe, S. In Vitro Toxicity of Silver Nanoparticles at Noncytotoxic Doses to HepG2 Human Hepatoma Cells. *Environ. Sci. Technol.* **2009**, *43*, 6046–6051.

(185) Huang, X.; Ye, W.; Zhuang, J.; Hu, C.; Dong, H.; Lei, B.; Liu, Y. π-Conjugated Structure Enhances the UV Absorption Performance of Carbon Dots and Application in the Design of Light-Colored Sunglasses. *ACS Sustain. Chem. Eng.* **2024**, *12*, 10399–10410.

(186) Nakabayashi, T.; Oshita, S.; Sumikawa, R.; Sun, F.; Kinjo, M.; Ohta, N. PH Dependence

of the Fluorescence Lifetime of Enhanced Yellow Fluorescent Protein in Solution and Cells. *J. Photochem. Photobiol. A Chem.* **2012**, *235*, 65–71.

(187) Dutta Choudhury, S.; Chethodil, J. M.; Gharat, P. M.; Praseetha, P. K.; Pal, H. PH-Elicited Luminescence Functionalities of Carbon Dots: Mechanistic Insights. *J. Phys. Chem. Lett.* **2017**, *8*, 1389–1395.

(188) Shangguan, J.; He, D.; He, X.; Wang, K.; Xu, F.; Liu, J.; Tang, J.; Yang, X.; Huang, J. Label-Free Carbon-Dots-Based Ratiometric Fluorescence PH Nanoprobes for Intracellular PH Sensing. *Anal. Chem.* **2016**, *88*, 7837–7843.

(189) Ye, X.; Xiang, Y.; Wang, Q.; Li, Z.; Liu, Z. A Red Emissive Two-Photon Fluorescence Probe Based on Carbon Dots for Intracellular PH Detection. *Small* **2019**, *15*, 1901673.

(190) Mishra, M. K.; Kundu, S.; De, G. Stable Fluorescent CdS:Cu QDs and Their Hybridization with Carbon Polymer Dots for White Light Emission. *J. Mater. Chem. C* **2016**, *4*, 1665–1674.

(191) Eby, D. M.; Schaeublin, N. M.; Farrington, K. E.; Hussain, S. M.; Johnson, G. R. Lysozyme Catalyzes the Formation of Antimicrobial Silver Nanoparticles. *ACS Nano* **2009**, *3*, 984–994.

(192) Cheng, F.; Betts, J. W.; Kelly, S. M.; Schaller, J.; Heinze, T. Synthesis and Antibacterial Effects of Aqueous Colloidal Solutions of Silver Nanoparticles Using Aminocellulose as a Combined Reducing and Capping Reagent. *Green Chem.* **2013**, *15*, 989–998.

(193) Zhang, Y.; Peng, H.; Huang, W.; Zhou, Y.; Zhang, X.; Yan, D. Hyperbranched Poly(Amidoamine) as the Stabilizer and Reductant to Prepare Colloid Silver Nanoparticles in Situ and Their Antibacterial Activity. *J. Phys. Chem. C* **2008**, *112*, 2330–2336.

(194) Singh, P.; Lamanna, G.; Ménard-Moyon, C.; Toma, F. M.; Magnano, E.; Bondino, F.;

Prato, M.; Verma, S.; Bianco, A. Formation of Efficient Catalytic Silver Nanoparticles on Carbon Nanotubes by Adenine Functionalization. *Angew. Chemie - Int. Ed.* **2011**, *50*, 9893–9897.

(195) Shi, S.; Wang, X.; Li, Z.; Meng, J.; Chu, X.; Zhang, P.; Sun, B.; Zhang, J.; Gao, Y.; Xu, W.; Song, Q.; Xu, X.; Wu, J.; Zhou, N. Multifunctional Integrated Superhydrophobic Coatings with Unique Fluorescence and Micro/Micro/Nano-Hierarchical Structures Enabled by In Situ Self-Assembly. *ACS Appl. Mater. Interfaces* **2023**, *15*, 7442–7453.

(196) Li, Y.; Gao, A.; Liu, A.; Wang, Y.; Wei, Z.; Liu, Y.; Peng, H.; Yang, R.; Wang, F. Protein-Tannin Organic Polymer-Based Oxygen-Enriched Graded Porous Carbon as a Cathode for Metal-Ion Hybrid Capacitors. *ACS Appl. Mater. Interfaces* **2025**, *17*, 15468–15479.

(197) Sundar, S.; Kumar, D.; Nadene, N.; Kroukamp, E. M.; Abrahamse, H. Cellular Imaging and Bactericidal Mechanism of Green-Synthesized Silver Nanoparticles against Human Pathogenic Bacteria. *J. Photochem. Photobiol. B Biol.* **2018**, *178*, 259–269.

(198) Sen, C. K. Human Wounds and Its Burden: An Updated Compendium of Estimates. *Adv. Wound Care* **2019**, *8*, 39–48.

(199) Ma, L.; Zheng, J. J.; Zhou, N.; Zhang, R.; Fang, L.; Yang, Y.; Gao, X.; Chen, C.; Yan, X.; Fan, K. A Natural Biogenic Nanozyme for Scavenging Superoxide Radicals. *Nat. Commun.* **2024**, *15*, 233.

(200) Tan, X.; Lin, N.; Yang, S.; Gong, H.; Wang, M.; Li, N.; Liu, F.; Rao, D.; Wu, Y.; Tang, J.; Yang, Q. AuCu@CuO2 Aerogels with H2O2/O2 Self-Supplying and Quadruple Enzyme-Like Activity for MRSA-Infected Diabetic Wound Management. *Adv. Sci.* **2025**, 2502391.

(201) Yang, P.; Ju, Y.; Shen, N.; Zhu, S.; He, J.; Yang, L.; Lei, J.; He, X.; Shao, W.; Lei, L.;

Fang, B. Exos-Loaded Gox-Modified Smart-Response Self-Healing Hydrogel Improves the Microenvironment and Promotes Wound Healing in Diabetic Wounds. *Adv. Healthc. Mater.* **2024**, *14*, 2403304.

(202) Wang, X.; Li, Q.; Miao, Y.; Chen, X.; Zhang, X.; Shi, J.; Liu, F.; Wang, X.; Li, Z.; Yang, Y.; Zhang, X.; Wang, J.; Duan, J. A 0D-2D Heterojunction Bismuth Molybdate-Anchored Multifunctional Hydrogel for Highly Efficient Eradication of Drug-Resistant Bacteria. *ACS Nano* **2023**, *17*, 15568–15589.

(203) Singh, Y. P.; Bandyopadhyay, A.; Mandal, B. B. 3D Bioprinting Using Cross-Linker-Free Silk-Gelatin Bioink for Cartilage Tissue Engineering. *ACS Appl. Mater. Interfaces* **2019**, *11*, 33684–33696.

(204) Nur, G.; Rahman, M.; Dip, T. M.; Hossain, H.; Binta, N.; Baratchi, S. Recent Advances in Bioactive Wound Dressings. *Wound Rep Reg.* **2025**, *33*, e13233.

(205) Mandal, B. B. Wearable E-Bandage with Antimicrobial Ionogel as an Integrated Electroceutical Device for Accelerated Wound Healing. *ACS Mater. Lett. 2024,* **2024**, *6*, 3453–5461.

(206) Zhang, J.; Wang, L.; Xu, C.; Cao, Y.; Liu, S.; Reis, R. L.; Kundu, S. C.; Yang, X.; Xiao, B.; Duan, L. Transparent Silk Fibroin Film-Facilitated Infected-Wound Healing through Antibacterial, Improved Fibroblast Adhesion and Immune Modulation. *J. Mater. Chem. B, 2024*, **2024**, *12*, 475–488.

(207) Kuddushi, M. Recent Advances in Novel Materials and Techniques for Developing Transparent. *J. Mater. Chem. B, 2023,* **2023**, *11,* 6201–6224.

(208) Ajiteru, O.; Joo, O.; Kim, J.; Jin, Y.; Seung, J.; Lee, H.; Sultan, T.; Hum, C. Fabrication and Characterization of a Myrrh Hydrocolloid Dressing for Dermal Wound Healing. *Colloid Interface Sci. Commun.* **2022**, *48*, 100617.

(209) Yang, Y.; Ma, Y.; Wang, J.; Zhang, R.; Wu, M.; Zhong, S.; He, W.; Cui, X. An Injectable Thermosensitive Hydrogel with Antibacterial and Antioxidation Properties for Accelerating Wound Healing. *ACS Appl. Mater. Interfaces* **2024**, *16*, 46053–46065.

(210) Kelly, C. N.; Miller, A. T.; Hollister, S. J.; Guldberg, R. E.; Gall, K. Design and Structure – Function Characterization of 3D Printed Synthetic Porous Biomaterials for Tissue Engineering. *Adv. Healthc. Mater. 2018*, **2018**, *1701095*, 1–16.

(211) Zhang, K.; Bai, X.; Yuan, Z.; Cao, X.; Jiao, X.; Li, Y. Biomaterials Layered Nano Fi Ber Sponge with an Improved Capacity for Promoting Blood Coagulation and Wound Healing. *Biomaterials* **2019**, *204*, 70–79.

(212) Jiang, J.; Carlson, M. A.; Teusink, M. J.; Wang, H.; Macewan, M. R.; Xie, J. Expanding Two-Dimensional Electrospun Nano Fi Ber Membranes in the Third Dimension By a Modi Fi Ed Gas-Foaming Technique. *ACS Biomater. Sci. Eng.* **2015**, *1*, 991–1001.

(213) Hassan, S.; Rezaei, Z.; Luna, E.; Yilmaz-Aykut, D.; Lee, M. C.; Perea, A. M.; Jamaiyar, A.; Bassous, N.; Hirano, M.; Tourk, F. M.; Choi, C.; Becker, M.; Yazdi, I.; Fan, K.; Avila-Ramirez, A. E.; Ge, D.; Abdi, R.; Fisch, S.; Leijten, J.; Feinberg, M. W.; Mandal, B. B.; Liao, R.; Shin, S. R. Injectable Self-Oxygenating Cardio-Protective and Tissue Adhesive Silk-Based Hydrogel for Alleviating Ischemia After Mi Injury. *Small* **2024**, *20*, 2312261. https://doi.org/10.1002/smll.202312261.

(214) Gounden, V.; Singh, M. Hydrogels and Wound Healing: Current and Future Prospects. *Gels* **2024**, *10*, 43. https://doi.org/10.3390/gels10010043.

(215) Korting, HC., Schollmann, C., White, R. Management of Minor Acute Cutaneous Wounds : Importance of Wound Healing in a Moist Environment. *J. Eur. Acad. Dermatol. Venereol.* **2011**, *25*, 130–137.

(216) Xu, X.; Jerca, V. V.; Hoogenboom, R. Materials Horizons Bioinspired Double Network

Hydrogels : From Covalent Double Network Hydrogels via Hybrid Double Network Hydrogels to Physical Double Network Hydrogels. *Mater. Horiz.* **2021**, *8*, 1173–1188.

(217) Leonhardt, E. E.; Kang, N.; Hamad, M. A.; Wooley, K. L.; Elsabahy, M. Absorbable Hemostatic Hydrogels Comprising Composites of Sacrificial Templates and Honeycomb-like Nanofibrous Mats of Chitosan. *Nat. Commun.* **2019**, *10*, 2307.

(218) Guo, S.; Ren, Y.; Chang, R.; He, Y.; Zhang, D.; Guan, F.; Yao, M. Injectable Self-Healing Adhesive Chitosan Hydrogel with Antioxidative , Antibacterial , and Hemostatic Activities for Rapid Hemostasis and Skin Wound Healing. *ACS Appl. Mater. Interfaces* **2022**, *14*, 34455.

(219) Fan, X.; Zhou, W.; Chen, Y.; Yan, L.; Fang, Y.; Liu, H. An Antifreezing / Antiheating Hydrogel Containing Catechol Derivative Urushiol for Strong Wet Adhesion to Various Substrates. *ACS Appl. Mater. Interfaces* **2020**, *12*, 32031−32040.

(220) Xing, Q.; Zhen, L.; Zhou, X.; Zhong, S.; Li, F.; Li, J.; Meng, R. Cohesion Regulation of Polyphenol Cross-Linked Hydrogel Adhesives : From Intrinsic Cross-Link to Designs of Temporal Responsiveness. *Adv. Funct. Mater.* **2025**, *35*, 2414294.

(221) Li, H.; Zhou, X.; Luo, L.; Ding, Q.; Tang, S. Bio-Orthogonally Crosslinked Catechol–Chitosan Hydrogel for Effective Hemostasis and Wound Healing. *Carbohydr. Polym.* **2022**, *281*, 119039.

(222) Kostev, N. Magnetic Interactions and in Vitro Study of Biocompatible Hydroca Ff Eic Acid-Stabilized Fe – Pt Clusters as MRI Contrast Agents †. *RSC Adv.* **2018**, *8*, 14694–14704.

(223) Lin, Y.; Chen, C.; Wang, C.; Pu, F.; Ren, J.; Qu, X. Silver Nanoprobe for Sensitive and Selective Colorimetric Detection of Dopamine via Robust Ag-Catechol Interaction. *Chem. Commun.* **2011**, *47*, 1181–1183.

(224) Han, Y.; Lupitskyy, R.; Chou, T. M.; Stafford, C. M.; Du, H.; Sukhishvili, S. Effect of Oxidation on Surface-Enhanced Raman Scattering Activity of Silver Nanoparticles: A Quantitative Correlation. *Anal. Chem.* **2011**, *83*, 5873–5880.

(225) Shin, M.; Park, S.; Oh, B.; Kim, K.; Jo, S.; Lee, M. S.; Oh, S. S.; Hong, S.; Shin, E.; Kim, K.; Kang, S.; Lee, H. Complete Prevention of Blood Loss with Self-Sealing Haemostatic Needles. *Nat. Mater.* **2017**, *16*, 147.

(226) Zvarec, O.; Purushotham, S.; Masic, A.; Ramanujan, R. V.; Miserez, A. Catechol-Functionalized Chitosan/Iron Oxide Nanoparticle Composite Inspired by Mussel Thread Coating and Squid Beak Interfacial Chemistry. *Langmuir* **2013**, *29*, 10899–10906.

(227) Huang, W. C.; Ying, R.; Wang, W.; Guo, Y.; He, Y.; Mo, X.; Xue, C.; Mao, X. A Macroporous Hydrogel Dressing with Enhanced Antibacterial and Anti-Inflammatory Capabilities for Accelerated Wound Healing. *Adv. Funct. Mater.* **2020**, *30*, 1–10.

(228) Li, J.; Yu, F.; Chen, G.; Liu, J.; Li, X. L.; Cheng, B.; Mo, X. M.; Chen, C.; Pan, J. F. Moist-Retaining, Self-Recoverable, Bioadhesive, and Transparent in Situ Forming Hydrogels to Accelerate Wound Healing. *ACS Appl. Mater. Interfaces* **2020**, *12*, 2023–2038.

(229) Tokatlian, T.; Cam, C.; Segura, T. Porous Hyaluronic Acid Hydrogels for Localized Nonviral DNA Delivery in a Diabetic Wound Healing Model. *Adv. Healthc. Mater.* **2015**, *4*, 1084–1091.

(230) Qu, J.; Zhao, X.; Liang, Y.; Zhang, T.; Ma, P. X.; Guo, B. Antibacterial Adhesive Injectable Hydrogels with Rapid Self-Healing , Extensibility and Compressibility as Wound Dressing for Joints Skin Wound Healing. *Biomaterials* **2018**, *183* (July), 185–199.

(231) Feng, P.; Luo, Y.; Ke, C.; Qiu, H.; Wang, W.; Zhu, Y.; Hou, R.; Xu, L.; Wu, S. Chitosan-

Based Functional Materials for Skin Wound Repair: Mechanisms and Applications. *Front. Bioeng. Biotechnol.* **2021**, *9*, 650598.

(232) Li, X.; Ji, X.; Chen, K.; Wajid, M.; Li, B.; Cao, J.; Xiao, L.; Xiao, J.; Yang, G. Bioactive Materials Immobilized Thrombin on X-Ray Radiopaque Polyvinyl Alcohol / Chitosan Embolic Microspheres for Precise Localization and Topical Blood Coagulation. *Bioact. Mater.* **2021**, *6*, 2105–2119.

(233) Paul, P.; Roy, H.; Bhattacharjee, G.; Baruah, N.; Kundu, L. M. Amine-Rich Carbon Dots Synthesized from Kappa-Carrageenan and L-Lysine as a Dual Probe for Detection of Folic Acid and Tumor-Targeted Delivery of Therapeutics. *ACS Appl. Bio Mater.* **2024**, *7*, 6034.

LIST OF PUBLICATIONS

1. Baruah, N., **Paul, P.**, Bhattacharjee, G., Kundu, L.M*. "Unveiling Hetero-atom Containing Carbon Dots from Indigenous Soil Bacterial Metabolites and Their Application in Toxic Cr6+ Detection". *Environmental Science: Nano* **2026**, 13, 364.

2. Paul, P., Baruah, N., Roy, S., Das, H., Kundu, L.M*. "Carbon Dot-Capped Silver Nanoparticle-Embedded Double-Network Chitosan Hydrogel as Multifunctional Biomaterials in Antibacterial, Hemostasis and Wound Dressing". *ACS Biomater. Sci. Eng.* **2025**, 11, 7554−7569

3. Paul, P., Chakraborty, A., Kundu, L.M*. "Revealing the Potential of Biogenic Carbon Dots-Based Nanosensor for the High-Throughput Detection of Carcinogenic Hg^{+2} and Tetracyclines". *Microchim Acta* **2025**, 192:581

4. Paul, P.; Roy, H.; Bhattacharjee, G.; Baruah, N.; Kundu, L. M*. "Amine-Rich Carbon Dots Synthesized from Kappa-Carrageenan and L-Lysine as a Dual Probe for Detection of Folic Acid and Tumor-Targeted Delivery of Therapeutic". *ACS Appl. Bio Mater.* **2024**, *7*, 6034.

5. Paul, P., Das, H., Horo, H., Kundu, L.M. "DNA-Based Hydrogel in Drug Delivery". Biomaterial-based Hydrogels. Springer, Singapore. Springer. (Book Chapter 2024). doi.org/10.1007/978-981-99-8826-6_11.

LIST OF CONFERENCE PRESENTATIONS

1. Pallabi Paul, Lal Mohan Kundu. *One-day symposium on Ending Plastic Pollution, World Environment Day 2025*. IIT Guwahati, Assam, India. 5th June, 2025. (Poster)

2. Pallabi Paul, Lal Mohan Kundu. *21st International Conference on Modern Trends in Inorganic Chemistry (MTIC-XXI).* IIT Kharagpur, West Bengal, India. 14th-17th December, 2024. (Poster)

3. Pallabi Paul, Lal Mohan Kundu. *International Conference on Environmental Challenges, Opportunities and Sustainable Solutions (Environment 2024).* IIT Guwahati, Assam, India. 9th-11th December, 2024. (Best poster award)

4. Pallabi Paul, Hirakjyoti Roy, Gourav Bhattacharjee, Neeharika Baruah, Lal Mohan Kundu. *International Conference on Frontiers in Chemical Sciences (FICS-2024).* IIT Guwahati, Assam, India. 2nd-4th December, 2024. (Oral)

5. Pallabi Paul, Lal Mohan Kundu. *32nd CRSI National Symposium in Chemistry*. BITS Pilani, Pilani Campus, Rajasthan, India. 2nd-4th February, 2024. (Poster)